

NLO CALCULATIONS OF DIRECT PHOTONS AND MEASUREMENT OF  
NEUTRAL PIONS WITH THE ALICE EXPERIMENT

HENDRIK POPPENBORG, DISSERTATION 2019







Experimentelle Physik

# **NLO Calculations of Direct Photons and Measurement of Neutral Pions with the ALICE Experiment**

Inaugural-Dissertation  
zur Erlangung des Doktorgrades  
der Naturwissenschaften im Fachbereich Physik  
der Mathematisch-Naturwissenschaftlichen Fakultät  
der Westfälischen Wilhelms-Universität Münster

vorgelegt von  
**Hendrik Poppenborg**  
aus Münster

– 2019 –

Dekan: Prof. Dr. Gerhard Wilde

Erster Gutachter: Prof. Dr. Christian Klein-Bösing

Zweiter Gutachter: Prof. Dr. Michael Klasen

Tag der mündlichen Prüfung: \_\_\_\_\_

Tag der Promotion: \_\_\_\_\_

# CONTENTS

---

1	INTRODUCTION	1
2	STRONG INTERACTION AND THE QCD PHASES	3
2.1	The Theory of Strong Interaction	3
2.1.1	Hadrons and the Static Quark Model	3
2.1.2	Deep-Inelastic Scattering and the Parton Model	4
2.1.3	Quantum Chromodynamics	5
2.2	Kinematic Variables	10
2.3	The Quark-Gluon Plasma	14
2.4	Direct Photons and Neutral Pions in Hadron and Heavy-Ion Collisions	19
3	PARTICLE PRODUCTION IN HADRON-HADRON COLLISIONS	27
3.1	Factorization	27
3.2	Parton Densities	29
3.3	The Partonic Cross Section at NLO	32
3.4	Monte Carlo Parton Shower	33
3.5	Lund Model of Hadronization	36
3.6	Hadron Collisions and Soft Processes	38
3.7	Jets	40
4	DIRECT PHOTON PRODUCTION	43
4.1	Pythia 8	43
4.1.1	Discussion of Tuning	45
4.2	Powheg	46
4.3	Jetphox	48
5	EXPERIMENTAL SETUP	51
5.1	Large Hadron Collider	51
5.2	Jet and Photon Reconstruction at ATLAS, CMS and LHCb	52
5.3	The ALICE Detector	54
5.3.1	Inner Tracking System (ITS)	55
5.3.2	Time Projection Chamber (TPC)	55
5.3.3	Electromagnetic Calorimeter (EMCal)	56
5.3.4	Other Detectors	57
5.3.5	Triggering	59
5.4	Luminosity and Cross Section Measurement	60
5.5	Software	61
6	NEUTRAL PION MEASUREMENT FROM MERGED CLUSTERS	63
6.1	Neutral Pion Reconstruction in ALICE	63
6.2	Data set	67
6.2.1	Event selection	67
6.2.2	EMCal Triggers	68
6.2.3	Monte Carlo Simulations	69
6.2.4	Quality Assurance for Events and EMCAL Clusters	70

6.3	Cluster Selection . . . . .	71
6.3.1	Cluster Reconstruction . . . . .	71
6.3.2	General Cluster Selection . . . . .	72
6.3.3	Cluster Energy Correction . . . . .	75
6.4	Neutral Pion Analysis . . . . .	77
6.4.1	Acceptance and Reconstruction Efficiency . . . . .	78
6.4.2	Background Clusters, Shower Shape Cut and Signal Purity . . . . .	79
6.4.3	Correction for Secondary Neutral Pions . . . . .	84
6.5	Systematic Uncertainties . . . . .	86
6.6	Results . . . . .	92
7	DIRECT PHOTON PREDICTIONS FOR THE LHC . . . . .	95
7.1	Isolated Photon Production in pp Collisions with ATLAS . . . . .	95
7.2	Photon-Jet Correlations in pp and p-Pb Collisions with CMS . . . . .	98
7.3	Baseline for the Direct Photon Signal $R_\gamma$ . . . . .	102
7.3.1	Discussion of the Infrared Cutoff from the QED Parton Shower . . . . .	103
7.4	Nuclear Parton Densities and Photon-Jet Pairs in p-Pb Collisions . . . . .	105
	Summary . . . . .	111
	Zusammenfassung . . . . .	115
A	DELPHI UND BASHPHOX . . . . .	119
B	DETAILS ON NUCLEAR PDFS EPPS16 AND NCTEQ15 . . . . .	123
	List of Figures . . . . .	127
	List of Tables . . . . .	133
	Lebenslauf . . . . .	151
	Danksagung . . . . .	153



## INTRODUCTION

---

Collisions of protons that have been accelerated in the Large Hadron Collider ([LHC](#)) lead to the creation of up to dozens of mostly unstable particles. Particles with small mass that obey the strong interaction are especially abundant. Amongst them is the neutral pion ( $\pi^0$ ) which decays rapidly into two photons so that decay photons are a common signal from these collisions.

On the other hand, photons can be produced also directly in hard scattering of quarks and gluons that are the constituents of the colliding protons. This kind of *direct* photon signal is very rare compared to the abundance of decay photons, but contains valuable information about the production mechanisms of energetic quarks and gluons as well as the initial distribution of quarks and gluons in the colliding protons.

A fraction of the [LHC](#) uptime is dedicated to the research of ultra-relativistic heavy-ion collisions. Lead ions are used to provide conditions necessary for the creation of the Quark-Gluon Plasma ([QGP](#)), a state of hot nuclear matter where quarks and gluons are no longer bound in protons, neutrons or other hadrons. The unscreened color charges of quarks and gluons are the decisive degrees of freedom in a [QGP](#), so that it offers a unique playground for the fundamental theory of strong interaction, Quantum Chromodynamics ([QCD](#)).

The production of neutral pions and direct photons is thoroughly understood within the framework of perturbative QCD ([pQCD](#)). On the other hand, the improvement of measurements as well as theoretic descriptions must not halt — not only to drive the tests of [pQCD](#) to unprecedented accuracy, but also to constrain components of the theory for which there is no analytic solution due to the strongly coupled nature of the theory.

In the research history of the [QGP](#), neutral pions were among the first probes to confirm a strongly coupled environment in heavy-ion collisions. They were found to be significantly suppressed in comparison to the neutral pion production in proton-proton collisions and deuteron-gold collisions, where no effect of hot nuclear matter is conceived. Direct photons, on the other hand, are color-neutral objects and are only weakly modified by the [QGP](#); in that sense, they are complementary to probes like neutral pions. In fact, the direct photon probe helped to verify that the initial production of photons, quarks and gluons is not significantly modified in heavy-ion collisions, so that the strong final-state modification due to a [QGP](#) remained the only explanation.

We see that neutral pions and direct photons have played significant roles in the research of [QCD](#) in general and of the [QGP](#) in particular. This thesis contributes to their understanding in two ways: One part of this thesis is dedicated to the reconstruction of these neutral pions in proton-proton collisions at  $\sqrt{s} = 8$  TeV with the [ALICE](#) experiment, providing a baseline measurement for nuclear effects and constraining empirical inputs to [pQCD](#). The second part of this thesis deals with the phenomenolog-

ical treatment of direct photon observables in proton-proton collisions. Predictions for direct photon productions are provided and compared to data if available. These results are based on different phenomenological approaches, namely fixed-order calculations at Leading Order (LO) and Next-to-Leading Order (NLO) as well as parton shower descriptions.

The thesis is structured as follows: Ch. 2 provides a review of the strong interaction, an introduction of common variables and a brief review of hot nuclear matter research and the QGP. Next, Ch. 3 introduces how particle production in hadron-hadron collisions is described with the means of pQCD, the Parton Shower (PS) approach and models for soft processes. In Ch. 4, the three programs for theoretical predictions are introduced which are used in this thesis to describe direct photon production: JETPHOX, PYTHIA 8 and POWHEG. The experimental setup of the LHC and the ALICE experiment are introduced in Ch. 5 in view of the neutral pion measurement that is presented in Ch. 6. The subsequent Ch. 7 presents theoretical predictions of direct photon observables for various scenarios at the LHC including isolated photon production, photon-jet correlations and direct photon production at low transverse momenta.

## STRONG INTERACTION AND THE QCD PHASES

---

For a brief review of the strong interaction, it is instructive to follow history, which is being done in the following section. Then, common kinetic variables are introduced. Afterwards, a section provides a brief introduction of heavy-ion collisions and the QGP, providing the context of heavy-ion physics for this work. The last section discusses the role of direct photons and neutral pions in hadron-hadron and heavy-ion collisions.

### 2.1 THE THEORY OF STRONG INTERACTION

Before a dynamic description of the strong interaction was provided by Quantum Chromodynamics (QCD), many important concepts had already been developed that are still valid today. The next subsections cover the static quark model which defines the classification of baryons and mesons, the parton model whose concepts still apply, and finally, elementary aspects of QCD.

#### 2.1.1 Hadrons and the Static Quark Model

*The finder of a new elementary particle used to be rewarded by a Nobel Prize, but such a discovery now ought to be punished by a \$10,000 fine.* This sentence, itself a quotation in the Nobel lecture of W. E. Lamb, maybe expresses best the discomfort of the particle physics community around 1955. With the era of particle accelerators, the amount of known hadrons exploded with no apparent constraint. Comfort in the community was restored in 1964 by Murray Gell-Mann and George Zweig who invented a system that fitted the proverbial particle zoo [1] [2].

The lines along which hadrons could be classified are given by the quantum numbers of isospin and strangeness, which had been identified before as conserved quantum numbers with respect to hadronic interactions. The seminal achievement was to assume quarks as fundamental fermions and building blocks for hadrons, carrying spin, isospin, strangeness and a certain fraction of electric charge. On the basis of SU(3), the known mesons (consisting of quark and antiquark,  $q\bar{q}$ ) and baryons (consisting of three quarks,  $qqq$ ) could be classified in multiplets. These are shown for the lightest and most abundant hadrons in Fig. 2.1 and Fig. 2.2.

The static quark model had many successes besides the classification of hadrons. Based on the model, successful calculations of scattering cross sections for mesons and baryons were carried out. The mass splitting of mesons and baryons was explained as well as their magnetic moments. What was maybe most impressive at this time: The  $\Omega^-$  baryon has been predicted and discovered for one spot in the baryon decuplet that had remained empty, with strangeness  $-3$  and isospin 0. On the other hand, the model explains why certain particles are not found such as doubly charged mesons.

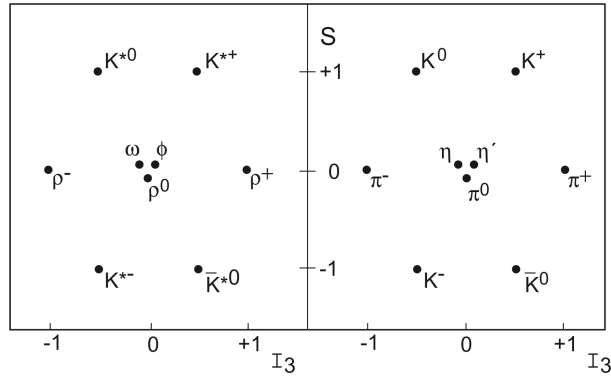


Figure 2.1: Multiplets of the lightest vector mesons (left) and pseudoscalar mesons (right) [3].

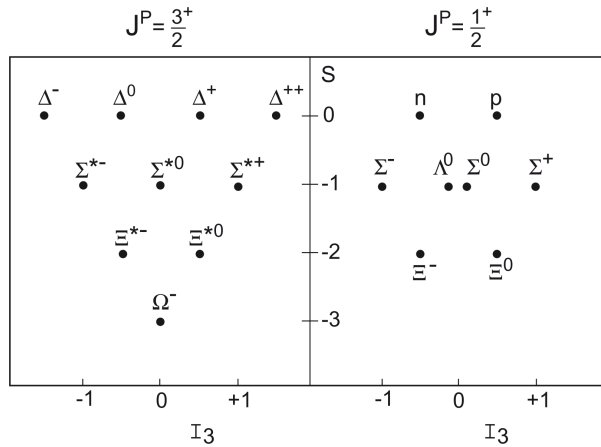


Figure 2.2: Multiplets of the lightest baryons [3].

By today, quarks are known to come in six different flavors: up, down, strange, charm, bottom and top. In principle, the classification can be generalized to include the three latter types<sup>1</sup>, but the large quark mass differences of larger 1 GeV leave the underlying symmetry of the static quark model broken. Already the small mass differences between up, down and strange quark lead to a slightly broken symmetry; with an unbroken symmetry, all hadron masses would be the same.

So, following the fruitful proposal of Gell-Mann and Zweig, quarks were considered the underlying degrees of freedom that determine the structure of baryons and mesons. Accordingly, quarks have been searched for in cosmic rays, accelerators of ever increasing energies and in "substances ranging from oyster shells to moon rocks" [4], but were nowhere to be found. Many physicists at that time considered quarks a manifestation of some elusive mechanism — a mere mathematical reality.

### 2.1.2 Deep-Inelastic Scattering and the Parton Model

Evidence for the physical reality of quarks was reported in 1968 and the following years from deep-inelastic scattering of electrons and nucleons. Electron energies up to 25 GeV made it possible to resolve the internal structure of nucleons and to make decisive observations in favor of the quark hypothesis. Similar to classical Rutherford scattering, a form factor associated with the scattering target revealed that the electron scattered elastically against point-like constituents of the nucleon.

For the theoretical description, James Bjorken and others developed the *parton model*. In this model, the partons are point-like constituents that share a fraction of the parent nucleon that moves fast within the scattering frame. Despite the presumably complex substructure of the nucleon, the reaction cross section is assumed to be the incoherent sum of partonic cross sections rather than a sum of amplitudes. In other words, the struck parton is free in the moment of scattering. This assumption was later developed to become an invaluable bridge between the results of hadron collisions and theoretical particle physics (see Sec. 3.1).

The reaction cross section  $\sigma$  was parametrized in terms of the structure function  $F_2(x, Q^2)$ , which is the charge weighted sum of parton momentum densities  $xf_i(x, Q^2)$ :

$$F_2(x, Q^2) = \sum e_i^2 x f_i(x, Q^2) \quad (2.1)$$

$$\frac{d^2\sigma}{dx dQ^2} \sim F_2(x, Q^2) \quad (2.2)$$

The point-like character of partons was proven with the key observation that the structure function did not rely on the hard scattering scale,  $F_2(x, Q^2) = F_2(x)$  (Bjorken Scaling). Accounting for the polarization of the exchanged virtual photon, the partons in deep-inelastic electron-nucleon scattering had to carry a spin 1/2 (Callan-Gross Relation). Ultimately, they were subdivided in *valence quarks* and virtual pairs of *sea quarks* ( $q\bar{q}$ ). In the sense that the three valence quarks account for the quantum numbers of the nucleon, they can be identified with the quarks Murray Gell-Mann and George Zweig had in mind.

Two further findings of the deep-inelastic elastic scattering experiments paved the way to **QCD**: Neutrino-nucleon scattering experiments revealed that half of the nucleon momentum is actually carried by a color-neutral constituent that was later identified as the gluon, the gauge boson of **QCD**. Also, close inspection of the structure functions revealed a small  $Q^2$  dependence, a scale-breaking pattern that would later be attributed to gluon radiation and quark-antiquark pair formation.

### 2.1.3 Quantum Chromodynamics

In hindsight, it is surprising to learn that **QCD** was not immediately accepted in 1973, when David Politzer [5], David Gross and Frank Wilczek [6] made their seminal contribution. Several other theories were seriously considered to explain the Deep Inelastic Scattering (**DIS**) results [7], such as an extended resonance model (with unlimited resonances to explain scale invariance), the vector dominance models (explaining the large cross section with the duality of photon and vector mesons) or a nucleon model with a substructure of virtual (and point-like) pions and nucleons. All theories revealed deficiencies at some point, but objection to **QCD** was particular, because the issue of quark confinement was too problematic for many [8].

Anyway, empirical evidence favored the quantum field theory: The characteristic logarithmic corrections of **QCD** were able to describe the scale breaking pattern in **DIS**. Also, the total cross section of  $e^+e^- \rightarrow$  hadrons was consistently described after the inclusion of the charm quark that was discovered in late 1974. Several successes later, **QCD** received a decisive confirmation in 1979 when the gluon was discovered in three-jet events [9].

### THE QCD LAGRANGIAN DENSITY

We assume that all features of the strong interaction are encoded in the **QCD** Lagrangian (density). One might say, some features like the formation of bound states are downright *encrypted*, because we are only partially able to provide solutions. In order to understand the character of the strong interaction it is instructive to take a look at the Lagrangian of Quantum Electrodynamics (**QED**):

$$\mathcal{L}_{\text{QED}} = -\frac{1}{4}F_{\mu\nu}F^{\mu\nu} - m_e\bar{\psi}_e\psi_e - \bar{\psi}_e\gamma^\nu[\partial_\mu + ieA_\mu]\psi_e \quad (2.3)$$

The first term describes the free electromagnetic field with the field tensor  $F_{\mu\nu}$  using the four-potential  $A^\mu$ :

$$F_{\mu\nu} = \partial_\mu A_\nu - \partial_\nu A_\mu \quad (2.4)$$

The second term describes the free electron using the Dirac four-spinor  $\psi_e$  at rest mass. The last term describes the kinetic energy of the electron and its interaction with the electromagnetic field  $A_\mu$ . Introducing the **QCD** Lagrangian with quark fields  $\psi_q$  and gluon fields  $A_\nu^C$ , we find a very similar structure:

$$\mathcal{L}_{\text{QCD}} = -\frac{1}{4}F_{\mu\nu}^C F_C^{\mu\nu} - \sum_q m_q \bar{\psi}_q \psi_q - \sum_q \bar{\psi}_q \gamma^\nu [\partial_\mu - ig_s A_\mu^C t_C] \psi_q \quad (2.5)$$

The electron charge  $-e$  has turned to the strong charge  $g_s$  and instead of one electron field, we find  $n = 6$  quark fields corresponding to the six quark flavors. Additionally,  $SU(3)$  color symmetry introduces the gluon-color index  $C = 1, \dots, 8$  and  $3 \times 3$  matrices  $t_C$  (Gell-Mann matrices).

By now, **QED** terms have only been redefined or extended to account for more fermion flavors and a new octet of fields. The particular nature of the strong interaction is revealed in the gluonic field tensor

$$F_{\mu\nu}^C = \partial_\mu A_\nu^C - \partial_\nu A_\mu^C + g_s f_{AB}^C A_\mu^A A_\nu^B. \quad (2.6)$$

Here, the **QCD** structure functions  $f_{AB}^C$  enter, relating to the Gell-Mann matrices  $t_C$  via the commutation relation

$$[t_A, t_B] = if_{AB}^C t_C. \quad (2.7)$$

In comparison to Eq. (2.4) we find a third term in eq. (2.6) that describes an interaction between the boson fields. More explicitly, we find three-gluon terms and four-gluon terms when expanding  $F_{\mu\nu}^C F_C^{\mu\nu}$ . The gluon-gluon interaction arises because the generators do not commute,  $f_{AB}^C \neq 0$ . In the mathematical scope of gauge theories, **QCD** is therefore regarded as a non-Abelian gauge theory.

### THE ROLE OF COLOR

The quarks carry a single color charge (r, g or b), while the eight Gell-Mann matrices of color  $SU(3)$  correspond to eight gluon types that each carries a charge pair of color and anti-color. Because no color charged objects have been observed so far, it is assumed that only color singlet states can exist as free particles (color confinement hypothesis). Color singlets can be formed by three quarks of different color or by a quark-antiquark pair, which allows for the existence of baryons and mesons<sup>2</sup>.

In practice, scattering amplitudes always contain the sum over all possible color paths. The recurring pattern of color flows is accounted for by color factors that can be associated with certain processes:

$$C_F = \frac{4}{3} \text{ (gluon emission from a quark)} \quad (2.8)$$

$$C_A = 3 \text{ (gluon emission from a gluon)} \quad (2.9)$$

$$T_R = \frac{1}{2} \text{ (gluon split to } q\bar{q}\text{)} \quad (2.10)$$

The color factors modify the strong coupling  $\alpha_s = g_s^2/4\pi$  in the respective processes. For instance, gluon emission off a gluon instead off a quark is favoured by a factor  $3/(4/3) = 9/4$ .

### SOLVING QCD

QCD is not fully solvable and one has to consider some sort of approximation. Besides effective models, there are two approaches that allow predictions calculated from the first principles encoded in the QCD Lagrangian: One approach is Lattice QCD (LQCD) which, on the basis of a discretized space-time, allows unprecedented insights into non-perturbative phenomena like confinement, hadron masses and gluon self-interaction [10]. For a multitude of high-energy problems, however, pQCD can be applied: QCD becomes analytically solvable where the interaction can be regarded as a small perturbation of the free theory. The coupling constant  $\alpha_s$  of the strong interaction then serves as the parameter for a series expansion around the free theory<sup>3</sup>.

## THE RUNNING COUPLING

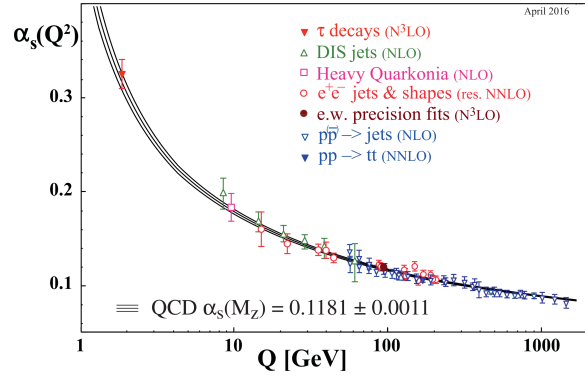


Figure 2.3: The running coupling  $\alpha_s$  and measurements extracted at a given order of perturbation theory and energy scale  $Q$  [10].

The *running* coupling  $\alpha_s(Q^2)$  of the strong interaction is governed by the beta function  $\beta(\alpha_s)$ :

$$\beta(\alpha_s) = \frac{\partial \alpha_s}{\partial \log Q^2} = -\alpha_s^2 (b_0 + b_1 \alpha_s + b_2 \alpha_s^2 + \dots) \quad (2.11)$$

Here, the technique of renormalization has been used to treat Ultraviolet (UV) divergent terms that arise in loop diagrams. A *renormalization group equation* like the beta function above follows from the requirement that the physical result must not depend on a change of scale  $Q^2$ . The LO (1-loop) coefficient  $b_0$  is given by

$$b_0 = \frac{11C_A - 4T_R n_f}{12\pi}, \quad (2.12)$$

where the first and second term arise due to gluon and quark loops, respectively. The scale dependency (the *running* of  $\alpha_s$ ) depends on the number of quark flavors  $n_f$  that only enter at an energy scale above the respective quark mass. For six quarks,  $b_0$  is still positive so that  $\beta_s$  is negative and  $\alpha_s$  tends logarithmically against zero. This is the important feature of *asymptotic freedom* that allows to treat quarks and gluons as quasi-free particles above some scale.

The value of  $\alpha_s$  is usually given for a certain reference scale, the Z boson mass,  $Q^2 = M_Z^2$ . Values of  $\alpha_s$  at different scales are given by the solution of the renormalization group equation (2.11):

$$\alpha_s(Q^2) = \alpha_s(M_Z^2) \frac{1}{1 + b_0 \alpha_s(M_Z^2) \log(Q^2/M_Z^2) + \mathcal{O}(\alpha_s^2)} \quad (2.13)$$

The resulting running of the strong coupling is depicted in Fig. 2.3 together with selected measurements. An alternative representation of the running coupling is sometimes given through

$$\alpha_s(Q^2) = \frac{1}{b_0 \log(Q^2/\Lambda_{\text{QCD}}^2)}, \quad (2.14)$$

where the divergence at  $\Lambda_{\text{QCD}} \sim 200 \text{ MeV}$  (Landau pole) becomes apparent. This kind of representation has gone out of fashion, also because reference to the Landau pole becomes ambiguous beyond LO.



First measurements of the running coupling had been performed from the description of the scaling violations found in DIS.

Modern methods to determine  $\alpha_s$  can be categorized as follows [10]:

- Hadronic  $\tau$  decays allow to measure the strong coupling at a very low scale  $M_\tau = 1.777 \text{ GeV}$ . The extraction is based on a perturbative series up to NNNLO, for which 5-loop calculations were carried out with around 20000 Feynman diagrams. In terms of scale, a complementary measurement is given by the hadronic decay of the Z boson, usually referred to as electroweak precision fit.
- A recent method to determine the strong coupling is given by LQCD, where the physical input for the lattice scale is given by the mass splitting in the Y spectrum.
- Scale deviations in structure functions are still being considered as a constraint for  $\alpha_s$ , but with NNLO accuracy.
- Inclusive jet cross sections from DIS are considered as well as jet shapes (e. g. jet broadening) and three-jet events at the Large Electron-Positron Collider (LEP).

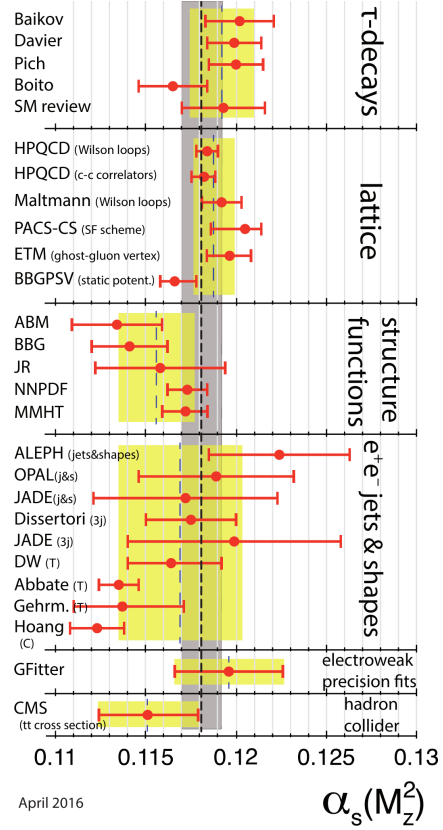


Figure 2.4: Relevant measurements for the current world average of  $\alpha_s$  [10].

As already indicated above, determinations of  $\alpha_s$  are only considered for the world average value if the respective extraction is at least NNLO accurate. Currently, this excludes the traditional determination from quarkonia decays and also all current results on jet production from the LHC except for the top-pair production.

To conclude and to indicate the progress in the description of QCD, Fig. 2.5 depicts the world average of the strong coupling from 1992.

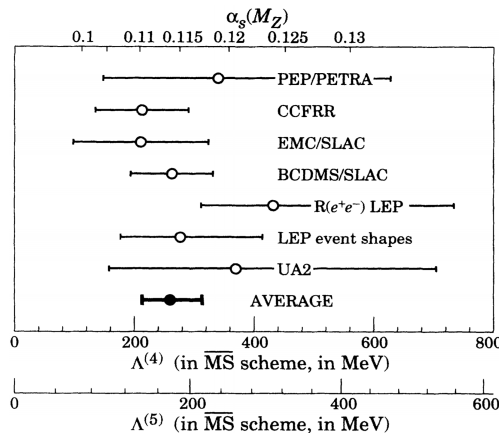


Figure 2.5: World average of  $\alpha_s$  in 1992 [11].

## 2.2 KINEMATIC VARIABLES

## CENTER-OF-MASS ENERGY &amp; MANDELSTAM INVARIANTS

The center-of-mass (**cm**) energy that is available in a collision of any two particles with initial four-momenta  $\mathbf{p}_1, \mathbf{p}_2$ , and final state momenta  $\mathbf{p}_3, \mathbf{p}_4$  in case of a  $2 \rightarrow 2$  process, is given by the square root of the Mandelstam invariant  $s$  [12]:

$$\sqrt{s} = \sqrt{(\mathbf{p}_1 + \mathbf{p}_2)^2} = \sqrt{(\mathbf{p}_3 + \mathbf{p}_4)^2} \quad (2.15)$$

$\sqrt{s}$  is a key quantity of any collision experiment: It determines the maximum resolution power of the experiment and the potential to create high-energy phenomena such as the production of massive particles. Since  $\sqrt{s}$  is Lorentz invariant, direct comparison is possible between different frames, for instance between a symmetric collider experiment and a fixed-target experiment.

Two other Mandelstam invariants  $t$  and  $u$  describe the momentum transfer between the initial and final state particles:

$$t = (\mathbf{p}_1 - \mathbf{p}_3)^2 = (\mathbf{p}_2 - \mathbf{p}_4)^2 \quad (2.16)$$

$$u = (\mathbf{p}_1 - \mathbf{p}_4)^2 = (\mathbf{p}_2 - \mathbf{p}_3)^2 \quad (2.17)$$

In Quantum Field Theory (**QFT**), the exchanged four-momentum squared  $q^2$  determines the hard scattering scale  $Q^2 = -q^2$ . Depending on the nature of the process, the squared momentum transfer equals one of the Mandelstam invariants. They are therefore used to classify Feynman diagrams, of which there can be one or more to describe a physical process (Fig. 2.6).

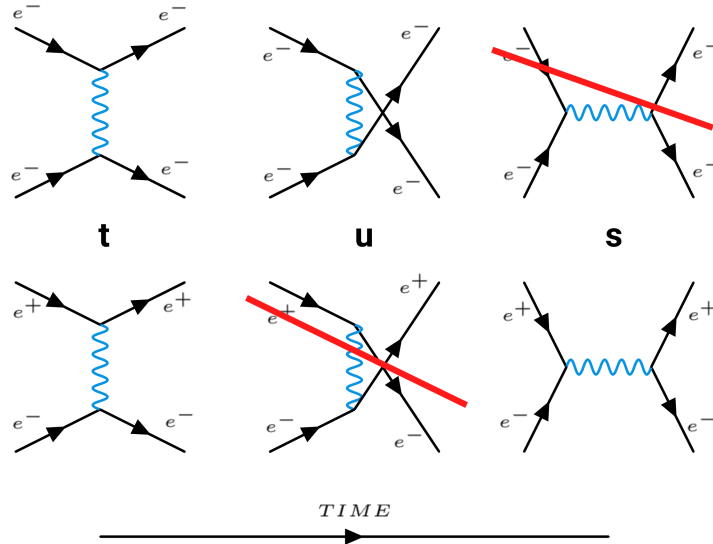


Figure 2.6: Mandelstam invariants characterize possible paths of intermediate particles in a  $2 \rightarrow 2$  scattering. Not every path is always allowed by physical constraints. In this case, a doubly charged photon would be necessary to allow the  $u$ -channel in  $e^-e^+ \rightarrow e^-e^+$  or the  $s$ -channel in  $e^-e^- \rightarrow e^-e^-$ .

## TRANSVERSE AND LONGITUDINAL KINEMATICS

The reference frame of a given process does not necessarily coincide with the **cm** system of the colliding beam particles. Instead, a Lorentz boost has to be considered along the beam axis, usually defined as the  $z$ -axis. Kinematic variables in particle physics are chosen accordingly<sup>4</sup>.

Unaffected by a boost along the beam axis is the momentum transverse to the beam axis  $p_T$  and the azimuthal angle  $\varphi$  within the transverse plane. Concerning the longitudinal kinematics, along the beam axis, a more convenient quantity than the velocity  $\beta_z$  or the momentum  $p_z$  is the rapidity  $y$ :

$$y = \frac{1}{2} \log \frac{E + p_z}{E - p_z} = \frac{1}{2} \log \frac{1 + \beta_z}{1 - \beta_z} \quad (2.18)$$

Longitudinal momentum or velocity are now recast in a way that allows for an easier transformation under Lorentz boosts along the beam axis. In case a frame  $B$  is boosted with  $y_{\text{boost}}$  with respect to frame  $A$ , the rapidity  $y_A$  in frame  $A$  is given by rapidity  $y_B$  in frame  $B$  such that

$$y_B = y_A - y_{\text{boost}}. \quad (2.19)$$

The rapidity measured in system  $B$  is given by a simple addition. As an important consequence of this transformation rule, the length of rapidity intervals  $\Delta y$  is Lorentz invariant.

In the limit of large momenta or small masses, ( $E \approx p$ ), a useful simplification takes place:

$$\lim_{p \rightarrow E} = \frac{1}{2} \log \frac{p + p_z}{p - p_z} = \frac{1}{2} \log \frac{1 + \cos \theta}{1 - \cos \theta} = -\log \tan \frac{\theta}{2} =: \eta \quad (2.20)$$

In this approximation, the rapidity is called pseudorapidity  $\eta$  and can be determined solely with the angle  $\theta$  between particle and beam axis. Using the pseudorapidity  $\eta$  as a proxy for the longitudinal momentum is a great convenience from the experimentalist's perspective, because it can be derived from geometric properties that are readily available, and it is not required to identify particles to determine  $E$ . Accordingly, the longitudinal acceptance of a detector is usually given in terms of pseudorapidity  $\eta$ . Typical values of (pseudo-)rapidities are exemplified in table 2.1.

Since the three variables  $p_T$ ,  $\varphi$  and  $y$  (or  $\eta$ ) describe the possible kinematic configurations, they span the space that is simply called the *phase space*.

$E$	$y$	$\eta$	$\theta$	comment
100 GeV	5.3	$\infty$	0	RHIC beam
6.5 TeV	9.5	$\infty$	0	LHC beam
320 EeV	27.3	$\infty$	0	Oh-My-God particle [13]
200 MeV	0.56	0.88	45°	low energy pion in ALICE-TPC acceptance limit
10 GeV	0.88	0.88	45°	high energy pion in ALICE-TPC acceptance limit
200 MeV	0.87	2.44	10°	low energy pion in CMS acceptance limit
10 GeV	2.43	2.44	10°	high energy pion in CMS acceptance limit

Table 2.1: Examples for rapidity and pseudorapidity.

## PARTON MOMENTUM FRACTION

Sufficiently hard interactions of hadrons are described in terms of parton scatterings, i. e. interactions of the single quarks or gluons that make up the mother hadrons. The essential variable to describe the parton momentum inside the hadron, before the scattering, is the Bjorken scale variable  $x$ . It can be interpreted as the hadron momentum fraction carried by the parton<sup>5</sup>. Parton distribution functions are necessary to describe hadron collisions, but cannot yet be calculated from first principles so that their measurement is a crucial task.

At LO, the momentum fractions  $x_1$  and  $x_2$  of massless partons that take part in a  $2 \rightarrow 2$  scattering can be related to the previously introduced kinematic variables:

$$\sqrt{s_{12}} = x_1 x_2 \sqrt{s} \quad (2.21)$$

$$x_1 = \frac{p_T}{\sqrt{s}} (\exp(\eta_3) + \exp(\eta_4)) \quad (2.22)$$

$$x_2 = \frac{p_T}{\sqrt{s}} (\exp(-\eta_3) + \exp(-\eta_4)) \quad (2.23)$$

Unfortunately, the outgoing partons 3 and 4 are no stable objects; to be measured is the multitude of hadrons that the partons evolve into. However, the original momentum of the outgoing parton can be accessed by suitable observables such as jets (see Sec. 3.7). Also, single particles can be used if the relation between particle momentum and parton momentum is known (fragmentation function). In rare cases, one of the outgoing particles of the  $2 \rightarrow 2$  process can also be a photon. Measurement of these *prompt photons* are thus a straightforward way to probe the parton momentum distribution.

A useful pocket formula to estimate the  $x$ -region probed by an experiment with a cm energy  $\sqrt{s}$  is

$$x \approx \frac{2p_T}{\sqrt{s}}, \quad (2.24)$$

where  $p_T$  is the transverse momentum of a jet or just the most energetic particle measured at mid-rapidity  $y \approx 0$ . To give an example, the ALICE detector at the LHC measures jets in a transverse momentum interval of roughly 10 – 100 GeV so that the probed  $x$  regime is 0.002 – 0.02 for the typical LHC energy of around 10 TeV. Parton distribution functions QCD will be discussed in greater detail in Sec. 3.2.

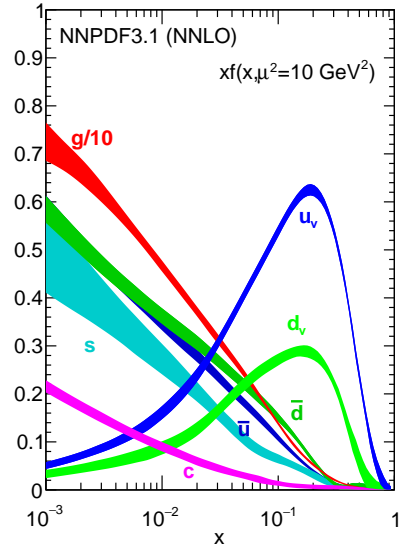


Figure 2.7: Example for a parton distribution function [14].

## CM ENERGY AND RAPIDITY IN HEAVY-ION COLLISIONS

The maximum momentum  $p$  of a beam particle with charge  $q$  in a particle accelerator is constrained by the magnetic rigidity  $B\rho$  of the dipole magnets [15]:

$$B\rho = \frac{p}{q} \quad (2.25)$$

For a given magnetic field strength  $B$  and a required bending radius  $\rho$ , the ratio  $p/q$  is constant. Accordingly, beam momentum is lowered for heavy-ion beams carrying neutrons that contribute mass but no charge. For two ion beams with mass numbers  $A_{1,2}$  and charge numbers  $Z_{1,2}$ , the **cm** energy per nucleon-pair  $\sqrt{s_{\text{NN}}}$  relates to the energy available in proton-proton collisions  $\sqrt{s}$  as follows:

$$\sqrt{s_{\text{NN}}} = \sqrt{(E_1^2 + E_2^2) - (\vec{p}_1 + \vec{p}_2)^2} \approx \sqrt{4p_1p_2} = \sqrt{\frac{Z_1Z_2}{A_1A_2}} \sqrt{s} \quad (2.26)$$

In case of asymmetric collision systems, the different beam momenta imply a rapidity shift  $\Delta y$  of the **cm** frame with respect to the lab frame:

$$\Delta y = \frac{1}{2} \log \left( \frac{Z_1A_2}{Z_2A_1} \right) \quad (2.27)$$

## 2.3 THE QUARK-GLUON PLASMA

Ordinary nuclear matter can be heated or compressed to the point where the hadron wave functions overlap so that quarks and gluons are no longer confined to hadronic boundaries [16]. Thermodynamic considerations suggested even before the emergence of QCD a limiting temperature, the Hagedorn temperature  $T_H \approx 160$  MeV, for systems that assume purely hadronic degrees of freedom [17]. This temperature regime is in line with the results of modern LQCD calculations that predict a transition from hadronic matter to a QGP at around  $T = 156 \pm 1.5$  MeV [18]. Such temperatures can be achieved in high-energy heavy-ion collisions.

## HEAVY-ION COLLISIONS

In order to understand what is happening in heavy-ion collisions, it is instructive to look at measurements of the net proton production ( $N_{\text{proton}} - N_{\text{anti-proton}}$ ) as a function of rapidity (left panel of Fig. 2.8).

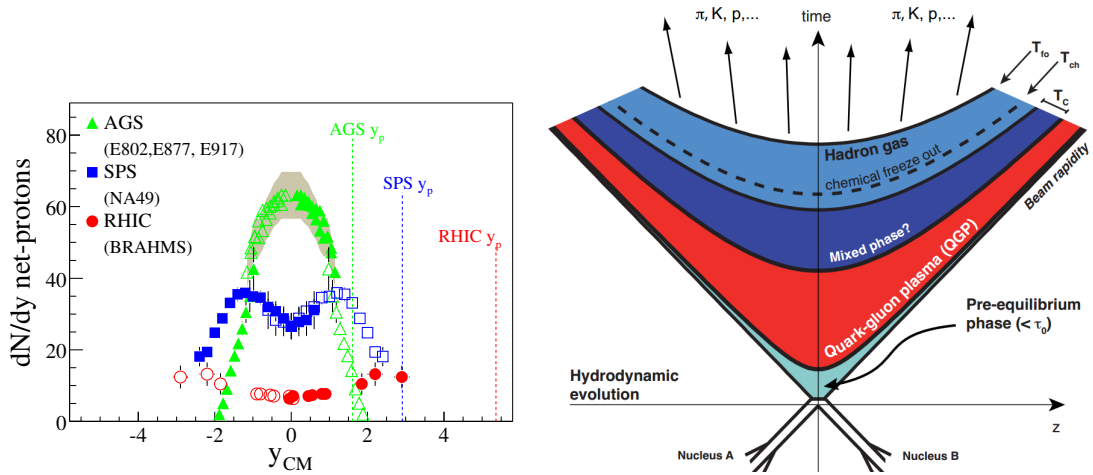


Figure 2.8: Net proton production for various energies:  $\sqrt{s_{NN}} = 5$  GeV (AGS),  $\sqrt{s_{NN}} = 17$  GeV (SPS) and  $\sqrt{s_{NN}} = 200$  GeV (RHIC). Dashed lines denote the respective beam rapidity (left). Light-cone diagram of a collision in the Bjorken picture with the evolution of a QGP [19].

The stopping of the constituting nucleons can be seen as a shift in rapidity so that it can be concluded that nucleon stopping is only prevalent at low energies, much below  $\sqrt{s_{NN}} \approx 200$  GeV [16]. This does not imply, however, that nuclei pass through each other with less interaction at higher energies. Instead, the nuclei become transparent in the sense that only the small  $x$  constituents are resolved and interact. As a result, much energy is distributed during the collision, but not through the valence content that is associated with a significant net-baryon production. The evolution of the highly excited matter produced in a heavy-ion collision at high energy is illustrated in the right panel of Fig. 2.8. Assuming a free streaming evolution in time and longitudinal direction  $z$  (Bjorken expansion), the initial energy density  $\epsilon_0$  reached in the highly excited volume at early times can be calculated:

$$\epsilon_0 = \frac{1}{A} \frac{1}{\tau_0} \left. \frac{dE_T}{dy} \right|_{y=0} \quad (2.28)$$

That means by measuring the particle production at mid-rapidity ( $y = 0$ ), the initial density  $\epsilon_0$  can be estimated for an overlap area  $A$  and at a time  $\tau_0 \approx 0.2$  fm, where the medium is considered thermalized. For central Pb-Pb collisions at the LHC, the estimated initial energy density is well above  $10 \text{ GeV}/\text{fm}^3$  which in turn is well above the conjectured critical energy density  $\epsilon_C \approx 0.5 \text{ GeV}/\text{fm}^3$  necessary to create a QGP.

### THE BAG MODEL

Basic properties of the QGP can be demonstrated from a simplified picture, the *MIT bag model* [20][21], which maintains the two key features of QCD: asymptotic freedom and confinement. The bag model assumes spherical bags for hadrons with a volume  $V$  and radius  $R$  in a perturbative vacuum where the quarks can be considered free. The kinetic pressure of the quarks is balanced by the *bag pressure*  $B$  accounting for their confinement.  $B$  represents thus the difference between the true QCD vacuum pressure and the perturbative vacuum pressure. The energy  $E$  of the bag now consists of the kinetic energy of the  $N = 3$  quarks and the bag volume energy  $B \cdot V$  needed to sustain the perturbative region:

$$E = \frac{2.04 N}{R} + B \frac{4}{3} \pi R^3 \quad (2.29)$$

With  $E$  and  $R$  the proton mass and radius, and applying the stability criterion  $dE/dR = 0$ , this relation yields a value of  $B^{1/4} \approx 220 \text{ MeV}$ .

Assuming an ideal gas of massless quarks, the pressure  $P$  of the QGP corresponds to a temperature  $T$  via the Stefan-Boltzmann equation

$$P_{\text{QGP}} = \left( 2 \cdot 8 + \frac{7}{8} (3 \cdot 2 \cdot 2 \cdot 2) \right) \frac{\pi^2}{90} T^4 - B = 37 \frac{\pi^2}{90} T^4 - B, \quad (2.30)$$

where the factors account for the degrees of freedom from spin (2) and color degeneracy of gluons (8) and quarks (3). Further factors for the quarks consider antiparticles and the allowed quark flavors up/down as well as a factor  $7/8$  for fermion statistics. For the temperature regime of about  $100 \text{ MeV}$ , the hadron gas phase can be described as a pion gas with only three degrees of freedom for the three charge states of the pion:

$$P_\pi = 3 \frac{\pi^2}{90} T^4 \quad (2.31)$$

At the phase transition,  $P_\pi$  and  $P_{\text{QGP}}$  are the same (fig. 2.9 a)), which implies a critical temperature  $T_C \approx 160 \text{ MeV}$ . Due to the several additional degrees of freedom in a QGP, the energy density  $\epsilon$  rises accordingly (fig. 2.9 b)).

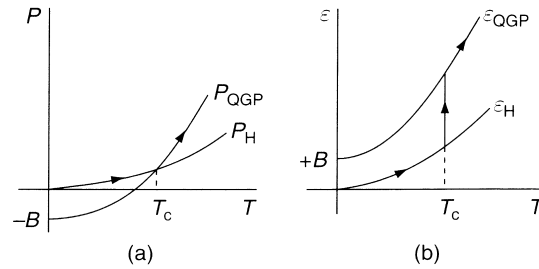


Figure 2.9: Pressure  $P$  and energy density  $\epsilon$  for a hadron gas and for the bag model QGP above the critical temperature  $T_C$  [16].

## RESULTS FROM LATTICE QCD

The left panel of Fig. 2.10 shows a calculation from LQCD. Besides the sudden rise in energy density  $\epsilon$  around the critical temperature, one notices that the energy density remains below the Stefan-Boltzmann prediction for an ideal gas of massless constituents, which is an indicator for the remaining interaction of the constituents. While the bag model suggests a first-order phase transition, ongoing studies show that the nature of the transition is more complicated. Assuming quark masses  $m_q \rightarrow 0$  or  $m_q \rightarrow \infty$  a first order transition is in fact expected, but the point with the physical quark masses lies in a region of a smooth *crossover* transition [22] (right panel of Fig. 2.10).

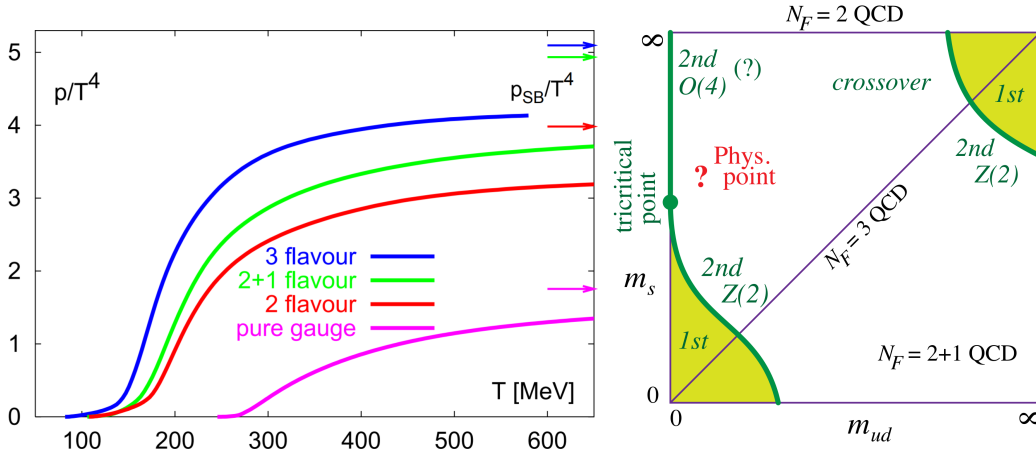


Figure 2.10: Energy density calculated for two light quark flavors, three light quark flavors, two light plus one strange quark and infinitely heavy quarks (pure gauge) (left) [23]. Character of the QGP transition for different quark masses (right) [24].

## FINITE BARYOCHEMICAL POTENTIAL

The considerations above involve the simplification that the baryochemical potential  $\mu$  or equivalently, the net baryon density, equals zero. The current conjecture of the QCD phase diagram in temperature  $T$  and baryochemical potential  $\mu$  is sketched in the left panel of Fig. 2.11. To increase  $\mu$  means to increase the baryon density which can also lead to the formation of a QGP, as nucleons will simply overlap by close packing. The lower limit on  $\mu$  for such a phase transition to occur is obviously the nucleon mass,  $\mu_c = M$  for  $T = 0$ . Straightforward calculations at zero temperature further require an upper limit of  $\mu_c = 3M/2\sqrt{2}$  [12]. Effective models suggest that the smooth crossover region at low  $\mu_B$  is followed by a critical point at intermediate  $\mu_B$  which in turn is followed by a first-order transition [25].

The scenario of very dense nuclear matter at low temperatures is presumably found in neutron stars [26]. Similar to an electric superconductor one also expects a color superconducting phase in this region, where quarks form Cooper pairs [27]. Unfortunately, there is no possibility in sight to reproduce these conditions on earth.



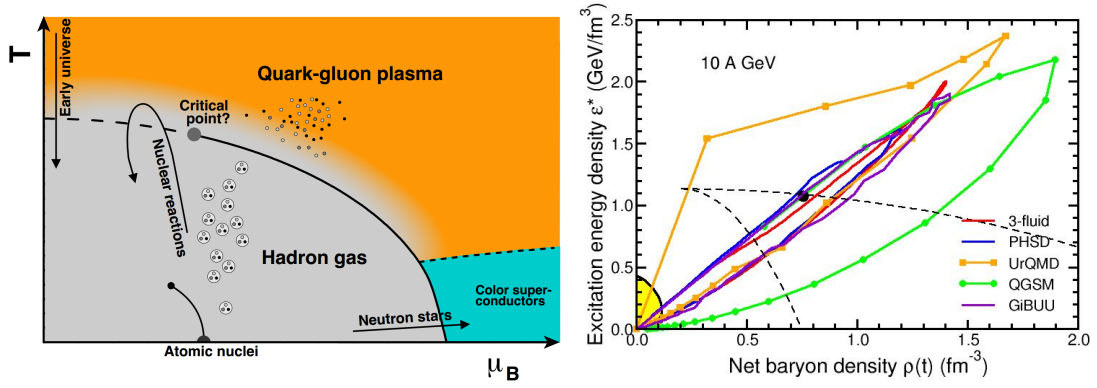


Figure 2.11: Schematic QCD phase diagram (left) [19]. Time evolution of the excitation energy and net baryon density as predicted by various models in heavy-ion collisions at moderate energy (right) [25]. The model curves, to be followed in clockwise sense, cross a region of coexisting hadronic and quarkonic phase (enclosed by dashed lines).

Heavy-ion collisions at large energies are carried out at RHIC ( $\sqrt{s_{NN}} = 200$  GeV) and LHC ( $\sqrt{s_{NN}} = 5000$  GeV). The energies imply that the region in the QCD phase diagram is probed at a high temperature and a low baryochemical potential. Future collision experiments such as CBM at the accelerator facility FAIR aim for moderate energies, so that the temperature and energy density will be reduced, but the baryochemical potential will be larger (right panel of Fig. 2.11).

#### PROBES OF THE QUARK-GLUON PLASMA

Several signatures of the QGP have been measured already. A few probes can be mentioned briefly:

- Since the QGP acts as an energy bath with temperatures above  $T = 150$  MeV, the production of strangeness is expected to be greatly enhanced. By today, the strangeness enhancement has also been measured in smaller systems for high-multiplicity events, so that there might be an interesting duality in the description of small and large collision systems [28].
- The size of the fireball can be deduced by interferometry with identical hadrons. Measurements of central Pb–Pb collisions at  $\sqrt{s_{NN}} = 2.76$  TeV suggest a fireball radius of at least 6 fm at kinetic freeze-out after approximately  $t = 10$  fm [29].
- The deconfined quark-gluon structure is associated with a distinct hydrodynamic behaviour. The hydrodynamic evolution can lead to specific flow patterns of energy, of which the most prominent is the elliptic flow measured in semi-central heavy-ion collisions [30] [31].
- Quarkonia are expected to be suppressed due to Debye color screening and on the other hand, to be enhanced due to statistical regeneration at hadronic freeze-out. Measurements agree with both conjectures [32].

Two further effects of the QGP are the suppression of high- $p_T$  hadrons and the low- $p_T$  production of thermal direct photons that will be introduced as a part of the following section. These effects constitute the context for the measurement of neutral

pions in pp collisions as well as the theoretical description of direct photons in pp collisions, which are presented in this thesis.

## 2.4 DIRECT PHOTONS AND NEUTRAL PIONS IN HADRON AND HEAVY-ION COLLISIONS

First generation measurements of direct photons in hadron-hadron collisions were carried out at CERN ISR and Fermilab around 1980 [33]. At this time, a few years after the emergence of QCD, a photon signal from parton scattering had already been anticipated. Production rates were expected to be significant compared to photon rates from the electromagnetic decay of the  $\pi^0$  and other hadrons.

A measurement from the R806 collaboration is shown in the left panel of Fig. 2.12, where the direct photon contribution is revealed by the ratio of single<sup>6</sup> photon yield (circles) over neutral pion yield. The smooth curve depicts the Monte Carlo (MC) prediction assuming no direct photon production.

The right panel of Fig. 2.12 shows the angular correlation in azimuth between triggers of single photons (stars) or neutral pions (circles) and associated charged particles, measured by R806/R807. In comparison with single photon triggers, the near-side yield ( $\Delta\Phi = 0$ ) is much reduced, which is consistent with the idea of photons being emitted back-to-back from a parton scattering.

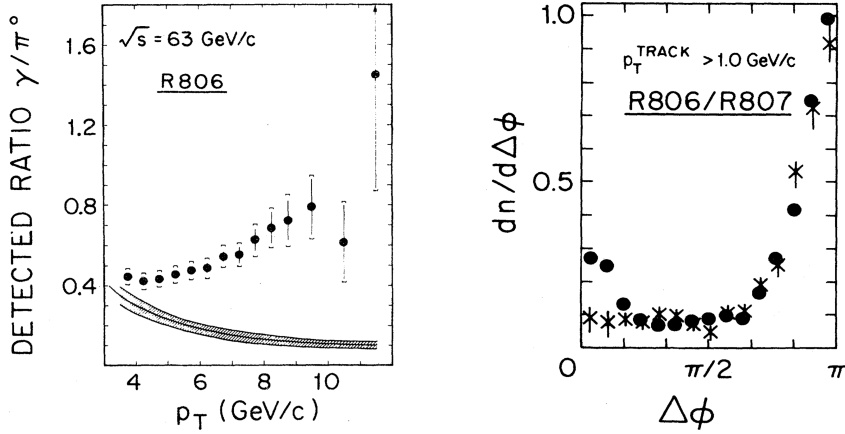


Figure 2.12: Left panel: Observed ratio of  $\gamma/\pi^0$  (points) and expected values from background sources (curve). Right panel: Azimuthal angle difference ( $\Delta\Phi$ ) between single photons (stars) or neutral pions (points), with  $p_T > 4.5$  GeV, and tracks from charged particles with  $p_T > 1.0$  GeV, corrected for meson-induced background [33].

Phenomenologically, direct photons are simply classified as all photons that do not stem from hadron decays, then the particle yield is

$$\gamma_{\text{inclusive}} = \gamma_{\text{direct}} + \gamma_{\text{decay}}. \quad (2.32)$$

In hadron-hadron collisions, the yield of direct photons can be explained exclusively by hard parton scatterings. In a LO picture, they arise either as *prompt photons* from hard  $2 \rightarrow 2$  processes, such as  $qg \rightarrow q\gamma$ , or as *fragmentation photons* from the fragmentation of outgoing partons in purely partonic processes  $gg \rightarrow gg$ ,  $qg \rightarrow qg$  and so on. Purely partonic  $2 \rightarrow 2$  processes are much more abundant due to the dominance of the strong coupling over the fine-structure constant, but on the other hand, production of hard fragmentation photons from these configurations is suppressed for the same reason. As a result, fragmentation photons dominate at low and prompt photons at high transverse momenta. In the historic example given above, the boundary

is clearly below  $p_T = 4 \text{ GeV}$  so that these results address the properties of prompt photons.

The production of prompt photons is almost exclusively given by the two processes of Compton-like scattering  $qg \rightarrow q\gamma$  and quark-antiquark annihilation  $q\bar{q} \rightarrow g\gamma$ . Accordingly, prompt photons are suited to constrain especially initial gluon densities through the Compton process. This is particularly interesting, considering that the precise constraints from DIS experiments (lepton-hadron collisions) apply only to the charged quark content. In principle, the production of fragmentation photons could also be linked to the initial parton distribution. However, the relation of fragmentation photons to the hard scattering has to be modeled first by *fragmentation functions*  $D_{q \rightarrow \gamma}$  and  $D_{g \rightarrow \gamma}$  in analytic calculations or, alternatively, as explicit Bremsstrahlung ( $q \rightarrow q\gamma$ ) in a Parton Shower (PS) algorithm (cf. Sec. 3.4). As a result, the research tradition of fragmentation photons has followed the opposite direction: Photon fragmentation functions are studied on the basis of lepton collider data, particularly because there is no complication from the initial state [34].

A photon fragmentation measurement in two-jet events at the LEP is depicted in Fig. 2.13, where  $z_\gamma = E_\gamma / (E_\gamma + E_{\text{had}})$  is the fraction of energy carried by photons in a jet. The points are the measurement, the lines are a photon fragmentation function  $D_{q \rightarrow \gamma}(z_\gamma)$  for different scales  $Q$  and values of  $\Lambda_{\text{QCD}}$ . The data point at  $z_\gamma \approx 1$  corresponds to the measurement of prompt photons that are back-to-back to a  $q\bar{q}$  pair that is resolved as one jet.

With the progress of hadron-hadron colliders and in absence of a new lepton collider, constraints on photon fragmentation from proton-proton collisions have been considered [36]. Considering fragmentation functions in general, it is to note that lepton annihilation produces only quarks at leading order,  $e^+e^- \rightarrow q\bar{q}$ . Gluons enter as subleading NLO corrections so that constraints for a fragmentation function  $D_{g \rightarrow X}$  are, in that sense, weaker at lepton colliders.

The overwhelming background of decay photons is the general obstacle for direct photon measurements. The usual approach is to apply an isolation criterion, where only a certain additional energy is tolerated in the vicinity of the signal photon (applies also to the measurement above).

Besides the dependence on the initial state and a possible final-state evolution, one has to keep in mind that the description of the underlying hard scattering of partons can also be tested. The actual cross section and coarse emission topology of producing anything relies on the perturbative description of the hard scattering kernel. The perturbative description is a main focus of this thesis, where three different approaches towards direct photon production are considered, with an accuracy that goes beyond leading order calculations.

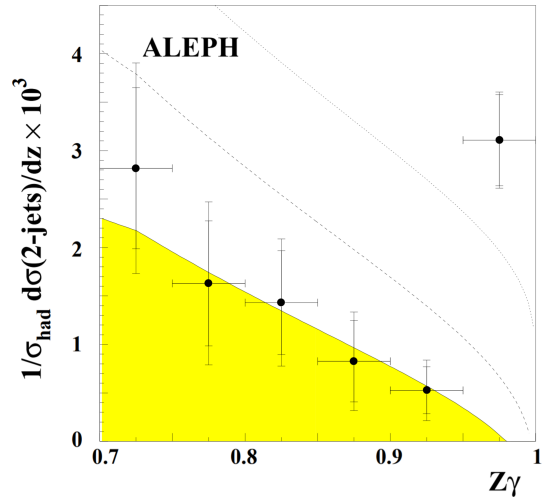


Figure 2.13: Measurement of a photon fragmentation function (dots), theoretical predictions (lines). Figure adapted from [35].

## NEUTRAL PIONS IN HADRON-HADRON COLLISIONS

Only discussed as a source of background so far, hadron production itself can provide constraints on the initial parton distribution. As for the fragmentation photons, a fragmentation function has to be provided to translate partons into hadrons or in an alternative approach, a hadronization model combined with a parton shower (cf. Sec. 3.5), in order to describe the production of identified mesons or baryons. Fragmentation functions are also given for inclusive hadron production, which has been measured up to transverse momenta of  $p_T = 100 \text{ GeV}$  and beyond [37]. In anticipation of Sec. 3.7, we note that the dependence on the actual fragmentation can be suppressed with the use of *jets*. Instead of single particles, jets measure the entire energy flow in a certain region, which can be related to the hard scattering regardless of the precise fragmentation pattern of hadrons. Jets have been measured up the TeV scale [38].

Fig. 2.14 provides an illustration of fragmentation functions. The variable  $z$  denotes the parton momentum fraction that is carried by the hadron. The ordinate accordingly denotes the momentum fraction density  $zD(z)$  of the hadrons. In contrast to fragmentation photons and direct photons in general, hadrons are produced in much greater multiplicity. As the lightest hadrons with a mass  $m \approx 140 \text{ MeV}$ , pions are most abundant. The kinematics of charged pions are usually determined to good accuracy in tracking detectors. However, the separation from other charged hadron species is often limited to a certain transverse momentum, e.g. at around  $p_T = 2 \text{ GeV}$  at CMS [40] or  $p_T = 20 \text{ GeV}$  at ALICE [41] which is particularly equipped for particle identification (PID).

Neutral pions, on the other hand, can be identified via their decay into two photons which are measured in calorimeters and also in tracking detectors via pair production  $\gamma \rightarrow e^+e^-$ , also called photon conversion. The  $\pi^0$  has been successfully measured up to  $p_T = 35 \text{ GeV}$  via an invariant mass analysis of the photons [42]. This thesis aims to push this limit even further with an analysis of single calorimeter clusters, also called *merged* clusters, which has been used already to measure neutral pions up to  $p_T = 40 \text{ GeV}$  [43]. The reconstruction of neutral pions in  $pp$  collisions at  $\sqrt{s} = 8 \text{ TeV}$  is presented in Ch. 6.

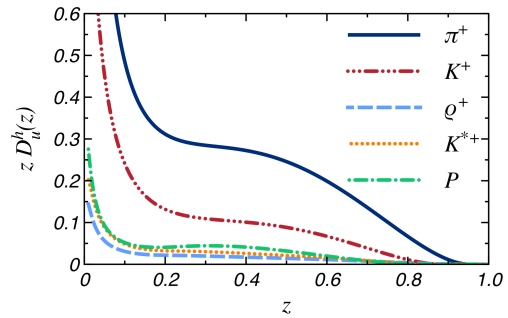


Figure 2.14: Illustration of various quark-to-hadron fragmentation functions [39].

## PHOTONS AND NEUTRAL PIONS IN HEAVY-ION COLLISIONS

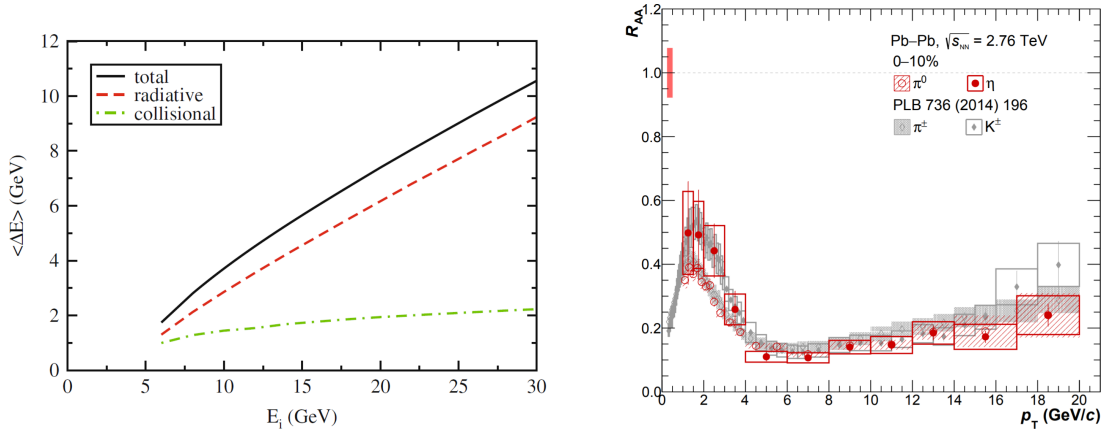


Figure 2.15: Radiative and collisional parton energy loss in a QGP [44] (left). Nuclear modification factor measured for pions, eta meson and charged kaons in Pb-Pb collisions at  $\sqrt{s_{NN}} = 2.76$  TeV (right) [45].

Photons and hadrons play complementary roles in study of the QGP. From the hot medium of deconfined color charged, an enhanced energy loss of traversing partons is expected, but not for photons. Gluons and light quarks are expected to lose a significant amount of their energy due to induced gluon radiation (left panel of Fig. 2.15); radiative energy loss for heavier quarks is suppressed, however (dead cone effect). The signal associated to parton energy loss is *jet quenching*<sup>7</sup>, which is well established and illustrated in the right panel of Fig. 2.15. The suppression of different particle species is expressed as the *nuclear modification factor*  $R_{AA}$  that compares particle yields in heavy-ion collisions with those in pp collisions:

$$R_{AA} = \frac{1}{\langle N_{\text{coll}} \rangle} \frac{(dN/dp_T)_{AA}}{(dN/dp_T)_{pp}} \quad (2.33)$$

Here, the factor  $1/\langle N_{\text{coll}} \rangle$  accounts for the number of binary nucleon collisions in heavy-ion collisions<sup>8</sup> ( $\langle N_{\text{coll}} \rangle \approx 1500$ ). Suppression above a transverse momentum  $p_T \approx 6$  GeV is similar for different hadron species from light quarks, which is in line with the conjecture that hard partons are indeed suppressed, but hadronization still takes place in the vacuum.

The difference in suppression below  $p_T \approx 6$  GeV is attributed to radial flow: The fireball of hot matter expands so that low momentum hadrons inherit an additional boost depending on the hadron mass. Also, the flow of baryons is much different from the flow of mesons (not shown here, see [41]), for which a modified parton recombination mechanism may be an explanation.

The research history of the QGP is accompanied by several ambiguous signatures [46], whereas the *jet quenching* effect is probably the most unambiguous one, because no other hypothesis than a medium of unscreened color charges is consistent with the observed extent of suppression. A *cold* nuclear suppression effect in the initial parton distributions has been investigated in p-Pb collisions (Fig. 2.16 left). Only for lowest transverse momenta a suppression was found, which is consistent with the current description of cold nuclear matter effects (cf. Sec 3.2) and which does not explain the strong modification in final state that is found in Pb-Pb collisions.

Photons from hard parton scatterings have been used for a further test of the **QGP** hypothesis: By measuring a nuclear modification factor for isolated direct photons, the nucleon scaling assumption in Eq. (2.33) could be validated (Fig. 2.16 right). Again, cold nuclear effects are expected to be well below the current uncertainties from nuclear parton densities and data.

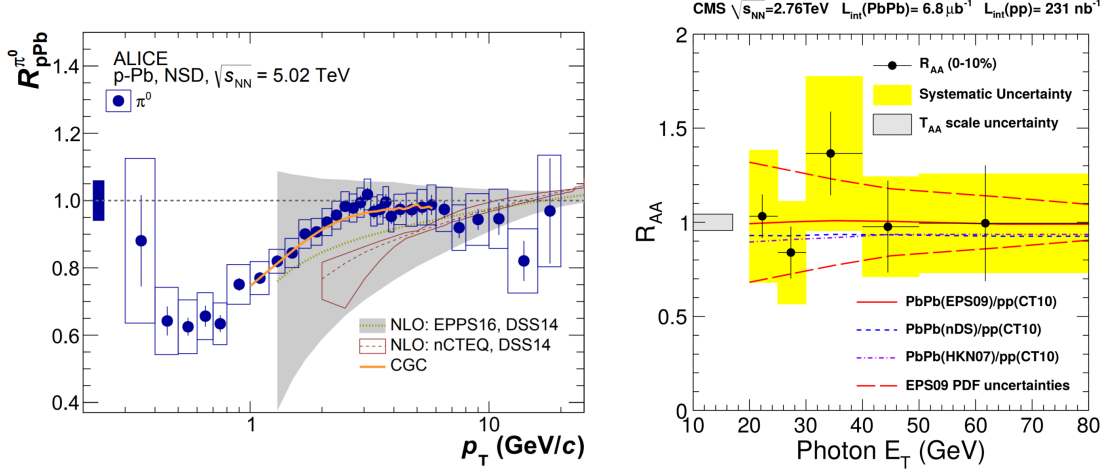


Figure 2.16: Control measurements for the **QGP** hypothesis: Neutral pions measured in p-Pb collisions at  $\sqrt{s_{NN}} = 5.02$  TeV (left) [47]. The nuclear modification factor in Pb-Pb collisions measured for isolated photons at  $\sqrt{s_{NN}} = 2.76$  TeV (right) [48].

Direct photons are not only used as a control measurement for the suppression of high- $p_T$  probes, but are themselves a probe for the **QGP**<sup>9</sup> [49] [50]. Besides the direct component, as produced in pp collisions, additional direct *thermal* photons are produced throughout the fireball evolution in a heavy-ion collision. The production rates of thermal photons from the **QGP** phase are well understood and progress has been made in describing the contribution from the hot hadronic phase.

In contrast to the measurement of direct photons associated with hard parton scattering, the measurement of thermal photons cannot be facilitated through isolation from hadronic energy due to the uncorrelated thermal emission pattern. Instead, the main challenge is to describe accurately the background of photons from hadronic decay such that it can be subtracted from the inclusive photon yield. The signal-to-background ratio is just some percent points above unity in the region below  $p_T^\gamma = 5$  GeV, where a significant thermal photon signal is expected.

The measured direct photon signal is usually defined in terms of a double ratio

$$R_\gamma(p_T) = \left( \frac{\gamma_{\text{incl}}}{\pi^0} \right)_{\text{meas}} / \left( \frac{\gamma_{\text{dec}}}{\pi^0} \right)_{\text{sim}}, \quad (2.34)$$

where  $\gamma_{\text{incl}}$  is the measured inclusive photon spectrum and  $\pi_{\text{param}}^0$  a parametrization of the measured neutral pion spectrum. Systematic uncertainties are expected to cancel to a large degree, since the neutral pion is measured also via photons. The decay photon spectrum  $\gamma_{\text{dec}}$  is simulated from a hadron cocktail that is based mainly on the measured  $\pi^0$  spectrum, so that uncertainties in the background description correlated to the measurement cancel as well.

Given that thermal radiation of the **QGP** is the dominant mechanism for additional direct photons at low  $p_T^\gamma$ , the excess of thermal photons over direct photons from parton scattering follows an exponential form,  $\exp(-p_T^\gamma/T_{\text{eff}})$ , with an effective temperature  $T_{\text{eff}}$ . The **ALICE** collaboration has measured direct photons in Pb-Pb collisions

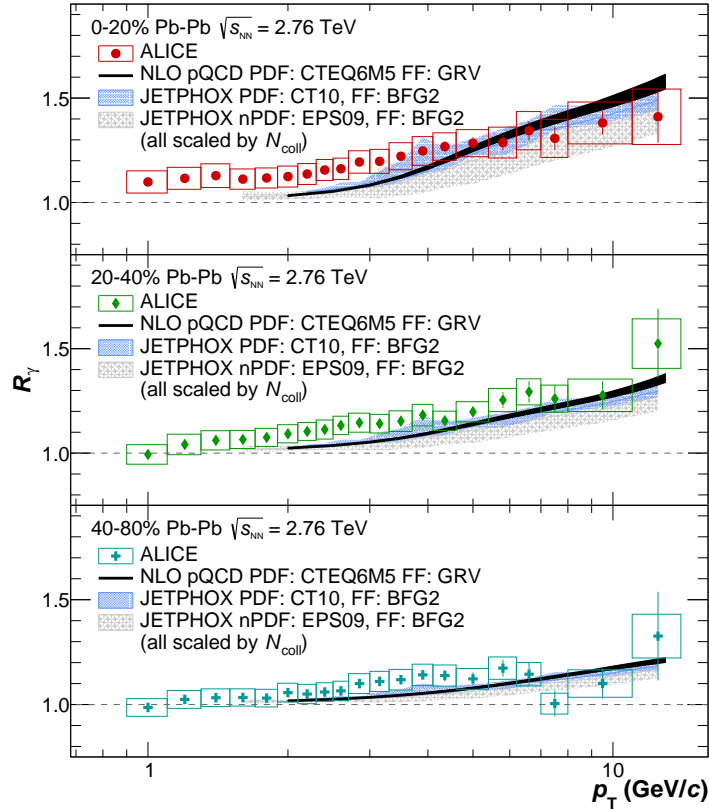


Figure 2.17: Ratio of inclusive photons over decay photons, measured in Pb-Pb collisions at  $\sqrt{s_{\text{NN}}} = 2.76$  TeV, for three different collision centralities (0% = most central) [51]. NLO predictions for direct photons from hard parton scattering are given (taking into account the number of binary collisions in a Pb-Pb collisions).

at  $\sqrt{s_{\text{NN}}} = 2.76$  TeV in the transverse momentum range 0.8–14 GeV [51] (Fig. 2.17). The measurement gave an effective temperature  $T_{\text{eff}} = 304 \pm 58$  MeV [52].

An additional conjectured source of direct photons in heavy-ion collisions are photons from jet conversion in the medium, which are supposed to dominate in the transverse momentum region above  $p_T^\gamma = 6$  GeV.

The necessary baseline for the excess of additional photons in heavy-ion collisions is given by the respective measurement in pp collisions or by a pQCD calculation, which is one of the results in this thesis. Currently, the direct photon measurement at low energies is subject to large uncertainties, especially in pp collisions, where a suppression of the hadronic background is not present. Therefore, accurate pQCD calculations are a viable alternative.



## NOTES

<sup>1</sup>The top quark is not able to form hadrons. Owing to its large mass of 173 GeV it decays too quickly, most frequently via  $t \rightarrow W^+ b$ .

<sup>2</sup>Further exotic combinations are possible, such as pentaquarks ( $qqq\bar{q}q$ ) and tetraquarks ( $q\bar{q}q\bar{q}$ ). Both have been measured recently at LHCb [53]. Also, there are candidates for *glueballs*, where the valence content is entirely given by two or more gluons [10].

<sup>3</sup>In order to perform perturbation theory, a choice of gauge has to be defined for the propagator of the gluon field. Details of this procedure can be found in [54]. The key step is to add a gauge fixing term  $\mathcal{L}_{\text{gauge-fixing}}$  as well as a so called ghost Lagrangian  $\mathcal{L}_{\text{ghost}}$ . The latter has to be supplemented due to the non-Abelian nature of the theory. Then, the rules for perturbation theory — the Feynman rules — can be derived from the phase of transition amplitudes

$$S_0 = i \int \mathcal{L}_0(x) d^4x, \quad S_I = i \int \mathcal{L}_I(x) d^4x. \quad (2.35)$$

Here,  $\mathcal{L}_0$  and  $\mathcal{L}_I$  refer to the free part and the interacting part of the theory, respectively. Accordingly, one finds separate rules for parton propagation and parton interaction.

<sup>4</sup>Here and in all chapters, the convention  $c = 1$  is assumed, except for the neutral pion reconstruction in Ch. 6.

<sup>5</sup>This straightforward interpretation of  $x$  is valid only for momentum transfers much larger than the hadron mass. Also, any initial transverse movement of partons is neglected in this discussion. It is interesting to note that research began on *generalized parton distribution functions* that describe the transverse hadron structure and other properties such as the angular parton momentum [55].

<sup>6</sup>Here, *single photons* means single photons as opposed to two-photon detection from neutral meson decay. Single photons had been selected due to a rejection based on the invariant mass of resolved photon pairs. An alternative, statistical method for unresolved photons was given through photon conversion, where two otherwise unresolved photons are revealed through the doubled abundance of conversion events.

<sup>7</sup>The term *jet quenching* also refers to suppression of single hadrons, because they are still a valid proxy for the original hard parton.

<sup>8</sup>Geometrical quantities such as the collision centrality, the number of participating nucleons or the number of binary nucleon collisions can be related to event activity on basis of the Glauber Model [56]. Such a measurement will be briefly presented in Sec. 5.3.4, where the ALICE will be introduced.

<sup>9</sup>In a broader scope, which is not discussed here, the elliptic flow of direct photons is also an important probe. It is hotly discussed because the hydrodynamic flow of direct photons and the rate of thermal photon production are not consistently described. For a brief overview of this topic, see [57].



In this chapter, the necessary concepts to describe particle production in hadron-hadron collisions will be discussed [58] [59]. The approach of *factorization* will be introduced, which allows to separate the part of particle production that can be described by pQCD, namely the hard scattering and the evolution of scales above  $Q^2 \gtrsim 1 \text{ GeV}^2$ , from non-perturbative parts such as parton densities in a hadron. Next, the parton shower approach will be introduced, which is a MC algorithm used to generate an entire, kinematically determined succession of parton branchings that is applied to the ingoing and outgoing partons of a hard scattering. In this sense, the parton shower is an explicit way to account for the scale breaking in QCD. In general-purpose event generators, the parton shower is evolved down to an Infrared (IR) cutoff scale, from where a hadronization model has to be used, which is the Lund String Model in our case. Afterwards, the phenomenology of hadron-hadron collisions will be covered briefly as well as the idea of multiparton interactions which describes additional, soft particle production in hadron-hadron collisions. The last section is dedicated to the concept of jets, which are used as inclusive observables that relate to the hardest emission structures of an event.

### 3.1 FACTORIZATION

Perturbation theory demands a high energy scale that implies a sufficiently small  $\alpha_s$ . This is fulfilled in a hard scattering of free partons, but the requirement is obviously not fulfilled for the initial and final state of a hadron collision, which are given by bound QCD states. Likewise, the process of hadronization of partons into a hadron is out of the reach of pQCD. Fortunately, the concept of the parton model, that was originally developed for DIS (see Sec. 2.1.2), can be applied to nucleon-nucleon collisions.

In two approaching nucleons, a given parton will find the partonic structure of the incoming hadron frozen by time dilation: During the passage of the hadrons, there is no interaction seen between the partons in the respective nucleon and it becomes sensible to speak of a definite number of partons carrying a fraction of the hadron momentum. In a similar fashion, any non-perturbative development of outgoing partons (fragmentation) can be considered independent from the hard scattering. This way of separating long-distance and short-distance physics is known as collinear *factorization* [60]. The process of particle production in hadron-hadron collisions has become a convolution of three incoherent steps:

$$\frac{d\sigma}{dO} = \sum_{a,b} \int dx_a x_b \sum_f \int d\Phi_f f_A(x_a, \mu^2) f_B(x_b, \mu^2) \frac{d\hat{\sigma}_{ab \rightarrow f}}{d\hat{O}} D_f(\hat{O} \rightarrow O, \mu^2) \quad (3.1)$$

Here,  $O$  denotes the measurable observable after fragmentation of the partons and  $\hat{O}$  the observable on the partonic final state. The parton distribution functions  $f_{A,B}$  describe the probability to find, at some resolution scale  $\mu$ , a certain parton carrying a momentum fraction  $x_{a,b}$  in the respective hadron. It is combined with the partonic

cross section  $d\hat{\sigma}_{ab\rightarrow f}$  and the fragmentation function  $D_f$  that translates outgoing partons into some defined final state, e. g. neutral pions. The final state evolution of the partons can also be described by a Monte Carlo (MC) Parton Shower (PS), which will be covered in Sec. 3.4.

Divergent parts can occur in the perturbative series describing the hard process, which are absorbed by the factorization scale  $\mu$  (similar to the renormalization scale  $\mu_R$  which was introduced to absorb divergent parts in  $\alpha_s$ ).  $\mu$  is usually identified with the hard scattering scale,  $\mu^2 = Q^2$ , or in case of  $s$ -channel resonance production with the resonance mass squared  $\mu^2 = M^2$ . Of course, the physical result should not depend on the scale choice, but a dependence appears as an artifact of the incomplete perturbation series. Accordingly, the inclusion of higher-order terms stabilizes the cross section and the theoretical uncertainty can be estimated by a variation of scales.

## 3.2 PARTON DENSITIES

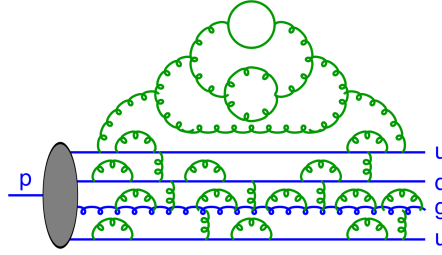


Figure 3.1: A nucleon is understood as a dynamic object, where gluons are constantly emitted and absorbed or quark-antiquark pairs are created or annihilated. After a parton density has been measured at some hard scattering scale  $Q^2$  (resolution scale so to speak), the **DGLAP** equations are used to describe the resolved fluctuations at some other scale [61].

The parton density in the initial state is described by a Parton Distribution Function (**PDF**), preferably of the same formal accuracy as the partonic cross section calculation. A **PDF**  $f(x, \mu^2)$  describes the effective density of gluons and different quark flavors (or even photons) that is resolved at a scale  $\mu^2 = Q^2$ . The actual parametrization of a **PDF** is usually provided in form of a grid of several thousand values of the momentum density  $xf(x, Q^2)$  in the space  $(Q^2, x, \text{type/flavor})$ , from which the precise value can be interpolated. The evolution in  $Q^2$  is governed by the perturbative **DGLAP** equation, here shown for a quark density  $q(x, Q^2)$  evolved from another quark:

$$Q^2 \frac{\partial}{\partial Q^2} q(x, Q^2) = \frac{\alpha_s(Q^2)}{2\pi} \int_{x,1} \frac{d\zeta}{\zeta} P_{qq} \left( \frac{x}{\zeta}, \alpha_s(Q^2) \right) q(\zeta, Q^2) \quad (3.2)$$

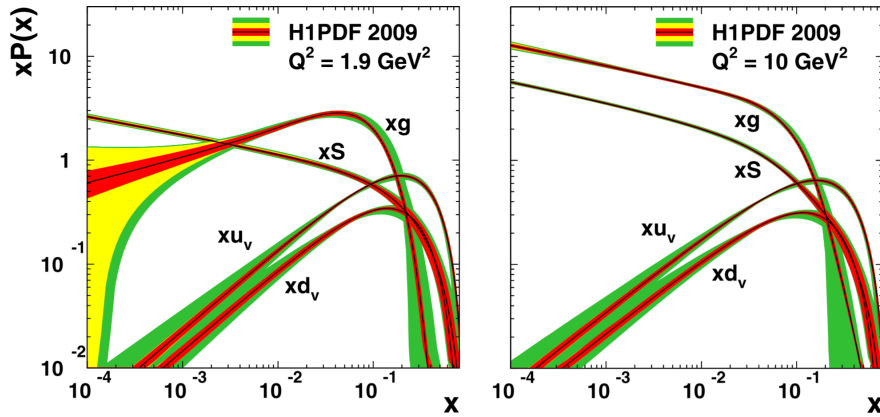


Figure 3.2: Parton distribution function at two different scales  $Q^2$  [62].

For the solution of the **DGLAP** equation, the boundary condition has to be provided by measurement. The *splitting function*  $P_{ab}$  is a perturbative series,

$$P_{ab}(x, \alpha_s) = P_{ab}^{(0)}(x) + \frac{\alpha_s}{2\pi} P_{ab}^{(1)}(x) + \dots, \quad (3.3)$$

where the **LO** term can be interpreted as the probability of finding a parton of type  $a$  in a parton of type  $b$  with a fraction  $x$  of the longitudinal momentum of the par-

ent parton. Quarks and gluons can originate from parent partons via four possible splitting functions (here, without treatment of divergences and virtual terms):

$$P_{qq}^{(0)} = C_F \left( \frac{1+x^2}{1-x^2} \right) \quad (3.4)$$

$$P_{qg}^{(0)} = T_R (x^2 + (1-x)^2) \quad (3.5)$$

$$P_{gq}^{(0)} = C_F \left( \frac{1+(1-x)^2}{x} \right) \quad (3.6)$$

$$P_{gg}^{(0)} = 2C_A \left( \frac{x^4 + 1 + (1-x)^4}{x(1-x)} \right) \quad (3.7)$$

The effect of a scale change is illustrated in Fig. 3.2. Generally, less quarks with large momenta are found and more gluons and sea-quarks become resolved for a growing scale  $Q^2$ . It is expected that the steady growth of gluon density at low  $x$ , as suggested by the **DGLAP** evolution, is balanced by a recombination of overlapping gluons so that a gluon saturation sets in. Colliders have reached energies so high that very small  $x$  can be probed with a  $Q^2 \gtrsim 1 \text{ GeV}^2$ , in a reach that is tractable by theory. The nonlinear gluon growth at low  $x$  and low  $Q^2$  is better described by the Balitsky-Fadin-Kuraev-Lipatov (**BFKL**) equation, based on which a predictive model called Color Glass Condensate (**CGC**) has been developed to describe the saturation regime [63] (Fig. 3.3). The **CGC** is a significant conjecture for high-energy heavy-ion collisions, because it is associated with a specific phase before the **QGP**, a *Glasma*. The Glasma consists of longitudinal color flux tubes that stretch from the **CGC** configurations of the nuclei. The expected experimental signature for such a phase are long-range particle correlations in rapidity that stem from these very early correlations.

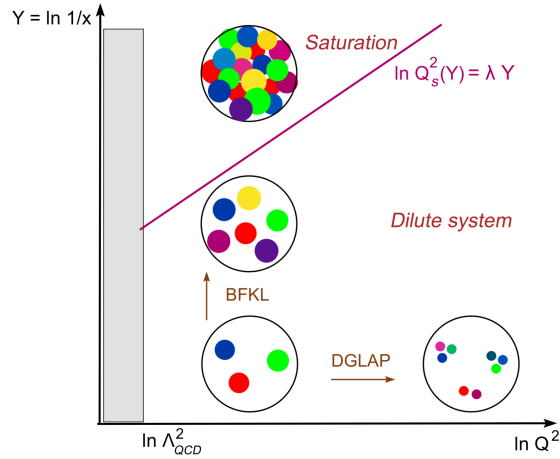


Figure 3.3: Schematic evolution of parton densities for decreasing  $x$  and increasing  $Q^2$ . The saturation regime is assumed at low parton momenta  $x$  and low resolution power  $Q^2$  [63].

### NUCLEAR PARTON DISTRIBUTION FUNCTIONS

Parton distributions of protons bound in nuclei differ from those in free protons. A coarse classification of nuclear effects is given for different regimes of Bjorken  $x$  (illustrated in Fig. 3.4), for which different mechanisms are being discussed [64]:

- A smearing of Fermi motion is expected leading to an enhancement at  $x \gtrsim 0.8$ . Parton momenta larger than  $x = 1$  become possible.
- A depletion called EMC effect was surprisingly discovered at  $x > 0.3$  in 1983 [65] with no established explanation to this day.
- Another depletion is found at  $x \lesssim 0.1$ , called nuclear shadowing. There are several theoretical descriptions, usually based on multiple scattering, but no consensus on phenomenological details.
- An enhancement at  $0.1 \lesssim x \lesssim 0.3$ , between the regimes of shadowing and EMC effect, is called anti-shadowing. Usually, anti-shadowing is being discussed on the basis of momentum sum rules, rather than being attributed to any particular mechanism.
- Saturation effects below  $x = 0.001$  are expected. In heavy-ion collisions, the saturation scale is expected to be enhanced ( $Q_s^2 \sim A^{1/3}$ ).

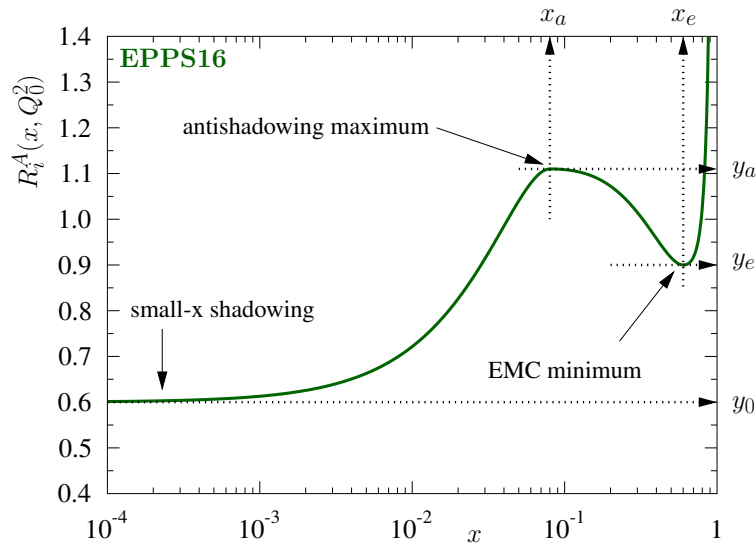


Figure 3.4: Illustration of nuclear effects using a recent parametrization from [66].

## 3.3 THE PARTONIC CROSS SECTION AT NLO

The differential partonic cross section in Eq. (3.1) is given by

$$d\hat{\sigma}_{ab \rightarrow f} = \frac{1}{2\hat{s}} |\mathcal{M}_{ab \rightarrow f}|^2(\Phi_f, \mu, \mu_R), \quad (3.8)$$

where  $1/2\hat{s}$  is the partonic flux and  $|\mathcal{M}_{ab \rightarrow f}|$  is the respective matrix element squared and averaged over the possible spin and color configuration in the initial state. The matrix elements are the sum of Feynman diagrams associated with the given process. The phase space for some final state, say  $n$  partons, is

$$d\Phi_n = \prod_{i=1}^n \frac{d^3 p_i}{(2\pi)^3 2E_i} (2\pi)^4 \delta^{(4)}(p_a + p_b - \sum_{i=1}^n p_i), \quad (3.9)$$

where the parton and hadron momenta enter,  $p_{a,b} = x_{a,b} P_{a,b}$ .

In addition to the **LO** contribution (Born-level) of a cross section  $\int d\Phi_n \mathcal{B}(\Phi_n)$ , the cross section for a  $2 \rightarrow n$  scattering at **NLO** contains virtual ( $\mathcal{V}$ ) and real emission corrections ( $\mathcal{R}$ ):

$$\sigma_{\text{NLO}} = \int d\Phi_n [\mathcal{B}(\Phi_n) + \mathcal{V}(\Phi_n)] + \int d\Phi_{n+1} \mathcal{R}(\Phi_{n+1}) \quad (3.10)$$

At this point, **UV** divergences occur in the loop integrals of the virtual corrections. They are removed by one of the several methods of regularization, so that  $\mathcal{V} \rightarrow \tilde{\mathcal{V}}$ . **IR** divergences occur in both virtual and real-emission corrections, but on the basis of the Kinoshita-Lee-Nauenberg (**KLN**) theorem, these divergences must mutually cancel order-by-order for an **IR** safe observable. It is not trivial to match both divergences, because they are associated with different phase space integrals. However, counter terms  $\mathcal{C}$  can be found so that each integral is finite:

$$\begin{aligned} \sigma_{\text{NLO}} = & \int d\Phi_n \left[ \mathcal{B}(\Phi_n) + \tilde{\mathcal{V}}(\Phi_n) + \sum_{\alpha} (\bar{\mathcal{C}}(\Phi_n))_{\alpha} \right] \\ & + \int d\Phi_{n+1} \left[ \mathcal{R}(\Phi_{n+1}) - \sum_{\alpha} (\mathcal{C}(\Phi_{n+1}))_{\alpha} \right] \end{aligned} \quad (3.11)$$

The counter terms are a sum of terms, each of which regulates one of the singular regions  $\alpha$  in the matrix element. In the integral over the  $n$ -particle phase space  $\Phi_n$ ,  $\bar{\mathcal{C}}$  are the counter terms integrated over the phase space of the real emission. In this thesis, the automated method of **IR** regularization by Frixione, Kunszt and Signer (FKS) [67] is used for the direct photon generation at **NLO** with POWHEG.



## 3.4 MONTE CARLO PARTON SHOWER

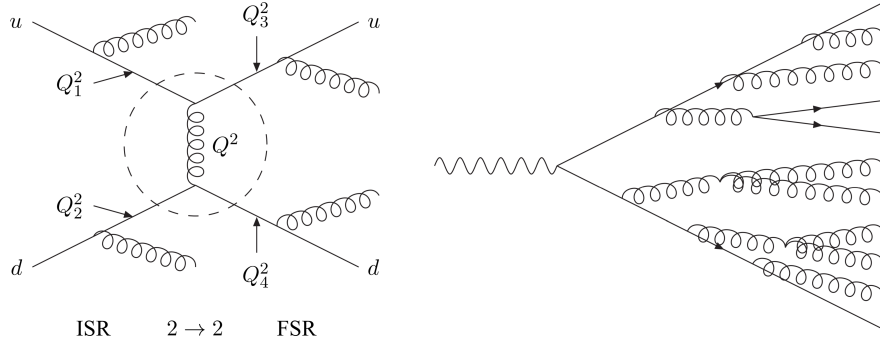


Figure 3.5: The factorization of the hard scattering process and the parton showers applied to ingoing and outgoing partons (left). Parton shower generated by successive parton splittings (right) [61].

A **MC PS** is applied to partons from a Matrix Element (**ME**) calculation, usually a  $2 \rightarrow 2$  process at **LO** (Fig. 3.5). It allows to describe realistic particle multiplicities and the small-angle structure within jets. These properties are described by higher-order corrections, which are not accessible by the conventional Fixed-Order (**FO**) approach due to the proliferation of Feynman diagrams. In the **PS** approach, however, these higher-order corrections are organized as a series of successive parton splittings. This is feasible on the basis of the *collinear approximation* that will be motivated in the following [58].

Suppose a cross section  $\sigma_{q\bar{q}}$  for the generation of a quark pair in a collision, e.g. in  $e^+e^- \rightarrow q\bar{q}$ . In case of an emitted gluon in the final state, the corresponding cross section  $\sigma_{q\bar{q}g}$  can be approximated by

$$\frac{d\sigma_{q\bar{q}g}}{d\cos\theta dz} \approx \sigma_{q\bar{q}} \frac{4}{3} \frac{\alpha_s}{2\pi} \frac{2}{\sin^2\theta} \frac{1+(1-z)^2}{z} \quad (3.12)$$

The differential form is given with respect to the extra gluon:  $\theta$  is the angle between quark and gluon;  $z$  is the relative quark momentum fraction carried away by the gluon. We note the soft divergence for  $z \rightarrow 0$  as well as the collinear divergences  $\theta \rightarrow 0$  and  $\theta \rightarrow \pi$ . The angular dependence can be rewritten to

$$\frac{2}{\sin^2\theta} \approx \frac{1}{1-\cos\theta} + \frac{1}{1-\cos\theta'} \quad (3.13)$$

where  $\theta$  is still the angle between quark and gluon and  $\theta'$  the angle between antiquark and gluon. The separate collinear divergence for quark and antiquark is now apparent. Since only one of the divergences can occur, both terms of the sum can be considered independent from each other in the limit of small angles. In usual terms of **pQCD**, only one specific Feynman diagram will contribute in a collinear region. Accordingly, Eq. (3.12) can be recast into a sum over the two quarks:

$$d\sigma_{q\bar{q}g} \approx \sigma_{q\bar{q}} \sum_{\text{partons}} \frac{4}{3} \frac{\alpha_s}{2\pi} \frac{d\theta^2}{\theta^2} dz \frac{1+(1-z)^2}{z} \quad (3.14)$$

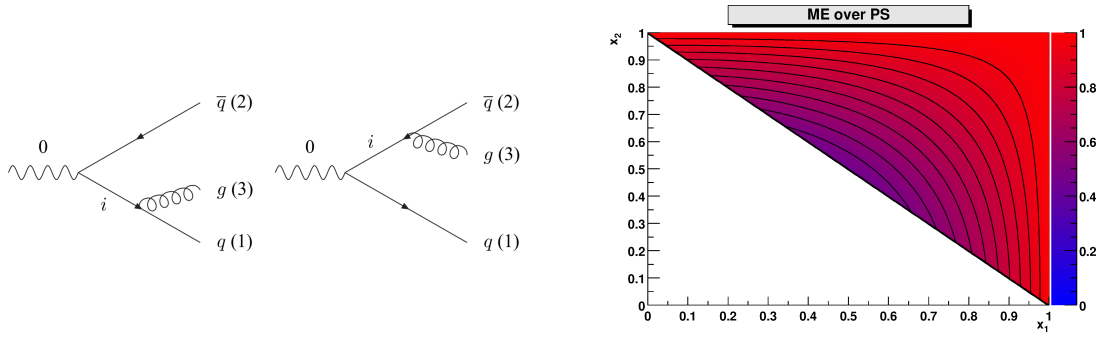


Figure 3.6: A gluon can be radiated from one of the quarks. In case of collinear radiation, both contributions factorize (left) [61]. Contour plot of the cross section ratio  $\text{ME}/\text{PS}$ . The  $\text{PS}$  fails to describe hard, large angle gluon radiation (right) [68].

We would arrive at a similar result in the collinear limit for the virtuality  $q^2$  of the quark propagator or the gluon momentum  $k_{\perp}^2$  transverse to the parent quark instead of the angle  $\theta$ :

$$q^2 = z(1-z)\theta^2 E^2 \quad (3.15)$$

$$k_{\perp}^2 = z^2(1-z)^2\theta^2 E^2 \quad (3.16)$$

$$\Rightarrow \frac{d\theta^2}{\theta^2} = \frac{dq^2}{q^2} = \frac{dk_{\perp}^2}{k_{\perp}^2} \quad (3.17)$$

Results of  $\text{PS}$  algorithms are derived from the finite part close to the exact collinear limit, so that results actually depend on the choice of variable. A  $\text{PS}$  ordered in transverse momentum or angle, for instance, automatically account for the effect of *color coherence* that suppresses radiation such that wide-angle radiation precedes narrow-angle radiation. The deficiency of the  $\text{PS}$  approach due to the collinear approximation in comparison with a full  $\text{ME}$  calculation is illustrated in Fig. 3.6, where the ratio  $d\sigma_{\text{PS}}/d\sigma_{\text{ME}}$  is given for the process  $e^+e^- \rightarrow qqg$ .

The factorized structure in Eq. (3.14) is universal and can be used to describe any extra emission accompanying two flavors produced by a hard scattering:

$$d\sigma_{q\bar{q}g} \approx \sigma_{q\bar{q}} \sum_{\text{partons}} \frac{4}{3} \frac{\alpha_s}{2\pi} \frac{d\theta^2}{\theta^2} dz P_{i \rightarrow j}(z, \phi) d\phi . \quad (3.18)$$

The functions  $P_{i \rightarrow j}(z, \phi)$  for a parton  $i$  giving rise to a parton  $j$  can be identified with the splitting functions from Eq. (3.7). In the  $\text{DGLAP}$  evolution of parton densities, the splitting functions were used to describe the enhancement or depletion of soft gluons and quarks that follows a change of scale  $\mu^2 = Q^2$ . Likewise, the splitting functions are used here to describe steps of radiation explicitly in a  $\text{PS}$ , starting from the hard scattering scale  $Q^2$  down to some  $\text{IR}$  cutoff  $Q_0^2$ . In other words: While the accompanying partons in the conventional  $\text{DGLAP}$  evolution are only implicit, the additional partons from the splittings are used to iteratively construct the parton shower.

In addition to the  $\text{QCD}$  splittings, photon radiations occur via  $q \rightarrow q\gamma$ . The splitting function is then given in analogy to  $P_{q \rightarrow qg}$ :

$$P_{q \rightarrow q\gamma} = \frac{\alpha_{\text{em}}}{2\pi} e_q^2 \frac{1+z^2}{1-z} \quad (3.19)$$

From comparison, the suppression of photon radiation is apparent:

$$\frac{P_{q \rightarrow q\gamma}(z)}{P_{q \rightarrow qg}(z)} = \frac{\alpha_{\text{em}} e_q^2}{\alpha_s C_F} \approx \frac{1}{200} \quad (3.20)$$

The competition with QCD radiation is even more severe because gluons do not emit photons.

The evolution from a IR cutoff scale  $Q'_0$ , from where a flavor is fetched from the PDF, to the hard scattering scale is accompanied by Initial-State Radiation (ISR). The subsequent evolution down to the cutoff scale  $Q_0$  is accompanied by Final-State Radiation (FSR). In the end, a hadronization model turns the final-state partons into primary hadrons which can decay further (Sec. 3.5). Due to the dominance of collinear splittings, ISR gives rise mostly to particles close to beam rapidity, where no detectors are available in colliders. Nevertheless, ISR shifts the energy available in the hard process and has therefore a large influence on differential cross sections and some event shapes.

Using the virtuality  $q$  of the internal parton line, the branching probability of a parton  $a$  to a parton pair  $bc$  between  $q^2$  and  $q^2 + dq^2$  is given by

$$d\mathcal{P}_{a \rightarrow bc} = \frac{\alpha_s}{2\pi} \frac{dq^2}{q^2} dz P_{a \rightarrow bc}(z) . \quad (3.21)$$

This is essentially the DGLAP equation, Eq. (3.2), for a specific splitting with a given parton momentum fraction  $z$ .

In order to respect the fact that a branching can only occur if no branching occurred before (at larger  $q$ ), we define a differential equation accordingly, depending on a non-branching probability  $\Delta_i(Q^2, q^2)$  starting from a maximum scale  $Q^2$ :

$$\frac{d\Delta_i(Q^2, q^2)}{dq^2} = \Delta_i(Q^2, q^2) \frac{d\mathcal{P}_i}{dq^2} \quad (3.22)$$

The solution to this<sup>10</sup> is the Sudakov form factor  $\Delta_i$ :

$$\Delta_i(Q^2, q^2) = \exp \left( - \int_{q^2}^{Q^2} \frac{dk^2}{k^2} \frac{\alpha_s}{2\pi} \int_{Q_0^2/k^2}^{1-Q_0^2/k^2} dz P_{a \rightarrow bc}(z) \right) \quad (3.23)$$

It should be stressed again that this is the probability for a parton *not to undergo a branching* between the two scales  $Q^2$  and  $q^2$ . The branching probability Eq. (3.21) then becomes:

$$d\mathcal{P}_{a \rightarrow bc} = \frac{\alpha_s}{2\pi} \frac{dq^2}{q^2} dz P_{a \rightarrow bc}(z) \exp \left( - \sum_{b,c} \int_{q^2}^{Q^2} \frac{dk^2}{k^2} \frac{\alpha_s}{2\pi} \int_{Q_0^2/k^2}^{1-Q_0^2/k^2} dz P_{a \rightarrow bc}(z) \right) \quad (3.24)$$

In the discussion of higher-order corrections, the Sudakov form factor, Eq. (3.23), accounts for the unresolved splittings and virtual corrections.

The implementation of Eq. (3.23) for a MC algorithm and the determination of the kinematic variables are straightforward for each parton branching:

1. Generate a random number  $R_q \in [0, 1]$  and solve  $R_q = \Delta(Q^2, q^2)$  for  $q^2$ .
2. If  $q < Q_0$ , the branching is not resolved and evolution terminates, otherwise continue.

3. Choose the value of  $z$  according to  $P_{a \rightarrow bc}$ .
4. With a random number  $R_\phi \in [0, 1]$  solve  $R_\phi = \phi/2\pi$ . The necessary kinematic variables of the splitting are now determined.
5. Reiterate with updated maximum scale  $Q^2 = q^2$ .

### 3.5 LUND MODEL OF HADRORIZATION

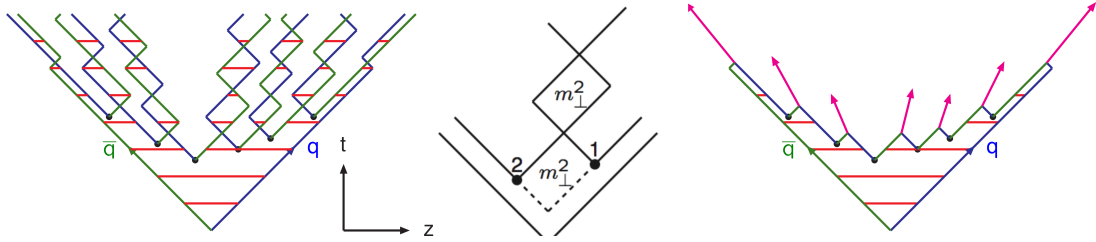


Figure 3.7: Motion and breakup pattern of a system of quarks and snapshots of strings (left). Through the long range QCD potential, the space-time variables are associated to a transverse mass  $m_\perp$  (middle). Fragmentation of  $q\bar{q}$  pairs to mesons (right). [69]

Two prominent methods to translate a final set of partons into hadrons are cluster fragmentation and string fragmentation [58]. Cluster fragmentation splits all gluons to quark-antiquark pairs, followed by formation of color-neutral quark-antiquark pairs. These clusters decay isotropically within their rest frame into hadrons with mass and momentum according to the available phase space. In the following, however, the focus lies on the Lund string model of hadronization, which is used in PYTHIA 8.

The quarks and gluons from the parton shower are colored objects, where the long range force of QCD grows between them as they depart from each other. In the quark-antiquark potential, we identify the long range potential as  $V(r) = \kappa r$ , with a string tension  $\kappa \approx (420 \text{ MeV})^2 \approx 0.9 \text{ GeV/fm}$  (the short-range Coulomb term is neglected). Accordingly, a quark serves as an endpoint to a string in the Lund model. Gluons left over from the parton shower are considered endpoints to two strings. Based on the  $q\bar{q}$  potential, the Lund model provides a prescription of the breaking of strings into further  $q\bar{q}$  pairs and a subsequent fragmentation to mesons and baryons Fig. 3.7.

The form of the potential leads to a simple relationship between space-time and momentum-energy variables:

$$\left| \frac{dE}{dz} \right| = \left| \frac{dp_z}{dz} \right| = \left| \frac{dE}{dt} \right| = \left| \frac{dp_z}{dt} \right| = \kappa \quad (3.25)$$

Note that transverse variables are still relatable, so that

$$m_\perp^2 = E^2 - p_z^2 = \kappa^2((\Delta z)^2 - (\Delta t)^2). \quad (3.26)$$

The probability to create a quark-antiquark pair with masses  $m_q$  and a momentum transverse to the string axis  $p_{\perp q}$  is described by a tunneling probability

$$P(m_q^2, p_{\perp q}) \sim \exp\left(\frac{-\pi m_q^2}{\kappa}\right) \sim \exp\left(\frac{-\pi m_q^2}{\kappa}\right) \exp\left(\frac{-\pi p_{\perp q}^2}{\kappa}\right). \quad (3.27)$$

Virtually no charm and bottom quarks are created from this distribution due to their large mass; strange quarks are suppressed roughly by a factor 3 with respect to up or down quarks. From Eq. (3.27) we see how the breaking of a string yields a momentum contribution transverse to the string axis: Although the transverse momentum is balanced between the created quark and antiquark, the distribution of momentum kicks have a certain width,  $\langle p_{\perp}^2 \rangle \approx (250 \text{ MeV})^2$ , which is later transferred to a hadron receiving a contribution from two different pairs so that  $\langle p_{\perp h}^2 \rangle \approx (500 \text{ MeV})^2$ .

Mesons are formed from the quark of one string with the antiquark from a neighbor string. To describe this hadronization, the total probability for a certain configuration with  $(n - 1)$  break-up vertices and  $n$   $q\bar{q}$  pairs could be sampled with help of Eq. (3.27). Instead, a more economical, but equivalent procedure was developed, combining the  $q\bar{q}$  pairs to hadrons starting from the maxima of lightcone momenta  $E \pm p_z$  to mid-rapidity of the event. The probability to create a hadron with  $m_{\perp}$  that takes a fraction  $z$  of the available lightcone momentum in the respective iteration reads as follows:

$$f(z) \sim \frac{1}{z} (1-z)^a \exp\left(\frac{bm_{\perp}^2}{z}\right) \quad (3.28)$$

Here,  $a$  and  $b$  enter as parameters that basically define the hardness of the fragmentation and have to be tuned to data. Because always a fraction of the remaining lightcone momentum is taken (lightcone scaling), the hadronization pattern will reproduce the well-known flat rapidity plateau.

Eq. (3.28) is modified for heavy quarks. Baryon production is possible on the basis of several successive string breaks (*Popcorn Model*).

Since gluons have two strings attached, the string force is doubled in case where a gluon endpoint is considered. The factor two can be seen as a consequence of the  $N_C \rightarrow \infty$  limit ( $C_A/C_F = 2/(1 - 1/N_C) = 2$ ), which is a simplifying assumption that underlies Lund hadronization as well as many other models where color flow has to be organized.

The string character of the model has been confirmed in  $q\bar{q}g$  final states, where angular regions between the quarks were depleted in comparison to the two angular regions between quarks and gluon.

As an important property, the Lund model is IR and collinear safe: The addition of collinear or soft gluons that will change the resulting fragmentation pattern only slightly.

## 3.6 HADRON COLLISIONS AND SOFT PROCESSES

The cross section for anything to happen in a proton-proton collision is the total cross section  $\sigma_{\text{tot}}$ . It can be further differentiated for elastic and inelastic collisions:

$$\sigma_{\text{tot}} = \sigma_{\text{el}} + \sigma_{\text{inel}} \quad (3.29)$$

When two protons collide, they can remain intact in the regime of small momentum transfers  $|t| < (2\text{GeV})^2$ . The cross section of these elastic events  $\sigma_{\text{el}}$  makes up 25 – 30% of the total cross section  $\sigma_{\text{tot}}$  at LHC energies. Elastic and total cross section are measured in dedicated experiments like TOTEM reporting  $\sigma_{\text{tot}} = 85\text{ mb}$  at  $\sqrt{s} = 2.76\text{ TeV}$  up to  $\sigma_{\text{tot}} = 111\text{ mb}$  at  $\sqrt{s} = 13\text{ TeV}$  [70].

However, High-Energy Physics (HEP) experiments usually probe the inelastic cross section that is associated with the production of new particles. The inelastic cross section is again subdivided, into a diffractive<sup>11</sup> and a non-diffractive part:

$$\sigma_{\text{inel}} = \sigma_{\text{non-diffractive}} + \sigma_{\text{diffractive}} \quad (3.30)$$

The significant role is played by the non-diffractive events which imply large energy transfers and abundant particle production over a large region of phase space (Fig. 3.8).

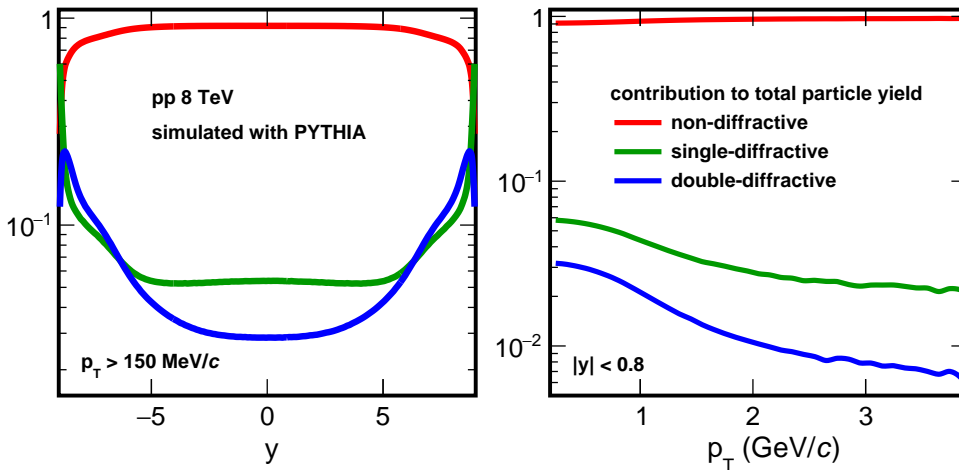


Figure 3.8: Relative contributions of the three dominating processes to the total particle yield for a typical LHC scenario, simulated by PYTHIA 8 (Monash 2013 tune), plotted against particle rapidity  $y$  and transverse momentum  $p_T$ , respectively.

## MULTIPARTON INTERACTION

A hard parton scattering event in a hadron-hadron collision is typically accompanied by an underlying event which accounts for particle production at low transverse momenta and which is found to be independent, to first approximation, from the hard scattering [58]. Conventionally, this underlying event is understood as scatterings from additional parton pairs of the colliding hadrons.

Consider a  $2 \rightarrow 2$  parton scattering with a partonic cross section that goes roughly with

$$d\hat{\sigma}_{\text{two-jet}} \sim \frac{dp_T^2}{p_T^4}. \quad (3.31)$$

The differential inclusive jet cross section  $\sigma_{\text{two-jet}}$ , after convolution and integration with a PDF, is depicted in the left panel of Fig. 3.9.

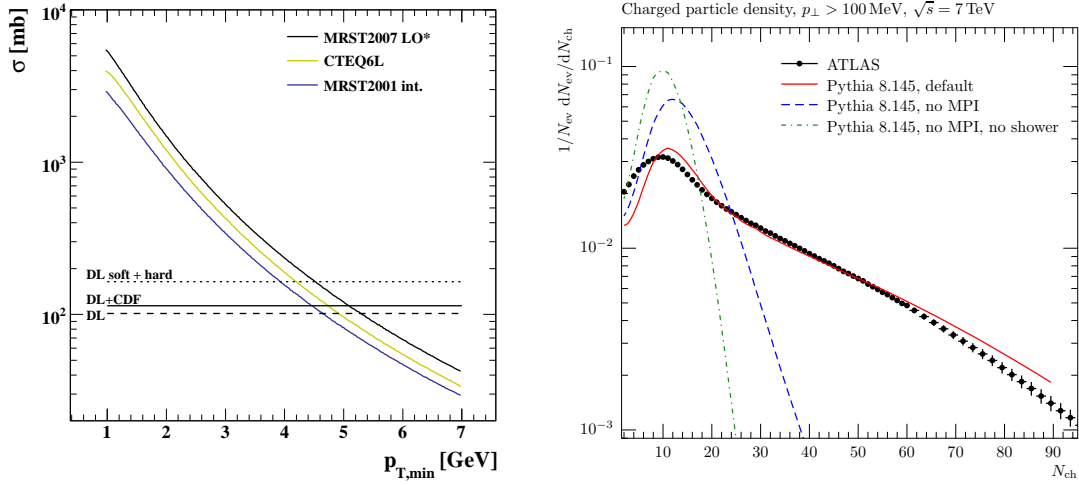


Figure 3.9: Inclusive jet production for three PDFs at LO and extrapolations of the total pp cross section at  $\sqrt{s} = 14$  TeV (left). Multiplicity of charged particles at low transverse momentum measured by ATLAS, compared with PYTHIA 8 with and without multiparton interaction (right) [58].

A paradox arises: The differential cross section grows larger than the different extrapolations of the total pp cross section. Recognizing that the two-jet cross section might be included multiple times in the total cross section  $\sigma_{\text{tot}}$ , the paradox can be resolved:

$$\hat{\sigma}_{\text{two-jet}}(\hat{p}_{T,\text{min}}) = \langle n \rangle (\hat{p}_{T,\text{min}}) \sigma_{\text{tot}} \quad (3.32)$$

Here, we assume an average number  $\langle n \rangle$  of independent parton scatterings. As a result, the number of scatterings is divergent for  $\hat{p}_{T,\text{min}} \rightarrow 0$  instead of the two-jet cross section.

From the parent hadron, there is a maximum of momentum that can be used so that the number of multiple scatterings should be constrained accordingly; for instance, the sum of used Bjorken  $x_1$  or  $x_2$  may never exceed unity. However, this will not cure the divergence so that another mechanism has to be considered.

One sensible explanation for a regulation at  $\hat{p}_{T,\text{min}} \rightarrow 0$  is the screening of color charges. With an effective wavelength  $1/\hat{p}_T$  the color charges become less resolved, leading to a vanishing seen color charge in the limit of low exchanged momentum. Another sensible explanation is the saturation of initial state partons by recombination, which has also been discussed in Sec. 3.2. Regardless of the question which mechanism is the dominant one, the effect of screening or saturation permits the introduction of a regulation term,

$$\frac{\alpha_s^2(\hat{p}_T^2 + \hat{p}_{T,0}^2)}{\alpha_s^2(\hat{p}_T^2)} \frac{\hat{p}_T^4}{(\hat{p}_T^2 + \hat{p}_{T,0}^2)^2}, \quad (3.33)$$

which acts a factor on the cross section.

A typical observable to constrain the Multiparton Interaction (MPI) model, or underlying event models in general, is the particle multiplicity (right panel of Fig. 3.9).

## 3.7 JETS

Following the last sections, we are now downright able to describe the identity of all particles in the final state and their kinematic properties. This is a seminal achievement, because we can describe the reality measured in particle detectors and because we become sensitive to the phenomena at the boundary of perturbative and non-perturbative QCD.

However, it is often neither advisable nor necessary to pursue this degree of detail in the final state: From an experimentalist's perspective, detectors often do not allow particle identification and sometimes cannot even resolve particles that are close to each other. From the theorist's perspective, the description of hard scale processes should be safe from a possible convolution of low scale final-state processes such as fragmentation. This is where jets enter [71].

In a jet, final-state particles are clustered in a well-defined way in a certain region of space. After summarizing the four-momenta of the selected particles, the jet is like a single energy flow along the jet axis and serves as a proxy for the hardest partons. To give an example from history, with the help of jets it was possible to validate QCD in two-jet and multi-jet events in a time where parton fragmentation was very poorly understood [72]. To give a modern example, jets in heavy-ion collisions relate to the properties of hard partons that undergo energy loss in a QGP, and they do so in a more robust way than the detection of single particles would.

A jet cluster algorithm, which can be applied on measured particles or just unresolved energy depositions in an experiment, should be *infrared* and *collinear safe* in order to be applied in theoretical calculations in an unambiguous way. The resulting jet should not be changed due to soft gluon emission or due to a collinear splitting of particles. Accordingly, it is not sufficient to draw a cone with a certain radius  $\Delta R = \sqrt{\Delta\eta + \Delta\phi}$  around a hard particle (fixed cone algorithm), because the particle might also undergo a splitting that changes the reference axis of the cone. Infrared safety is usually not found in algorithms that depend on an initial set of soft seed particles (e. g. split-merge cone algorithm).

A class of IR and collinear safe jet algorithms are the sequential recombination algorithms, among which the *anti- $k_T$  algorithm* has become the de-facto standard for usual jet physics analyses [73]. The anti- $k_T$  algorithm will be employed later in this work to define photon-jet correlations. A discussion of further advantages of the algorithm is omitted here, but the clustering procedure shall be given briefly:

1. Calculate the distance  $d_{ij}$  between all particles with the definition

$$d_{ij} = \min(p_{ii}^2, p_{ij}^2) \frac{\Delta R_{ij}^2}{R^2}. \quad (3.34)$$

2. Calculate the distance

$$d_{iB} = p_{ii}^2. \quad (3.35)$$

3. Merge particles  $i$  and  $j$  with the smallest distance to a new *protojet*.
4. If  $d_{iB}$  is the smallest, call  $i$  a final jet and remove it from the list.
5. Recalculate the distances of particles and protojets.
6. Repeat until there are no more particles and protojets.



An illustration of anti- $k_T$  jets is given in the following figure.

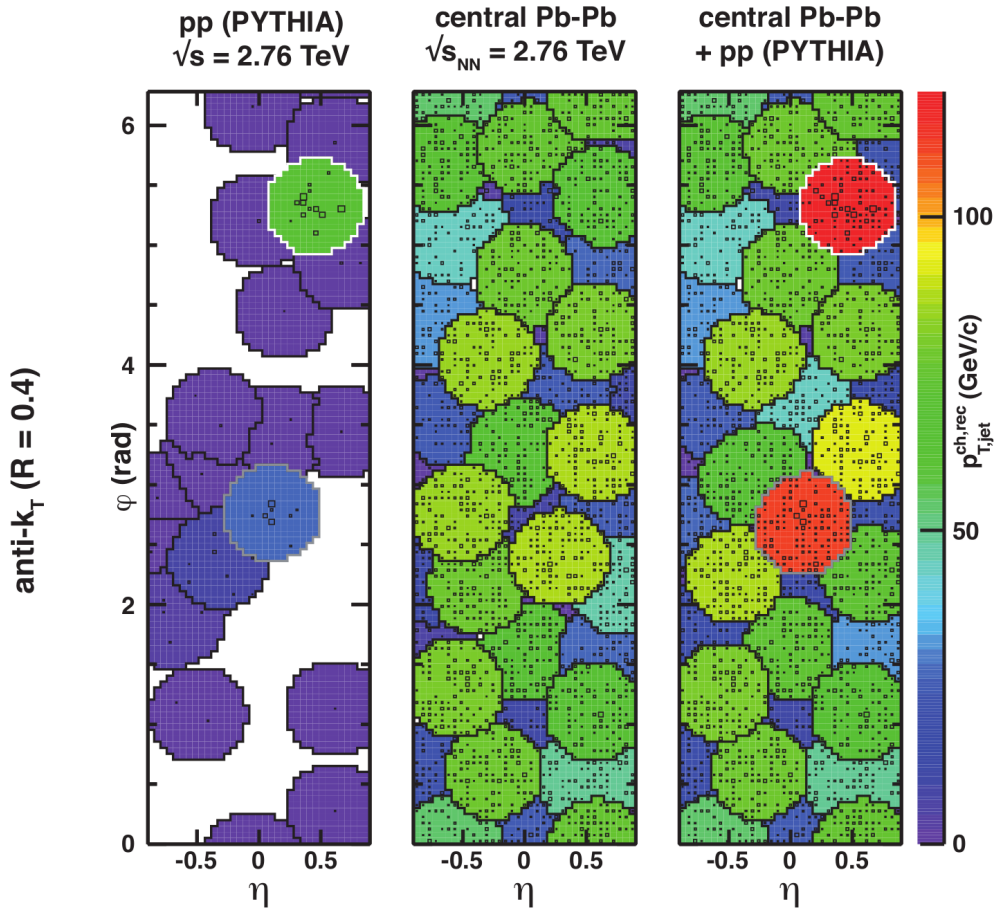


Figure 3.10: Anti- $k_T$  jets in the plane of pseudorapidity and azimuthal angle, as measured by the tracking system of ALICE. Shown are a simulated pp event with two high- $p_T$  jets (left), a measured heavy-ion event (middle) and the simulated event embedded in the heavy-ion event (right). Note that, by virtue of the anti- $k_T$  definition, the two leading jets have not changed significantly in the heavy-ion event except for additional momentum from the huge underlying event [19].

## NOTES

<sup>10</sup>Another very instructive way to motivate this solution is given in [61] with an analogy to the law of nuclear decay. It should be repeated here: The probability for nothing to happen is related to the probability for something to happen by conservation of total probability, or in the distinguished language of a particle physicist, by unitarity:

$$\mathcal{P}_{\text{nothing}} = 1 - \mathcal{P}_{\text{something}} \quad (3.36)$$

For an evolution in time  $t$ ,  $\mathcal{P}_{\text{nothing}}$  is multiplicative:

$$\mathcal{P}_{\text{nothing}}(0 < t \leq T) = \mathcal{P}_{\text{nothing}}(0 < t \leq T_1)\mathcal{P}_{\text{nothing}}(T_1 < t \leq T) \quad (3.37)$$

Generalizing to  $n$  subdivisions with  $T_i = (i/n)T$ ,  $0 \leq i \leq n$ , we get:

$$\begin{aligned} \mathcal{P}_{\text{nothing}}(0 < t \leq T) &= \lim_{n \rightarrow \infty} \prod_{i=0}^{n-1} \mathcal{P}_{\text{nothing}}(T_i < t \leq T_{i+1}) \\ &= \lim_{n \rightarrow \infty} \prod_{i=0}^{n-1} (1 - \mathcal{P}_{\text{something}}(T_i < t \leq T_{i+1})) \\ &= \exp\left(\lim_{n \rightarrow \infty} \sum_{i=0}^{n-1} \mathcal{P}_{\text{something}}(T_i < t \leq T_{i+1})\right) \\ &= \exp\left(-\int_0^T \frac{d\mathcal{P}_{\text{something}}}{dt} dt\right) \end{aligned} \quad (3.38)$$

The probability for the first thing to happen at a time  $t = T$  is the probability for something to happen following the condition that nothing happened before, so we get:

$$d\mathcal{P}_{\text{first}} = d\mathcal{P}_{\text{something}}(T) \exp\left(-\int_0^T \frac{d\mathcal{P}_{\text{something}}}{dt} dt\right) \quad (3.39)$$

This result can be related to nuclear decay, where we have  $dN/dt = -\lambda N(t)$  with the well known solution  $N(t) = N_0 \exp(-\lambda t)$ . If  $\lambda$  was time dependent the solution would resemble the result above:

$$N(t) = N_0 \exp\left(-\int_0^t \lambda(t') dt'\right) \quad (3.40)$$

$$\Rightarrow \frac{dN}{dt} = -\lambda(t)N_0 \exp\left(-\int_0^t \lambda(t') dt'\right) \quad (3.41)$$

<sup>11</sup>In a diffractive event, one or both nucleons become excited losing a very small amount of kinetic energy. Subsequently, a small number of particles is created in limited intervals of rapidity, usually close to the parent nucleon. In contrast, non-diffractive events involve substantial energy loss and lead to a much larger number of created particles that can be found within a large interval of rapidity, the fragmentation region.

Most aspects of particle production in non-diffractive events can be described from first principles; they can be addressed in terms of parton scattering within the framework of perturbative QCD (pQCD). Elastic and diffractive hadron collisions on the other hand, as representatives of *soft* hadron physics, are only in part tractable by pQCD. Instead, the usual description relies on a long tradition of scattering theory, *Regge theory*, and the assumption of a *Pomeron*, which is a quasi-particle that allows to encapsulate non-perturbative features of the strong interaction such as multi-gluon exchange at low energies [74].

## DIRECT PHOTON PRODUCTION

---

In this thesis, two approaches to direct photon production are used: Fixed-Order (FO) calculations and the Monte Carlo (MC) Parton Shower (PS). In addition to the last chapter, it should be pointed out again how the different approaches relate to each other.

FO calculations cover only the hard process, which results in a partonic event which may be followed by a fragmentation function to account for particles from the non-perturbative evolution, e.g. hadrons or fragmentation photons. These calculations give rise to a few final-state particles, accounting only for the large angle emission topology, respectively the coarse jet structure of an event.

Generators based on a PS, on the other hand, manage to turn these low-multiplicity states into events with realistic particle multiplicities. They are therefore indispensable tools to generate the input for the simulation of detector responses. It is an iterative procedure that stops at some infrared cutoff, where a phenomenological model has to be used to describe the non-perturbative hadronization process. PS algorithms are complementary to FO QCD calculations in the sense that they describe small angle parton splittings, in the collinear limit. The last decade saw many solutions combining PS algorithms and FO calculations, which is a non-trivial effort beyond leading order.

In the following, the different approaches, respectively software, used in this thesis will be introduced: PYTHIA 8 as representative of the parton shower approach (LO+PS), POWHEG as an extension of the former (NLO+PS), and JETPHOX as a fixed-order calculation at NLO.

### 4.1 PYTHIA 8

PYTHIA 8 is general-purpose event generator that plays an essential role for LHC physics analyses [75] [58]. It is used for studies on the generator level as well as input for detector simulations which are a necessary for all measurements. The next paragraphs describe the features of PYTHIA 8 that are used in this work to describe jet and direct photon production in pp collisions.

#### JET PRODUCTION

QCD jets are simulated using the process group HardQCD, which comprises the partonic  $2 \rightarrow 2$  processes ( $gg \rightarrow gg, qg \rightarrow qg, \dots$ ) including the production of charm and bottom jets. These processes account for the general production of hadrons, but are also necessary to describe fragmentation photons that arise in the final-state parton shower ( $q \rightarrow q\gamma$ ). Note that photons produced by the initial-state shower are almost exclusively emitted near beam rapidity.

#### PROMPT PHOTON PRODUCTION

Prompt photons are produced by the process group PromptPhoton, among which one finds the dominant processes of  $qg \rightarrow q\gamma$  and  $q\bar{q} \rightarrow g\gamma$ .

### SOFT QCD PROCESSES

The processes above are dominated by  $t$ -channel processes so that the cross section diverges roughly like  $d\hat{p}_T^2/d\hat{p}_T^4$  for  $\hat{p}_T \rightarrow 0$ . To generate a realistic cross section for events produced with an initial transverse momentum scale  $\hat{p}_T \lesssim 15$  GeV, the process group SoftQCD has to be used. Among other processes, these regularized processes include both jet and direct photon production and can also be used to generate diffractive and elastic hadron-hadron collisions, which are however not relevant for this work (see Sec. 3.6). The regularization and other details will be explained for the MPI framework, on which SoftQCD processes are based on.

### PARTON SHOWER

The perturbative evolution of the parton after the hard processes is given by a transverse momentum-ordered parton shower. ISR, FSR as well as MPI are described in one common progression of decreasing  $\hat{p}_T$  values, so that they are evolved in a uniform way towards increasing resolution. This means in particular that the ISR is evolved backwards in time. Note that FSR only redistributes the outgoing parton energy, while ISR can actually change the initial transverse momentum scale afterwards, so that the influence of ISR on a spectrum is significant.

The shower follows a *color dipole* approach: Partons will be assigned a color and matching color-anticolor partners will form a dipole. If a radiation occurs at one of the ends, the recoil partner's kinematics will be modified so that energy and momentum is conserved between the three partners. In case of ISR, the recoil acts on the entire previously created partonic system (global recoil)<sup>12</sup>.

The final-state shower terminates at a sharp cutoff that was chosen to be  $p_{T,min} = 0.5$  GeV for QCD emissions from partons and for the photon coupling to a quark. The initial-state has a smooth cutoff for the strong coupling by multiplying the QCD emission probability by a factor  $\hat{p}_T^2/(\hat{p}_{T,0}^2 + \hat{p}_T^2)$ .

### MULTIPARTICLE INTERACTION

The initial hard processes can occur more than once per pp collisions, which is modeled by the MPI framework of PYTHIA 8 (introduced in Sec. 3.6). Similar to the smooth IR cutoff for ISR, the divergent cross section for  $\hat{p}_T \rightarrow 0$  is multiplied by a regularization factor of  $\hat{p}_T^4/(\hat{p}_T^2 + \hat{p}_{T,0}^2)^2$ ; also, a regularized strong coupling  $\alpha_S(\hat{p}_T + \hat{p}_{T,0})$  is assumed. The parameter  $\hat{p}_{T,0}$  itself is given by a power law parametrization depending on the collision energy  $\sqrt{s}$ :

$$\hat{p}_{T,0}(\sqrt{s}) = \hat{p}_{T,0,Ref} \left( \frac{\sqrt{s}}{E_{CM,Ref}} \right)^n \quad (4.1)$$

with the parameters  $E_{CM,Ref} = 7000$ ,  $n = 0.215$  and most significantly,  $\hat{p}_{T,0,Ref} = 2.28$ .

In order to ensure momentum conservation, PDFs are rescaled, i.e. the probed Bjorken  $x$  can be changed to take momentum shifts (also flavor content changes) into account from ISR, FSR and MPI.

Measurements show that events with a hard scale have more underlying activity, which has come to be known as the *jet pedestal effect*. PYTHIA 8 describes it by a im-

compact parameter-based model: Central collisions have a higher probability for hard interactions.

For a more realistic description of the transverse structure of parton distributions, a *primordial*  $k_T$  is applied to the scattered parton system and balanced by the beam remnants.

The **MPI** framework provides optional models to describe even more details of hadron-hadron collisions. They are turned off by default, but provide an outlook of possible advances in the future<sup>13</sup>.

As a final comment on the interplay with **PDFs**, the **MPI** framework explicitly interprets **PDFs** as physical number densities, which is generally only true for **LO PDFs** [59].

#### 4.1.1 Discussion of Tuning

General-purpose event generators like PYTHIA 8 are traditionally based on a **LO** code to describe the underlying hard process. On the other hand, there are many programs and calculations available to describe specific phenomena at **NLO** or beyond, such as the production of multiple jets, weak boson production or as in this thesis, direct photon production. Still, **LO** event generators often perform equally well for many observables, because they are tuned to data with several parameters, of which we encountered some in the previous section. One might doubt the theoretical value of this kind of phenomenology, if deficiencies in the underlying theoretical description are simply alleviated by a set of parametrizations. But it is quite the contrary.

The tuning experts are well aware of the general limitations of their approach. For instance, no effort will be made to stretch the parameters such that multi-jet events can be described by  $2 \rightarrow 2$  matrix elements alone. (Also, that would probably worsen the description of other observables.) Instead, the chosen parameters often lie on the boundary between non-perturbative and perturbative regime. In that sense, the act of tuning points out limitations of our phenomenological treatment of **QCD** and may point to the direction that higher-order calculations have to go.

There is a multitude of parameters not because it is easier, but because we arrived at a stage where many detailed manifestations of **QCD** have been identified. Accordingly, single parameters are always to be understood with a phenomenological conception of **QCD** so that, again, they may point out the aspects that matter. (Take for instance the treatment of color flow that may play a role in understanding collective effects in proton-proton collisions.) For the given reasons it is interesting to describe aspects of general tuning strategies [58] and selected aspects of the PYTHIA 8 Monash 2013 tune [76] that is used in this thesis.

#### TUNING STRATEGY

The main parameter for the hard processes to describe the total inelastic cross section of pp collisions is the strong coupling. Next, the final-state shower and the hadronization model is investigated. This is done with transverse momentum spectra, event shapes and identified particle yields preferably from  $e^+e^-$  colliders, because it avoids the dependency on initial-state effects found in hadron colliders. Key parameters at this point are the strong coupling used for the final-state shower, the infrared cutoff for **FSR** and the parameters that govern the respective hadronization model.

The initial-state shower is parameterized next, with the aim to reach the best description in the perturbative regime before the heavily parameterized MPI framework is touched. Among the possible observables are jet shapes, dijet or photon-jet correlations and transverse momentum spectra. The main parameters to constrain are again the strong coupling and the infrared cutoff used in the initial-state shower. Here, the primordial  $k_T$  of the Monash 2013 tune is chosen according to transverse spectra of lepton pairs from  $pp \rightarrow Z \rightarrow l^+l^-$ .

Last, the MPI framework is constrained, preferably with all kinds of minimum bias data and underlying event observables. Frequently used are inclusive spectra of charge particle multiplicities against transverse momentum and rapidity, but also jet observables that are sensitive to the underlying event. For the description of MPI, the infrared regularization parameter  $\hat{p}_{T,0,\text{Ref}}$  from eq. (4.1) is most influential. At this point, one reason can be given why a certain tune is usually associated with a certain choice of PDF: PDFs with many gluons at low  $x$  tend to require a larger regularization parameter  $\hat{p}_{T,0,\text{Ref}}$  and vice versa.

Currently, the description of events with extremely low or extremely large particle multiplicity is problematic as well as the strange meson and baryon yields, which points out an issue in the current models of MPI and Hadronization of PYTHIA 8. This issue and a rough comparison of involved models are illustrated in a recent measurement of ALICE [28].

## 4.2 POWHEG

Depending on the observable, the LO prescription of hard processes in general-purpose event generators such as PYTHIA 8 may not be sufficient. LO cross sections are often found to lack the proper normalization, because significant production processes are only available at NLO. Traditionally, this can be alleviated by a so-called  $K$ -factor. Even then, one might find the kinematic configuration described by the LO+PS not realistic, in particular for the first hard radiation.

Different approaches have been developed to provide a better description of the hardest emission, taking into account the full NLO cross section. One successful example is MC@NLO [77], where the parton shower contribution is subtracted from the real-emission contribution of the NLO cross section and combined with the virtual correction. However, the implementation of the technique depends on the parton shower algorithm. Also, events can be generated with negative weights, because the subtracted contribution from the splitting function can overestimate the NLO real-emission contribution.

These problems have been addressed by the POWHEG method (Positive Weight Hardest Emission Generator) [78] [79]. Subsequently, a framework called POWHEG Box [80] has been developed, making the method accessible to users, who have to provide the Born matrix elements  $\mathcal{B}(\Phi_n)$ , the renormalized virtual matrix elements  $\mathcal{V}$  and the real-emission matrix elements  $\mathcal{R}(\Phi_{n+1})$  of the respective process. Via this framework, the POWHEG method has been applied to several processes, which are listed in [81]. In this work, the POWHEG method is used to calculate direct photon production at NLO, which was introduced to POWHEG Box in [82]. In the following, it will be described how the hardest emission in a parton shower is modified by the POWHEG method.

From the general equation of a regularized **NLO** cross section, Eq. (3.11), a **NLO**-weighted Born contribution  $\tilde{\mathcal{B}}$  can be defined:

$$\tilde{\mathcal{B}}(\Phi_B) = \mathcal{B}(\Phi_B) + \mathcal{V}(\Phi_B) + \int d\Phi_R [\mathcal{R}(\Phi_B, \Phi_R) - \mathcal{C}(\Phi_B, \Phi_R)] \quad (4.2)$$

Here,  $\mathcal{B}(\Phi_B)$  is the **LO** contribution,  $\Phi_B$  is the n-particle phase space of the **LO** Born process and  $\Phi_R$  is the phase space for the emission of an extra parton. The loop correction term  $\mathcal{V}(\Phi_B)$  is finite, because it includes the counter terms integrated over the phase space of the real emission. The same counter terms  $\mathcal{C}(\Phi_B, \Phi_R)$  regulate the real-emission contribution  $\mathcal{R}(\Phi_B, \Phi_R)$ .

$\tilde{\mathcal{B}}$  can now be coupled to a parton shower. The inclusive cross section of a parton shower considering only the first emission reads as follows:

$$d\sigma^{\text{PS}} = d\Phi_0 \mathcal{B}(\Phi_0) \left[ \Delta(Q^2, Q_0^2) + \int_{Q_0^2} \frac{dq_1^2}{q_1^2} \int dz_1 \frac{\alpha_s}{2\pi} P(z_1) \Delta(Q^2, q_1^2) \right] \quad (4.3)$$

Following the discussion of the Sudakov form factor  $\Delta$ , Eq. (3.22), the first term in the bracket accounts for the non-emission probability going from the hard scattering scale  $Q^2$  to the **IR** cutoff  $Q_0^2$ , while the second term is the probability for a branching at  $q_1^2$ , given that no branching occurred before. Following the POWHEG method, three modifications take place:

- The Born-level cross section  $d\Phi_0 \mathcal{B}(\Phi_0)$  is replaced by the **NLO**-weighted cross section  $d\Phi_0 \tilde{\mathcal{B}}(\Phi_0)$ .
- The splitting function gets replaced with the real emission matrix element:

$$\frac{dq_1^2}{q_1^2} dz_1 \frac{\alpha_s}{2\pi} P(z_1) \rightarrow d\Phi_R \frac{\mathcal{R}(\Phi_B, \Phi_R)}{\mathcal{B}(\Phi_0)} \quad (4.4)$$

- The replacement above is also applied to the Sudakov form factor:

$$\tilde{\Delta}(Q^2, q^2) = \exp \left[ - \int d\Phi_{R,(>q^2)} \alpha_s \frac{\mathcal{R}(\Phi_B, \Phi_R)}{\mathcal{B}(\Phi_0)} \right] \quad (4.5)$$

As a result, the **NLO** accurate first emission can then be generated similar to a parton shower with

$$d\sigma^{\text{POWHEG}} = d\Phi_0 \tilde{\mathcal{B}}(\Phi_0) \left[ \tilde{\Delta}(Q^2, Q_0^2) + \int d\Phi_{R,(>Q_0^2)} \alpha_s \frac{\mathcal{R}(\Phi_B, \Phi_R)}{\mathcal{B}(\Phi_0)} \tilde{\Delta}(Q^2, q_1^2) \right]. \quad (4.6)$$

To avoid double counting of the regular **PS** and the **NLO**-accurate first emission from POWHEG, any emission from the **PS** must be vetoed, if the transverse momentum is larger than the first and hardest emission from POWHEG. In this work, direct photon events generated with POWHEG are coupled with the **PS** of PYTHIA 8, which is ordered in transverse momentum. The **PS** is allowed to evolve from the kinematical limit, but the  $p_T$  of emissions generated by PYTHIA 8 will be translated to the POWHEG definition and emissions will be vetoed if they are harder than the POWHEG scale. Note that different scales are used for the **QCD** and the **QED** shower, which are the Born scale of the underlying event  $Q^2$  and the scale of a possible POWHEG radiation  $q_1^2$ , respectively.

## 4.3 JETPHOX

JETPHOX [83] allows to compute the inclusive direct photon cross section ( $h + h \rightarrow \gamma + X$ ) and direct photon production in association with a jet ( $h + h \rightarrow \gamma + \text{jet} + X$ ) [84] at NLO. An important feature of JETPHOX is the possibility to apply an isolation cut on the photon, requiring that the hadronic energy is below some threshold within a distance  $R$  to the photon:

$$E_{T,\text{iso}} \geq E_T^{\text{had}} \quad (4.7)$$

$$R^2 \geq (y - y_\gamma)^2 + (\varphi - \varphi_\gamma)^2 \quad (4.8)$$

The threshold energy or isolation energy  $E_{T,\text{iso}}$  can also be  $E_T^\gamma$ -dependent as employed by isolated photon measurements of the ATLAS collaboration [85].

The inclusive photon cross section is as follows:

$$\sigma(p_\gamma) = \sum_{a=g,q,\bar{q}} \int_0^1 \frac{dz}{z} \hat{\sigma}^a(p_\gamma/z; \mu_R, \mu, \mu_F) D_a^\gamma(z; M_F) + \hat{\sigma}^\gamma(p_\gamma; \mu_R, \mu, \mu_F) \quad (4.9)$$

Here,  $\hat{\sigma}^\gamma$  is the cross section of a photon produced in a hard process.  $\hat{\sigma}^a$  is the purely partonic cross section combined with a fragmentation function  $D_a^\gamma$ .  $p_\gamma$  is the photon momentum and  $z$  is the fraction of momentum carried over from a parton to the fragmentation photon. Three scales are involved: the renormalization scale  $\mu_R$  to determine the value of  $\alpha_s$ , the factorization scale  $\mu$  at which the PDF is probed and the fragmentation scale  $\mu_F$ .

Concerning the choice of words,  $\hat{\sigma}^\gamma$  gives rise to prompt photons, whereas  $\hat{\sigma}^a D_a^\gamma$  gives rise to fragmentation photons; the sum of both are called direct photons. This terminology is common among experimentalists, but unfortunately in contradiction with most phenomenological research, where photons from ME calculation are called direct and the sum of photons is called prompt.

The partonic cross sections are known up to NLO in  $\alpha_s$ :

$$\hat{\sigma}^\gamma(p; \mu_R, \mu, \mu_F) = \left( \frac{\alpha_s(\mu)}{\pi} \right) \sigma_{\text{Born}}^\gamma(p; \mu) + \left( \frac{\alpha_s(\mu)}{\pi} \right)^2 \sigma_{\text{HO}}^\gamma(p; \mu_R, \mu, \mu_F) \quad (4.10)$$

$$\hat{\sigma}^a(p; \mu_R, \mu, \mu_F) = \left( \frac{\alpha_s(\mu)}{\pi} \right)^2 \sigma_{\text{Born}}^a(p; \mu) + \left( \frac{\alpha_s(\mu)}{\pi} \right)^3 \sigma_{\text{HO}}^a(p; \mu_R, \mu, \mu_F) \quad (4.11)$$

We see that for higher corrections the fragmentation scale  $\mu_F$  appears not only in the purely partonic part  $\sigma_{\text{HO}}^a$ , which is associated to the fragmentation function  $D_a^\gamma$  in Eq. (4.9), but also in the prompt contribution  $\sigma_{\text{HO}}^\gamma$ . Here, we touch the reason why the distinction of prompt and fragmentation photons is not sensible beyond LO. Due to the necessity to factorize collinear singularities, the distinction relies on the choice of the respective factorization scheme and the fragmentation scale  $\mu_F$ . This arbitrariness vanishes in the sum of prompt and fragmentation photons so that only the sum is the physical observable.

In order to calculate the cross section for isolated photon cross section, the contributions that do not fulfill the isolation criterion Eq. (4.8) are subtracted from the inclusive cross section Eq. (4.9).



## NOTES

<sup>12</sup>Color dipoles can also be formed between IS and FS partons. In this case, PYTHIA 8 uses also a global recoil although the pure dipole picture would allow only a local recoil on the final state partner.

<sup>13</sup> An *enhanced color screening* can be chosen in PYTHIA 8: Depending on the event activity (number of MPI and ISR), the cross section can be decreased.

Also, the *rescattering* of partons, as a consequence of multiple hard scatterings, can be modeled. The issue of parton rescattering is connected to possible color reconnections between partons, for which also several models are available. The features of rescattering and color reconnection may be significant for the description of collective effects in small systems.



## EXPERIMENTAL SETUP

In the following, an introduction of the Large Hadron Collider (**LHC**) will be given. Next, a brief description of photon reconstruction by the detector experiments **ATLAS**, **CMS**, **LHCb** follows, in view of the theoretical predictions presented in Ch. 7. A more extensive description will be given for the **ALICE** detector experiment, which is required for the neutral pion reconstruction presented in Ch. 6.

## 5.1 LARGE HADRON COLLIDER

The **LHC** [86] at the European Organization for Nuclear Research (**CERN**) is a 27 km long synchrotron designed to accelerate protons and ions up to energies of 7 TeV per proton. So far, center of mass energies per nucleon pair of 13, 8 and 5 TeV have been reached for pp, p–Pb and Pb–Pb, respectively. A brief detour was taken for one day in October 2017, when Xe–Xe collisions were carried out.

Before entering the **LHC**, bunches of protons or ions are preaccelerated via several stages up to 450 GeV per proton. A maximum of 2808 proton bunches (each containing around 100 billion protons) are filled into the **LHC** via two transfer lines in opposing directions. Final acceleration is given by high-frequency cavities that deliver up to 16 MeV per lap and charge unit. Magnetic fields of up to 8 T force the beams onto the circular path.

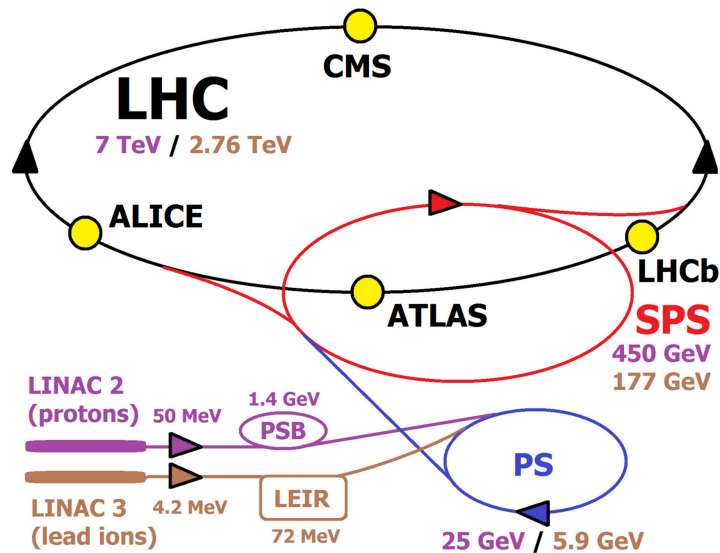


Figure 5.1: Schematic of the **LHC** and preaccelerators with respective beam energies per nucleon (design values) for protons and for lead ions. [87].

Beam injection and acceleration is usually followed by several hours of data taking. Collisions can be carried out simultaneously at four interaction points, where the detector experiments are situated. The four largest projects are A Toroidal LHC Apparatus (**ATLAS**) [88], Compact Muon Solenoid experiment (**CMS**) [89], A Large Ion

Collider Experiment ([ALICE](#)) [90] and LHC beauty experiment ([LHCb](#)) [91]. [ATLAS](#) and [CMS](#) are general-purpose detectors that use high interaction rates in order to collect signals in the Higgs sector and possible signs of physics beyond the Standard Model ([SM](#)). The [ALICE](#) detector is designed for heavy-ion collisions, resolving signals of hot nuclear matter in an environment of high particle multiplicities. [LHCb](#) focuses on the precise measurement of rare decay modes of B mesons and signals from Charge Parity ([CP](#)) violation.

Most of the [LHC](#) operation time is dedicated to proton-proton collisions, while the heavy-ion program usually uses only a few weeks each year. [LHC](#) operation is being improved continuously which is illustrated in table 5.1, comparing the design goal with the achieved values in selected run periods, including the proton-proton period of 2012 which is the basis for the neutral pion analysis presented in this thesis.

	design pp	pp 2010	pp 2012	pp 2017	PbPb 2015
beam energy [TeV]	7	3.5	4	6.5	2.6
bunch intensity	$1.15 \cdot 10^{11}$	$1.0 \cdot 10^{11}$	$1.5 \cdot 10^{11}$	$1.25 \cdot 10^{11}$	$2.2 \cdot 10^8$
bunch spacing [ns]	25	150	50	25	100
$\mathcal{L}_{\text{peak}}$ [ $10^{34} \text{ cm}^{-2} \text{ s}^{-1}$ ]	1.0	0.0021	0.77	2.1	$3.0 \cdot 10^{-7}$
integrated $\mathcal{L}$ [ $\text{fb}^{-1}$ ]		0.0048	23	50.6	0.076

Table 5.1: Comparison of [LHC](#) running conditions for selected periods and the design goals for proton-proton collisions. Note that the integrated luminosity is given per nucleon-nucleon collision [92] [93].

## 5.2 JET AND PHOTON RECONSTRUCTION AT ATLAS, CMS AND LHCb

### CMS

The main feature of the [CMS](#) detector is a superconducting solenoid that provides a magnetic field of 3.8 T [94]. Silicon pixel and strip detectors measure charged particles within a pseudorapidity range  $|\eta| < 2.5$ . An even larger acceptance of  $|\eta| < 3.0$  is covered by the Electromagnetic Calorimeter ([ECAL](#)) and the Hadronic Calorimeter ([HCAL](#)). Muons are detected in gas-ionization chambers that are embedded in the steel flux-return yoke outside the solenoid.

Photons are reconstructed from energy deposited in the [ECAL](#), however only in the barrel region,  $|\eta| < 1.48$ , within the scope of this work. Electron contamination is reduced by a matching of calorimeter clusters to tracks from the preceding tracking system. The cluster energy is additionally corrected for material interaction in front of the [ECAL](#). In order to protect the isolated photon signal from contamination of isolated hadrons and hadron decay photons, a maximum allowed energy deposition in the [HCAL](#) is defined. Within a cone of radius  $\Delta R = 0.15$  around the photon candidate the measured energy in the [HCAL](#) must not exceed 10% of the photon candidate energy in the [ECAL](#). In addition, a cut on the shower shape further suppresses the contribution from decay photons.

Jets are reconstructed following a standardized procedure (the [CMS particle-flow algorithm](#) [95]), where information is combined from electrons, muons, photons,

charged hadrons and neutral hadrons. The jet energy is not corrected for the underlying event in pp collisions.

## ATLAS

The [ATLAS](#) detector features a superconducting solenoid with a magnetic field of 2 T [85]. Charged-particle tracking is provided by silicon pixel and strip detectors with an acceptance of  $|\eta| < 2.5$ , complemented by a transition radiation tracker with slightly smaller acceptance  $|\eta| < 2.0$ . Electromagnetic and hadronic calorimeter systems provide a large acceptance  $|\eta| < 4.9$ . The measurement of jets and photons, however, is usually restricted to  $|\eta| < 2.1$  and  $|\eta| < 2.5$ , respectively, by constraints of the tracking system. Due to the segmentation of the calorimeter systems, measurements are usually reported for four different pseudorapidity intervals within  $|\eta| < 2.5$ .

Photons and electrons are reconstructed from energy deposition in the electromagnetic calorimeter, whereby the latter are identified from tracks measured by the tracking system. Photon identification relies primarily on the shower shape in a second layer of the electromagnetic calorimeter, where most of the photon energy is contained. Converted and unconverted photons are treated differently, based on a different constraint on the shower shape in the first electromagnetic calorimeter layer. Converted photons are identified as such from the tracking system, from conversion vertices in some minimum distance from the primary collision vertex.

Photon isolation is based on energy depositions in the calorimeter system. To avoid convolution with the photon signal, the energy in an area  $\Delta\eta \times \Delta\phi = 0.125 \times 0.175$  around the photon candidate is not considered for isolation. The estimated contribution from the underlying event and from remaining leakage of the photon signal ( $E \approx 2 \text{ GeV}$ ) is subtracted from the isolation energy.

## LHCb

The [LHCb](#) detector is a single-arm forward spectrometer with an pseudorapidity acceptance of  $2 < \eta < 5$  [96]. [LHCb](#) is designed for the investigation of heavy-flavor decays, but provides all the detector elements usually associated with general-purpose detector experiments. The tracking system consists of silicon-strip detectors in front of a dipole magnet with a bending power of about 4 Tm and silicon-strip detectors and straw drift tubes behind the magnet. A calorimeter system of scintillating-pad and preshower detectors, an electromagnetic and a hadronic calorimeter are used to identify hadrons, photons and electrons.

Jets are usually reconstructed from charged tracks and neutral clusters with a minimum transverse momentum of  $p_T^{\text{jet}} = 20 \text{ GeV}$ . Photons, however, can be measured down to transverse momenta as low as  $p_T^\gamma = 1 \text{ GeV}$  with converted photons [97]. In order to improve the isolation of photons, energy depositions in the [ECAL](#) from unconverted photons are also used to find contributions from neutral pion decay.

## 5.3 THE ALICE DETECTOR

With the exception of hard probes like jets or photons, the research of hot nuclear matter has to focus on low particle momenta, usually below  $10 \text{ GeV}/c$ . In this regime, many signals associated with the nuclear fireball are found such as the signs of hydrodynamic expansion (flow), thermal radiation or the enhancement or suppression of hadrons from heavy quarks. The other large experiments [CMS](#) and [ATLAS](#) usually restrict themselves to rare events with defined event topologies like isolated depositions of large energies. [ALICE](#), on the other hand, dedicates a large fraction of time to the sampling of Minimum Bias (MB) events, since rare triggers cannot be used to enrich most of hot nuclear matter probes. The [ALICE](#) detector is designed to capture a detailed picture of the collision using particle reconstruction down to low momenta ( $\sim 100 \text{ MeV}$ ), with a high efficiency even in the particle-dense environment of heavy-ion collisions. Furthermore, good PID capabilities allow to disentangle hot nuclear effects that are sensitive to mass or flavor.

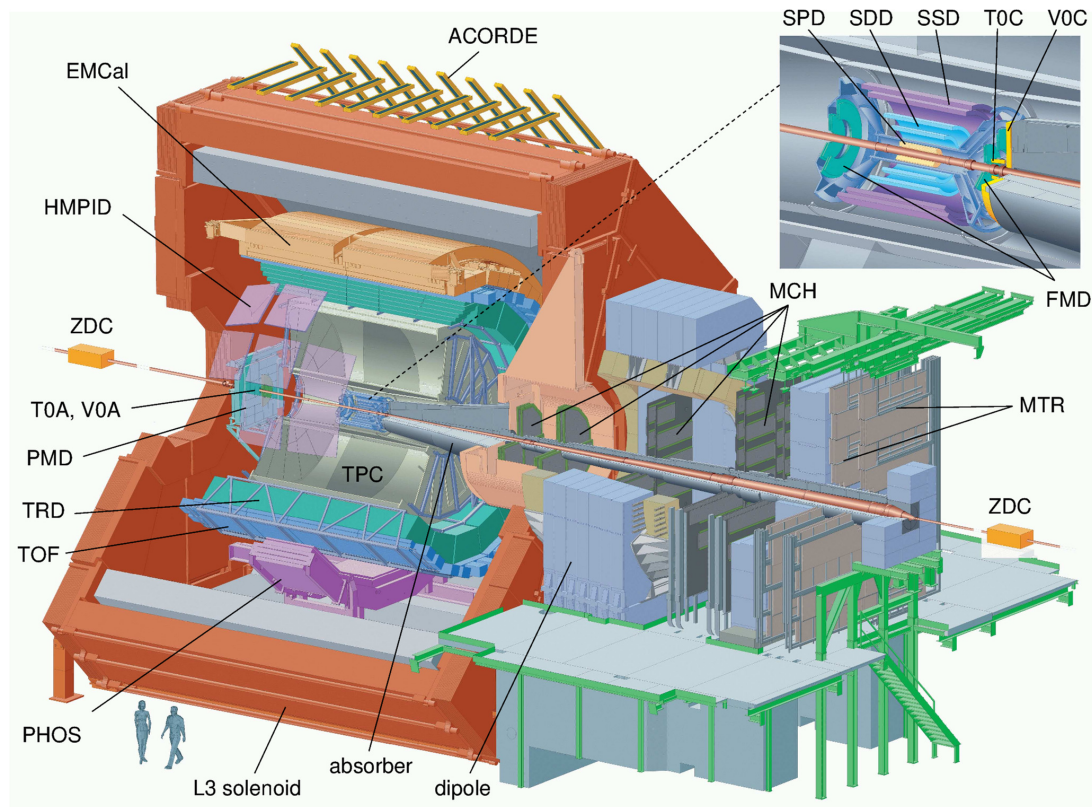


Figure 5.2: The ALICE experiment with its several detector systems (status of 2012) [90]. The general structure is as follows: Within the L3 solenoid magnet are the central barrel detectors ([ITS](#), [TPC](#), [TRD](#), [TOF](#), [EMCal](#), [PHOS](#), [HMPID](#)); near the beam pipe are the forward detectors ([V0](#), [T0](#), [PMD](#), [FMD](#), [ZDC](#)); also in forward direction is a muon spectrometer ([MCH](#), [MTR](#)) featuring a separate dipole magnet. On top of the solenoid one finds the cosmic ray detector [ACORDE](#).

In this analysis, photon signals from neutral pion decay are given by energy deposits in the [EMCal](#) calorimeter. In addition, the inner tracking detectors [ITS](#) and [TPC](#) are used to identify and suppress background signals that stem from charged particles. In the following, these three detector subsystems and aspects of calorime-

try and charged particle tracking will be covered. Methods of particle identification and collision centrality determination are not relevant for this analysis, but will still be illustrated, because they play a key role towards the physics goal of ALICE. The various other detectors of ALICE will be touched only briefly. The section will be concluded by a part on the ALICE trigger system and a part on luminosity determination.

### 5.3.1 Inner Tracking System (ITS)

The ITS is the detector closest to the interaction point and consists of six concentric layers of silicon detectors [98] (see upper right of Fig. 5.2). The innermost part of the ITS are the two layers of the Silicon Pixel Detector (SPD) that provide best granularity in the particle-dense environment close to the interaction vertex. Accordingly, the SPD plays a crucial role identifying the primary vertex of the collision and secondary vertices from weak decays. Then, two layers of the Silicon Drift Detector (SDD) follow and two layers of the Silicon Strip Detector (SSD). These systems contribute, like the SPD, to the charged-particle tracking and in addition, they provide energy loss information that can be used to identify charged particles at low momenta. The ITS covers full azimuth and a longitudinal range of  $|\eta| < 0.9$ .

### 5.3.2 Time Projection Chamber (TPC)

The TPC is the main tracking device of ALICE. The cylindrical TPC contains an active gas volume spanning over 1.5 m in radius after the ITS and 5 m along beam direction Fig. 5.3. Charged particles leave a trace of ionized molecules in the gas mixture (90% Ne - 10% CO<sub>2</sub>). An electric field let the resulting electrons drift towards the end caps, where they are detected by Multi-Wire Proportional Chambers (MWPC) including energy loss information. Accordingly, the signals on the end plates form a two-dimensional projection of the trajectories, which is complemented by a measurement of the drift time so that three-dimensional tracks of charged particles are available. The TPC allows the simultaneous tracking of several thousand charged particles, which is required in case of head-on heavy-ion collisions. In accordance with the ITS, the TPC covers full azimuth and a longitudinal range of  $|\eta| < 0.9$ .

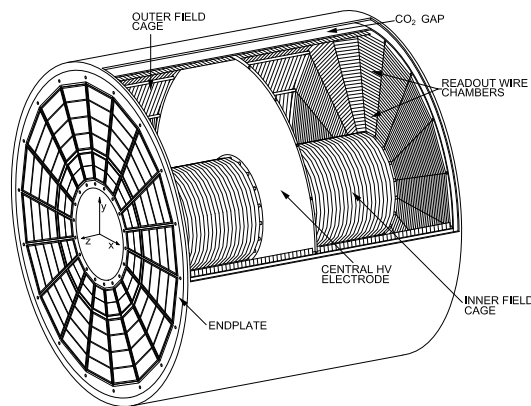


Figure 5.3: Schematic of the TPC [99].

### 5.3.3 Electromagnetic Calorimeter (EMCal)

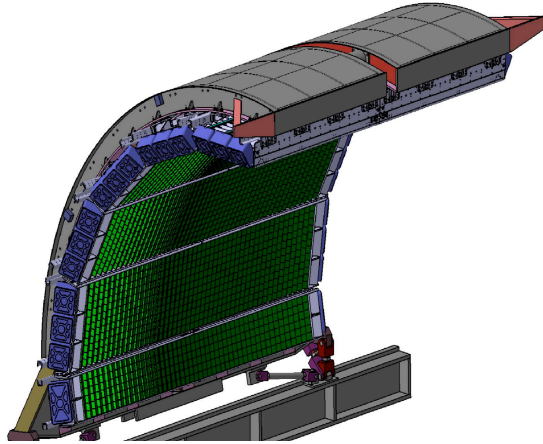


Figure 5.4: The EMCal supermodules installed in their support structure [100].

The EMCal (Fig. 5.4) has an azimuthal acceptance of  $80^\circ < \varphi < 187^\circ$  and covers a pseudorapidity interval of  $|\eta| < 0.7$ . It is a Shashlik-type calorimeter composed of 77 layers of lead and plastic scintillator for effective energy deposition and signal generation, respectively. The size of an EMCal cell, the smallest sensitive element, is  $6\text{ cm} \times 6\text{ cm}$ . At a distance of 430 cm to the collision point, this granularity translates into a spatial resolution of  $\Delta\eta \times \Delta\varphi = 0.0143 \times 0.0143$ . With the large acceptance, the EMCal is designed to measure the neutral energy of jets, complementing the TPC that measures the charged components.

The energy resolution of a calorimeter is usually parametrized by a quadratic sum of terms [101]:

$$\frac{\sigma_E}{E} = \frac{a}{\sqrt{E}} \otimes b \otimes \frac{c}{E} \quad (5.1)$$

The stochastic term ( $1/\sqrt{E}$ ) arises due to statistical fluctuations in energy deposit, energy sampling and scintillation light collection. The constant term  $b$  stems from systematic effects such as non-uniformity of the detector, channel-by-channel calibration errors, but also shower leakage. The noise term  $c/E$  accounts for deviations of the energy reconstruction by electronic noise. From electron test beams at PS and Super Proton Synchrotron (SPS) the energy resolution could be parametrized [102] (Fig. 5.5). Expected cluster energies for this analysis are well above 5 GeV, where the relative momentum resolution is better than 5%.



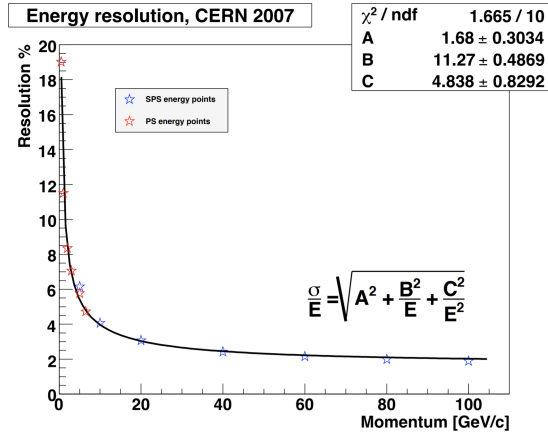


Figure 5.5: Energy resolution of the [EMCal](#) as determined from an electron test beam of known energy [102].

For the installed [EMCal](#) modules during the measurements, the absolute energy scale can be calibrated by detection of electrons that have been identified and measured before by the tracking system of [ALICE](#). More important, the neutral pion invariant mass spectrum built from all combination of [EMCal](#) clusters, is used to confirm the absolute energy calibration. Relative gain factors between the calorimeter cells are determined via Minimum Ionizing Particle ([MIP](#)) data, which is usually available in great statistics.

In view of the neutral pion analysis in this work, two additional circumstances should be noted: First, the material budget between interaction point and the [EMCal](#) surface amounts to around 0.45 radiation lengths, which implies that every second  $\pi^0$  decay involves at least one photon conversion. Second, photons and electrons with large energies above 100 GeV/c lead to electromagnetic showers that are not entirely contained within the calorimeter. This effect of longitudinal shower leakage has been accounted by measurements with electron test beams with energies up to 175 GeV.

#### 5.3.4 Other Detectors

##### PHOTON SPECTROMETER (PHOS)

Similar to the [EMCal](#), the [PHOS](#) is an electromagnetic calorimeter measuring photons and electrons. In contrast to the [EMCal](#), the [PHOS](#) is a homogeneous calorimeter based on lead tungstate crystals. It covers only a very limited region,  $|\eta| < 0.12$  and  $220^\circ < \varphi < 320^\circ$ , but features a better energy and position resolution than the [EMCal](#).

##### TRANSITION RADIATION DETECTOR (TRD)

The [TRD](#) consists of six layers of multi-wire proportional chambers that allow tracking of charged particles, which helps to measure high- $p_T$  tracks and to align [TPC](#) tracks in case of space charge distortions. Additional layers of radiator material generate transition radiation for very fast charged particles ( $\gamma > 1000$ ), which allows to separate the light electron from the much heavier pions. The [TRD](#) delivers complex

information within a few microseconds so that it can be used as a trigger detector for high- $p_T$  tracks, jets and heavy nuclei.

#### TIME-OF-FLIGHT DETECTOR (TOF)

The **TOF** uses Multigap Resistive Plate Chambers (MRPCs) to measure the time-of-flight of charged particles with a time resolution of 80 ps [103]. This detector complements the particle identification capabilities of the **ITS** and the **TPC** in the intermediate momentum region of minimal ionization where the Bethe-Bloch curves of the various particle species cannot be separated.

#### HIGH MOMENTUM PARTICLE IDENTIFICATION DETECTOR (HMPID)

The **HMPID** is a Ring Imaging Cherenkov Detector allows **PID** at even higher momenta than **TOF**. As a drawback, **HMPID** features only very limited acceptance. Figure 5.6 provides a comparison with the other detectors used for hadron identification.

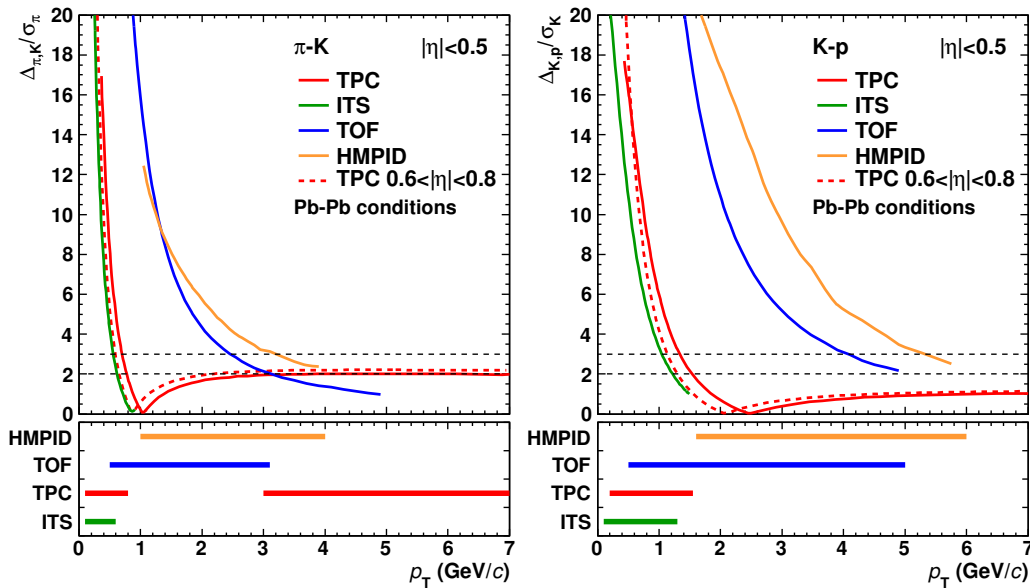


Figure 5.6: Separation power for pion-kaon (left) and kaon-proton (right) in heavy-ion collisions, given for **ITS**, **TPC**, **TOF** and **HMPID** as a function of transverse momentum [90].

#### FORWARD DETECTORS

Close to the beam line are several forward detectors that provide the determination of global event quantities such as the charged particle multiplicity, collision time and event reaction plane.

The Forward Multiplicity Detector (**FMD**) and the Photon Multiplicity Detector (**PMD**) are designed to measure charged particles and photons, respectively, at around  $|\eta| \approx 3$ .

The **V0** detector (**V0**) consists of two scintillator arrays at  $2.8 < \eta < 5.1$  (**V0-A**) and at  $-3.7 < \eta < -1.7$  (**V0-C**). The positioning allows to reject beam-gas interactions on basis of the time difference between the opposing arrays. The combined amplitude of the **V0** is used in heavy-ion collisions as a quantity that can be related to collision centrality. Most important, the **V0** information is used for the interaction trigger.

The Timing and Trigger detector at ALICE (**T0**), located at  $4.6 < \eta < 4.9$  (T0-A) and  $-3.3 < \eta < -3.0$  (T0-C), consists of Cherenkov counters that determine the event time with an uncertainty of 50 ps. The fast and precise time information provides the reference for the **TOF** and the wake-up signal for the **TRD**. Furthermore, time differences point to the longitudinal position of the primary vertex, which allows to trigger on events near the nominal collision point, away from peripheral beam-gas interactions.

Two versions of the Zero Degree Calorimeter (**ZDC**) are located 116 m away from the interaction point, one at each side. Only ions that fulfill the nominal charge-to-mass ratio will maintain a stable path along the LHC. Ions with different charge-to-mass ratios, emerging as the leftover from heavy-ion collisions, will depart from this path and can therefore be detected by the **ZDC**. The energy deposition by these *spectator ions* is an additional quantity related to the centrality of a heavy-ion collision.

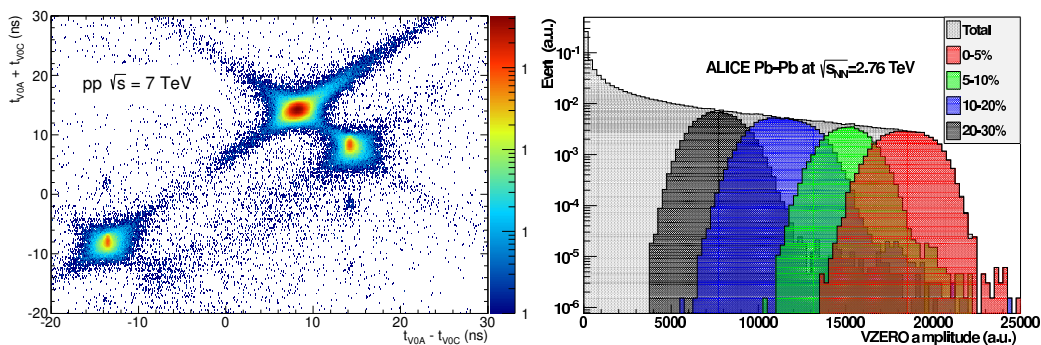


Figure 5.7: Left: The correlation of signal times in both **V0** arrays allows to distinguish collisions (largest spot) from background events [90]. Right: Classification of the collision centrality in Pb-Pb collisions from combined information of **V0** and **ZDC** [104].

## MUON SPECTROMETER

The muon spectrometer located in the forward arm of ALICE is divided in tracking chambers (**MCH**) and trigger chambers (**MTR**). Measurement of muon pairs allows to measure vector resonances; single muons can be used to measure open Heavy Flavor (**HF**) decays and the W-Boson. The muon spectrometer covers a pseudorapidity of  $-4.0 < \eta < -2.5$ .

## ACORDE

The ALICE Cosmic Ray Detector (**ACORDE**) [105] is an array of fast scintillators located on top of the L<sub>3</sub> magnet. It can be used to trigger the readout of ALICE in order to conduct separate studies on high-energy cosmic rays. The foremost purpose, however, is the calibration of the ALICE tracking detectors via the trajectories of single muons.

### 5.3.5 Triggering

The read-out of the entire ALICE detector happens on basis of a trigger system that is subdivided, according to time restrictions, into three levels:

**LEVEL-0 (L0):** Only the fastest detectors contribute to this trigger class ( $< 1.2 \mu\text{s}$ ). At this stage, global event quantities like multiplicity or centrality can be measured. Important detectors are the **V0** and **T0** that define the fundamental **MB** trigger decision.

**LEVEL-1 (L1):** Within  $6.5 \mu\text{s}$  after a collision, it is possible to test more time consuming trigger conditions such as the energy deposition in a certain part of a calorimeter. Accordingly, events with high- $p_T$  photons or jets can be identified at this stage. Due to the large distance of the **ZDC** from the interaction point, additional information about the event centrality only becomes available at this stage.

**LEVEL-2 (L2):** The last trigger L2 is issued after the drift-time of the **TPC** of about  $90 \mu\text{s}$ . The data buffered in each detector is then gathered and propagated to the High Level Trigger (**HLT**). Note that, except for some special cases, the L2 trigger accepts any decision made by the preceding triggers. It is therefore not a trigger in the practical sense, but rather an instance where the slow **TPC** can issue a veto.

**HLT:** Before the data is stored, it will be filtered by the High Level Trigger (**HLT**), a purely computational instance with the main task to combine the different inputs (event building) and to compress the data.

Due to the time constraint given by the **TPC**, the sampling rate is of the order of 10 kHz for **MB** events. For the sampling of rare triggers, the rate can be increased to 500 kHz in pp collisions.

In case of Pb–Pb and p–Pb collisions, the **LHC** delivers a luminosity that is below or around the possible data taking rate of ALICE. In case of pp collisions, however, the interaction rate has to be reduced severely by separating the beams up to 3.5 times the RMS of the transverse beam profile. For the data taking period of 2012, examined in this thesis, one even adopted a scheme where the main bunches of one beam collide only with the sparsely populated *satellite bunches* of the other beam.

#### 5.4 LUMINOSITY AND CROSS SECTION MEASUREMENT

The measured yield of any observable is based on the trigger choice of the detector experiment. It follows that for a comparison with theory or any other experiment the yield has to be scaled such that a cross section  $\sigma_x$  independent of the trigger choice can be reported<sup>14</sup>. The accumulated yield  $N_x$  of a measured observable has to be divided by the integrated luminosity  $\mathcal{L}_{\text{int}}$ :

$$\sigma_x = \frac{N_x}{\mathcal{L}_{\text{int}}} \quad (5.2)$$

$$\text{with } \mathcal{L}_{\text{int}} = \frac{N_{\text{events}} \cdot R}{\sigma_{\text{ref}}} \quad (5.3)$$

Here,  $N_{\text{events}}$  is the number of analyzed events and  $\sigma_{\text{ref}}$  is the reference cross section determined in a van der Meer (**vdM**) beam scan. The additional trigger rejection factor  $R$  accounts for any additional scaling from the reference trigger to the trigger used in the respective physics analysis. The minimum bias trigger can often be identified with the reference trigger used in an **vdM** scan ( $RF = 1$ ).

In a **vdM** scan, the two beams are moved across each other in transverse direction. The trigger rate  $R(\Delta x, \Delta y)$  is measured as a function of the beam separation  $\Delta x$  and  $\Delta y$ . The integral along  $R(\Delta x, 0)$  and  $R(0, \Delta y)$ , respectively, divided by the head-on rate  $R(0, 0)$  yields the effective widths  $h_x$  and  $h_y$  of the convoluted beams [106]. The bunch crossing frequency divided by the effective beam area yields the luminosity:

$$\mathcal{L} = \frac{N_1 N_2 f_{\text{revo}}}{h_x h_y} \quad (5.4)$$

Here,  $N_{1,2}$  are the number of bunches for the two beams and  $f_{\text{revo}}$  is the revolution frequency in the accelerator. Finally, one obtains the cross section for the reference process dividing the head-on interaction rate by the luminosity:

$$\sigma_{\text{ref}} = \frac{R(0, 0)}{\mathcal{L}} \quad (5.5)$$

Fig. 5.8 gives an example on the beam profile and cross section measurement in a **vdM** scan. Further details of the luminosity determination for the 2012 period that has been used in this thesis can be found in [107].

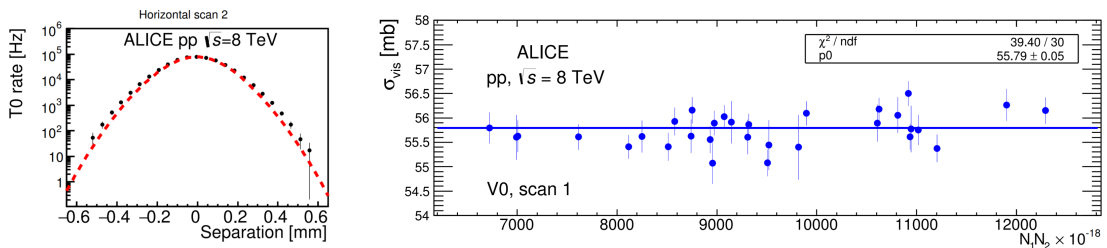


Figure 5.8: Interaction rate measured by the T0 detector against beam separation. Right: Measured cross section of the V0 detector based trigger condition for different bunch filling schemes of the LHC.

## 5.5 SOFTWARE

The backbone of the analysis framework is ROOT [108], a C++ based software designed for the typical tasks necessary in HEP, e. g. simulation, event reconstruction, physics analysis and graphical output of results. On top of ROOT, the ALICE collaboration uses the add ons ALIROOT, which provides fundamental tasks like detector simulation and event reconstruction, and ALIPHYSICS, which is the collection of all physics analyses.

There are several MC generators available in ALIROOT for the description of pp collisions and heavy-ion collisions. However, only PYTHIA 8 (Sec 4.1) will be relevant for the data analysis part of this thesis. For a full event description, the simulation on *generator level* is followed by a propagation of final-state particles through the detector. The entire ALICE detector is modeled within GEANT 3 or GEANT 4 [109], a software which allows to describe the detector response including material interactions and details of the electronic read-out.



## NEUTRAL PION MEASUREMENT FROM MERGED CLUSTERS

In this chapter, the measurement of neutral pions from the reconstruction of single calorimeter clusters, so-called merged clusters, will be presented. In the next section, the signal definition and the reconstruction method will be outlined and discussed in context of the other neutral pion reconstruction methods used in ALICE. Three sections will describe the used data set, the selection of calorimeter clusters of the Electromagnetic Calorimeter (EMCal) and the subsequent analysis for neutral pions. Then, the evaluation of systematic uncertainties follows as well as the presentation of the corrected transverse momentum spectra.

### 6.1 NEUTRAL PION RECONSTRUCTION IN ALICE

The neutral pion mostly decays into two photons,  $\pi^0 \rightarrow \gamma\gamma$ , with a branching ratio of  $98.823\% \pm 0.034\%$  [10]. The second decay mode, the Dalitz decay  $\pi^0 \rightarrow e^+e^-\gamma$  with a branching ratio of  $1.174\% \pm 0.035\%$ , will also be considered in this analysis. Exotic decays, such as  $\pi^0 \rightarrow e^+e^+e^-e^-$  are not explicitly accounted for, since their branching fractions are well below  $10^{-3}$ .

We may conclude that most of the neutral pion signal stems simply from two photons. However, since a significant material budget is located before the EMCal calorimeter, the actual signal often comprises electrons and positrons from pair production, also known as photon conversion.

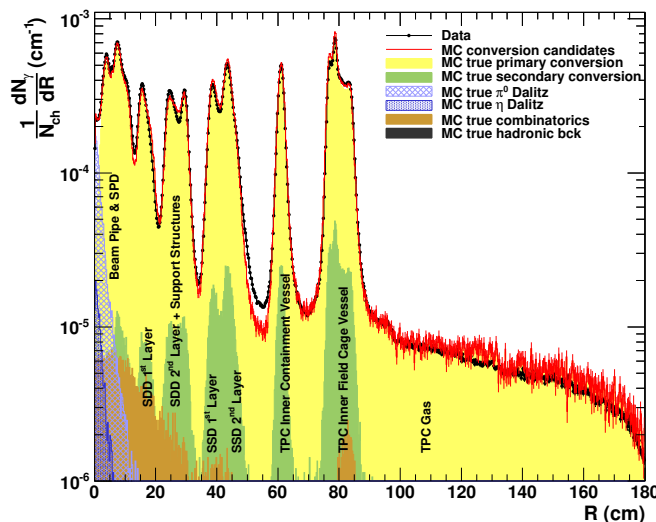


Figure 6.1: Radial distribution of reconstructed photon conversion points (black) from the primary vertex up to the first half of the TPC. Also shown in red is a comparison to MC simulations based on the PHOJET event generator [110]. A contamination from Dalitz decays is found only very near the primary vertex.

Depending on the respective construction method, the momentum of the original photon can be reconstructed from both leptons. This kind of signal is denoted as a

*conversion photon*. Photon conversion can be accounted for by the detector simulation, but only to a certain degree of accuracy due to limited knowledge of the material budget.

Fig. 6.1 shows a radial distribution of photon conversion points within the ALICE material budget, reconstructed from actual data and from MC. Such a reconstruction is limited to the center of the TPC, at a distance  $R = 180$  cm to the collision point, because at least half of the available TPC clusters are required for a reliable tracking of the electrons. The abundance of photon conversions at larger radii (Fig. 6.4) is solely derived from MC, relying on a correct material budget description within the detector simulation of the outer detectors TRD, TOF and the support structures.

The reconstruction of neutral mesons via photon conversions is denoted as the Photon Conversion Method (PCM) within ALICE. Neutral mesons can be identified via the invariant mass distribution of conversion photon pairs. The method greatly benefits from the good momentum resolution of tracks within ITS and TPC, so that neutral mesons can be reconstructed down to transverse momenta as low as  $0.3 \text{ GeV}/c$  [42]. However, since both decay photons have to undergo conversion, the low conversion probability for one photon of around 9% translates into a reconstruction efficiency below 1%. Accordingly, the transverse momentum range of this method is limited due to insufficient statistics. The efficiency of the PCM method, including factors of longitudinal and azimuthal acceptance, is shown in Fig. 6.2, compared to other methods of neutral pion reconstruction.

The other methods consider a calorimeter signal of some sort: The methods of EMCal and PHOS require two well-separated energy depositions (di-clusters) in the respective calorimeter. As for PCM, an invariant mass analysis allows to select the neutral pions from the multitude of photon candidate pairs.

As seen from Fig. 6.2, the EMCal method boasts an impressive efficiency, also due to its larger acceptance in comparison with PHOS. However, the efficiency declines sharply at around  $10 \text{ GeV}/c$  for the EMCal method. At this point, the two decay photons of the neutral pion receive such a large boost that the angle between them can no longer be resolved within the given granularity of the EMCal. The photons are no longer detected as two resolved energy depositions, but as a single, *merged* cluster (Fig. 6.3). For PHOS, the cluster merging happens at even larger transverse momenta due to the fine granularity of its calorimeter cells.

One option to avoid the merged cluster problem is to combine calorimeter clusters with conversion photons. In this case, a small angle between the decay photons can still be resolved so that the invariant mass analysis is feasible for larger transverse momenta. This method, called PCM-EMCal Method (PCM-EMCal), extends the transverse momentum range beyond  $20 \text{ GeV}/c$ , but again is limited due to the small conversion probability.

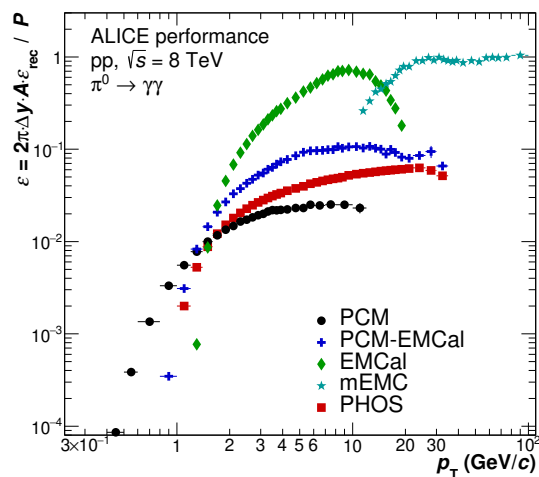


Figure 6.2: Efficiency (including acceptance and purity) of neutral pion reconstruction for different methods.



### NEUTRAL PION RECONSTRUCTION FROM MERGED CLUSTERS

A second option is to abandon the invariant mass requirement all along and use the merged clusters as the signal. The obvious gain of this method, denoted merged EMCAL method (**mEMC**), is the large efficiency of the **EMCAL**. However, it should be noted that this strength can only be exploited with the use of **EMCAL** triggered events that greatly enrich the available event statistics at transverse momenta beyond  $10 \text{ GeV}/c$ . Before the actual analysis is presented in the next sections, it is instructive to anticipate key assumptions of the analysis.

Without the invariant mass information, the merged cluster signal can be contaminated by a multitude of sources such as decay photons from other neutral hadrons, direct photons, electrons (mostly from weak decays), and even hadrons that deposit only part of their energy in the electromagnetic calorimeter, but come in great multiplicity. However, it is expected that decay photons from neutral pions still dominate. That means the raw signal already comes with a high purity and uncertainties in background sources may not be a grave problem. The yield of background sources is described by the MC. It has to be ensured that this description is reliable or otherwise, has to be corrected.

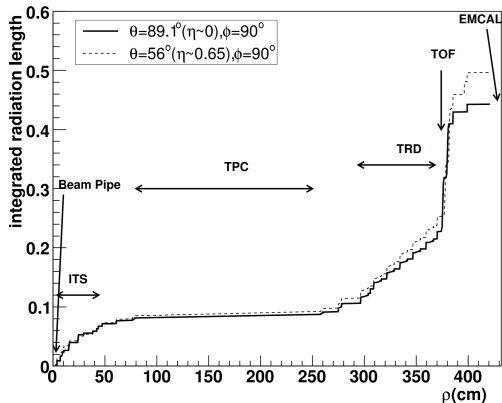


Figure 6.4: Integrated radiation length in front of **EMCAL** [100].

There is a significant material budget in front of the **EMCAL**, which leads to frequent photon conversions complicating the situation (Fig. 6.4). Due to the large boost, the electrons from conversions may entirely be contained within the merged cluster. In this beneficial case, the entire energy is still contained in the cluster. Both electrons might also be well separated considering the magnetic field, such that not the entire energy of the neutral pion is found in the cluster. The most extreme scenario is a cluster which stems from a neutral pion, but consists only of one electron. In every case, there is a very specific relation between true and measured momentum (resolution matrices), which has a large leverage on the corrected spectrum. These considerations also apply to the Dalitz decay  $\pi^0 \rightarrow e^+e^-\gamma$ , but its contribution is considered rather insignificant.

A large fraction of background clusters stems only from single particles, unlike the merged clusters from neutral pion that mostly originate from two or more photons or electrons. Therefore, merged clusters and single-like clusters should be distinguishable to some degree by their cluster shape, which is the projection of energy deposition along the calorimeter towers onto the **EMCAL** surface. The merged clusters

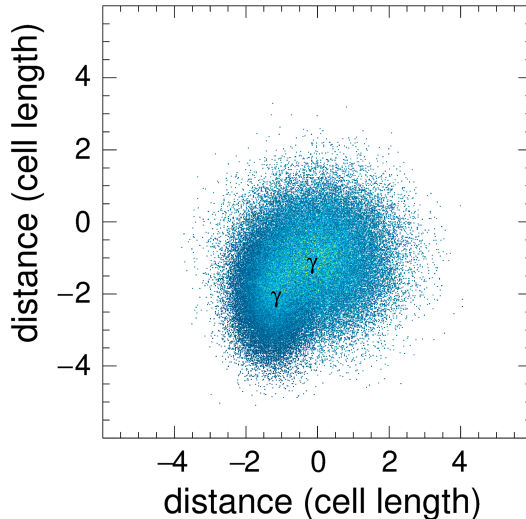


Figure 6.3: Example of a merged cluster from two decay photons, illustrated with arbitrarily fine granularity.

are expected to be elongated or rather elliptic compared to single-like clusters, which are rather circular. One significant exception among the background sources is the  $\eta$  meson decay: Elongated cluster shapes are also expected from the decay  $\eta \rightarrow 2\gamma$  (branching ratio  $39.4\% \pm 0.2\%$ ). Due to the larger mass however ( $m^\eta = 548 \text{ MeV}/c^2$ ), merged clusters from the photons of the  $\eta$  meson decay are expected at larger transverse momenta.

In case a background cluster stems from a charged particle, it could be identified as such, since it should appear as a track within the central barrel. If a connection can be reliably drawn between these tracks and a cluster, a procedure denoted as *cluster-track matching*, the contamination by charged particles can be suppressed.

Neutral pions do not only arise from parton fragmentation, but also from the decay of other hadrons. It is a convention to reduce this entanglement based on the decay length of mother hadrons. In the end, the neutral pion spectra should only describe *primary* neutral pions, which are defined here either as neutral pions that directly come from parton fragmentation or from particles with decay lengths smaller than  $c\tau = 1 \text{ cm}$ . Accordingly, the primary neutral pion definition also comprises strong decays such as  $\eta \rightarrow 3\pi^0$ . Neutral pions from weak decays on the other hand, with  $c\tau > 1 \text{ cm}$  such as  $K_S^0 \rightarrow 2\pi^0$ , are defined as *secondary* neutral pions that have to be properly subtracted from the final spectra.

To conclude this introduction, it is instructive to anticipate the parts from which the final neutral pion cross section is constructed.

$$E \frac{d^3\sigma}{dp^3} = \frac{1}{2\pi p_T} \frac{N_{\text{raw}}}{\Delta y \Delta p_T} \frac{\sigma_{\text{MB-AND}}}{N_{\text{ev}}} \frac{P}{\epsilon A} \frac{1}{R} \quad (6.1)$$

Here,  $N_{\text{raw}}$  is the raw yield measured in several transverse momentum bins of width  $\Delta p_T$  and within the rapidity  $|y| < 0.6$  so that  $\Delta y = 1.2$ .  $P$  is the signal purity,  $\epsilon$  is the reconstruction efficiency and  $A$  the geometrical acceptance.  $\epsilon$  and  $A$  are entirely determined from MC simulation.  $P$  is also determined from MC simulation, but will be corrected additionally for known deficiencies.  $N_{\text{ev}}$  denotes the number of events and  $\sigma_{\text{MB-AND}}$  the cross section of the Minimum Bias (MB) trigger. The trigger rejection factor  $R$  accounts for the per-event yield enhancement for each of the two **EMCal** triggers that will be used. Each trigger is fully efficient for the minimum transverse momentum of  $p_T = 10 \text{ GeV}/c$ , which is the kinematic region where merged clusters start to appear.

The analysis is structured as follows: First, the underlying data will be introduced as well as the associated **MC** detector simulation. Event selection cuts will be described and the use of **EMCal** event triggers in addition to the **MB** trigger. The process of cluster reconstruction follows and the cluster cuts for the rejection of clusters that stem from different proton bunch crossings and from possible distortions in the **EMCal** read-out. Also, a fine-tuning of the cluster energy information will be introduced and the rejection of charged particles based on cluster-track matching. Afterwards, the analysis for neutral pions from the selected cluster sample follows. After a discussion of the signal definition, a cut on the cluster shower shape will be applied and the resulting signal purity, along with other key factors from Eq. (6.1), will be determined. In the last section, systematic uncertainties are determined and the corrected neutral pions cross section will be presented.

## 6.2 DATA SET

This analysis covers the [ALICE](#) data taking campaign of 2012, where pp collisions have been carried out at  $\sqrt{s} = 8$  TeV. The entire data set of this campaign is subdivided into run periods labeled LHC12a, LHC12b, LHC12c, LHC12d, LHC12f, LHC12h and LHC12i. Each period corresponds to roughly one month of data taking and comes with partially different issues. However, any modifications in the detector configuration are usually reflected in the detector simulation; [MC](#) sets are said to be *anchored* to certain run periods.

### 6.2.1 Event selection

[MB](#) events are selected on the basis of forward energy depositions near the beam line. For the given analysis, an event is selected in case of a coincidence in both [V0](#) detectors. The associated cross section is denoted as  $\sigma_{\text{MB-AND}}$ , but the technical name INT7 from the [ALICE](#) classification of triggers will be used to denote [MB](#) events.  $\sigma_{\text{MB-AND}}$  for the given pp collisions at  $\sqrt{s} = 8$  TeV was determined from a [vdM](#) scan, as described in Sec. 5.4, with a value of  $\sigma_{\text{MB-AND}} = 55.8 \pm 1.5$  mb [107]. This is a large fraction of the inelastic cross section, which was determined to be  $\sigma_{\text{inel}} = 74.7 \pm 1.7$  mb [111].

Before the analysis, the respective data sample is filtered for appropriate events. Calibration events are discarded by the *physics selection* as well as events that have been assigned to beam-gas interactions or distortions (see Sec. 5.3.4).

Background particles that cross one of the two layers of the [SPD](#) are nearly parallel to the beam axis. As a result, hits in the [SPD](#) may arise from background particles, but a cluster pair from both layers will only by chance be combined to a tracklet, because the tracking procedure is constrained to the primary vertex. A rejection of events will therefore be performed if the number of [SPD](#) clusters is large compared to the number of reconstructed [SPD](#) tracklets:

$$N_{\text{SPD,cluster}} > 4 \cdot N_{\text{SPD,tracklet}} + 65 \quad (6.2)$$

The detection of multiple pp collisions can occur within a given bunch crossing (in-bunch pileup). Multiple primary vertices can be resolved by the [SPD](#), so that the number of events with in-bunch pileup can be significantly reduced. Also, the measurement of particles from successive collisions may not be resolved in time (out-of-bunch pileup). Out-of-bunch pileup in the [EMCal](#) will be accounted for on analysis-level by a cut on the cluster time information.

The primary vertex of an event has to be within a distance of the nominal collision point along the beam axis,  $|z_V| < 10$  cm. Events where no primary vertex could be reconstructed still count for the event normalization, because these are still visible events with respect to the underlying cross section. Therefore, the number of events  $N$  used for normalization is given by the number of events  $N_{<10\text{cm}}$ , where a vertex was determined for the given cut, and the number of those events, where no vertex was reconstructed for the given cut:

$$N = N_{<10\text{cm}} + N_{\text{no vtx}} \cdot \frac{N_{<10\text{cm}}}{N_{<10\text{cm}} + N_{>10\text{cm}}} \quad (6.3)$$

This normalization is being done for each trigger subset. For the given data set and the MB trigger INT7, the fraction of events rejected after the physics selection amounts to roughly 3%.

### 6.2.2 EMCal Triggers

Aside from the INT7 trigger, which detects mostly low energetic events, two EMCal-based triggers have been used in the sampling of pp collision. The EMC7 trigger is based on the fast EMCal Lo trigger, that selects an event if the summed amplitude over a region of  $4 \times 4$  cells in a Trigger Region Unit (TRU) exceeds a value that corresponds to an energy deposition of roughly 2 GeV. The L1 photon trigger EGA requires an even larger energy deposit of around 10 GeV. As more time is available for a L1 trigger, the energy can be summed over several TRU, increasing the trigger efficiency. Roughly  $110 \cdot 10^6$  events have been sampled for INT7,  $36 \cdot 10^6$  for EMC7 and  $2.1 \cdot 10^6$  for EGA. The raw cluster spectra obtained from the three triggers and normalized per event are given in the following figure.

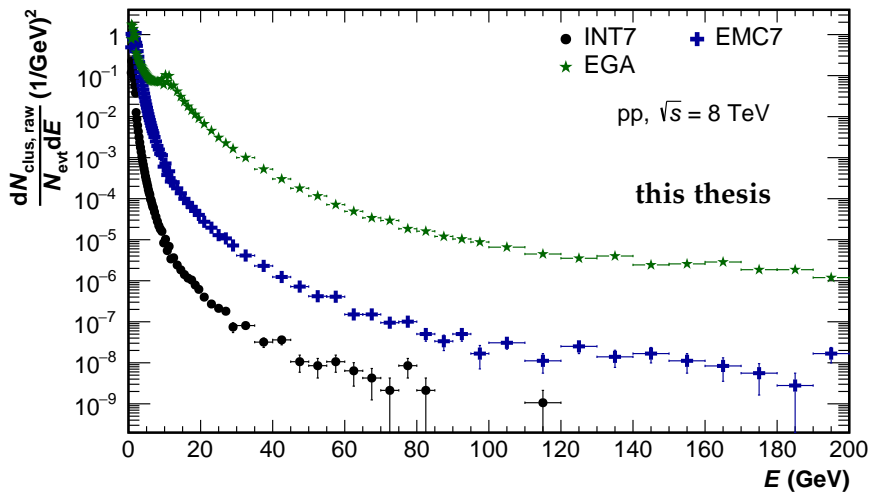


Figure 6.5: Energy spectrum of the raw cluster yield from each trigger, normalized to the respective number of events.

By far, the EGA trigger provides the most high- $p_T$  clusters per event. However, since EMC7 exceeds EGA in pure event abundance by a factor 17, the EMC7 trigger will still contribute to the final result up to energies about 40 GeV.

The INT7 trigger, on the other hand, will not be used for the final reconstruction of the neutral pion spectrum, because the available statistics are already insufficient in the transverse momentum region around of 10–15 GeV/ $c$ , where the merging of clusters from the neutral pions sets in. However, the cluster spectrum of MB is necessary to derive the per-event enhancement factor, i. e. the trigger rejection factor  $R$ , for the EMC7 trigger. The rejection factor for the EGA trigger, in turn, is derived from the EMC7 trigger. The relative rejection factors have been derived from a constant fit in the respective plateau region and are shown in Fig. 6.6.

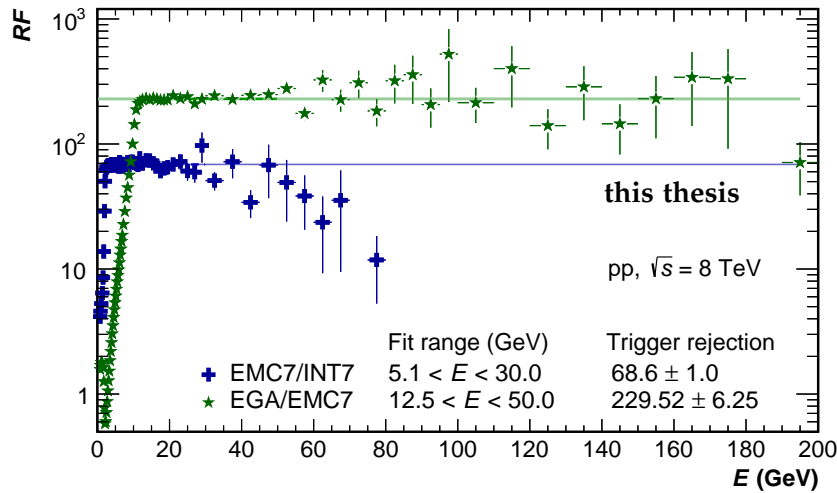


Figure 6.6: Trigger rejection factors extracted from a fitted ratio of raw cluster yields.

The trigger conditions are not explicitly described within the [MC](#) simulation, but a procedure called trigger mimicking is used, which reproduces the characteristic trigger turn-on curve using an energy threshold and a Gaussian energy smearing that is modeled from data. Anyway, since the merged cluster analysis takes place in a kinematic regime above 10 GeV, the correct description of the turn-on poses no particular problem.

### 6.2.3 Monte Carlo Simulations

The development of the analysis and the determination of correction factors like the reconstruction efficiency is carried out on the basis of [MC](#) events generated by PYTHIA 8 (described in [Sec. 4.1](#)) and coupled to a detector simulation provided by GEANT 3.

For this analysis, purely partonic scattering processes ( $qg \rightarrow qg$ ,  $gg \rightarrow gg$ , ...) including heavy quarks are considered. These processes refer to the `HardQCD:all` switch in PYTHIA 8 and are also called Jet-Jet events in the analysis context of the [ALICE](#) collaboration. These processes describe the non-diffractive part of the inelastic proton-proton cross section down to some minimum hard scattering scale and are used to describe hadron production for the given transverse momentum region of 10–200 GeV/ $c$ .

The Jet-Jet processes do not account for prompt photons and electrons from weak boson decay, which are an additional source of background to the neutral pion signal. Instead of using full detector simulations to describe these additional processes, a correction factor will be considered, based on dedicated generator-level simulations from PYTHIA 8 and POWHEG.

To ensure homogeneous statistics along the steeply falling spectrum, events are created in bins of the transverse momentum transfer  $\hat{p}_T$  of the underlying partonic  $2 \rightarrow 2$  process. Accordingly, events are weighted with  $\omega_{JJ}$  for the production cross section of the respective  $\hat{p}_T$ -bin:

$$\omega_{JJ} = \sigma_{\text{evt}} \frac{N_{\text{generated}}}{N_{\text{trials}}} \quad (6.4)$$

Here,  $\sigma_{\text{evt}}$  is the cross section for one event as reported by PYTHIA 8. Only events with a jet transverse energy of at least 5 GeV within ALICE acceptance are considered for storage, other events are discarded from the MC sample.  $N_{\text{trials}}$  denote the number of trials necessary to generate  $N_{\text{generated}}$  accepted events.

#### 6.2.4 Quality Assurance for Events and EMCAL Clusters

Before a physics analysis is carried out, the respective data set has to be checked for irregularities that would distort the final result. Generally, data gets discarded in case of unstable run conditions, detectors malfunctioning and also if key quantities show large deviations for any reason. On the other hand, data can still be kept in case the distortions are sufficiently described by the MC simulation anchored to the respective data taking period.

A first instance of quality assurance (QA) is achieved using available information from the ALICE Run Condition Table (RCT) in order to exclude single runs where important detectors, such as TPC, ITS and EMCal, have been flagged as problematic. For further assessment, quantities averaged per event are cross checked between runs, such as the number of charged tracks or the number of EMCal cluster candidates. For a given run, the energy spectrum as well as distributions in  $\eta$  and  $\varphi$  of cluster candidates are checked for irregularities. Single calorimeter cells can be identified as *hot* cells or *dead* cells if they constantly show abnormally high or small activity, respectively. Detailed studies are based on the energy spectrum and the distribution of the timing information of single calorimeter cells.

### 6.3 CLUSTER SELECTION

In the following, it will be explained how a cluster in the **EMCal** calorimeter is defined and which selection cuts are applied before the cluster sample is further processed to reconstruct the neutral pion spectrum.

#### 6.3.1 Cluster Reconstruction

A deposition of energy in the **EMCal** leads to a signal from an elementary cell of the calorimeter. In general, several neighboring cells are also activated due to the lateral expansion of the electromagnetic shower within the calorimeter. Also, the longitudinal expansion of the electromagnetic shower can cross cell borders, because the calorimeter towers do not point to the interaction vertex except for mid-rapidity. Accordingly, most of the energy is usually found in one cell, but the measurement of the entire energy deposition requires the clusterization of all associated cells. The transverse energy/momentum can then be deduced from the angle between the line that connects the energy-weighted cluster centroid with the the primary vertex.

Two prescriptions are used in **ALICE** for clusterization. The **V1**-clusterizer starts out with a seed cell exceeding some energy threshold  $E_{\text{seed}}$ . Cells that share a border with the seed cell are added if the cell energy is above some aggregation threshold  $E_{\text{cell}}$ . The cluster grows until no more valid cells are found. The **V2**-clusterizer similarly starts with a seed cell. Aggregation of neighboring cells, however, continues only as long as the energy of the new cell remains below the energy of the respective reference cell. The different behavior of the two clusterizer algorithms with respect to the merged cluster analysis is illustrated in the following Fig. 6.7.

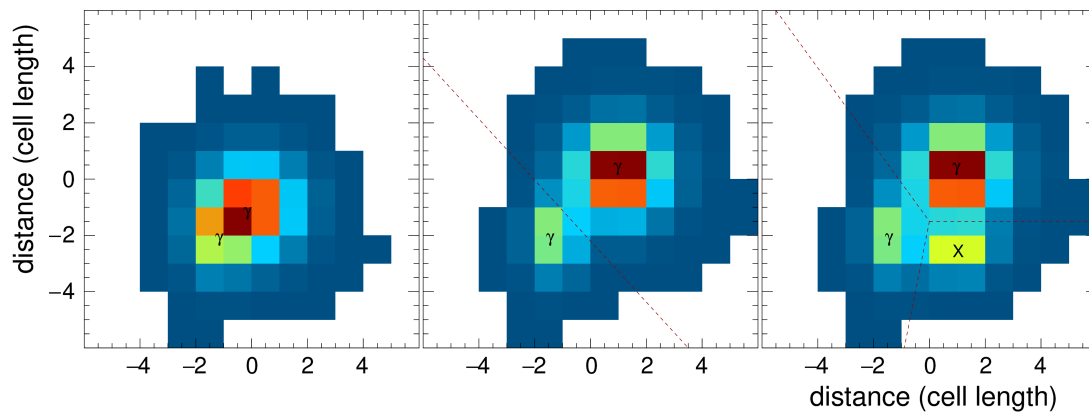


Figure 6.7: Illustrated energy deposition of decay photons from a neutral pion decay in the calorimeter for an unresolved case (left), a resolved case (center) and with an additional energy deposition (right). The dashed lines indicate the approximate splitting done by the **V2**-clusterizer.

Three cases are presented: An unresolved pair of photons (left), a resolved pair of photons (center) and the two resolved photons plus some extra energy deposition **X** (right). In the first case, the **V1**-clusterizer and the **V2**-clusterizer would arrive at the same definition of the cluster, because there is only one local maximum of energy. In the case of two resolved photons, however, the **V2**-clusterizer would define two separate clusters, which is indicated by the dashed line. The **V1**-clusterizer still

defines such a configuration as one single cluster with two local maxima due to the clusterization definition given above. Accordingly, both clusterizer algorithms will have a different response to an additional energy deposition in the vicinity of a true signal, which is illustrated in the right panel. The  $V_1$ -clusterizer simply includes the additional energy and the single cluster remains, whereas the  $V_2$ -clusterizer splits the cluster once more.

At this point, one should note that each of the clusterizers would be suitable for the analysis, if the simulation would accurately describe the abundance of additional particles and the shower shape. However, it has been pointed out in the course of a previous analysis [43] that the MC (from Jet-Jet events) disagrees significantly with the data with respect to the particle multiplicity in high-multiplicity events. As a consequence, the  $V_2$ -clusterizer has been chosen for the merged cluster analysis so that the influence of additional energy depositions in the vicinity of a signal is reduced. With the  $V_2$ -clusterizer, a resolved additional energy deposition can lead to a different amount of energy accumulated in the soft periphery of the cluster, but the additional energy itself would not be included.

### 6.3.2 General Cluster Selection

In the following, the general selection of clusters before the neutral pion analysis will be described.

#### CELL ENERGY AND CLUSTER TIME

In accordance with other **EMCal** analyses, the values of the seed energy is  $E_{\text{seed}} = 500 \text{ MeV}$  and  $E_{\text{cell}} = 100 \text{ MeV}$  for the minimum aggregation energy of the cells. The restriction on the minimum aggregation energy is not given by an intrinsic limit on energy resolution, but rather by considerations based on the proper timing information of cells. Generally, the timing information of a cell becomes more reliable for larger energy depositions. Conversely, it has been shown that values below  $E_{\text{cell}} = 100 \text{ MeV}$  allow that cells from a different bunch crossing can contribute to a cluster from a given bunch crossing. Unfortunately, there is no MC description available for the time information of **EMCal** cells. To account for this deficiency, the readout time window of the **EMCal** will not be constrained for the aggregation of cells (cell time), i. e.  $|t_{\text{cell}}| < 500 \text{ ns}$ . Instead, a variation of the cell time in data alone will account for a possible systematic uncertainty.

For the timing of clusters, however, a strict timing cut is required, in view of the bunch spacing of 50 ns employed by the **LHC** for the pp period in 2012. The cluster time  $t_{\text{cluster}}$  is defined by the cell time information of the most energetic cell. Clusters are only accepted for a certain cluster time,  $-30 \text{ ns} < t_{\text{cluster}} < 35 \text{ ns}$ . Note that the required precision on the cluster time is given in most cases for  $E_{\text{seed}} > 0.5 \text{ GeV}$  and even more so in the presented neutral pion analysis with cluster energies well above that value.

In the general selection, clusters are required to have an energy  $E_{\text{cluster}} > 0.7 \text{ GeV}$  and a minimum number of cells,  $N_{\text{cell}} \geq 2$ , because the isolated activation of single cells is associated with unphysical distortions in the **EMCal** read-out, such as neutrons hitting the photo diode that gathers the scintillation light.



## CLUSTER SHOWER SHAPE

The shower shape of the cluster in the  $\eta$ - $\phi$  plane can be characterized by the short and the long axis of an ellipse. The long axis of this ellipse  $\sigma_{\text{long}}^2$  is defined by the cell coordinates in azimuth and pseudorapidity, including a weighting for cell energy:

$$\sigma_{\text{long}}^2 = 0.5 \left( \sigma_{\phi\phi}^2 + \sigma_{\eta\eta}^2 + \sqrt{(\sigma_{\phi\phi}^2 - \sigma_{\eta\eta}^2)^2 + 4\sigma_{\phi\eta}^4} \right) \quad (6.5)$$

$$\sigma_{xy}^2 = \langle xy \rangle - \langle x \rangle \langle y \rangle \quad (6.6)$$

$$\langle x \rangle = \frac{1}{w_{\text{tot}}} \sum w_i x_i \quad (6.7)$$

$$w_i = \max(0, 4.5 + \log(E_i/E)) \quad (6.8)$$

$$w_{\text{tot}} = \sum w_i \quad (6.9)$$

Circular shower shapes of around  $\sigma_{\text{long}}^2 = 0.2$  are rather associated with single-shower clusters as opposed to elongated, merged clusters from several physical hits with  $\sigma_{\text{long}}^2 > 0.25$ . As mentioned earlier, the **EMCal** read-out can be distorted by nuclear reactions. These are single high-energy clusters, which can also be accompanied by low-energy cells activated by noise. Due to the usual energy imbalance between both cells, such a cluster has still very small values of  $\sigma_{\text{long}}^2$ . The general cluster selection therefore includes only clusters with a minimum elongation,  $\sigma_{\text{long}}^2 > 0.1$ . The selection of merged clusters based on the shower shape will be discussed later on.

## CLUSTER-TRACK MATCHING

Charged tracks measured in the central barrel can be associated with **EMCal** clusters in order to reduce the background from charged particles. The cluster-track matching takes place after the other cuts of the general cluster selection and is carried out as follows for every track:

The track is extrapolated in steps of 20 cm up to  $R = 430$  cm, right before the **EMCal** surface. Modification of the trajectory due to additional energy loss before the **EMCal** is accounted by a predefined Bethe-Bloch parametrization. Further propagation of the track takes place in smaller steps of  $\leq 5$  cm until the **EMCal** cluster is reached. Clusters can then be discarded for small distances  $\Delta\eta$  and  $\Delta\phi$  between cluster and track:

$$|\Delta\eta(p_T)| < a_\eta + (p_T + (\frac{1}{b_\eta - a_\eta})^{(1/n_\eta)})^{-n_\eta} \quad (6.10)$$

$$|\Delta\phi(p_T)| < a_\phi + (p_T + (\frac{1}{b_\phi - a_\phi})^{(1/n_\phi)})^{-n_\phi} \quad (6.11)$$

For large transverse momenta  $p_T \gtrsim 30$  GeV/ $c$ , these cuts converge against  $\Delta\eta = 0.01$  and  $\Delta\phi = 0.015$ , respectively.

In contrast to clusters, the timing information is not precise enough for all tracks to ensure that tracks from out-of-bunch pileup are not falsely considered for the cluster-track matching. Unfortunately, the **MC** does not model the out-of-bunch pileup, so only tracks will be used that are constrained by a hit in the **SPD**, which has the necessary timing precision. Although this restriction is not considered mandatory for pp collisions with the given collision scheme, it is introduced in view of the same analysis in p-Pb collisions, so that a nuclear modification factor can be reconstructed from both systems with a similar prescription. As a result of the restriction to **SPD**

constrained tracks, the probability to identify a cluster that stems from a charged particle, is decreased. This cluster-track matching efficiency  $\epsilon_{\text{TM}}$  for different cluster sources as determined from MC is depicted in the left panel of Fig. 6.8.

With a cluster-track matching efficiency of 50% and better, the procedure identifies electrons (green rectangles) and charged particles that have been created within a distance  $R = 5$  cm of the primary vertex (blue triangles). The efficiency is not as good for secondary charged particles. As a result of the cluster-track matching, the signal purity, that will be discussed later, is increased by about 10% percent points at cluster energies of about 20 GeV, but only by about 3% percent points at cluster energies of about 100 GeV.

At large transverse momenta, jets become more collimated and the probability increases that a track points close to a cluster from a neutral pion. Therefore, it has been investigated if a significant fraction of neutral pion clusters gets falsely rejected by the cluster-track matching (red circles in the left panel of Fig. 6.8). As expected, more neutral pion clusters are rejected for larger cluster energies. The reduction in neutral pion yield amounts to about 30% at 100 GeV, which is not insignificant, but also not a heavy tribute in view of the improved purity.

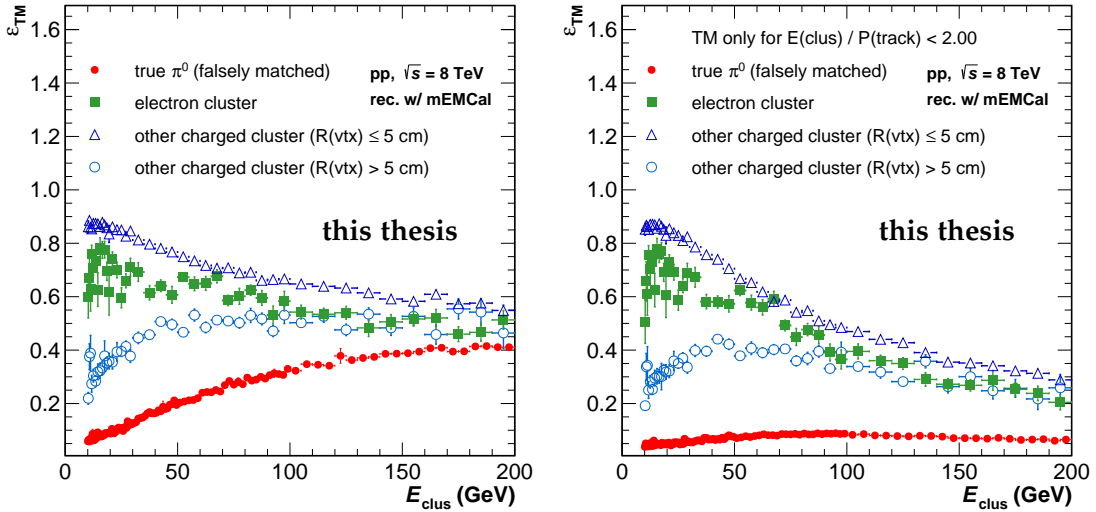


Figure 6.8: Cluster-track matching efficiency for clusters from neutral pions (red circles), from electrons (green rectangles), from other charged particles produced near the primary vertex (blue rectangle) and from other charged particles produced in a distance  $R > 5$  cm from the primary vertex.

It has been further investigated if the false matching of neutral pion clusters could be reduced. Most of the neutral pion clusters with an energy  $E_{\text{cluster}}$  are falsely matched due to tracks with a much lower momentum  $P_{\text{track}}$  so that the ratio  $E_{\text{cluster}}/P_{\text{track}}$  is large. On the other hand, charged particles deposit only a fraction of their energy so that  $E_{\text{cluster}}/P_{\text{track}}$  is small in case of real charged background clusters. Electrons deposit their entire energy in the calorimeter  $E_{\text{cluster}}/P_{\text{track}} \approx 1$ . Therefore, by imposing a requirement  $E_{\text{cluster}}/P_{\text{track}} < X$  with  $X > 1$  for the matching, the fraction of falsely matched neutral pions can be reduced without affecting the matching efficiency for the background. This is demonstrated for  $X = 2$  in the right panel of Fig. 6.8. The fraction of falsely matched neutral pions is significantly reduced, while the matching efficiency for the charged background is only reduced significantly for  $E > 50$  GeV.

Ultimately, it was decided not to employ the  $E/P$  requirement, because it would introduce another systematic uncertainty that is not justified by the gain in neutral pion yield. Moreover, a further dependence would have been introduced on the correct description of the **MC**. For the same reason, it has not been considered to choose smaller cut values that were defined in Eq. (6.11).

### 6.3.3 Cluster Energy Correction

In addition to the **EMCal** energy calibration described in Sec. 5.3.3, further methods of energy fine-tuning, that are applied at the stage of the analysis, have been developed. For this analysis, the so-called Conv-Calo Ratio Fit (**CCRF**) calibration has been used for the correction of the final result, which is going to be introduced next. Note that systematic uncertainties from the fine calibration will be provided by variation of the respective methods. The term *Conv-Calo* in **CCRF** refers to the neutral meson reconstruction via invariant mass from the combined information on the two-photon decay from photon conversion (**PCM**) and from calorimetry. The invariant mass  $M$  of a meson reconstructed from a photon measured via **PCM** and a photon measured as a calorimeter cluster is

$$M = \sqrt{2E_{\text{PCM}}E_{\text{Cluster}}(1 - \cos \theta)}, \quad (6.12)$$

where  $\theta$  is the angle between the reconstructed conversion photon and the photon measured in the calorimeter. Considering the superior energy resolution of a photon measured via conversion, the invariant mass can be related to the cluster energy. For the energy correction, the reconstructed mass position of the neutral pion for a given cluster energy is compared for data and for **MC**. In order to cancel the mismatch in data and **MC**, the ratio of both descriptions of the mass peak is used as a correction factor for **MC**. This ratio is parametrized as

$$f(E_{\text{cluster}}) = p_0 + \exp(p_1 + p_2 E_{\text{cluster}}). \quad (6.13)$$

The **CCRF** parametrization is shown in the left panel of Fig. 6.9, along with the same parametrization based on different **MC** samples. Also shown are the parameterizations from a similar method, Calo Ratio Fit (**CRF**), where two clusters of similar energy are used instead of a cluster and a conversion photon. In addition to the two mentioned methods **CCRF** and **CRF**, which use ratio fit of mass peaks, two further methods that use fits for the mass position directly are the Conv-Calo Mass Fit (**CCMF**) and the Calo Mass Fit (**CMF**).

The correction factor converges against 1.04 for the cluster energies above 10 GeV. Due to the steeply falling neutral pion spectrum, this small factor has a significant impact. Accordingly, the different cluster energy correction methods will be used for an estimate of the systematic uncertainty.

The mentioned methods have in common that the respective correction factor is only applied to **MC** in order to match the description from data, which was perfectly fine for other neutral pion measurements that involved cluster energies way below 100 GeV. Cluster energies of 100 GeV and more can be expected with the data sample from the EGA trigger. In this regime, the energy may not be entirely deposited in the **EMCal**, because the electromagnetic shower becomes too large in longitudinal direction, and the particle energy is not entirely contained in the **EMCal** (shower

leakage). At this point, one might find an objection with respect to the merged cluster analysis: A merged cluster with an energy content of 100 GeV may stem from two particles that each initiated a shower with an incident energy of 50 GeV, so that the energy is well contained in the calorimeter. However, this argument does not hold, because asymmetric two-body decays prevail in case of relativistic mother particles.

The effect of shower leakage can be accounted for by correction factors determined in test beam measurements. One example is given in the left panel of Fig. 6.9, where a correction on the MC level is applied (kPi0MCv3), which is not further discussed here, but also a correction on data from a test beam (kTestBeamv3).

A recent electron test beam campaign at the SPS, where electron beams have been directed at spare EMCAL modules with energies of up to  $E = 175$  GeV. The parametrization of reconstructed energy ( $E_{\text{rec}}$ ) over incident energy ( $E_{\text{in}}$ ) is shown in the right panel of Fig. 6.9 for the measurement (black line) and for a simulation (red line). For cluster energies above 100 GeV, the effect of the presumed shower leakage becomes apparent, lowering the reconstructed energy by about 10% around 150 GeV. As a result of the test beam measurement, a new energy correction (kPi0MCv4/kTestBeamv4) has been defined, which will be included in the evaluation of systematic uncertainties to account for a possible impact from the modified response at high energies.

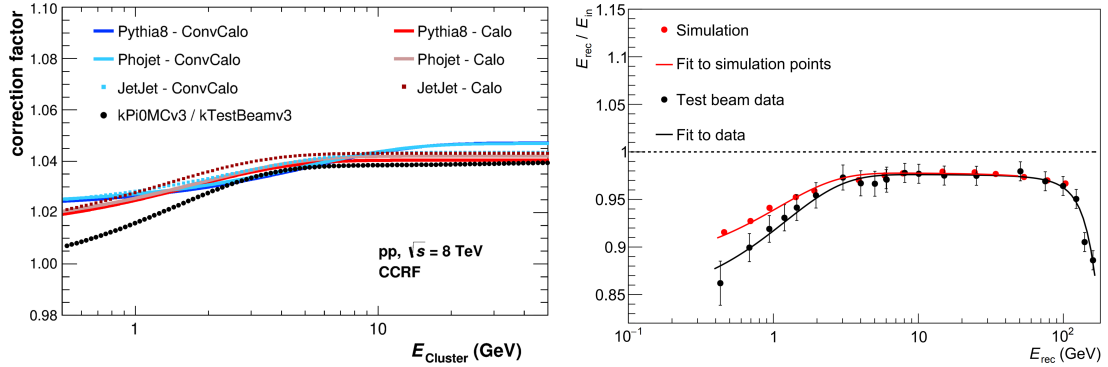


Figure 6.9: Cluster energy correction factor for three different MC productions and for two different methods CCRF (ConvCalo) and CRF (Calo) (left). The method CCRF based on the Jet-Jet MC is used for this work. Ratio of reconstructed energy  $E_{\text{rec}}$  over test beam energy  $E_{\text{in}}$  (right).

## 6.4 NEUTRAL PION ANALYSIS

The clusters that passed the general selection criteria presented in the last section are now analyzed for neutral pions. Clusters that stem from neutral pion decay and that are reconstructed with the V2-clusterizer start to merge at around 10 GeV, which is the minimum cluster energy on which the following steps are based. Maximum cluster energy is 200 GeV for now, although it is expected that the statistical uncertainties will suggest a much lower limit for the final result. Next, the signal definition will be discussed.

The analysis relies significantly on a correct MC description of the merged cluster properties. These properties can be vastly different in case the decay photons undergo conversion. In one case, the energy of the neutral pion can be entirely contained in a cluster, while in the other case, part of the energy may be carried away by an conversion electron that departed from the original photon's direction. The energy resolution, the relation of measured energy to the true neutral pion energy, is different in both cases.

Ideally, one would only select merged clusters with two photons due to the best resolution. However, there is no observable that allows a reliable distinction between these cases, so that a very broad signal definition is preferred with four different categories:

- Fully merged candidates:  
Both photons from the neutral pion are contained in the cluster or at least two of three particles from the Dalitz decay.
- Merged candidates with at least one conversion:  
At least one of the photons has converted and not both conversion electrons have to be contained in the cluster.
- Merged candidates from only one decay photon:  
Only one of the decay photons is contained in the cluster. In case of a conversion, both electrons have to be contained in the cluster.
- Merged candidates from only one electron:  
Only one electron (from conversion or Dalitz decay) is contained in the cluster.

The momentum resolution matrix of each cluster category is illustrated in Fig. 6.10. One can see that, for the first two cluster categories, a large fraction of events is reconstructed with a transverse momentum close to the true neutral pion momentum. The two other categories feature a resolution much worse, since only clusters with one photon or electron are considered.

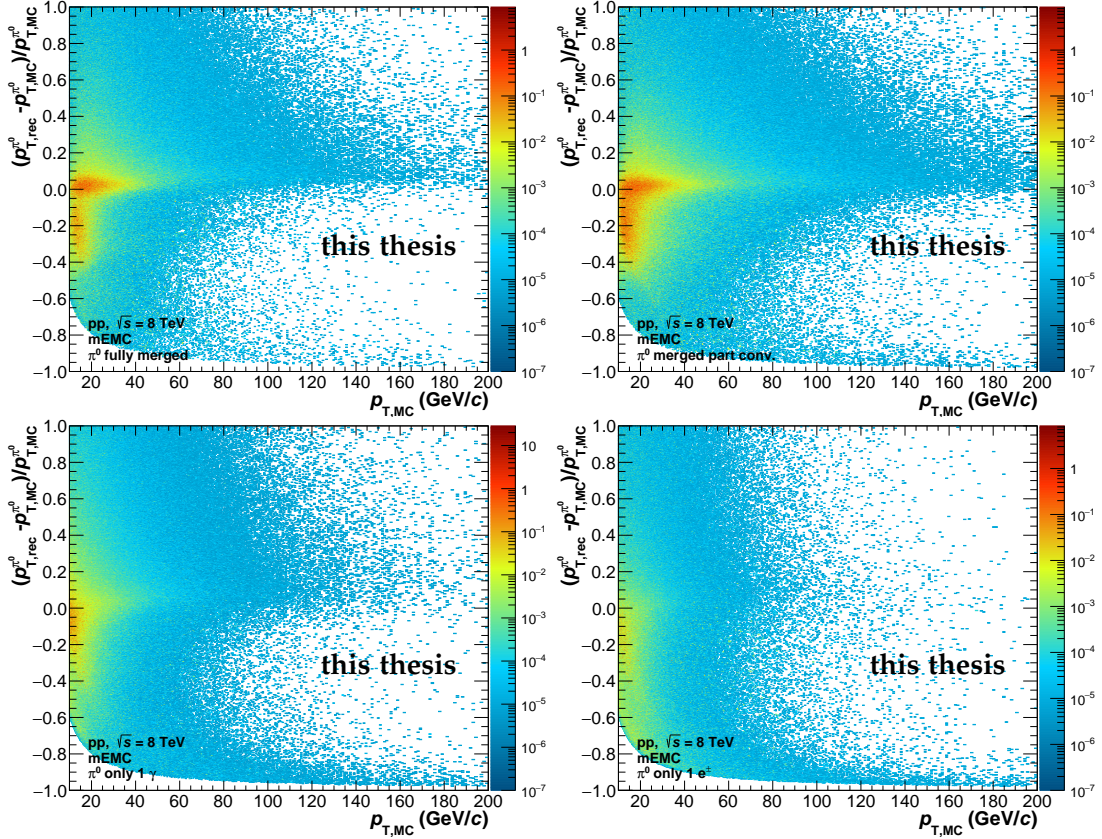


Figure 6.10: Resolution matrices of clusters that are fully merged (top left), with at least one photon converted (top right), with only one photon (bottom left) and with only one electron (bottom right). Shown is the relative transverse momentum shift from the true value of the neutral pion to the reconstructed value.

It follows from the significant difference between the four momentum resolution matrices that the actual proportion of each case — their respective share of signal — will have a great leverage on the corrected yield.

The momentum resolution as described by the MC is considered reliable, yet there is no accurate knowledge about the real fraction of each cluster category, since the amount of photon conversions in front of the [EMCal](#) is not well known. The resulting uncertainty will be estimated later by a toy model that involves variation of the cluster category fractions.

#### 6.4.1 Acceptance and Reconstruction Efficiency

The fiducial acceptance of the [EMCal](#) is  $|\eta| < 0.67$  and  $1.40 < \varphi < 3.15$ , respectively. The corrected yield, however, will be reported for full azimuth and in the rapidity interval  $|y| < 0.6$ , which is accounted for by an acceptance factor  $A$  derived from [MC](#):

$$A = \frac{N_{\pi^0, |y| < 0.6}^{\text{EMCal}}(p_{T, \text{gen}})}{N_{\pi^0, |y| < 0.6}(p_{T, \text{gen}})} \quad (6.14)$$

Here,  $N_{\pi^0, |y| < 0.6}(p_T)$  is the neutral pion yield in the given rapidity interval, unrestricted in azimuth.  $N_{\pi^0, |y| < 0.6}^{\text{EMCal}}(p_T)$  is the same quantity, but with the restriction that

at least one decay product of the neutral pion points to the [EMCal](#). As expected, the acceptance factor extracted from [MC](#) equals  $(3.15 - 1.40)/2\pi \approx 0.28$ , as depicted in the left panel of [Fig. 6.11](#). No transverse momentum dependence is seen; occasional fluctuations can be attributed to rare Jet-Jet events with a large weight.

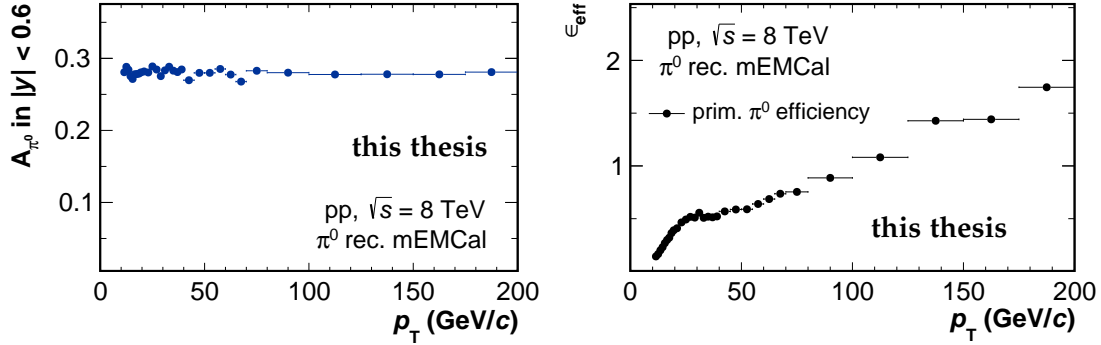


Figure 6.11: The acceptance factor against transverse momentum, derived from the comparison of all neutral pions and neutral pions, where one decay product points to the [EMCal](#) (left). Reconstruction efficiency of the neutral pion for different triggers against transverse momentum (right).

Also determined from [MC](#) is the reconstruction efficiency  $\epsilon$ , which is defined as the ratio of all reconstructed neutral pions that fit the signal definition,  $N_{\pi^0, \text{rec}}(p_{T, \text{rec}})$ , over all generated neutral pions  $N_{\pi^0, |y| < 0.6}^{\text{EMCal}}(p_T)$ :

$$\epsilon = \frac{N_{\pi^0, \text{rec}}(p_{T, \text{rec}})}{N_{\pi^0, |y| < 0.6}^{\text{EMCal}}(p_{T, \text{gen}})} \quad (6.15)$$

The reconstruction efficiency is depicted in the right panel of [Fig. 6.11](#). Note that the reconstruction efficiency also acts as an implicit correction for the momentum smearing that has been illustrated by the resolution matrices in [Fig. 6.10](#) so that the efficiency can exceed unity. An alternative approach would be an unfolding procedure via the resolution matrices, but this is not feasible for this analysis, because the large difference in transverse momentum bin sizes do not allow for a stable unfolding procedure. Since the reconstruction efficiency relies solely on the correct description by the [MC](#), the consequences of a possible mismatch between data and [MC](#) will be investigated for the evaluation of systematic uncertainties.

Owing to the broad signal definition, described in [Sec. 6.4](#), neutral pions can be reconstructed more than once. The percentage of double counted neutral pions resides at a low level of around 1%. Since the effect is not very pronounced, we rely on the [MC](#) to correct for this effect.

#### 6.4.2 Background Clusters, Shower Shape Cut and Signal Purity

The sample of selected clusters is contaminated by various background sources. This background include photons from other decays, direct photons and electrons, but also charged pions, kaons, protons and neutrons. It is expected that these background clusters can be separated to some degree from the merged clusters of neutral pions via a cut on the shower shape, by selecting rather elliptic clusters with a large  $\sigma_{\text{long}}^2$  as defined in [Eq. \(6.9\)](#). Likewise, this reduces the amount of neutral pion clusters

which stem from single photons or electrons and which are associated with a poor momentum resolution as discussed for the signal definition in Sec. 6.4. Since we rely on the description from MC, it was verified that the shower shape distribution from data is properly reproduced.

At first, the shower shape distribution is shown for neutral pions at low transverse momenta in the left panel of Fig. 6.12 and for high transverse momenta in the right panel. The distribution in both cases is subdivided for the different cluster categories of the signal definition. For this figure and the following, Fig. 6.13, the cluster-track matching has been omitted in order to study the original charged cluster abundance (after the remaining general cluster cuts).

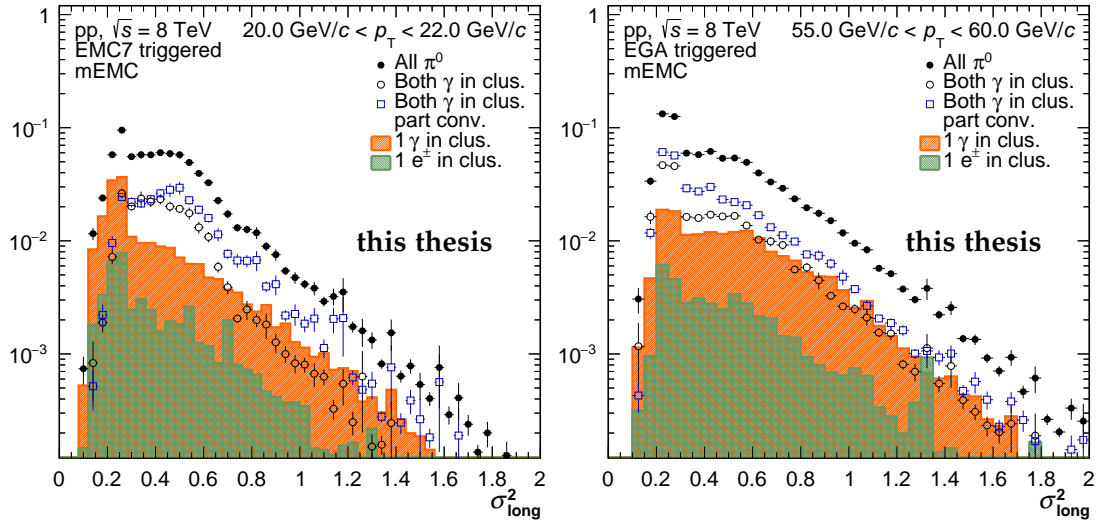


Figure 6.12: Cluster shower shape distribution  $\sigma_{\text{long}}^2$  of the neutral pion disentangled for different signal categories, shown for a low transverse momentum clusters (left) and for high transverse momentum clusters (right).

The distribution stretches to values  $\sigma_{\text{long}}^2 = 1$  and above, but most of the yield is found close to  $\sigma_{\text{long}}^2 = 0.25$ . The expected circular shape of clusters defined by only one photon or electron can be identified for the lower transverse momentum interval at a about  $\sigma_{\text{long}}^2 = 0.25$ , whereas for the high transverse momentum interval, the shape is spread out more evenly. The latter can be attributed to the broader lateral shower profile in the calorimeter.

Merged showers from two photons or conversions reveal their elongated shape for the lower transverse momentum interval. Here, a separation to the single-shower neutral pion clusters is given at  $\sigma_{\text{long}}^2 = 0.30\text{--}0.60$ . A cut on the shower shape could therefore reduce the fraction of the single-like neutral pion clusters that are associated with a poor momentum resolution. For the high transverse momentum interval, the elongated character of merged clusters diminishes so that the distribution is peaked around a low shower shape value  $\sigma_{\text{long}}^2 = 0.25$ .



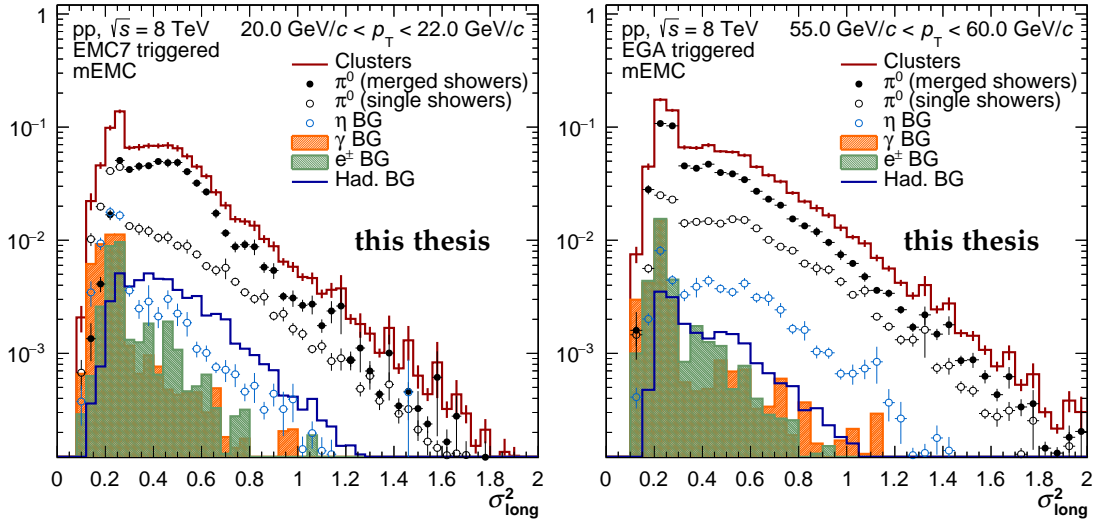


Figure 6.13: Same figure as before, but for all selected clusters and with a breakdown for background contributions.

In the same fashion as before, Fig. 6.13 shows the shower shape distribution of all clusters (after cluster selection) disentangled for the contribution of neutral pions and background sources. In the left panel it can be seen that direct photons and electrons give rise to rather circular clusters found at low values around  $\sigma_{\text{long}} = 0.2$ . A small contribution from the eta meson decay and the various hadronic sources is still found at larger values of  $\sigma_{\text{long}}^2$ .

The most significant change at larger transverse momenta, in the right panel, is the behavior of background cluster from the eta meson. The two-photon decay of the eta meson gives rise to merged clusters so that the eta meson contamination becomes significantly enhanced at large  $\sigma_{\text{long}}^2$ . Therefore, the eta meson contribution cannot be disentangled from the neutral pion contribution at large transverse momenta.

In order to suppress the single-shower background from photons, electrons and hadrons, a shower shape cut of  $\sigma_{\text{long}} = 0.27$  will be used for the analysis.

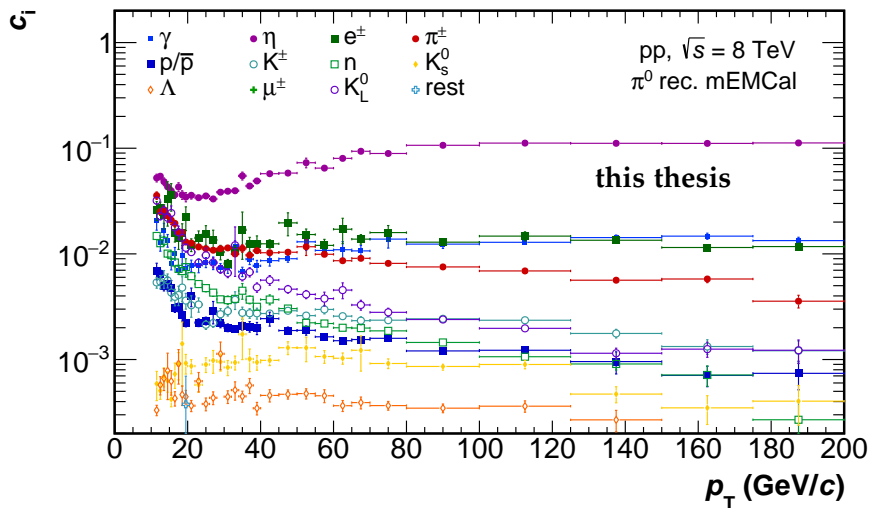


Figure 6.14: The relative contamination of the selected cluster sample from various background sources against transverse momentum. The contributions of muons and the sum of particles not accounted for (rest) is below  $4 \cdot 10^{-4}$ .

Fig. 6.14 shows the contributions of the various contamination sources as determined from MC against transverse momentum after all analysis cuts have been applied. The relative contamination from the eta meson dominates over the entire spectrum up to maximum values of about 11%, but is also suppressed by the shower shape cut at low transverse momenta,  $p_T < 50 \text{ GeV}/c$ . Further significant contamination stems from direct photons, electrons and charged pions, which contribute 1–3% each. At lowest transverse momenta,  $p_T < 20 \text{ GeV}/c$ , the relative contamination of almost all sources is visibly enhanced. This is the transition region with respect to the merging of neutral pion clusters. Here, only a fraction of neutral pions gives rise to merged clusters as defined by the V2-clusterizer.

### SIGNAL PURITY

Following the MC description of background sources, the yield of neutral pion candidates measured in data has to be decreased accordingly. The correction is carried out in terms of the signal purity  $P$ , defined as

$$P = \frac{\text{validated neutral pion candidates}}{\text{reconstructed neutral pion candidates}} = 1 - \sum_{i=1}^n c_i, \quad (6.16)$$

where  $c_i$  are the contaminations depicted in Fig. 6.14.

In order to improve the MC description based on PYTHIA 8, the contributions from eta mesons, direct photons and electrons are further modified.

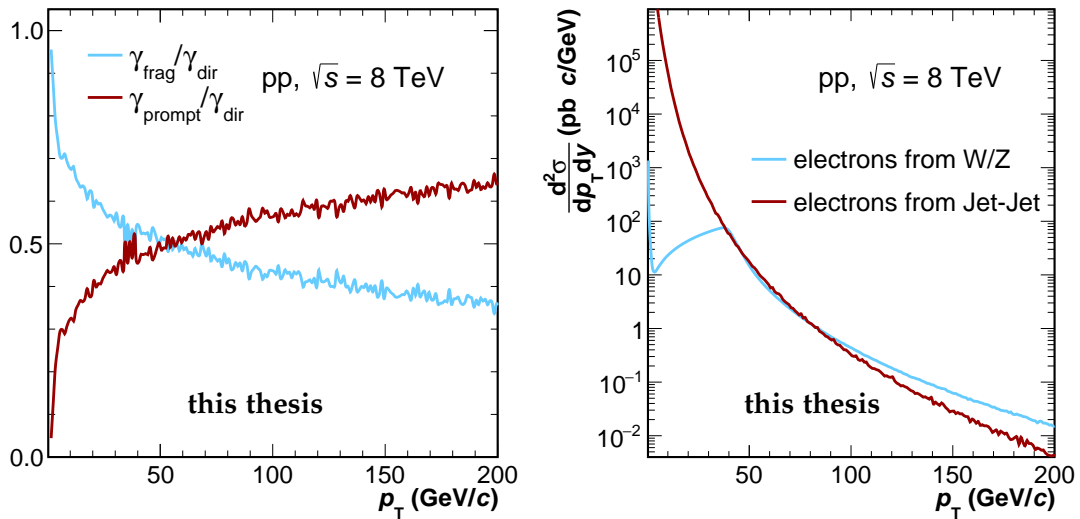


Figure 6.15: Contribution of prompt photons and fragmentation photons to the direct photons yield according to PYTHIA 8 (left). Electron cross section for electrons from weak-boson production in POWHEG+PYTHIA 8 and from Jet-Jet production in PYTHIA 8 (right).

The underlying Jet-Jet MC production only accounts for purely partonic  $2 \rightarrow 2$  processes, but no prompt production of photons such as  $qg \rightarrow q\gamma$  and  $q\bar{q} \rightarrow g\gamma$ . The left panel of Fig. 6.15 shows the proportions of fragmentation and prompt photons. The purity contamination by fragmentation photons from the Jet-Jet MC receives a correction  $\gamma_{\text{frag}} \rightarrow \gamma_{\text{frag}} + (\gamma_{\text{prompt}}/\gamma_{\text{frag}})_{\text{gen}} \times \gamma_{\text{frag}}$ . Here, the correction factor  $(\gamma_{\text{prompt}}/\gamma_{\text{frag}})_{\text{gen}}$  stems entirely from generator-level PYTHIA 8 simulations.

The purity is also corrected for electrons from weak boson decays, which are also not considered in the Jet-Jet MC. Electrons from Jet-Jet processes in PYTHIA 8 as well as electrons from weak boson production in POWHEG+PYTHIA 8 are displayed in Fig. 6.15 showing that electrons from weak bosons become an abundant contribution at  $p_T > 30 \text{ GeV}/c$ . The additional contribution has been estimated at NLO accuracy using the single weak boson production processes of POWHEG-Box/W and POWHEG-Box/Z [112] interfaced with the parton shower of PYTHIA 8. The resulting correction is  $e_{JJ} \rightarrow e_{JJ} + (e_{\text{WeakBoson}}/e_{JJ})_{\text{gen}} \times e_{JJ}$ .

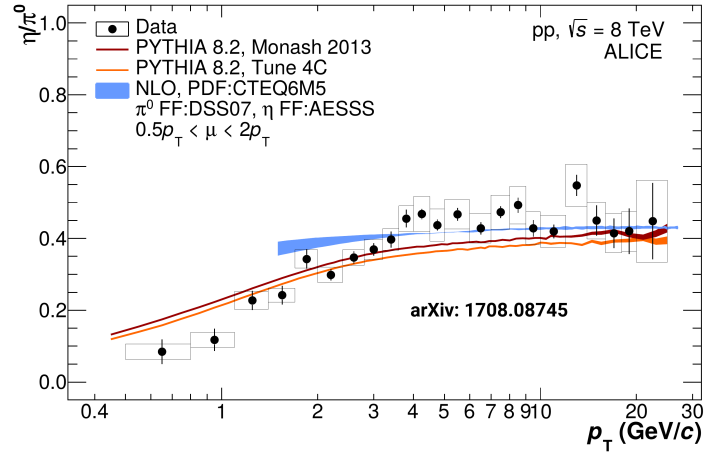


Figure 6.16: Measurement of the  $\eta/\pi^0$  ratio compared to NLO predictions and PYTHIA 8 [42].

In order to improve the description of the eta meson yield, the  $\eta/\pi^0$ -ratio from MC has been compared to results from an analysis of the same data set [42] (Fig. 6.16). The ratio approaches a constant  $c$  beyond  $p_T = 5 \text{ GeV}/c$ , with  $c_{\text{MC}} = 0.407$  for PYTHIA 8 and  $c_{\text{Data}} = 0.465$  for the result of the measurement. The contribution of the eta meson contamination is increased accordingly with a factor  $c_{\text{Data}}/c_{\text{MC}}$ .

The corrected purity  $P$  is shown in Fig. 6.17 in blue circles. The uncorrected purity, which was based on the Jet-Jet MC alone, is shown in open red circles. In addition, triangles depict the purity that would result from each of the three corrections alone. Notably, each of the three corrections leads to a significant decrease of the purity. Following the discussion of the shower shape cut, best purity is achieved in the regime of intermediate transverse momentum, around  $p_T = 30 \text{ GeV}/c$ , where most of the neutral pions form merged clusters that are significantly elongated, while the eta meson contribution is well suppressed by the shower shape cut.

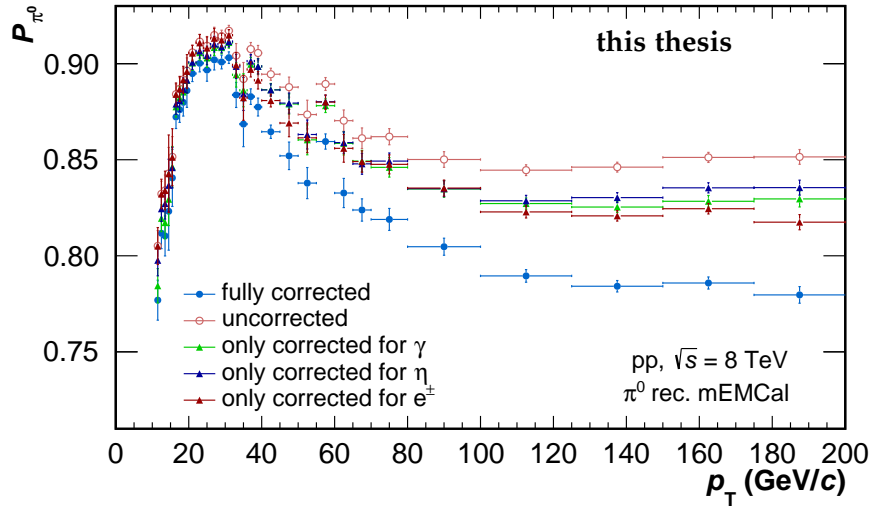


Figure 6.17: Signal purity against transverse momentum for the uncorrected case, as extracted from the MC events, and for the corrected case. The effect of each of the three corrections alone is also given.

### 6.4.3 Correction for Secondary Neutral Pions

For the final result, secondary neutral pions from the decay of long-lived particles and also neutral pions from material interaction in front of the **EMCal** will be subtracted. The material interaction has to be determined solely by the detector simulation, while the neutral pions *feed-down* from long-lived particles can be constrained by external knowledge. The dominant source for neutral pion feed-down is the process  $K_S^0 \rightarrow \pi^0\pi^0$  (BR 30.7%). The next-largest contributions are  $K_L^0 \rightarrow 3\pi^0$  (BR 19.5%),  $K_L^0 \rightarrow 3\pi$  (BR 12.5%) and  $\Lambda \rightarrow n\pi^0$  (BR 35.8%).

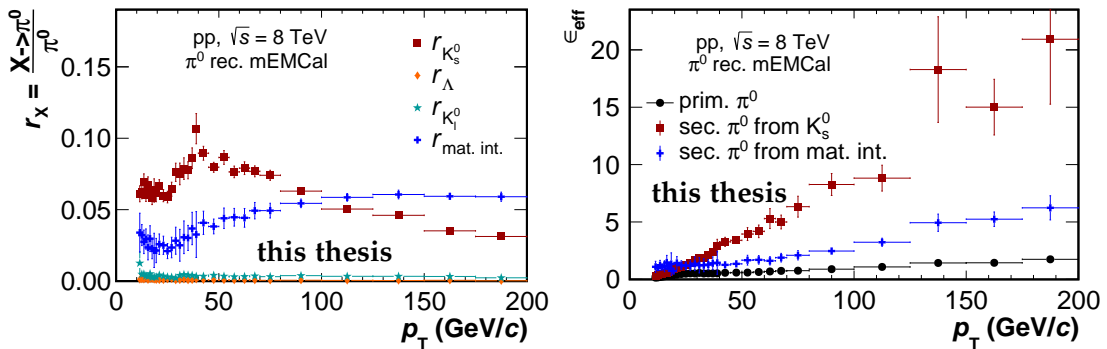


Figure 6.18: Secondary neutral pion fraction (left) from the decay of  $K_S^0$ ,  $\Lambda$  and  $K_L^0$  as well secondary neutral pions from material interaction (left). Reconstruction efficiency of secondary neutral pions from  $K_S^0$  and from material interaction with a comparison to the primary neutral pion efficiency.

To improve the description of secondary neutral pions, the **ALICE** cocktail framework is used. For this framework, up-to-date information on identified particle yield is gathered for various collisions energies and different systems. The measured yields of kaons etc. is used as an input for a particle decay algorithm so that yields of secondary neutral pions are created on the generator level. Next, the yields are scaled for the cross section of the **MB** trigger and multiplied with the respective trigger rejec-

tion factor. They are further multiplied with the secondary neutral pion acceptance and the secondary neutral pion reconstruction efficiency, which has been derived for each mother hadron type from the detector simulation. As a result, secondary neutral pion yields constrained by measurements are available at the raw-yield level and accordingly, are subtracted from the raw yield of clusters selected for the analysis.

The relative abundance of secondary neutral pions from  $K_S^0$ ,  $K_L^0$ ,  $\Lambda$  and from material interaction, as provided by the detector simulation, is given in the left panel of Fig. 6.18. The only significant secondary neutral pion contribution stems from the  $K_S^0$  (3–10%) and from material interaction (2–6%). The acceptance for both sources is very close to the acceptance of true neutral pions, but the reconstruction efficiency for both sources reaches considerable magnitudes as depicted in the right panel of Fig. 6.18 comparing the reconstruction efficiency of primary neutral pions (black points) and secondary neutral pions from material interaction (blue points) and  $K_S^0$  (red points). The reconstruction efficiency accounts for the momentum resolution, which is especially bad for  $K_S^0$ , since the point of decay can be far away from the primary vertex for the given energies, e. g.  $\gamma c\tau \approx 3$  m for a  $K_S^0$  with an energy of 60 GeV. The large leverage from the feed-down contribution from  $K_S^0$  will be accounted for in the evaluation of systematic uncertainties.

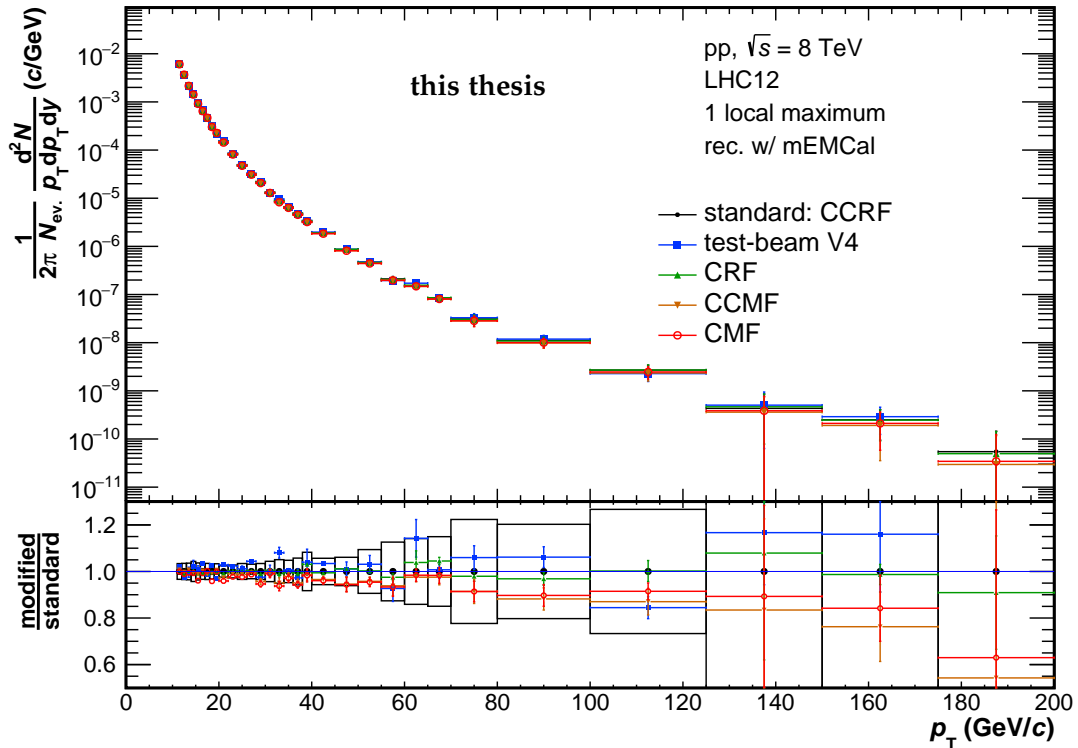


Figure 6.19: The change in corrected neutral pion yield by variation of the cluster energy correction method, here illustrated for the EGA trigger. Statistical uncertainties are given for the invariant yield in the upper panel and for the lower panel.

Next, follows the evaluation of systematic uncertainties for the corrected neutral pion yield and the presentation of the final result. Due to the statistical limitations of the event sample of the EGA trigger, the neutral pion analysis has been restricted to a transverse momentum of  $100 \text{ GeV}/c$ . Similar, a limit of  $p_T = 40 \text{ GeV}/c$  is imposed on the corrected neutral pion yield from the EMC7 trigger data sample.

## 6.5 SYSTEMATIC UNCERTAINTIES

Several cuts have been applied and assumptions have been made for the selection of clusters and for the extraction of the pion yield. In the following, they will be discussed as sources of systematic uncertainties. The cuts have been varied one cut at a time. The mean is taken from the maximum deviation of the resulting neutral pion yields in positive and negative direction from the central value (for each transverse momentum bin) and assigned as symmetric systematic uncertainty for the respective cut. Statistical fluctuations have been smoothed out by fits to the mean values.

### CLUSTER ENERGY CORRECTION

As discussed in Sec. 6.3.3, the default way to correct the cluster energy is the CCRF method. Three similar methods (CRF, CMF, CCMF) have been used to estimate a dependence of the cluster energy correction on the corrected yield. To further assess a possible distortion due to shower leakage, the correction factor from the test beam data (test beam V4) has also been included in the variation.

In order to illustrate the general variation procedure, the change in corrected neutral pion yield from the variation of cluster correction methods is given in Fig. 6.19

for the case of the EGA trigger. Up to a transverse momentum of  $100 \text{ GeV}/c$ , the correct yield changes by up to 10% due, which makes the cluster energy correction the second-largest source of systematic uncertainty at large transverse momentum. The variation shows visible statistical fluctuations, which are dealt with a fitting procedure as mentioned above. As for all variations, several fluctuations below  $40 \text{ GeV}/c$  can be attributed to events with large weights of the MC simulation. Other than that, the statistical uncertainties are dominated by the data sample.

No strong deviation is found for the cluster energy correction that is derived from test beam data (blue lines). Given the respective uncertainties, it is a strong indication that no shower leakage effect is present in the transverse momentum range of about  $80 \text{ GeV}/c$  and a weaker indication for the same conclusion at larger transverse momenta.

#### CLUSTER SHOWER SHAPE CUT

A cut on the shower shape has been used in order to suppress single-shower clusters. It is not guaranteed that the distribution is correctly modeled. Accordingly, the shower shape cut  $\sigma_{\text{long}}^{\text{min}} = 0.27$  has been varied with  $\sigma_{\text{long}} = 0.25\text{--}0.30$ . The resulting systematic uncertainty ranges from 2% at lowest transverse momentum,  $p_T = 10 \text{ GeV}/c$ , to 8% above  $80 \text{ GeV}/c$ , where the shower shape cut is the third-largest source of uncertainty.

#### SECONDARY CORRECTION

The feed-down of secondary pions from the  $K_S^0$  has a considerable influence of the corrected yield of primary neutral pions, as discussed in the last section. The secondary yield as described by MC has been replaced by a description that has been constrained to measurements. The inferior momentum resolution of the secondary neutral pions acts as a large leverage sensitive to this changed yield. In order to account for this issue, the underlying neutral kaon yield has been varied by 5%. The resulting uncertainty becomes the largest uncertainty with 14% in the upper transverse momentum limit.

#### CLUSTER-TRACK MATCHING

The cluster-track matching parameters  $a$ ,  $b$  and  $n$  from Eq. (6.11) have been varied, effectively varying the acceptance window for a cluster rejection. The resulting uncertainty from cluster-track matching reaches a maximum of 4% at large transverse momentum. The uncertainty is significantly reduced in comparison with a similar analysis at  $\sqrt{s} = 2.76 \text{ TeV}$ , which can be attributed to a more developed tracking procedure in ALICE and to the requirement that only SPD constrained tracks are used for the matching in this work.

#### CELL TIME

As discussed in Sec. 6.3.1, the clusterization of cells uses an open timing restriction of  $t_{\text{cell}} = \pm 500 \text{ ns}$  with respect to the leading cell. The same cut cannot be applied on MC level, because the timing information is not reproduced in MC, but a possible influence of this cut is assessed by varying it in data to smaller values  $t_{\text{cell}} = \pm 200 \text{ ns}$  and  $t_{\text{cell}} = \pm 100 \text{ ns}$ . The shower shape and the total energy deposition associated

with a cluster depend on low energy cells at the border of the cell. Low energy cells, in turn, are associated with a inferior timing information. As a result, the variation of the time, in which cells are considered for the clusterization process, has an influence of the corrected neutral pion yield. The resulting mean deviation increases to a value 7% at large transverse momentum, which is still a moderate value in comparison with other systematic uncertainties.

#### MINIMUM CELL AGGREGATION ENERGY

A similar reasoning as for the cell time variation applies to the variation of the minimum cell aggregation energy  $E_{\text{cell}} = 100 \text{ MeV}$ . To assess any influence from the minimum aggregation energy, the standard value has been varied to  $E_{\text{cell}} = 75 \text{ MeV}$  and  $E_{\text{cell}} = 125 \text{ MeV}$ . The resulting change in corrected neutral pion yield is almost negligible with about 2% for the entire kinematic range.

#### TRANSVERSE MOMENTUM RESOLUTION

In order to estimate the uncertainty from the mixing of different reconstruction qualities for the  $\pi^0$ , as discussed in the beginning of Sec. 6.4, a toy model was used that simulates the resulting raw yield for the four matrices of momentum resolution and recombines them according to a certain composition of the four cluster categories Fig. 6.20. The raw yields of the different components compared to the combined spectrum can be found in the top left, while the ratio to the original input is shown in the top right. Three different compositions of the cluster ensemble were tested:

1. The fraction of fully merged cluster is kept. Contributions from the partially converted clusters are decreased by 20% and contributions from the single photons are increased by 20%.
2. The fraction of single particle contributions is kept. The fraction of fully merged clusters is increased by 20% and the contribution from the partially converted clusters is decreased by 20%.
3. Again, the fraction of single particle contributions is kept. But the fraction of fully merged clusters is now decreased by 20% and the contribution from the partially converted clusters is increased by 20%.

The results of this variations with respect to the original one are shown in the bottom left of the figure. This in conjunction with the ratio of the smeared to the input leads to an uncertainty of 2% at highest transverse momenta, 6% at intermediate  $p_T = 50 \text{ GeV}/c$  and a maximum of 9% at lowest  $p_T = 10 \text{ GeV}/c$  (bottom right). This trend is due to the worse momentum resolution of the neutral pion reconstruction at low transverse momentum.



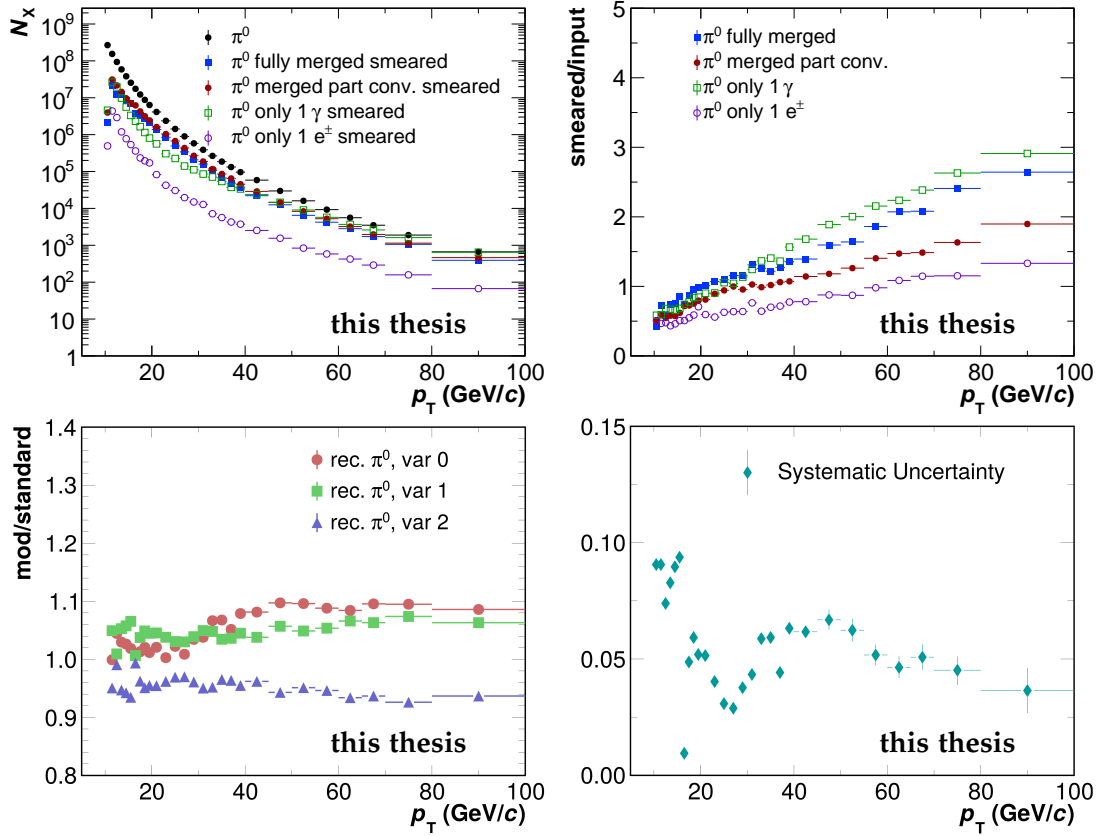


Figure 6.20: Toy model results to estimate the influence of different components in the signal definition and their respective resolutions. Top left: Smeared raw yield from different components weighted with their respective fraction and the summed raw yield in black. Top right: Smeared spectra compared to the original. Bottom left: Reconstructed spectra from the three fraction variations of the different components compared to the once obtained from the full MC. Bottom right: Resulting uncertainty given by momentum resolution associated with each cluster category combined with the yield modification through the fraction variation.

### MATERIAL BUDGET

It is not ensured the material budget is well described by the MC, especially between the TPC and EMCal. The mismatch between reality and simulation has been assessed in the EMCal di-cluster analysis [42], where the neutral pion spectrum has been compared for cases with and without TRD modules in front of the calorimeter modules. A significant material budget is also given by the TOF, which has also been investigated before. The estimated systematic uncertainty is roughly 3% in each case, so that the combined systematic error from material budget is 4.2%, which is a moderate contribution that becomes significant for intermediate values of the transverse momentum, around  $p_T = 50 \text{ GeV}/c$ .

### TRIGGER NORMALIZATION

Since the same event sample has already been analyzed in the invariant mass analysis, the respective uncertainty on the trigger normalization was carried over to this work. They have been determined by varying the transverse momentum fit range of

the trigger rejection factor. The uncertainty is 2% from the rejection factor calculated from  $\text{INT7} \rightarrow \text{EMC7}$  and 2.2% in case of  $\text{EMC7} \rightarrow \text{EGA}$ . By summation in quadrature, the trigger normalization uncertainty for the EGA is about 3%. Concerning a possible impact from out-of-bunch pileup, the rejection of out-of-bunch pileup by the SPD cuts in the scope of the event selection (Sec. 6.2.1) had been varied and was found to give a negligible contribution.

#### TOTAL SYSTEMATIC UNCERTAINTY

The total systematic uncertainty of the neutral pion yield for both trigger sets EMC7 and EGA with all contributions contributions is given in Fig. 6.21 and Fig. 6.22, respectively. The total systematic uncertainty in the transverse momentum range of 10–40 GeV/c is almost constant at a value of about 12%. At low transverse momentum, the momentum resolution of the neutral pion reconstruction dominates. At large transverse momenta, the diminishing contribution of the momentum resolution is balanced by the various sources that show a rise with transverse momentum, as indicated in the discussion above. Concerning the EGA trigger, the systematic uncertainties are found to be very similar, as expected. The trigger normalization uncertainty is larger for the EGA set, but this has not a significant impact. Most striking is the rise of the systematic uncertainties towards the upper limit of the kinematic range, where a value of about 18% is reached for the bin of largest transverse momentum. The enhancement is mainly driven by the uncertainty for the  $K_S^0$  feed-down, and to a moderate degree also by the uncertainties from the cluster energy correction, the shower shape cut and the cell time.

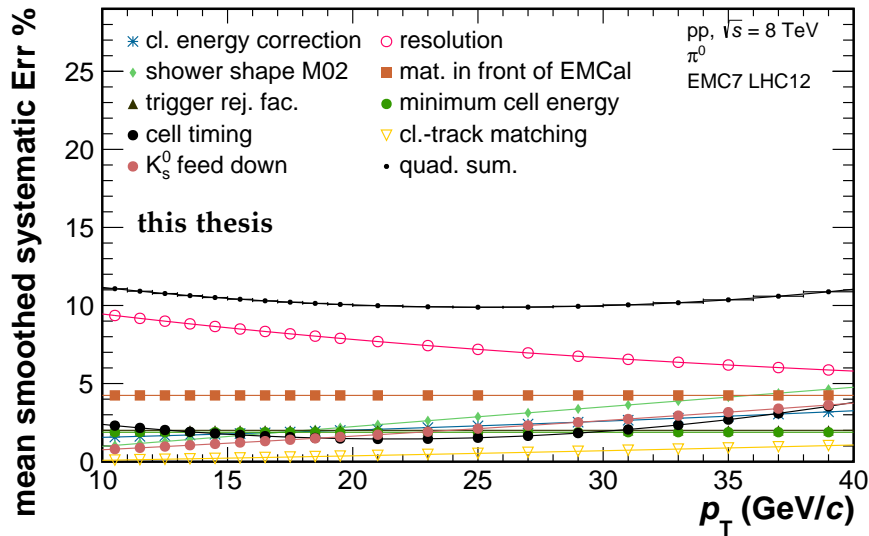


Figure 6.21: Total systematic uncertainty (small black dots) for the EMC7 trigger as computed from the quadratic sum of the various contributions of uncertainty, which are shown in different styles and colors.

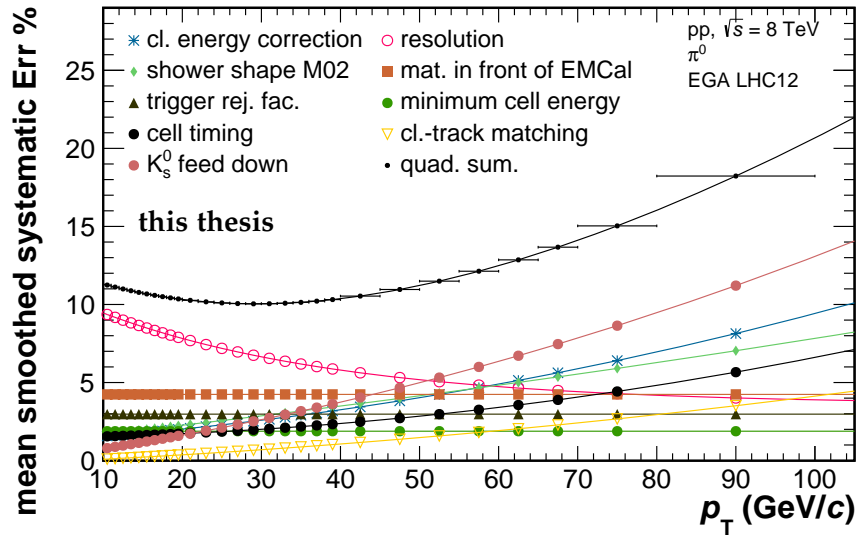


Figure 6.22: Same figure as before, but for the EGA trigger.

## 6.6 RESULTS

The differential invariant neutral pion yield at mid-rapidity of each event trigger is given by

$$\frac{d^3N}{2\pi p_T dp_T dy} = \frac{1}{2\pi p_T} \frac{N_{\text{raw}}}{\Delta y \Delta p_T} \frac{1}{N_{\text{ev}}} \frac{P}{\epsilon A} \quad (6.17)$$

The yield with respect to the **MB** cross section is given through an additional division by the respective trigger rejection factor  $R$ . The invariant cross section is then given by multiplication with the **MC** cross section  $\sigma_{\text{MB-AND}} = 55.8 \text{ mb}$ :

$$E \frac{d^3\sigma}{dp^3} = \frac{1}{2\pi p_T} \frac{N_{\text{raw}}}{\Delta y \Delta p_T} \frac{\sigma_{\text{MB-AND}}}{N_{\text{ev}}} \frac{P}{\epsilon A} \frac{1}{R} \quad (6.18)$$

The result for the invariant yield for each scaled trigger is presented in Fig. 6.23. A final spectrum was constructed from the combination of both data sets, which allows for a significant reduction of statistical uncertainties in the overlap region of  $p_T = 10\text{--}40 \text{ GeV}/c$ . The combination takes into account correlations of systematic uncertainties, based on [113]. However, the systematic uncertainties are reduced only slightly by the combination, since all systematic uncertainties are correlated between the EGA and the EMC7 trigger except for the trigger efficiency that is derived from the INT7 trigger. A smooth description of the combined spectrum is illustrated by dashed lines provided by a Two-Component Model (**TCM**) fit [114] that fits both the exponential shape at low transverse momentum and the power law tail at high transverse momentum.

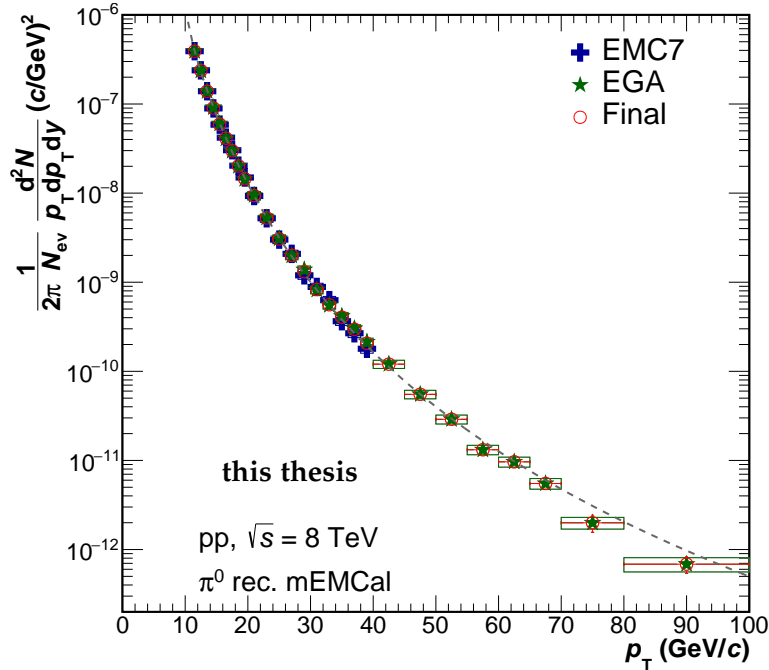


Figure 6.23: Differential invariant neutral pion yields in pp collisions at  $\sqrt{s} = 8 \text{ TeV}$  measured with the two trigger sets, EMC7 (blue) and EGA (green). Also shown are the combined yield (open circles) and the **TCM** fit (dashed lines). Statistical uncertainties are shown as lines, systematic uncertainties as boxes.

The ratio of both trigger contribution to the **TCM** fit is given in Fig. 6.24. Below  $p_T = 25 \text{ GeV}/c$ , the uncertainty is dominated by the systematic component and the

data points of both trigger sets are close to each other since they share the same systematic uncertainties. At intermediate transverse momentum up to  $p_T = 40 \text{ GeV}/c$ , the statistical uncertainties become comparable to the systematic uncertainties for the EMC7 trigger. Here, the combination of trigger sets effectively reduces the statistical uncertainty of the combined result. For transverse momenta larger than  $p_T = 40 \text{ GeV}/c$ , the EGA data points are compatible within  $1\sigma$  with the suggested spectrum from the TCM fit except for three bins. The last two bins may indicate a systematic trend that is caused by an insufficient description of the secondary pion feed-down from the  $K_S^0$ .

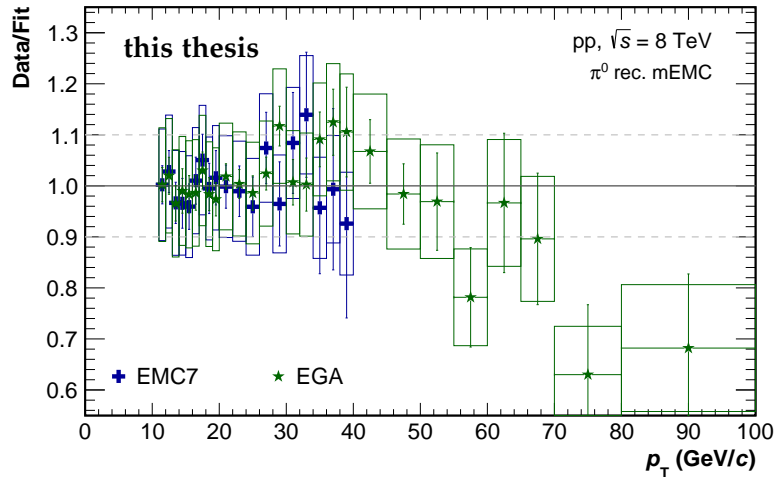


Figure 6.24: Ratio of the measured neutral pion spectra to the TCM fit. Shown are the results from the two trigger sets EMC7 (blue) and EGA (green). Statistical uncertainties are shown as lines, systematic uncertainties as boxes.

The differential invariant cross section of the neutral pion is given in Fig. 6.25 along with previous measurements in the same data set [42]. The entire spectrum covers a cross section of over twelve order of magnitude, from the PCM measurements that start at  $p_T = 300 \text{ MeV}/c$  up to the merged cluster analysis, which extends the limit by more than a factor two to a limit of  $p_T = 100 \text{ GeV}/c$ .

The five measurements are compared to a common TCM fit in Fig. 6.26. The result from the merged cluster analysis (stars) agrees well within the systematic uncertainties in the overlap region of the other measurements. Notably, the central values of the merged cluster analysis coincide right with the data points of the di-cluster analysis that was carried out for the EMCAL (diamonds), which indicates a common source of systematic uncertainty given by the calorimeter. Again, a significant deviation from the TCM fit description is given for the two last transverse momentum bins. As a conclusion, the merged cluster analysis presented in this work enhances the kinematic range of the neutral pion spectrum consistently to a limit of about  $p_T = 70 \text{ GeV}$ .

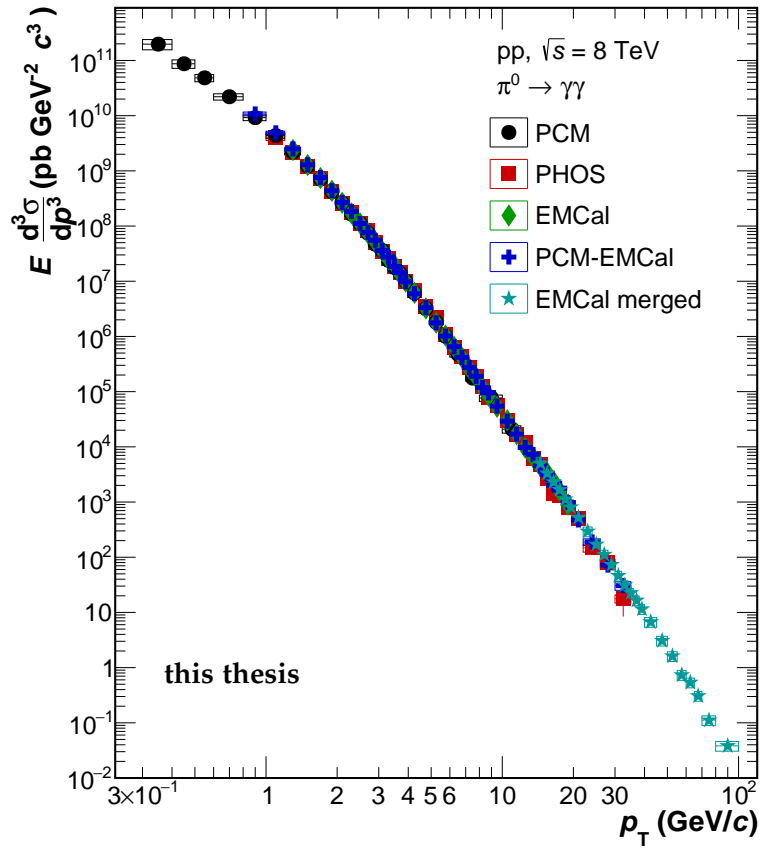


Figure 6.25: The collected measurements of the neutral pion invariant cross in pp collisions at  $\sqrt{s} = 8$  TeV with the invariant mass analyses from [42] and the merged cluster analysis from this work.

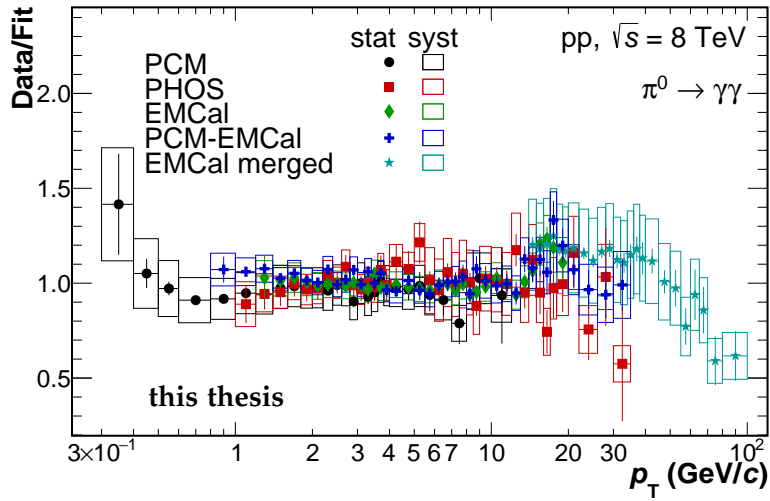


Figure 6.26: The collection of neutral pion measurements in pp collisions at  $\sqrt{s} = 8$  TeV compared to a common TCM fit. Statistical uncertainties are shown as lines, systematic uncertainties as boxes.

## DIRECT PHOTON PREDICTIONS FOR THE LHC

---

In the following chapter, direct photon results with the **NLO+PS** approach of POWHEG+PYTHIA 8 will be presented. These results comprise comparisons to **LHC** measurements of the last years, but also predictions for ongoing analyses. To further assess the phenomenological value of the POWHEG+PYTHIA 8 approach for direct photons, comparisons will be made to the results of PYTHIA 8 (**LO+PS**) and to the results of JETPHOX (**NLO**). Two frameworks have been developed to facilitate the usage of PYTHIA 8, POWHEG and JETPHOX, which is documented in the Appendix.

A description of isolated photon spectra at large transverse momenta,  $p_T^\gamma > 125 \text{ GeV}$ , will be given and compared to results from **ATLAS**. Photon-jet correlations will be investigated at intermediate energies  $p_T^{\gamma,\text{jet}} \approx 40 \text{ GeV}$ , as measured by **CMS**. Possible constraints of nuclear parton densities with photon-jet pairs will be investigated via the observable  $x_{\text{pb}}^{\text{obs}}$ , which is an approximation for the Bjorken  $x$ . Last, theoretical descriptions are given for the low  $p_T$  direct photon signal in pp collisions, which is an important baseline for the measurement of additional direct photon signals in heavy-ion collisions. The results presented in the following have also been published in [115], if not labeled otherwise.

### 7.1 ISOLATED PHOTON PRODUCTION IN PP COLLISIONS WITH ATLAS

Inclusive isolated photon production has been measured up to very large transverse energies and in various intervals of rapidity by the **ATLAS** collaboration. With the start of **LHC** Run II in 2015, **ATLAS** was able to take data at 13 TeV, close to the **LHC** design energy, with an integrated luminosity of  $3.2 \text{ fb}^{-1}$  that allowed for an isolated photon spectrum beyond the TeV scale [85]. These generous kinematic constraints of the **ATLAS** measurement allow for a wide-ranging test of the theoretical description of very hard photon production, with parton momentum fractions probed from  $x = 0.02$  up to  $x \approx 1$ .

The minimum transverse momentum of the measurement is  $E_T^\gamma = 125 \text{ GeV}$ . At this scale already most of the direct photons are produced well separated from hadron jets. However, an isolation cut is still necessary to separate these photons from the photon background from hadronic decays. The isolation cut provides a suppression of photons with an additional energy deposition of at least  $E_T^{\text{iso}}$  within a certain distance  $\Delta R = \sqrt{(\Delta\eta)^2 + (\Delta\phi)^2}$  from the photon. The definition of the isolation cut employed by **ATLAS** reads as follows:

$$E_T^{\text{iso}} < 4.8 + 4.2 \cdot 10^{-3} \cdot E_T^\gamma [\text{GeV}] \quad (7.1)$$

$$\Delta R = 0.4, \text{ excluding } \Delta\eta \times \Delta\phi = 0.125 \times 0.175 \text{ around the photon} \quad (7.2)$$

One of the latest **PDF**, NNPDF31\_NLO\_AS\_0118 [14], has been chosen as the initial state description in case of POWHEG+PYTHIA 8 and JETPHOX, while for PYTHIA 8, the **PDF** NNPDF23\_LO\_AS\_0130\_QED was chosen [116], because it is the default **PDF** of the PYTHIA 8 Monash 2013 tune [76]. For JETPHOX, the BFG II photon fragmentation function [117] has been used.

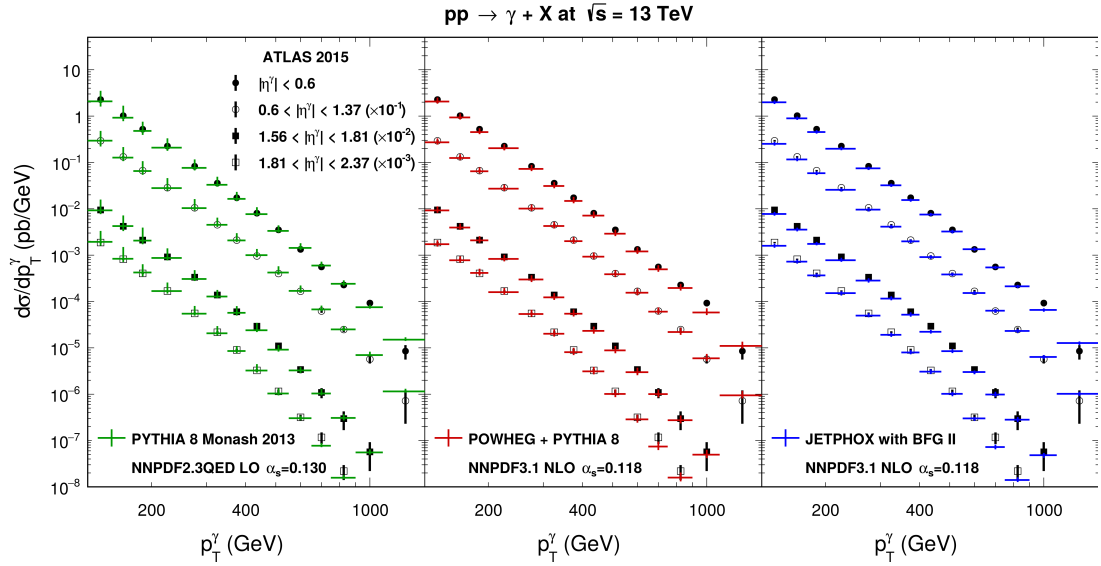


Figure 7.1: Transverse momentum spectra of isolated photons in pp collisions at  $\sqrt{s} = 13$  TeV in four rapidity bins. Data points from ATLAS [85] are compared to predictions at LO (PYTHIA 8, left), NLO (JETPHOX, right) and NLO+PS (POWHEG+PYTHIA 8, centre)

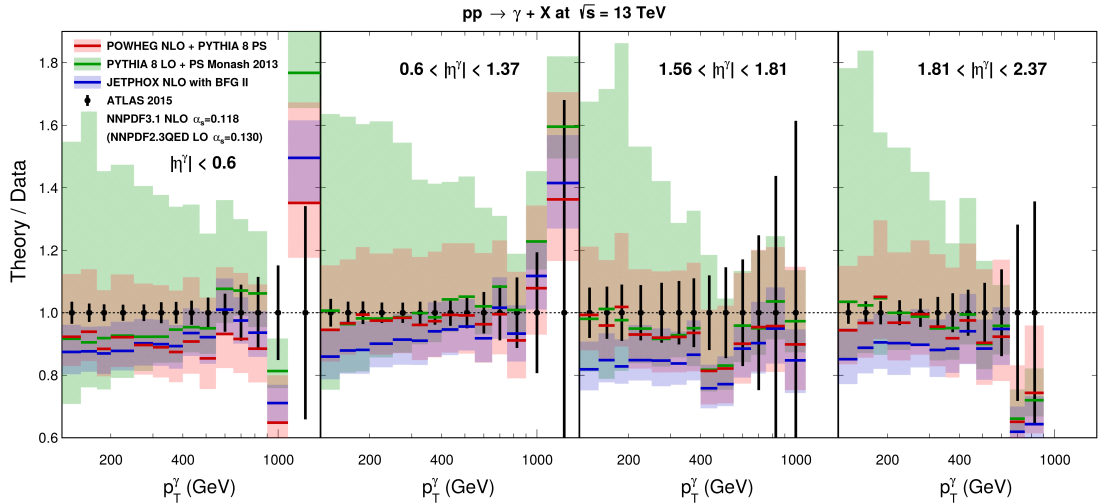


Figure 7.2: Theory predictions normalized to data in the four rapidity bins. Data points are shown with total experimental uncertainties (without luminosity uncertainty), theory uncertainties are from scale variation.

The measured isolated photon cross section is presented in Fig. 7.1 for four intervals of pseudorapidity together with a comparison to the three theoretical descriptions from PYTHIA 8, POWHEG+PYTHIA 8 and JETPHOX. For a better comparison, Fig. 7.2 shows the ratios of measured and predicted values.

Errors bars on the data points (black) depict the combined statistical and systematic uncertainty of the measurement, excluding the normalization uncertainty from the luminosity measurement which amounts to 2%. For the evaluation of theoretical uncertainties, shown as colored bands, definitions of renormalization scale  $\mu_R$  and factorization scale  $\mu_f$  have been varied independently by factors of 2, i.e.  $0.5E_T^\gamma < \mu_R, \mu_f < 2E_T^\gamma$ , but not such that  $4\mu_R = \mu$  or  $\mu_R = 4\mu_f$ .



The first striking observation is the large scale uncertainty from PYTHIA 8 due to the LO prescription as opposed to the NLO prescription of POWHEG and PYTHIA 8. On the other hand, the central values of PYTHIA 8 can easily compete due to a proper tuning of the strong coupling in the Monash 2013 tune of PYTHIA 8 ( $\alpha_s(M_Z) = 0.130$ ). All three theory description tend to underestimate the isolated photon cross section. The discrepancy is most striking for mid-rapidity, where theory does not agree within the data uncertainty except for largest transverse momenta. Nevertheless, for the three remaining rapidity intervals, the parton shower representatives PYTHIA 8 and POWHEG are able to describe the data. JETPHOX, on the other hand, underestimates the results by additional 10% compared to POWHEG.

It has been shown in [118] that a Next-to-Next-to Leading Order (NNLO) prescription and the additional resummation of electroweak contributions leads to a better agreement of the cross section for inclusive isolated photons at large momenta,  $p_T^\gamma > 100$  GeV. This is line with the conjecture that POWHEG+PYTHIA 8 is able to resum parts of these corrections through the parton shower, and provide thus a better normalization than JETPHOX.

## 7.2 PHOTON-JET CORRELATIONS IN PP AND P-PB COLLISIONS WITH CMS

Photon-jet correlations have been measured by the [CMS](#) collaboration in pp and Pb-Pb collisions at  $\sqrt{s} = 2.76$  TeV and in p-Pb collisions at  $\sqrt{s_{NN}} = 5.02$  TeV [119]. The comparison of jets in pp and p-Pb collisions shows how cold nuclear effects in the initial state may have an influence on the correlation between jet and photon. Moreover, possible final-state modifications of jets in p-Pb collisions can be revealed, because the associated photon receives no final-state modification. This measurement is therefore necessary for an unambiguous interpretation of strong final-state effects in Pb-Pb collisions.

In the following, theoretical comparisons for photon-jet observables are given by events from PYTHIA 6.422 (tune Z2) embedded in minimum-bias events of HIJING 1.383 to improve the underlying event description in case of p-Pb collisions (also from [119]). Predictions at the NLO level are given by POWHEG+PYTHIA 8 and, if applicable, by JETPHOX (this work).

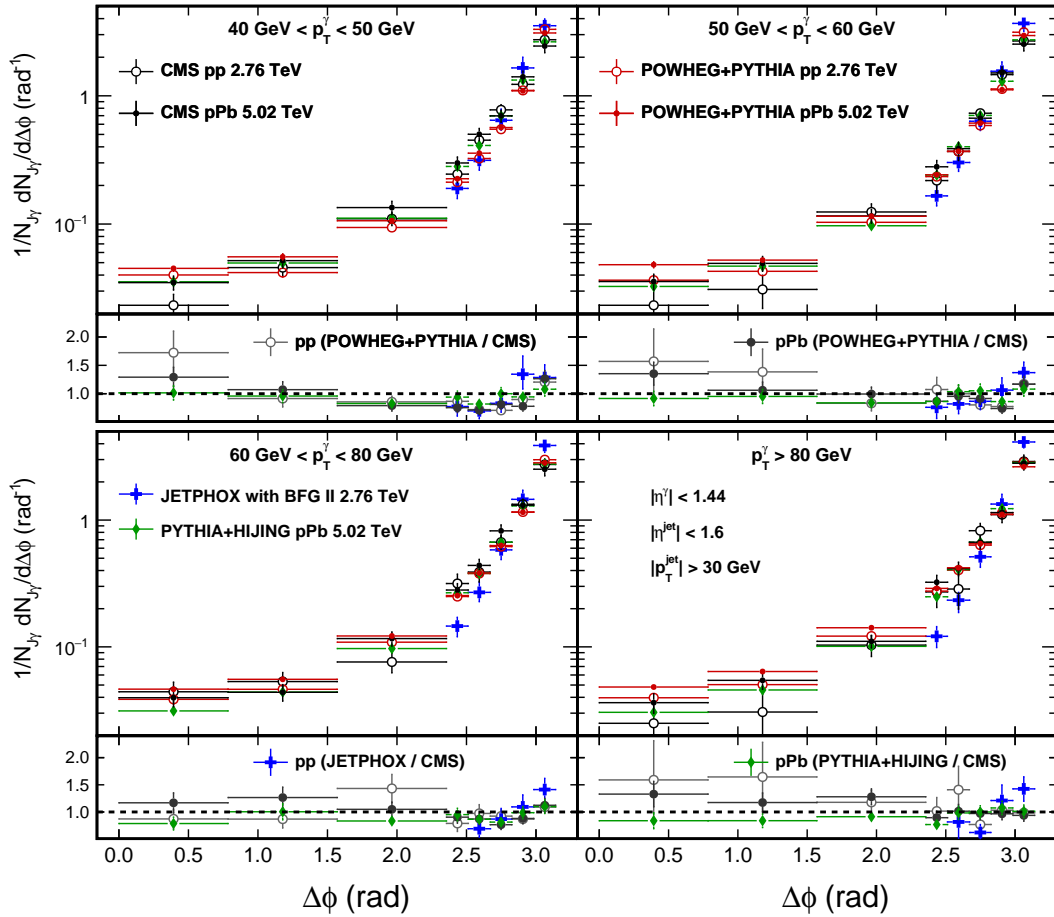


Figure 7.3: Distribution of the azimuthal angle between photons and jets in pp (open circles) and p-Pb (full circles) at  $\sqrt{s} = 2.76$  TeV and  $\sqrt{s_{NN}} = 5.02$  TeV, respectively. Four intervals of transverse momentum are presented, each figure with a lower panel that shows the theory predictions normalized to the respective data from [CMS](#).

The analysis relies on an isolation criterion with an allowed total energy of  $E^{\text{iso}} = 5$  GeV within a distance  $\Delta R = 0.4$  of the photon candidate. In order to remove electrons that could mimic a photon signal, [CMS](#) rejects photon candidates

which are close to tracks from charged particles, within  $|\eta^\gamma - \eta^{\text{track}}| < 0.02$  and  $|\eta^\gamma - \eta^{\text{track}}| < 0.15$ . The track matching is accounted for in events generated from POWHEG+PYTHIA 8, but not in JETPHOX events because of the missing description of final-state particles besides photon and jet. A transverse momentum of  $p_T^\gamma > 40$  GeV is required for the photon within an acceptance of  $|\eta^\gamma| < 1.44$ . Associated jets are defined by the anti- $k_T$  algorithm [73], with a distance parameter  $R = 0.3$ , requiring  $p_T^{\text{jet}} > 30$  GeV and  $|\eta^{\text{jet}}| < 1.6$ . If multiple jets of the same event fulfill these criteria, multiple photon-jet pairs can be constructed from one photon.

Fig. 7.3 shows the distribution of relative azimuthal angle ( $\Delta\phi_{J\gamma}$ ) between the photon and the jet axis, normalized on the number of photon-jet pairs, for four different intervals of photon transverse momentum. A ratio is provided in each case, comparing theory description and measurement for the respective energy.

Data points of pp collisions are compared with POWHEG+PYTHIA 8 and JETPHOX. There is fair to good agreement with POWHEG+PYTHIA 8 considering the experimental uncertainties. Striking is a systematic deviation in the comparison to JETPHOX. In contrast to POWHEG+PYTHIA 8, JETPHOX lacks a description of additional radiation beyond two jets, which is necessary here for a precise description of the photon-jet alignment. Likewise, JETPHOX fails to describe multi-particle configurations that populate the region below  $\Delta\phi_{J\gamma} = 2\pi/3$ . These are rare events where a hard fragmentation photon actually survives the isolation cut as well as events with a distinct multijet structure, which can be described with sufficient accuracy by the PS.

Data points of p-Pb collisions are compared also with POWHEG+PYTHIA 8, using the nuclear PDF nCTEQ15np, and with PYTHIA 6+HIJING which includes an explicit description of the enhanced underlying event in p-Pb collisions. Again, POWHEG+PYTHIA 8 describes the data in most bins within experimental uncertainties. Agreement is worst for the lowest  $p_T^\gamma$  and best for largest  $p_T^\gamma$ . A slightly better description is given by PYTHIA 6+HIJING, which indicates that a proper underlying background description is mandatory for accurate results in p-Pb collisions.

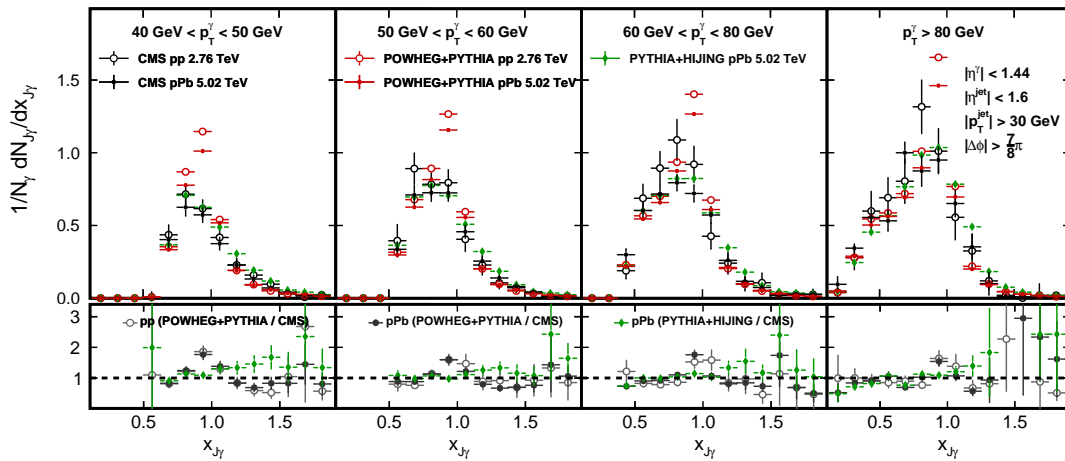


Figure 7.4: Transverse momentum ratio of jets over photons in pp collisions (open circles) and p-Pb collisions (full circles) at  $\sqrt{s} = 2.76$  TeV and  $\sqrt{s_{\text{NN}}} = 5.02$  TeV, respectively. Four intervals of transverse momentum are given, each figure with a lower panel that shows the theory predictions normalized to the respective data from CMS.

Fig. 7.4 shows the transverse momentum ratio of jets over photons,  $x_{J\gamma} = p_T^{\text{jet}} / p_T^\gamma$ . Again, a photon can be associated with more than one jet, which however is almost

never the case due to a restriction  $\Delta\phi_{J\gamma} > 7\pi/8$ . Despite the restriction on back-to-back configurations, the values are still smeared broadly around  $x_{J\gamma} = 1$ , also to larger relative jet momenta ( $x_{J\gamma} > 1$ ). Jet fragmentation becomes softer for larger photon transverse momenta, which is described by all theoretical descriptions. However, a distinct peak at  $x_{J\gamma} = 1$  is visible for POWHEG+PYTHIA 8, since the result has not been smeared for detector resolution. Comparing the data in pp and p–Pb collisions alone, there is no significant modification which could point to strong modifications from the initial state or in the jet final state.

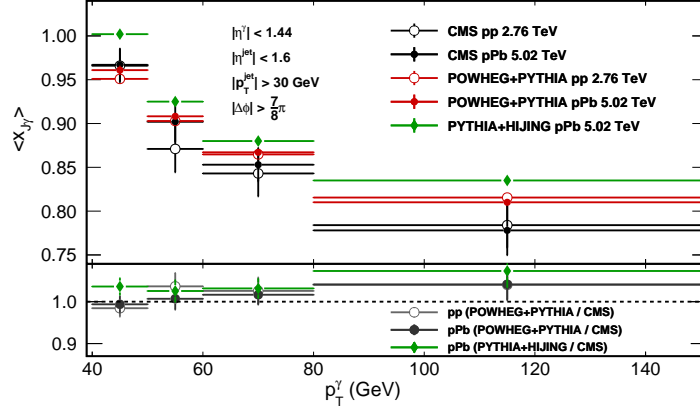


Figure 7.5: The average jet-over-photon momentum ratio as a function of photon transverse momentum in pp collisions (open circles) and p–Pb collisions (full circles) at  $\sqrt{s} = 2.76$  TeV and  $\sqrt{s_{NN}} = 5.02$  TeV, respectively. The lower panel shows the ratio of theory over data.

A similar observation is made for the averaged value of  $x_{J\gamma}$  presented in Fig. 7.5, where no significant modification is found between pp and p–Pb collisions. Concerning the theoretical description, the data is slightly in favor of the NLO+PS prescription by POWHEG+PYTHIA 8. Note that the missing detector resolution effect is expected to have a smaller influence on the averaged value.

Last, the fraction of photons which are actually associated to a jet,  $R_{J\gamma}$  is investigated in Fig. 7.6. Due to the cuts on the jet and due to the back-to-back constraint  $\Delta\phi_{J\gamma} > 7\pi/8$ , this fraction assumes values as low as 0.3 for the bin of lowest transverse momentum.

While the preceding observables allowed to draw the conclusion that no strong nuclear final-state modification of jets are present in p–Pb collisions, the fraction  $R_{J\gamma}$  reveals the influence of initial-state effects. From Eq. (2.24), one obtains from the photon momentum a probed  $x$  region of roughly 0.016–0.05 so that nuclear shadowing is expected, in particular gluon shadowing. The values for the p–Pb data lie consistently below those of the pp data, which can be attributed to the gluon shadowing. Less gluons in the initial state lead also to less quark jets, which have a harder fragmentation and so that they pass the jet energy cut more easily. In accordance with the nuclear shadowing hypothesis, the POWHEG+PYTHIA 8 results obtained from the nuclear PDF lie below those from the proton PDF, although they consistently overestimate the measured data points of  $R_{J\gamma}$ .

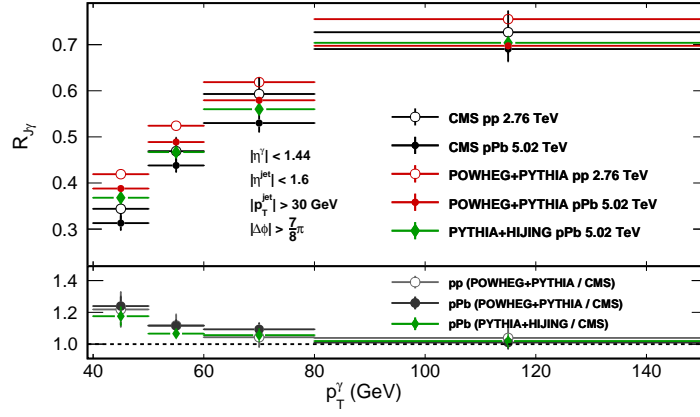


Figure 7.6: Fraction of photons associated to a jet for the given kinematic cuts as a function of photon transverse momentum in pp collisions (open circles) and p–Pb collisions (full circles) at  $\sqrt{s} = 2.76$  TeV and  $\sqrt{s_{NN}} = 5.02$  TeV, respectively. The lower panel shows the ratio of theory over data.

In summary, no observation could be made in favor of a final-state modification of jets in p–Pb collisions. An expected difference due to nuclear shadowing was presumably found through the reduction of quark jets. Most significant from the phenomenology perspective, photon-jet correlations could be described for the first time at [NLO](#) through the POWHEG+PYTHIA 8 prescription.

7.3 BASELINE FOR THE DIRECT PHOTON SIGNAL  $R_\gamma$ 

In order to assess hot medium effects, the direct photon excess ( $R_\gamma - 1$ ) has to be compared with a baseline pQCD photon spectrum, either simulated or measured in pp collisions, as described in Sec 2.4. Fig. 7.7 shows a simulated  $R_\gamma$  for pp collisions at  $\sqrt{s} = 13$  TeV as well as  $\sqrt{s} = 2.76$  TeV, in order to illustrate the extent of direct photon excess within the current LHC energy range. The ratio has been simulated as  $1 + \gamma_{\text{dir}}/\gamma_{\text{decay}}$ , where  $\gamma_{\text{dir}}$  is provided by PYTHIA 8, JETPHOX and POWHEG+PYTHIA 8 with uncertainties from scale variation. In each case, the description of the decay photon background  $\gamma_{\text{decay}}$  is given by PYTHIA 8.

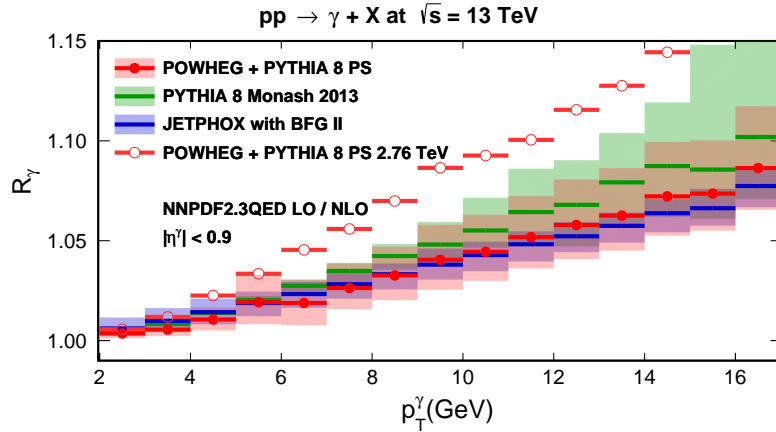


Figure 7.7: Ratio of inclusive over decay photon production in pp collisions at  $\sqrt{s} = 13$  TeV. LO predictions with PYTHIA 8 (green) are compared with those at NLO with JETPHOX (blue) and NLO+PS with POWHEG+PYTHIA 8 (red, full circles). The latter are also shown at  $\sqrt{s} = 2.76$  TeV (red, open circles).

Similar to the isolated photon production in Sec. 7.1 at large photon energies, the scale uncertainty of the NLO description by POWHEG+PYTHIA 8 and JETPHOX is much smaller compared to the LO description from PYTHIA 8. On the other hand, the scale uncertainty from PYTHIA 8 becomes very small for low transverse momenta,  $p_T^\gamma \lesssim 5$  GeV. This, however, can be attributed to the regularization of the underlying dijet cross section discussed in Sec. 3.6.

The direct photon yield at low transverse momenta is described by the fragmentation function (BFG II) in JETPHOX, but by the hard emission generated in POWHEG. Still, both descriptions agree with each other as far as this can be seen from the depicted  $R_\gamma$ . The PYTHIA 8 description is in agreement with the NLO description at lowest photon energies. However, in the region above  $p_T^\gamma = 5$  GeV, where the impact of the cross section regularization begins to vanish, a consistent deviation is established. The deviation of PYTHIA 8 will be discussed separately in the next section.

From the POWHEG+PYTHIA 8 description for a collision energy of  $\sqrt{s} = 2.76$  TeV, it can be seen that the direct photon excess becomes less pronounced with increasing CM energy: The underlying cross section for hard parton scattering becomes flatter so that photons from hadron decay, though reduced in energy by fragmentation and decay, are more abundant for a given transverse momentum bin.

In view of upcoming direct photon measurements in Pb–Pb collisions at  $\sqrt{s_{\text{NN}}} = 5.02$  TeV, it can be noted that the suppression of the hadronic background at  $\sqrt{s_{\text{NN}}} = 5.02$  TeV was found to be same at  $\sqrt{s_{\text{NN}}} = 2.76$  TeV [120]. On the other

hand, the thermal photon signal itself is expected to become slightly more significant compared to the pQCD photon yield [121].

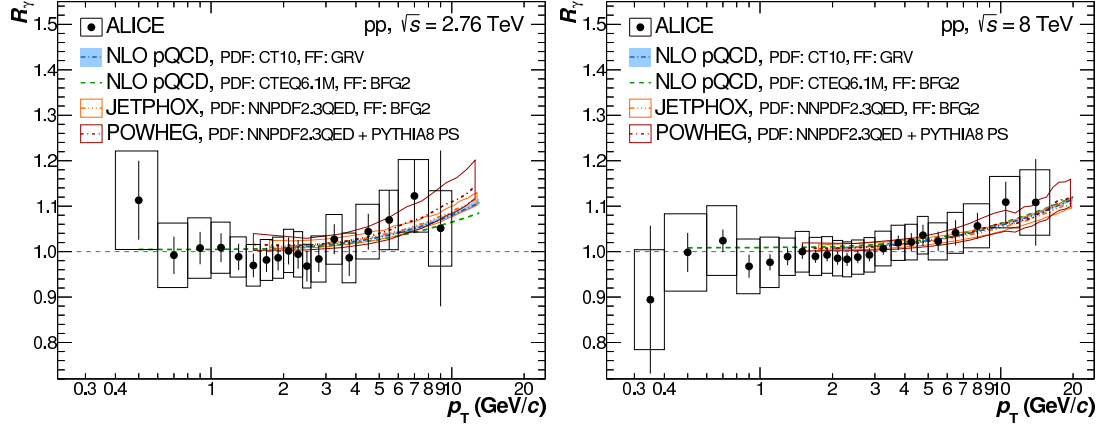


Figure 7.8: Measurement of the direct photon excess ratio in pp collisions at  $\sqrt{s} = 2.76$  TeV and  $\sqrt{s} = 8$  TeV with different theory descriptions at NLO [122].

In the course of this thesis, further predictions have been made to supply a recent publication of ALICE: Fig. 7.8 shows the measured baseline of direct photons at  $\sqrt{s} = 2.76$  TeV and  $\sqrt{s} = 8$  TeV, recently published by ALICE [122]. The theory descriptions from JETPHOX and POWHEG+PYTHIA 8 (this work) and from another NLO calculation are compatible with the measurement within the given uncertainties. From comparison with the experimental uncertainty one can conclude that pQCD calculations provide a meaningful contribution on the baseline determination for the direct photon signal in large systems. Concerning future prospects, similar measurements of direct photons are expected for pp collisions at  $\sqrt{s} = 5.02$  TeV and  $\sqrt{s} = 13$  TeV, for p–Pb collisions at  $\sqrt{s_{NN}} = 5.02$  TeV and  $\sqrt{s_{NN}} = 8.16$  TeV, and for Pb–Pb collisions at  $\sqrt{s_{NN}} = 5.02$  TeV.

### 7.3.1 Discussion of the Infrared Cutoff from the QED Parton Shower

In Fig. 7.7, it was seen that the direct photon cross section at around  $p_T^\gamma = 10$  GeV is overestimated by PYTHIA 8 in comparison with JETPHOX and POWHEG+PYTHIA 8. In PYTHIA 8, direct photons at low energies stem from photons generated as FSR in the PS. Accordingly, the direct photon yield depends on the underlying dijet cross section. This cross section, however, is expected to be properly tuned (via the choice of  $\alpha_s$  and the regularization), since it accounts for almost the entire hadron production in pp collisions. The emission probability in a PS also depends strongly on the cutoff scale  $Q_0$  near the collinear limit in the Sudakov form factor, Eq. (3.23). This parameter is not necessary in JETPHOX, where infrared singularities are absorbed by the fragmentation function, and it is not necessary for the POWHEG approach, where these singularities cancel from the NLO ME calculation and the PS.

To estimate the leverage from the cutoff, the default value from the Monash 2013 Tune,  $Q_0^{\text{QED}} = 0.5$  GeV, has been varied to extreme values,  $Q_0^{\text{QED}} = 0.1$  GeV and  $Q_0^{\text{QED}} = 2.0$  GeV. The resulting cross section for photons from the PS is depicted in Fig. 7.9 for a generic setup,  $\sqrt{s} = 7$  TeV and  $|\eta^\gamma| < 3.0$ . The lower cutoff parameter leads to a divergent cross section below  $p_T^\gamma = 2$  GeV and to a stable enhancement of

the cross section of around 10% above this value. Conversely, the large cutoff parameter leads to a decreased cross section of around 20%.

This parameter could therefore be adjusted to larger values in order to get the direct photon yield in better agreement with the descriptions by POWHEG+PYTHIA 8 and JETPHOX. Note that this discussion does not apply to the production of prompt photons from ME, which dominates at large energies as presented in Sec. 7.1.

The description of the Monash 2013 Tune [76] suggests that there is no particular motivation for the current default value  $Q_0^{\text{QED}} = 0.5 \text{ GeV}$  other than equality to the parameter for the QCD shower cutoff  $Q_0^{\text{QCD}} = 0.5 \text{ GeV}$ . The choice of the QCD shower cutoff, however, is based on an interplay with the Lund string hadronization model. Momentum kicks from the string breaking (see Sec. 3.5) play the role of a non-perturbative extension to the perturbative emission in the PS. Since this interplay applies only to hadron spectra, but not photon spectra, one can argue in favor of a modified shower cutoff  $Q_0^{\text{QED}}$ .

As a final remark, parameters should be tuned to measured data instead of theory descriptions. But in the absence of suitable photon spectra at low energies — ideally from a modern, high-energy lepton collider which is also not available — the guidance from the NLO prediction is a well justified approach.

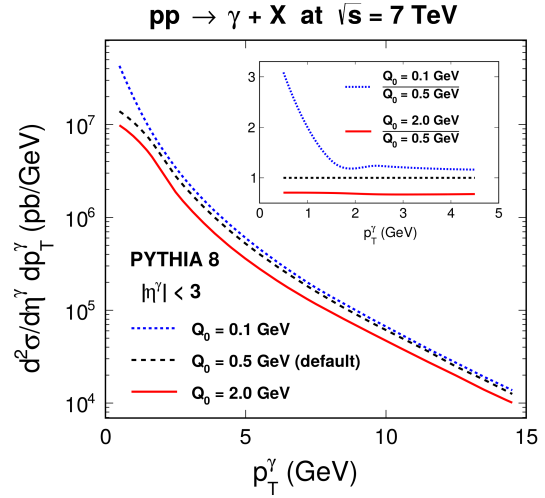


Figure 7.9: Transverse momentum spectrum for photon production in pp collisions at  $\sqrt{s} = 7 \text{ TeV}$  for different values of the PS cutoff scale.



## 7.4 NUCLEAR PARTON DENSITIES AND PHOTON-JET PAIRS IN P-PB COLLISIONS

In the following, the prospects of constraining nuclear PDF with photon-jet pairs are evaluated for the four LHC experiments ALICE, ATLAS, CMS and LHCb. Following the discussion in Sec. 2.2 and Eq. (2.23), the kinematic configuration of a photon-jet pair can be related to an *observed* parton momentum fraction  $x^{\text{obs}}$  of a lead nucleus:

$$x_{\text{Pb}}^{\text{obs}} := \frac{p_T^\gamma \exp(-\eta^\gamma) + p_T^{\text{jet}} \exp(-\eta^{\text{jet}})}{2E_{\text{Pb}}} \quad (7.3)$$

This variable has been applied to dijets from photoproduction measured in DIS at DESY HERA [123].

Predictions from POWHEG+PYTHIA 8 are given for the three nuclear Parton Density Function (nPDF) sets of nCTEQ15\_np, nCTEQ15 and EPPS16 in order to gauge the sensitivity of nuclear effects over a wide range of Bjorken  $x$ . Accordingly, uncertainties are evaluated from the respective sets of Hessian nuclear PDF errors. The respective proton reference PDF are assumed sufficiently constrained so that PDF uncertainties from the pp baseline are not accounted for. However, results from the pp baseline of nCTEQ15\_np at a different energy will be used to illustrate the extent of scale uncertainty, again from variation of renormalization and factorization scale by factors of two, but not by relative factors of four.

The predictions respect the specifications of the four major LHC experiments that use different kinematic cuts for the measurement of photon-jet pairs and rely on different definitions of photon isolation.

## ALICE

The ALICE detector is able to measure direct photons at low energies,  $p_T^\gamma > 1$  GeV, in an acceptance  $|\eta^\gamma| < 0.9$  as discussed for the direct photon measurement in Sec. 7.3. The necessary isolation cut relies accordingly on a low energy threshold of  $E_T^{\text{iso}} = 2$  GeV within a radius  $R = 0.4$  [124]. Previous analyses have also shown that anti- $k_T$  jets with  $R = 0.4$  in the kinematic range  $20 \text{ GeV} < p_T^{\text{jet}} < 120 \text{ GeV}$  can be measured within an acceptance  $|\eta^{\text{jet}}| < 0.5$  [125].

The distribution for  $x_{\text{Pb}}^{\text{obs}}$  for the given kinematic constraints is given in Fig. 7.10. The cross section for pp collisions is at least a factor two lower for p-Pb collisions over the probed region of  $x_{\text{Pb}}^{\text{obs}}$ . Striking, however, is that the scale uncertainty from the NLO+PS prescription of POWHEG+PYTHIA 8 is large in comparison with the uncertainties from the nuclear PDF. Therefore, a measurement in both systems, pp and p-Pb, has to be carried out, so that the scale uncertainty cancels in a ratio of cross sections.

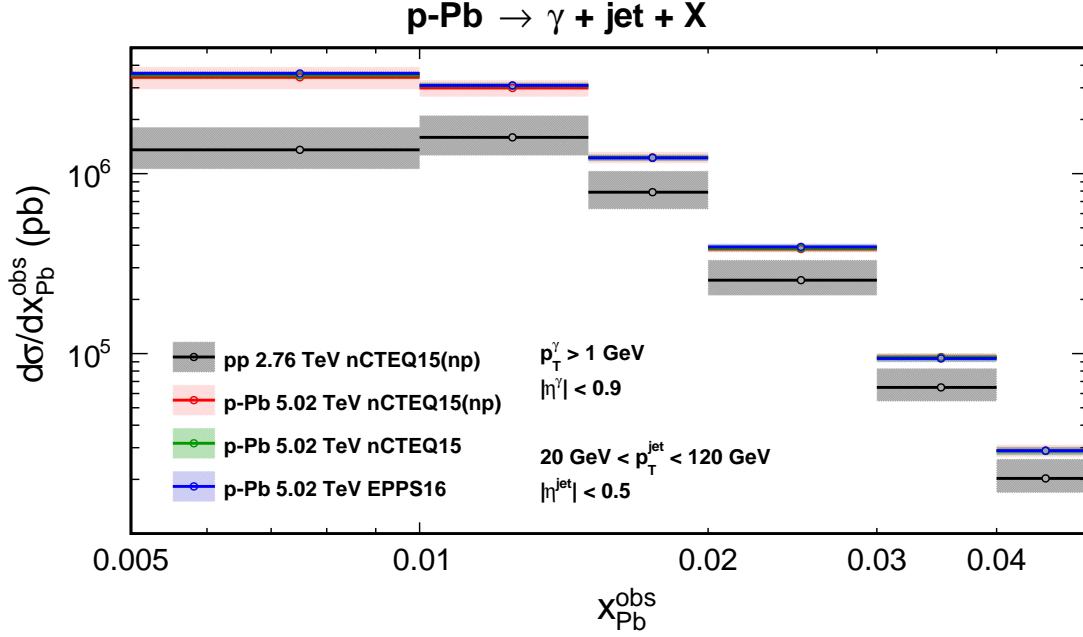


Figure 7.10: POWHEG+PYTHIA 8 prediction of observed parton momentum fraction  $x_{\text{Pb}}^{\text{obs}}$  reconstructed from photon-jet pairs with kinematic cuts for the central barrel detector system from ALICE. Two different collision systems are provided,  $\sqrt{s} = 2.76$  TeV (pp), illustrating the scale uncertainty, and  $\sqrt{s_{\text{NN}}} = 5.02$  TeV (p-Pb), showing nuclear PDF variations with nuclear PDF uncertainties.

It can be seen that the values from variation of nuclear PDF are not well separated within the uncertainties. In fact, the probed region of  $x_{\text{Pb}}^{\text{obs}}$  is very limited, regardless of the low transverse momentum reach of the photon. The upper limit of  $p_T^{\text{jet}} = 120$  GeV restricts to a maximum of about  $x_{\text{Pb}}^{\text{obs}} = 0.05$ . Conversely, the lower reach is already at around  $x_{\text{Pb}}^{\text{obs}} = 0.005$ , because the measurement is restricted to mid-rapidity. It can be seen from Eq. (7.3) that the rapidity range is a significant leverage for the minimum reach of probed parton momentum. In fact, there is an ALICE proposal for LHC long shutdown 3 to extend the reach where photons (and neutral pions) can be measured to about  $3.5 < |\eta| < 5$  [126].

#### CMS AND ATLAS

CMS and ATLAS have similar kinematic constraints for isolated photon and jet measurements, so the following result will roughly apply to both experiments. Following Sec. 7.3, photon isolation is ensured with an  $E_T^{\text{iso}} = 5$  GeV with an isolation cone radius  $R = 0.4$ . Anti- $k_T$  jets ( $R = 0.3$ ) are measured with  $p_T^{\text{jet}} > 30$  GeV and an acceptance  $|\eta^{\text{jet}}| < 1.6$ , while photons are constrained to  $p_T^{\gamma} > 40$  GeV and an acceptance  $|\eta^{\gamma}| < 1.44$ . The resulting distribution for the observed parton momentum, shown in Fig. 7.11, shows a similar minimum reach as in the ALICE case. The larger rapidity reach of CMS and ATLAS is offset by the requirement for higher transverse momentum of photons and jets. On the other hand, the probed region reaches into the region of anti-shadowing, around  $x_{\text{Pb}}^{\text{obs}} = 0.1$ . As for ALICE, only minute differences can be noticed between the three nuclear PDF.

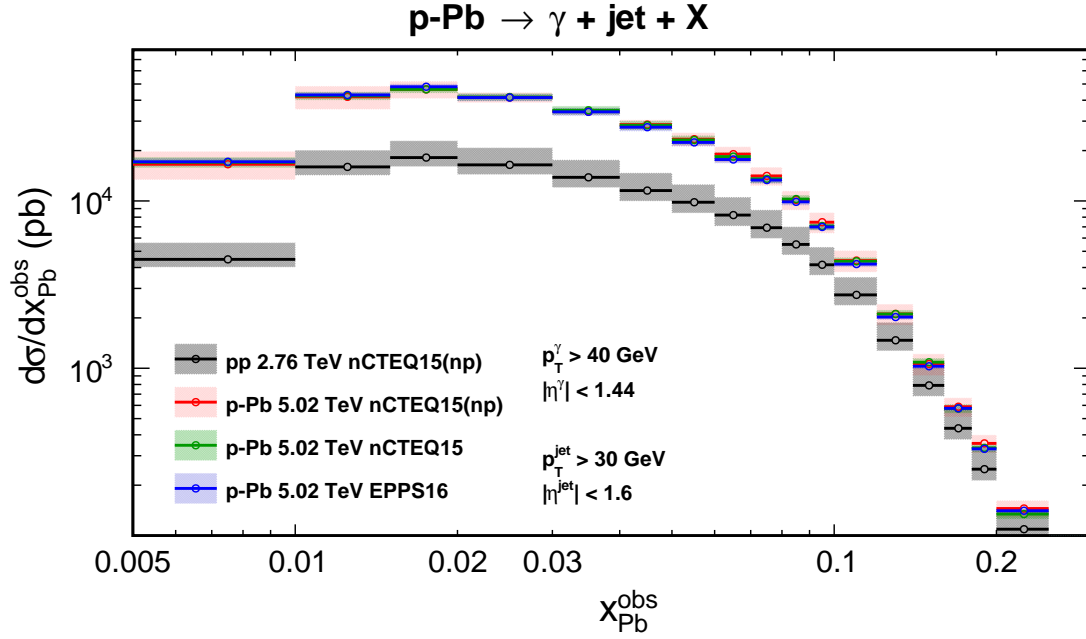


Figure 7.11: POWHEG+PYTHIA 8 prediction of observed parton momentum fraction  $x_{\text{Pb}}^{\text{obs}}$  reconstructed from photon-jet pairs with kinematic cuts including forward-rapidity detectors from [ATLAS](#) or [CMS](#). Two different collision systems are provided,  $\sqrt{s} = 2.76$  TeV (pp), illustrating the scale uncertainty, and  $\sqrt{s_{\text{NN}}} = 5.02$  TeV (p-Pb), showing nuclear PDF variations with nuclear PDF uncertainties.

Both [CMS](#) and [ATLAS](#) offer calorimetry at large forward rapidities, although this region is not so well controlled with respect to isolated photon and jet measurements, because charged particle tracking is restricted to  $|\eta| < 2.5$  for both experiments. If the acceptance could be extended to  $|\eta^{\text{jet}}| < 4.7$  and  $|\eta^{\gamma}| < 2.5$ , which was demonstrated in [127], the minimum reach of probed parton momentum could be extended, as seen from Fig. 7.12. Following the mentioned analysis, a gap in pseudorapidity  $1.44 < |\eta| < 1.57$  has been included, a slightly lowered jet energy cut,  $p_T^{\text{jet}} > 25$  GeV, and a minimum distance between jet and photon,  $\Delta R_{J\gamma} > 1.0$ .

Apparently, a significant cross section can be sampled in the core region of nuclear shadowing around  $x_{\text{Pb}}^{\text{obs}} = 0.002$ , where differences in the description of the three nuclear PDFs become visible, but still within the nuclear PDF uncertainties. Note that the nCTEQ15\_np uncertainties for the gluon dominated shadowing region are large, because the nCTEQ15\_np fits do not include data measured at [RHIC](#) in case of nCTEQ15, or [LHC](#) data in case of EPPS16. Accordingly, [LHC](#) spectra suggests a larger gluon abundance and less shadowing. As discussed in App. B, nCTEQ15\_np refrains from the inclusion of collider data in order to stay independent from the pion fragmentation function. However, our predictions show that the additional constraint from colliders has become vital for the deep shadowing region.

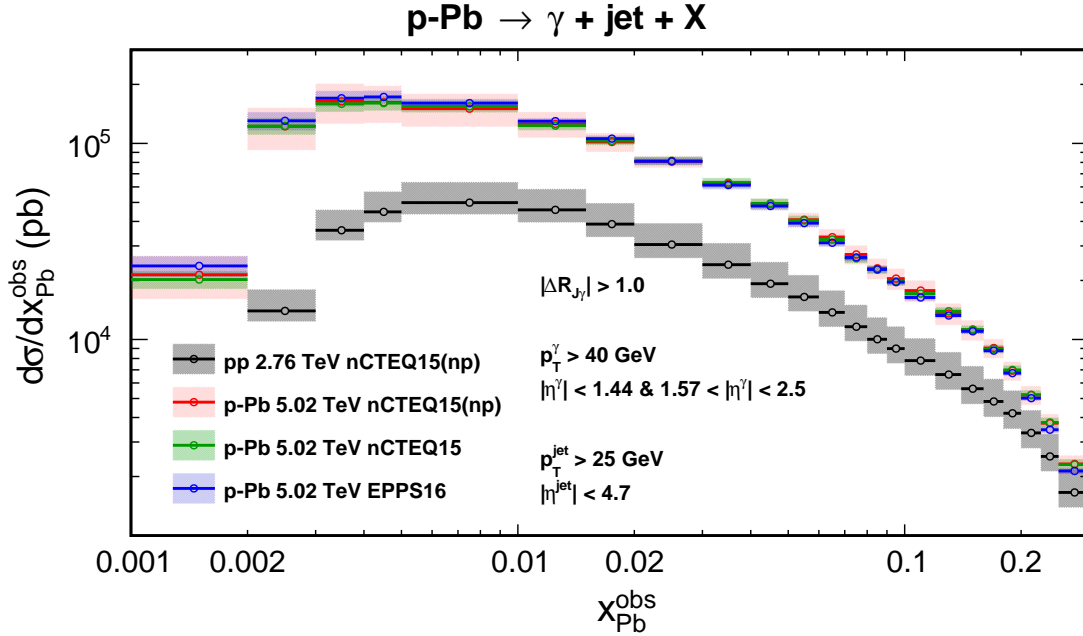


Figure 7.12: POWHEG+PYTHIA 8 prediction of observed parton momentum fraction  $x_{\text{Pb}}^{\text{obs}}$  reconstructed from photon-jet pairs with kinematic cuts for mid-rapidity detectors from [ATLAS](#) or [CMS](#). Two different collision systems are provided,  $\sqrt{s} = 2.76$  TeV (pp), illustrating the scale uncertainty, and  $\sqrt{s_{\text{NN}}} = 5.02$  TeV (p-Pb), showing nuclear [PDF](#) variations with nuclear [PDF](#) uncertainties.

#### LHCb

We have seen above that the minimum reach of probed parton momentum depends significantly on the ability to measure jets and photons at low transverse momenta and at large rapidities. The [LHCb](#) experiment offers both in its forward-arm setup, although the experiment is rather known to be designed for the analysis of heavy-flavor decays. In [128], the measurement of photons as low as  $p_T^\gamma > 3$  GeV within  $2 < \eta < 5$  is reported. Additionally, anti- $k_T$  jets ( $R = 0.5$ ) have been reconstructed for  $20 \text{ GeV} < p_T^{\text{jet}} < 100 \text{ GeV}$  in  $2.2 < \eta^{\text{jet}} < 4.2$  [96]. Due to the low photon transverse momentum, a photon isolation criterion similar to the one of [ALICE](#) is assumed.

According to the asymmetric setup of [LHCb](#), the simulated distribution of observed parton momentum is given separately for the proton going in direction of the forward detector arm (p-Pb) and for a lead-going direction (Pb-p). In the former case, low values of  $x$  from the Pb ion are probed and large values in the latter case.

As seen from the cross section presented in Fig. 7.13, the Pb-going mode (Pb-p) provides the opportunity to probe the region of the EMC effect,  $x_{\text{Pb}}^{\text{obs}} > 0.3$ , and in fact, the central values from the three nuclear [PDF](#) are visibly separated, but well within their uncertainties. However, the cross section already becomes small above  $x_{\text{Pb}}^{\text{obs}} > 0.2$ , so that a statistically significant measurement by [LHCb](#) may not be possible. This regime is the domain of [DIS](#) experiments, but supposedly, previous constraints have not been used such that our result from the three nuclear [PDF](#) accurately align.

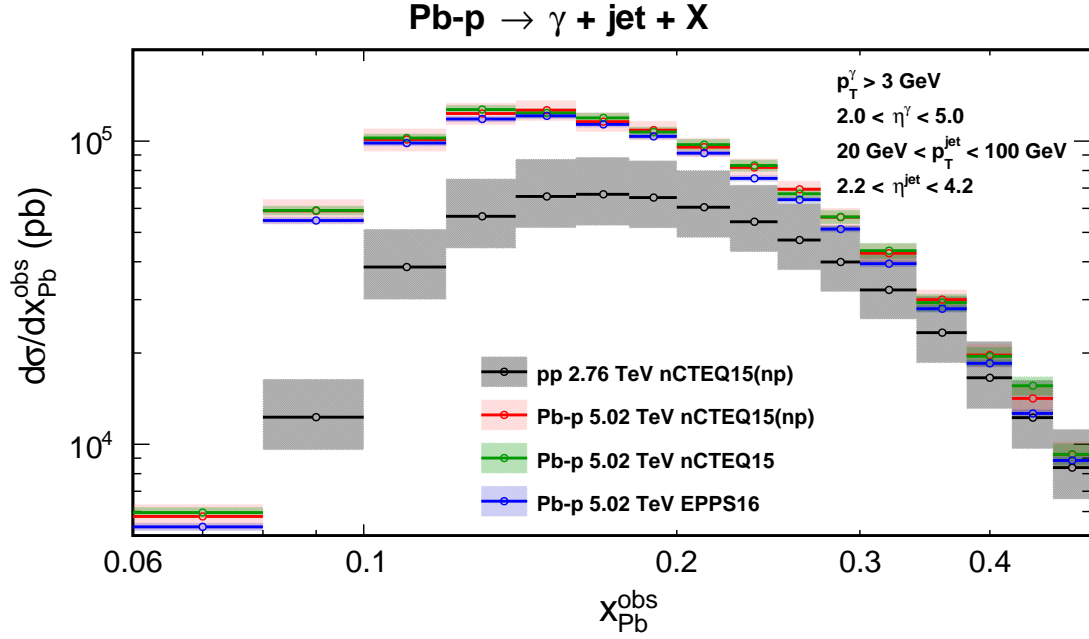


Figure 7.13: POWHEG+PYTHIA 8 prediction of observed parton momentum fraction  $x_{\text{Pb}}^{\text{obs}}$  reconstructed from photon-jet pairs with kinematic cuts for the forward detector from [LHCb](#) (Pb-going direction). Two different collision systems are provided,  $\sqrt{s} = 2.76$  TeV (pp), illustrating the scale uncertainty, and  $\sqrt{s_{\text{NN}}} = 5.02$  TeV (p-Pb), showing nuclear PDF variations with nuclear PDF uncertainties.

The [LHCb](#) detector stands out, when we turn to the p-going direction (p-Pb), as depicted in Fig. 7.14. A significant part of the cross section is probed in the region of  $x_{\text{Pb}}^{\text{obs}} = 0.0002$ , where not only the deep gluon shadowing region is probed, but also the enhanced saturation effects in heavy nuclei should become visible (see Sec. 3.2). A difference between EPPS16 and nCTEQ15 is seen, in accordance with the large-rapidity result for [CMS](#) and [ATLAS](#), at around  $x = 0.001$ . However, for smallest observed parton momenta, the central values from EPPS16 and nCTEQ15 coincide and predict consistently less gluon shadowing as nCTEQ15\_np, which does not rely on fits to collider data.

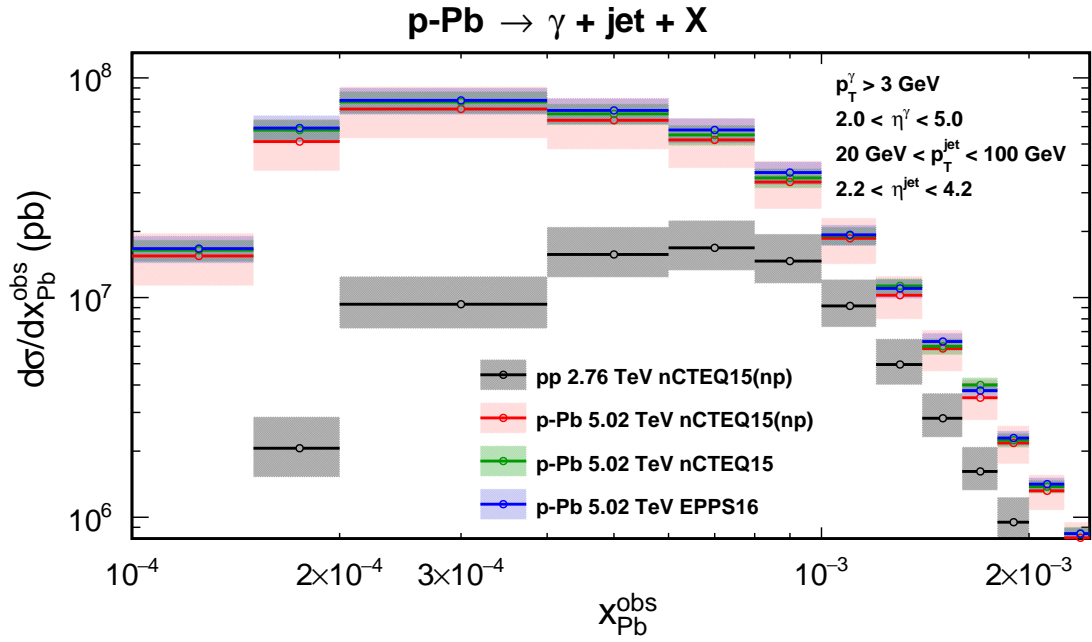


Figure 7.14: POWHEG+PYTHIA 8 prediction of observed parton momentum fraction  $x_{\text{Pb}}^{\text{obs}}$  reconstructed from photon-jet pairs with kinematic cuts for the forward detector from LHCb (p-going direction). Two different collision systems are provided,  $\sqrt{s} = 2.76 \text{ TeV}$  (pp), illustrating the scale uncertainty, and  $\sqrt{s_{\text{NN}}} = 5.02 \text{ TeV}$  (p-Pb), showing nuclear PDF variations with nuclear PDF uncertainties.

## SUMMARY

---

In this thesis, the measurement of neutral pions in pp collisions at  $\sqrt{s} = 8$  TeV with the [ALICE](#) detector at the Large Hadron Collider ([LHC](#)) is presented. In contrast to previous analyses, where an invariant mass analysis of neutral pions had been carried out, the neutral pion cross section was reconstructed on the basis of single clusters. This is possible for neutral pions with a large transverse momentum  $p_T > 10$  GeV, because decay photons and electrons from conversion and Dalitz decays give rise to calorimeter showers that cannot be resolved by the [ALICE EMCal](#) detector. The event sample provided by the [EMCal](#) triggers, which are sensitive to high energy depositions, allowed for a statistically significant result up to a transverse momentum of about 70 GeV. The unresolved showers are also called merged clusters, as opposed to single-shower clusters that stem from the stopping of single photons and electrons as well as from the partial energy loss of charged hadrons.

On one hand, the missing invariant mass information made it necessary to account for the background from other particles, but the return is a measurement of neutral pions that reaches beyond the transverse momentum limit of a previous di-cluster analysis at around 20 GeV. It was taken advantage of the fact that the two-photon decay of the neutral pions leads to an elongated shower shape, that can be approximated by an ellipse. Via a cut on the ellipticity of the given clusters, the neutral pion purity could be significantly enhanced. The separation of merged showers and single showers becomes less effective for larger transverse momenta,  $p_T > 40$  GeV, due to the increasing collimation of decay products. Furthermore, an additional background of merged showers emerges in this energy regime from decay photons of the eta meson. To a large degree, it was possible to reject the charged particle background through a matching of clusters to charged particle trajectories that have been measured in the tracking system of [ALICE](#).

The analysis depends to a large degree on a reliable [MC](#) simulation of pp collisions and the detector response. Sensitive properties in this sense are the description of the shower shape and the activity near the selected clusters. Moreover, the momentum resolution relies on the probability for photon conversions to occur in front of the [EMCal](#), which is provided by the detector simulation using [GEANT](#). A significant systematic uncertainty was estimated as a result, especially at the lower transverse momentum limit of the analysis at about 10 GeV. The secondary pion yield from weak decays has been subtracted from the final result, which leads to a significant systematic uncertainty from the description of the  $K_s^0$  yield that exerts a significant leverage on the final result through an inferior momentum resolution. The systematic uncertainties amounted to a total of about 10 – 20%, in contrast to values of 5–10% that had been provided by invariant mass analyses at lower transverse momentum.

In the context of heavy-ion physics, this analysis has to be seen in view of an upcoming analysis for data in p–Pb collisions at  $\sqrt{s_{NN}} = 8.16$  TeV, which has been recorded by [ALICE](#) in 2016. Determined by the comparison of the neutral pion yield in both systems, the nuclear modification factor  $R_{pPb}$  provides an important baseline measurement for Pb–Pb collisions.

The influence of cold nuclear matter effects must be considered for the interpretation of hot nuclear matter effects, namely for the extent of parton energy loss that has to be described by theory. Although the extent of cold nuclear matter effects is small at larger transverse momenta,  $p_T > 50$  GeV, a measurement of  $R_{pPb}$  by ALICE, which is possible on the basis of this work, will be significant, because it is the same energy regime for which a diminishing suppression of hadrons in Pb–Pb collisions has been reported. In fact, it would be the first measurement of its kind for an identified hadron species, since other identified hadron analyses have been restricted to  $p_T < 20$  GeV.

Regarding the measurement of  $R_{pPb}$  with a similar merged cluster analysis, the considerable systematic uncertainties found in the result of this work can be seen with a certain ease, since many uncertainty sources will be correlated. As a result, uncertainties such as the secondary neutral pion feed-down or the uncertainty of the conversion probability in the detector material will cancel. Deficiencies in the cluster energy correction are also mitigated, but still affect the accuracy of the absolute energy scale. However, by including the latest test beam results, this work has shown that no strong effects are expected from calorimeter leakage in the region of up to 100 GeV. A critical issue for the measurement of neutral pions in p–Pb will be the increased event activity: The analysis of merged clusters with all the refinements such as cluster-track matching and the shower shape cut will take place in an environment of enhanced particle multiplicity, which demands an accurate MC description.

Finally, the presented neutral pion measurement provides a constraint for the theoretical description of pp collisions. Rather than constraining parton densities in this energy regime, for which the measurement of jets, weak bosons and Drell-Yan lepton pairs is generally preferred, this measurement is an opportunity to constrain the fragmentation function of neutral pions. In fact, the previous invariant mass analyses of neutral pions have shown a clear discrepancy between data and fixed-order calculations at NLO.

For the second part of this thesis, a comprehensive set of theoretical predictions for direct photon observables in pp collisions at the LHC is presented. A recent implementation of direct photon processes in POWHEG BOX made it possible to describe direct photon production at Next-to-Leading Order (NLO) together with a Parton Shower (PS), provided by PYTHIA 8 in this work. Predictions are compared to those of PYTHIA 8, which is a representative of Leading Order (LO) general-purpose generators, and to JETPHOX, which is a representative of the fixed-order approach at NLO.

The description of isolation photons are tested over a broad kinematic range on the basis of a measurement of ATLAS. Although PYTHIA 8 with the Monash 2013 Tune can compete with an NLO approach, the deficiency of the LO accuracy of the underlying hard processes is revealed through a large scale uncertainty. All three theoretical description tend to underestimate the measured isolated photon cross section by 5 – 15% for most energies. It is shown that the approach POWHEG+PYTHIA 8 gives a better result than JETPHOX, which is attributed to the resummation of higher-order corrections through the PS. Further comparisons are made for correlations of isolated photons and jets, as measured by CMS in pp collisions and p–Pb collisions. Limitations of the fixed-order approach of JETPHOX are revealed, whereas the NLO+PS approach by POWHEG+PYTHIA 8 constitutes the first reliable description of photon-jet correlations at NLO.



The hot nuclear matter created in heavy-ion collisions gives rise to thermal photons at low transverse momenta. It is pointed out in this work that the necessary baseline of direct photon production from hard parton scatterings is not well constrained by data, so that theoretical expectations are a valuable contribution for the thermal interpretation of direct photon data in heavy-ion collisions. Comparing theoretical descriptions, it is shown that JETPHOX and POWHEG+PYTHIA 8 show a similar result for the excess of direct photons over inclusive photons, while PYTHIA 8 shows a larger deviation from the two other NLO-based descriptions. In order to improve the description of low energy photons in PYTHIA 8, it is argued that a variation of the infrared cutoff parameter of the QED PS of PYTHIA 8 should be considered with guidance from NLO calculations. By virtue of the NLO prescription, POWHEG+PYTHIA 8 does not rely on such a cutoff parameter.

The possibility to constrain nuclear parton densities with photon-jet pairs in p-Pb collisions with the four large experiments at the LHC is assessed. Accounting for the respective detector capabilities, limitations and opportunities for each experiment are explored. For a determination of very small parton densities, the measurement at large forward rapidities is mandatory. Accordingly, it is possible with the endcap calorimeter system of ATLAS and CMS to explore a regime of about  $x_{\text{Pb}}^{\text{obs}} = 0.001$ , where modern nuclear parton distribution functions start to disagree. A particular opportunity is found for the LHCb experiment, where photon-jet pairs can be sampled with a significant cross section down to the saturation regime of nuclear parton densities.

Concluding, the NLO+PS approach given by POWHEG+PYTHIA 8 is proven to be valuable extension of the phenomenological equipment for the description of direct photons due to the reliability of a direct photon cross section at NLO combined with a realistic description of the final state.

Results on direct photons presented in this work are published in JHEP 1803 (2018) 081.



## ZUSAMMENFASSUNG

---

Diese Arbeit präsentiert die Messung neutraler Pionen in pp Kollisionen bei  $\sqrt{s} = 8$  TeV mit dem [ALICE](#) Detektor am Large Hadron Collider ([LHC](#)). Im Gegensatz zu früheren Analysen, in denen eine Analyse der invarianten Masse durchgeführt wurde, wird der neutrale Pion Wirkungsquerschnitt anhand einzelner Cluster rekonstruiert. Dies ist möglich für neutrale Pionen mit einem großen Transversalimpuls  $p_T > 10$  GeV, weil Zerfallsphotonen und Elektronen von Konversionen und Dalitz-Zerfällen zu einem Teilchenschauer im Kalorimeter führen, der nicht aufgelöst werden kann mittels des [ALICE EMCal](#) Detektors. Die Menge an Ereignissen, bereitgestellt von den [EMCal](#) Triggern, die empfindlich sind für große Energieeinträge, ermöglichte ein statistisch signifikantes Ergebnis bis zu einem Transversalimpuls von ungefähr 70 GeV. Nicht aufgelöste Schauer werden auch merged Cluster genannt, im Gegensatz zu Einzelschauer Cluster, die von der Absorption einzelner Photonen und Elektronen herrühren sowie vom teilweisen Energieverlust geladener Hadronen.

Auf der einen Seite wurde es durch das Fehlen der Information über die invariante Masse notwendig, den Hintergrund durch andere Teilchen zu berücksichtigen, aber der Gewinn ist eine Messung, die über das Transversalimpulslimit der vorherigen Di-Cluster Analyse bei ungefähr 20 GeV hinausführt. Es wurde ausgenutzt, dass der Zwei-Photon-Zerfall des neutralen Pions zu einer gestreckten Schauerform führt, die angenähert werden kann durch eine Ellipse. Mittels eines Schnitts in die Elliptizität der gegebenen Cluster, konnte die Reinheit des Signals deutlich erhöht werden. Die Unterscheidung von merged Schauern und Einzelschauern ist weniger effektiv für größere Transversalimpulse,  $p_T > 40$  GeV, wegen der zunehmenden Kollimierung der Zerfallsprodukte. Überdies entsteht ein Untergrund zusätzlicher merged Cluster in diesem Energieregime durch die Zerfallsphotonen des Eta Mesons. Es war überwiegend möglich, den Hintergrund geladener Teilchen zu unterbinden anhand eines Abgleichs von Cluster und Teilchentrajektorien, die im Spurrekonstruktionssystem von [ALICE](#) gemessen wurden.

Die Analyse hängt im hohen Maße von einer zuverlässigen [MC](#) Simulation von pp Kollisionen und der Detektorantwort ab. Empfindliche Eigenschaften sind in dieser Hinsicht die Beschreibung der Schauerform und der Aktivität nahe der ausgewählten Cluster. Darüberhinaus hängt die Impulsauflösung von der Wahrscheinlichkeit für Photonenkonversionen vor dem [EMCal](#) ab, welche durch die Detektorsimulation mittels [GEANT](#) verfügbar ist. Eine signifikante systematische Unsicherheit wurde daher abgeschätzt, besonders beim unteren Transversalimpulslimit der Analyse bei ungefähr 10 GeV. Der Sekundärbeitrag neutraler Pionen durch schwache Zerfälle wurde abgezogen vom endgültigen Resultat, was zu einer signifikanten systematischen Unsicherheit führte durch die Beschreibung des Beitrags vom  $K_S^0$ , welche eine erhebliche Hebelwirkung auf das endgültige Resultat hatte aufgrund eines schlechten Impulsauflösungsvermögens. Es ergab sich eine gesamte systematische Unsicherheit von 10–20% im Gegensatz zu den Werten 5–10%, die sich durch die invariante Massenanalyse bei niedrigeren Transversalimpulsen ergeben hatte.

Im Bezug auf die Schwerionenphysik kann diese Analyse hinsichtlich einer Analyse von p-Pb Kollisionen bei  $\sqrt{s_{NN}} = 8.16$  TeV erachtet werden, die von [ALICE](#) im

Jahr 2016 aufgezeichnet worden sind. Anhand des Vergleichs der neutralen Pion Produktion in beiden Systemen stellt der nukleare Modifikationsfaktor  $R_{pPb}$  eine wichtige Referenzmessung für Pb–Pb Kollisionen.

Der Einfluss kalter Kernmaterie muss berücksichtigt werden für die Interpretation der Effekte heißer Kernmaterie, nämlich für das Ausmaß des Partonenenergieverlusts, der durch die Theorie beschrieben wird. Obwohl der Einfluss kalter Kernmaterie kleiner ist bei großen Transversalimpulsen,  $p_T > 50$  GeV, ist die Messung von  $R_{pPb}$  durch ALICE, die durch diese Arbeit ermöglicht wird, bedeutsam, da es jenen Energiebereich betrifft, in dem eine abnehmende Unterdrückung von Hadronen in Pb–Pb Kollisionen festgestellt wurde. Tatsächlich wäre es die erste Messung dieser Art für identifizierte Hadronen, da andere Analysen identifizierte Hadronen beschränkt war auf  $p_T < 20$  GeV. Hinsichtlich der Messung von  $R_{pPb}$  mit einer merged-Cluster-Analyse kann man den erheblichen systematischen Unsicherheiten im Ergebnis der vorliegenden Arbeit mit einer gewissen Gelassenheit begegnen, da viele Unsicherheitsquellen korreliert sind. Daher werden solche Unsicherheiten wie der Sekundärbeitrag neutraler Pionen oder die Konversionswahrscheinlichkeit weggelassen. Schwächen in der Energiekorrektur werden auch umgangen, jedoch bleibt die Genauigkeit der absoluten Energieskala betroffen. Jedoch hat die vorliegende Arbeit gezeigt, aufbauend auf Erkenntnissen einer Teststrahl-Kampagne, dass keine starken Verzerrungen zu erwarten sind im Bereich bis 100 GeV. Ein kritischer Punkt für die Messung neutraler Pionen in p–Pb wird die erhöhte Aktivität sein: Die merged-Cluster-Analyse mit all ihren Methoden, wie der dem Cluster-Spur-Abgleich und dem Schnitt auf die Schauerform, wird in einer Umgebung erhöhter Teilchenmultiplizität stattfinden.

Schließlich ist noch zu sagen, dass die vorliegende Messung die theoretische Beschreibung von pp Kollisionen eingrenzt. Jedoch eher nicht, um Partonendichten in diesem Energiebereich einzugrenzen, was eher durch die Messung von Jets, schwacher Bosonen und Drell-Yan Lepton-Paaren gegeben ist, sondern um die Fragmentationsfunktion neutraler Pionen einzugrenzen. Die vorherigen invariante-Masse-Analysen haben diesbezüglich eine klare Diskrepanz aufgezeigt zwischen der Messung der Fixed-Order Berechnungen bei NLO.

Im zweiten Teil dieser Arbeit ist ein umfassender Satz theoretischer Vorhersagen für direkte Photonproduktion in pp Kollisionen am LHC gemacht worden. Anhand einer kürzlich eingeführten Implementierung von direkten Photonprozessen in POWHEG Box wurde es möglich, direkte Photonproduktion bei NLO zusammen mit einem Parton Shower (PS) zu beschreiben, der in dieser Arbeit durch PYTHIA 8 verfügbar ist. Vorhersagen werden verglichen mit denen von PYTHIA 8, welches den Vertreter der LO Allzweck-Generatoren darstellt, und mit denen von JETPHOX, welches als Vertreter des Fixed-Order-Ansatzes bei NLO gilt.

Die Beschreibung isolierter Photonen wurde über einen weiten kinematischen Bereich geprüft anhand von Messungen von ATLAS. Obwohl PYTHIA 8 durch den Monash 2013 Tune mithalten kann mit dem NLO-Ansatz, offenbart sich doch die LO Genauigkeit der zugrundeliegenden Prozesse durch eine große Skalenunsicherheit. Alle drei theoretischen Beschreibungen tendieren dazu, den gemessenen Wirkungsquerschnitt isolierter Photonen um 5–15% zu unterschätzen. Es wird gezeigt, dass der Ansatz POWHEG+PYTHIA 8 ein besseres Resultat liefert als JETPHOX, was einer Resummierung von Korrekturen höherer Ordnung durch den PS zugeordnet wird. Weitere Vergle-

iche wurden angestellt für Korrelationen von isolierten Photonen und Jets, die von [CMS](#) in pp und p–Pb Kollisionen gemessen worden sind. Beschränkungen des Fixed-Order-Ansatzes von [JETPHOX](#) wurden herausgestellt, wo hingegen der Ansatz von [POWHEG+PYTHIA 8](#) die erste, zuverlässige Beschreibung von Photon-Jet-Korrelationen bei [NLO](#) darstellt.

Die heiße Kernmaterie, die in Schwerionenkollisionen erzeugt wird, führt zur Produktion niederenergetischer Photonen. Es wird gezeigt, dass die nötige Referenz direkter Photonenproduktion von harten Partonenstößen nicht gut eingegrenzt wird durch Daten, sodass theoretische Erwartungen einen wertvollen Beitrag darstellen für die Interpretation der direkten Photonen in Schwerionenkollisionen. Anhand eines Vergleichs theoretischer Beschreibungen wird gezeigt, dass [JETPHOX](#) und [POWHEG+PYTHIA 8](#) den direkten Photonenüberschuss gegenüber inklusiver Photonen ähnlich einschätzen, während [PYTHIA 8](#) eine größere Abweichung von den beiden [NLO](#)-Beschreibungen zeigt. Um die Beschreibung niederenergetischer Photonen in [PYTHIA 8](#) zu verbessern, wird für eine Änderung des infraroten Cutoffs des [QED PS](#) argumentiert, mithilfe des Vergleichs zu [NLO](#)-Rechnungen. Ein solcher Cutoff ist nicht nötig für [POWHEG+PYTHIA 8](#) aufgrund der [NLO](#)-Beschreibung.

Die Möglichkeit zur Untersuchung nuklearer Partondichten mittels Photon-Jet-Paaren in p–Pb Kollisionen an den vier großen Experimenten des [LHC](#) wurde untersucht. Beschränkungen und Möglichkeiten wurden für jedes Experiment aufgezeigt unter Berücksichtigung der jeweiligen Detektorspezifikationen. Dem folgend ist es mit den Endcap-Kalorimetern von [ATLAS](#) und [CMS](#) möglich, den Bereich um  $x_{\text{Pb}}^{\text{obs}} = 0.001$  zu erforschen, an jener Stelle, wo die modernen Beschreibungen nuklearer Partondichten sich uneins werden. Eine besondere Chance wurde für das [LHCb](#) Experiment aufgezeigt, wo Photon-Jet-Paare gemessen werden können mit einem erheblichen Wirkungsquerschnitt, der hinunterreicht bis in das Sättigungs-Regime.

Schlussendlich ist zu sagen, dass sich der [NLO+PS](#)-Ansatz von [POWHEG+PYTHIA 8](#) als eine wertvolle Erweiterung des phänomenologischen Repertoires erweist zur Beschreibung direkter Photonen wegen der Zuverlässigkeit eines Wirkungsquerschnitts direkter Photonen bei [NLO](#) zusammen mit der realistischen Beschreibung des Endzustands.

Ergebnisse über direkte Photonen in dieser Arbeit sind veröffentlicht in [JHEP 1803 \(2018\) 081](#).



## DELPHI UND BASHPHOX

---

In the following, two repositories Delphi and Bashphox that are used in this thesis are briefly introduced. They should make it easier also for students or anyone that wants to carry out theory calculations with PYTHIA 8, POWHEG and JETPHOX. To anticipate the most important for someone interested, here are the links for the software repositories that also include some predictions about direct photon production:

<https://github.com/hpoppenb/Delphi>

<https://github.com/hpoppenb/BashPhox>

### DELPHI

DELPHI is a set of Bash scripts and C++ code that should facilitate the use of PYTHIA 8 and POWHEG. Analysis code for generated events is given in `src/` for PYTHIA 8 and in `powhegShower/src/` for POWHEG. This separation has been considered since hard parton events are directly generated with PYTHIA 8, but have to be given separately for the PS for POWHEG events. On the other hand, all analysis methods such as isolation cuts are given through a bib of common functions in `src/PythiaAnalysisHelper.cxx` so that a consistent treatment on the analysis-level is given for both approaches. Furthermore, scripts are provided that allow for an easier use of PYTHIA 8 and POWHEG: Instead of tediously editing configurations for both, such specifications can better given directly, for example the hard processes, the energy and the PDF for the generation of PYTHIA 8 events.

### BASHPHOX

An enhanced version of JETPHOX is also presented, called BASHPHOX, that aims for an easier access to JETPHOX with the help of Bash scripts. In addition, small code changes allow the generation of asymmetric p–A collisions with any parton distribution following the LHAPDF standard. It is based on the official release 1.3.14 of JETPHOX and is published under <https://github.com/hpoppenb/BashPhox>.

Here are the features and some guiding words:

- **Automated generation in  $p_T^\gamma$ -bins for homogeneous statistics:**

The default jetphox directory is reworked and only contains the necessary code for a specific run in a pt bin, the jetphox code basis (i.e. the directories `pdfa`, `frag`, `bases`, `src`) you find now in the root directory of this repo. The Makefile in the jetphox working dir (`jp*/working`) has been modified accordingly.

Instead of only one jetphox directory you should create yourself several directories by copying the default directory `jp1`, one for each photon pt bin. The binning is defined in `run_jetphox.sh`.

- **Automation of parameter input and compilation:**

The script writes the config file `jp*/working/parameter.indat` in the working directory in each pt bin, then compiles and runs the program.

- **Bookkeeping:**

The root file and the directory containing it are named in a verbose way, so you can see from the name what has been run. This should especially help to maintain overview over the multitude of files in case of scale variations.

Additionally, a merge script `merge_...sh` is produced to add the histograms of all pt bins in the end. The merge script has to be invoked manually after it has been verified that output files have been produced in the according directories, e.g. `jp4/<date>_dir_NLO_8160GeV_400Mevts_....`

- **Cleanup:**

After you have merged everything correctly, you can free the subdirectories from temporary config files and the output files with `sh clean_histos_logfiles.sh`.

- **Generation of p–A collisions with freely chosen LHAPDF:**

The necessary source code changes have been made in `src/main/param_lhapdf.f` and `src/main/distfunb_lhapdf.f`. You can compare with the original files `...f_ORIGINAL` in order to understand the small changes, which now allow a second LHAPDF to be assigned in `jp*/working/parameter.indat`.

Finally, the script `run_jetphox.sh` allows to define a detailed input configuration, e.g. concerning CM energy, pdf, npdf usage, isolation cut, scale variation etc. So, you can call `run_jetphox.sh` with an additional script like this:

Listing A.1: An example bash script to start `run_jetphox.sh`

---

```
#Usage: run_jetphox.sh [name] [lhapdfname1] [lhapdfname2] [IS scale] [renorm.
  scale] [FS scale] [process] [HigherOrderTRUEorFALSE] [cmsenergy in gev] [
  maxrap] [minrap] [Inclusive=0 or withJets=1] [iso cone radius] [iso energy]
  [number of events] [randomseed]

DATE='date +%Y_%m_%d'
RANDOMX=12345
NEVENTS=5000000

# isolated photons (2 gev in R=0.4)
# -10.0 < y < 10.0
# sqrt(s) = 5020 gev
# only direct photons at L0

# p-Pb
sh run_jetphox.sh $DATE CT14nlo EPPS16nlo_CT14nlo_Pb208 1.0 1.0 1.0 dir FALSE
  5020 10.0 -10.0 0.4 2 $NEVENTS $RANDOMX
```

---

Some additional notes on the usage of BASHPHOX:

- In the current version, the script starts a SLURM script in the respective working directory. If you do not use SLURM, you have to replace this script according to your respective job scheduler.
- You have to specify your ROOT path in each `jp*/working/Makefile`.



- You have to specify your LHAPDF path in each `jp*/working/parameter.indat_template`.
- There is an example script.
- The program was tested with LHAPDF 6.1.6., JETPHOX 1.3.1.4, ROOT 6, Scientific Linux 7, GCC 4.8.5.
- If compilation fails, make `clean` in the working directory and try again, praying for the mercy of the Fortran god.

---

**Final remark: The underlying program Jetphox is not my creation, so please cite the authors if used for publication, e.g. [83].**



The LHAPDF nPDF grids are constructed from scaling of the free proton PDF with respect to the number of protons and neutrons, then multiplying by the nuclear modification factor  $R$ .

$$u^A(x, Q^2) = \frac{Z}{A} [R_{u_V}(x, Q^2)u_V^p(x, Q^2) + R_{\bar{u}}(x, Q^2)\bar{u}^p(x, Q^2)] + \frac{N}{A} [R_{d_V}(x, Q^2)d_V^p(x, Q^2) + R_{\bar{d}}(x, Q^2)\bar{d}^p(x, Q^2)] \quad (\text{B.1})$$

$$d^A(x, Q^2) = \frac{Z}{A} [R_{d_V}(x, Q^2)d_V^p(x, Q^2) + R_{\bar{d}}(x, Q^2)\bar{d}^p(x, Q^2)] + \frac{N}{A} [u_{d_V}(x, Q^2)u_V^p(x, Q^2) + R_{\bar{u}}(x, Q^2)\bar{u}^p(x, Q^2)] \quad (\text{B.2})$$

$$\bar{u}^A(x, Q^2) = \frac{Z}{A} [R_{\bar{u}}(x, Q^2)\bar{u}^p(x, Q^2)] + \frac{N}{A} [R_{\bar{d}}(x, Q^2)\bar{d}^p(x, Q^2)] \quad (\text{B.3})$$

$$\bar{d}^A(x, Q^2) = \frac{Z}{A} [R_{\bar{d}}(x, Q^2)\bar{d}^p(x, Q^2)] + \frac{N}{A} [R_{\bar{u}}(x, Q^2)\bar{u}^p(x, Q^2)] \quad (\text{B.4})$$

$$s^A(x, Q^2) = \bar{s}^A(x, Q^2) = R_s(x, Q^2)s^p(x, Q^2) \quad (\text{B.5})$$

$$c^A(x, Q^2) = \bar{c}^A(x, Q^2) = R_c(x, Q^2)c^p(x, Q^2) \quad (\text{B.6})$$

$$b^A(x, Q^2) = \bar{b}^A(x, Q^2) = R_b(x, Q^2)b^p(x, Q^2) \quad (\text{B.7})$$

$$g^A(x, Q^2) = R_g(x, Q^2)g^p(x, Q^2) \quad (\text{B.8})$$

Note that  $\bar{u}, \bar{d}$  represent the entire sea quark content despite the overline notation. Also, the PDF for the proton alone is sufficient as a baseline due to isospin symmetry.

There are 97 PDF member of EPPS16 [66]: one central value (0), 40 error sets for EPPS16 (1-40) and 56 error sets for the baseline PDF CT14nlo (41-96). This implies that variation of the first 40 error sets is often sufficient for uncertainty estimation, at least for most regions of Bjorken- $x$ , where uncertainty of the nuclear modification dominates.

For nCTEQ15, there are 33 PDF members [129]: one central value (0) and 32 error sets (1-33). There are actually two versions of the nCTEQ15 sets, where measurements of pion production at RHIC are included (nCTEQ15) or not (nCTEQ15\_np). The inclusion of this pion data generally improves the uncertainties (fig. B.1), but introduces a dependence on the pion fragmentation function, which is the reason that the version nCTEQ15\_np has been used throughout this work. The comparison between different fragmentation functions in the PDF analysis yields only a small difference (fig. B.2), but this does not exclude a larger deviation in case of some other fragmentation function.

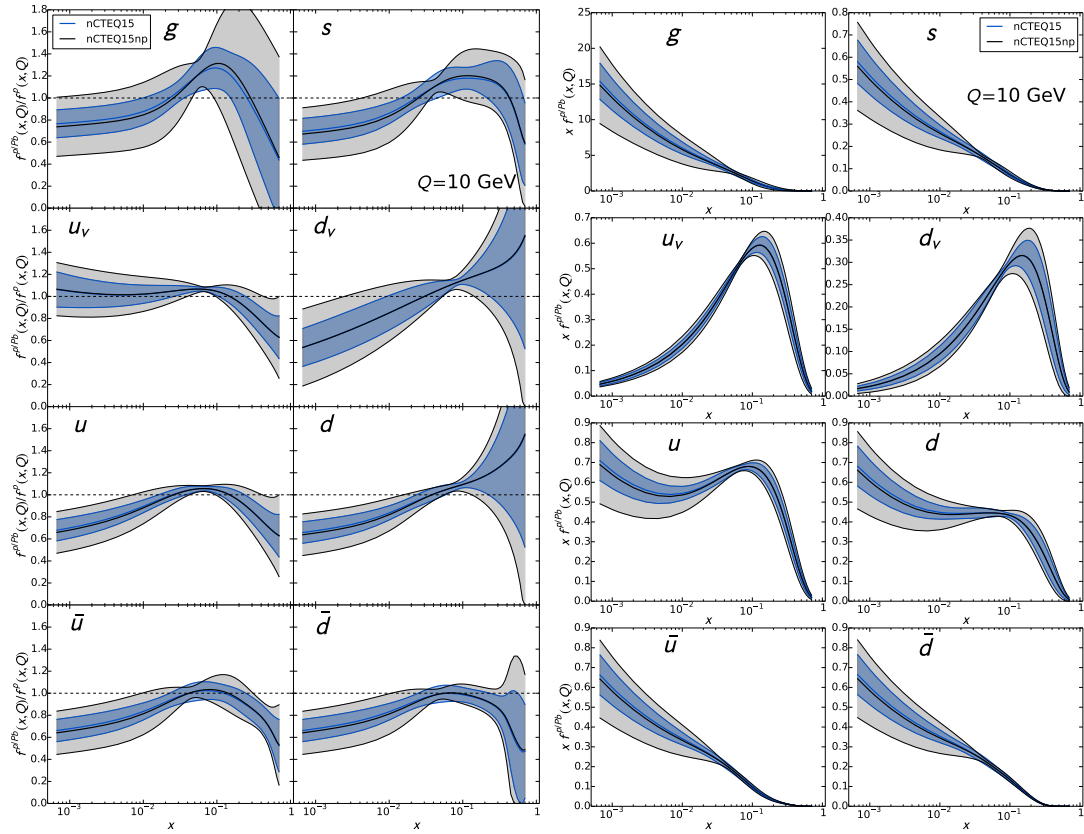


Figure B.1: Left panel: comparison of the nuclear modification fit with (nCTEQ15) and without the inclusion of pion data (nCTEQ15\_np) for  $Q = 10$  GeV. Right panel: the actual nPDF for  $Q = 10$  GeV [129].

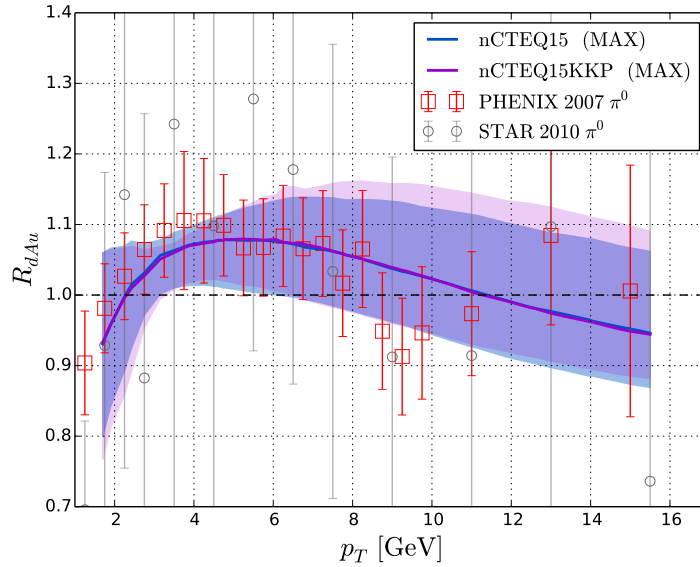


Figure B.2: Calculated nuclear modification  $R_{dAu}$  on the basis of pion data and two different fragmentation functions BKK (blue) and KKP (violet) [129].

Throughout this thesis, PDF uncertainties of observables  $\Delta X$  have been calculated with the CTEQ 'Master Formula', where  $\Delta X_i^+$  are  $X_i^-$  are the observables derived from the  $2N$  PDF error sets [130]:

$$\Delta X = \frac{1}{2} \sqrt{\sum_{i=1}^N (X_i^+ - X_i^-)^2} \quad (\text{B.9})$$



## LIST OF FIGURES

---

Figure 2.1	Multiplets of the lightest vector mesons (left) and pseudoscalar mesons (right) [3]. . . . .	4
Figure 2.2	Multiplets of the lightest baryons [3]. . . . .	4
Figure 2.3	The running coupling $\alpha_s$ and measurements extracted at a given order of perturbation theory and energy scale $Q$ [10]. . .	8
Figure 2.4	Relevant measurements for the current world average of $\alpha_s$ [10].	9
Figure 2.5	World average of $\alpha_s$ in 1992 [11]. . . . .	9
Figure 2.6	Mandelstam invariants characterize possible paths of intermediate particles in a $2 \rightarrow 2$ scattering. Not every path is always allowed by physical constraints. In this case, a doubly charged photon would be necessary to allow the $u$ -channel in $e^-e^+ \rightarrow e^-e^+$ or the $s$ -channel in $e^-e^- \rightarrow e^-e^-$ . . . . .	10
Figure 2.7	Example for a parton distribution function [14]. . . . .	12
Figure 2.8	Net proton production for various energies: $\sqrt{s_{\text{NN}}} = 5 \text{ GeV}$ (AGS), $\sqrt{s_{\text{NN}}} = 17 \text{ GeV}$ (SPS) and $\sqrt{s_{\text{NN}}} = 200 \text{ GeV}$ (RHIC). Dashed lines denote the respective beam rapidity (left). Light-cone diagram of a collision in the Bjorken picture with the evolution of a QGP [19]. . . . .	14
Figure 2.9	Pressure $P$ and energy density $\epsilon$ for a hadron gas and for the bag model QGP above the critical temperature $T_C$ [16]. . . . .	15
Figure 2.10	Energy density calculated for two light quark flavors, three light quark flavors, two light plus one strange quark and infinitely heavy quarks (pure gauge) (left) [23]. Character of the QGP transition for different quark masses (right) [24]. . . . .	16
Figure 2.11	Schematic QCD phase diagram (left) [19]. Time evolution of the excitation energy and net baryon density as predicted by various models in heavy-ion collisions at moderate energy (right) [25]. The model curves, to be followed in clockwise sense, cross a region of coexisting hadronic and quarkonic phase (enclosed by dashed lines). . . . .	17
Figure 2.12	Left panel: Observed ratio of $\gamma/\pi^0$ (points) and expected values from background sources (curve). Right panel: Azimuthal angle difference ( $\Delta\Phi$ ) between single photons (stars) or neutral pions (points), with $p_T > 4.5 \text{ GeV}$ , and tracks from charged particles with $p_T > 1.0 \text{ GeV}$ , corrected for meson-induced background [33]. . . . .	19
Figure 2.13	Measurement of a photon fragmentation function (dots), theoretical predictions (lines). Figure adapted from [35]. . . . .	20
Figure 2.14	Illustration of various quark-to-hadron fragmentation functions [39]. . . . .	21

Figure 2.15	Radiative and collisional parton energy loss in a QGP [44] (left). Nuclear modification factor measured for pions, eta meson and charged kaons in Pb-Pb collisions at $\sqrt{s_{NN}} = 2.76$ TeV (right) [45]. . . . .	22
Figure 2.16	Control measurements for the QGP hypothesis: Neutral pions measured in p-Pb collisions at $\sqrt{s_{NN}} = 5.02$ TeV (left) [47]. The nuclear modification factor in Pb-Pb collisions measured for isolated photons at $\sqrt{s_{NN}} = 2.76$ TeV (right) [48]. . . . .	23
Figure 2.17	Ratio of inclusive photons over decay photons, measured in Pb-Pb collisions at $\sqrt{s_{NN}} = 2.76$ TeV, for three different collision centralities (0% = most central) [51]. NLO predictions for direct photons from hard parton scattering are given (taking into account the number of binary collisions in a Pb-Pb collisions. . . . .	24
Figure 3.1	A nucleon is understood as a dynamic object, where gluons are constantly emitted and absorbed or quark-antiquark pairs are created or annihilated. After a parton density has been measured at some hard scattering scale $Q^2$ (resolution scale so to speak), the DGLAP equations are used to describe the resolved fluctuations at some other scale [61]. . . . .	29
Figure 3.2	Parton distribution function at two different scales $Q^2$ [62]. . . . .	29
Figure 3.3	Schematic evolution of parton densities for decreasing $x$ and increasing $Q^2$ . The saturation regime is assumed at low parton momenta $x$ and low resolution power $Q^2$ [63]. . . . .	30
Figure 3.4	Illustration of nuclear effects using a recent parametrization from [66]. . . . .	31
Figure 3.5	The factorization of the hard scattering process and the parton showers applied to ingoing and outgoing partons (left). Parton shower generated by successive parton splittings (right) [61]. . . . .	33
Figure 3.6	A gluon can be radiated from one of the quarks. In case of collinear radiation, both contributions factorize (left) [61]. Contour plot of the cross section ratio ME/PS. The PS fails to describe hard, large angle gluon radiation (right) [68]. . . . .	34
Figure 3.7	Motion and breakup pattern of a system of quarks and snapshots of strings (left). Through the long range QCD potential, the space-time variables are associated to a transverse mass $m_{\perp}$ (middle). Fragmentation of $q\bar{q}$ pairs to mesons (right). [69]. . . . .	36
Figure 3.8	Relative contributions of the three dominating processes to the total particle yield for a typical LHC scenario, simulated by PYTHIA 8 (Monash 2013 tune), plotted against particle rapidity $y$ and transverse momentum $p_T$ , respectively. . . . .	38
Figure 3.9	Inclusive jet production for three PDFs at LO and extrapolations of the total pp cross section at $\sqrt{s} = 14$ TeV (left). Multiplicity of charged particles at low transverse momentum measured by ATLAS, compared with PYTHIA 8 with and without multiparton interaction (right) [58]. . . . .	39



Figure 3.10	Anti- $k_T$ jets in the plane of pseudorapidity and azimuthal angle, as measured by the tracking system of ALICE. Shown are a simulated pp event with two high- $p_T$ jets (left), a measured heavy-ion event (middle) and the simulated event embedded in the heavy-ion event (right). Note that, by virtue of the anti- $k_T$ definition, the two leading jets have not changed significantly in the heavy-ion event except for additional momentum from the huge underlying event [19]. . . . .	41
Figure 5.1	Schematic of the LHC and preaccelerators with respective beam energies per nucleon (design values) for protons and for lead ions. [87]. . . . .	51
Figure 5.2	The ALICE experiment with its several detector systems (status of 2012) [90]. The general structure is as follows: Within the L3 solenoid magnet are the central barrel detectors (ITS, TPC, TRD, TOF, EMCal, PHOS, HMPID); near the beam pipe are the forward detectors (V0, T0, PMD, FMD, ZDC); also in forward direction is a muon spectrometer (MCH, MTR) featuring a separate dipole magnet. On top of the solenoid one finds the cosmic ray detector ACORDE. . . . .	54
Figure 5.3	Schematic of the TPC [99]. . . . .	55
Figure 5.4	The EMCal supermodules installed in their support structure [100].	56
Figure 5.5	Energy resolution of the EMCal as determined from an electron test beam of known energy [102]. . . . .	57
Figure 5.6	Separation power for pion-kaon (left) and kaon-proton (right) in heavy-ion collisions, given for ITS, TPC, TOF and HMPID as a function of transverse momentum [90]. . . . .	58
Figure 5.7	Left: The correlation of signal times in both V0 arrays allows to distinguish collisions (largest spot) from background events [90]. Right: Classification of the collision centrality in Pb-Pb collisions from combined information of V0 and ZDC [104]. . . . .	59
Figure 5.8	Interaction rate measured by the T0 detector against beam separation. Right: Measured cross section of the V0 detector based trigger condition for different bunch filling schemes of the LHC.	61
Figure 6.1	Radial distribution of reconstructed photon conversion points (black) from the primary vertex up to the first half of the TPC. Also shown in red is a comparison to MC simulations based on the PHOJET event generator [110]. A contamination from Dalitz decays is found only very near the primary vertex. . . . .	63
Figure 6.2	Efficiency (including acceptance and purity) of neutral pion reconstruction for different methods. . . . .	64
Figure 6.3	Example of a merged cluster from two decay photons, illustrated with arbitrarily fine granularity. . . . .	65
Figure 6.4	Integrated radiation length in front of EMCal [100]. . . . .	65
Figure 6.5	Energy spectrum of the raw cluster yield from each trigger, normalized to the respective number of events. . . . .	68
Figure 6.6	Trigger rejection factors extracted from a fitted ratio of raw cluster yields. . . . .	69

Figure 6.7	Illustrated energy deposition of decay photons from a neutral pion decay in the calorimeter for an unresolved case (left), a resolved case (center) and with an additional energy deposition (right). The dashed lines indicate the approximate splitting done by the V2-clusterizer. . . . .	71
Figure 6.8	Cluster-track matching efficiency for clusters from neutral pions (red circles), from electrons (green rectangles), from other charged particles produced near the primary vertex (blue rectangle) and from other charged particles produced in a distance $R > 5$ cm from the primary vertex. . . . .	74
Figure 6.9	Cluster energy correction factor for three different MC productions and for two different methods CCRF (ConvCalo) and CRF (Calo) (left). The method CCRF based on the Jet-Jet MC is used for this work. Ratio of reconstructed energy $E_{\text{rec}}$ over test beam energy $E_{\text{in}}$ (right). . . . .	76
Figure 6.10	Resolution matrices of clusters that are fully merged (top left), with at least one photon converted (top right), with only one photon (bottom left) and with only one electron (bottom right). Shown is the relative transverse momentum shift from the true value of the neutral pion to the reconstructed value. . . . .	78
Figure 6.11	The acceptance factor against transverse momentum, derived from the comparison of all neutral pions and neutral pions, where one decay product points to the EMCAL (left). Reconstruction efficiency of the neutral pion for different triggers against transverse momentum (right). . . . .	79
Figure 6.12	Cluster shower shape distribution $\sigma_{\text{long}}^2$ of the neutral pion disentangled for different signal categories, shown for a low transverse momentum clusters (left) and for high transverse momentum clusters (right). . . . .	80
Figure 6.13	Same figure as before, but for all selected clusters and with a breakdown for background contributions. . . . .	81
Figure 6.14	The relative contamination of the selected cluster sample from various background sources against transverse momentum. The contributions of muons and and the sum of particles not accounted for (rest) is below $4 \cdot 10^{-4}$ . . . . .	81
Figure 6.15	Contribution of prompt photons and fragmentation photons to the direct photons yield according to PYTHIA 8 (left). Electron cross section for electrons from weak-boson production in POWHEG+PYTHIA 8 and from Jet-Jet production in PYTHIA 8 (right). . . . .	82
Figure 6.16	Measurement of the $\eta/\pi^0$ ratio compared to NLO predictions and PYTHIA 8 [42]. . . . .	83
Figure 6.17	Signal purity against transverse momentum for the uncorrected case, as extracted from the MC events, and for the corrected case. The effect of each of the three corrections alone is also given. . . . .	84

Figure 6.18	Secondary neutral pion fraction (left) from the decay of $K_S^0$ , $\Lambda$ and $K_L^0$ as well secondary neutral pions from material interaction (left). Reconstruction efficiency of secondary neutral pions from $K_S^0$ and from material interaction with a comparison to the primary neutral pion efficiency. . . . .	84
Figure 6.19	The change in corrected neutral pion yield by variation of the cluster energy correction method, here illustrated for the EGA trigger. Statistical uncertainties are given for the invariant yield in the upper panel and for the lower panel. . . . .	86
Figure 6.20	Toy model results to estimate the influence of different components in the signal definition and their respective resolutions. Top left: Smearing raw yield from different components weighted with their respective fraction and the summed raw yield in black. Top right: Smearing spectra compared to the original. Bottom left: Reconstructed spectra from the three fraction variations of the different components compared to the once obtained from the full MC. Bottom right: Resulting uncertainty given by momentum resolution associated with each cluster category combined with the yield modification through the fraction variation. . . . .	89
Figure 6.21	Total systematic uncertainty (small black dots) for the EMC7 trigger as computed from the quadratic sum of the various contributions of uncertainty, which are shown in different styles and colors. . . . .	90
Figure 6.22	Same figure as before, but for the EGA trigger. . . . .	91
Figure 6.23	Differential invariant neutral pion yields in pp collisions at $\sqrt{s} = 8$ TeV measured with the two trigger sets, EMC7 (blue) and EGA (green). Also shown are the combined yield (open circles) and the TCM fit (dashed lines). Statistical uncertainties are shown as lines, systematic uncertainties as boxes. . . . .	92
Figure 6.24	Ratio of the measured neutral pion spectra to the TCM fit. Shown are the results from the two trigger sets EMC7 (blue) and EGA (green). Statistical uncertainties are shown as lines, systematic uncertainties as boxes. . . . .	93
Figure 6.25	The collected measurements of the neutral pion invariant cross in pp collisions at $\sqrt{s} = 8$ TeV with the invariant mass analyses from [42] and the merged cluster analysis from this work. . . .	94
Figure 6.26	The collection of neutral pion measurements in pp collisions at $\sqrt{s} = 8$ TeV compared to a common TCM fit. Statistical uncertainties are shown as lines, systematic uncertainties as boxes. . . .	94
Figure 7.1	Transverse momentum spectra of isolated photons in pp collisions at $\sqrt{s} = 13$ TeV in four rapidity bins. Data points from ATLAS [85] are compared to predictions at LO (PYTHIA 8, left), NLO (JETPHOX, right) and NLO+PS (POWHEG+PYTHIA 8, centre) . . . . .	96

Figure 7.2	Theory predictions normalized to data in the four rapidity bins. Data points are shown with total experimental uncertainties (without luminosity uncertainty), theory uncertainties are from scale variation. . . . .	96
Figure 7.3	Distribution of the azimuthal angle between photons and jets in pp (open circles) and p-Pb (full circles) at $\sqrt{s} = 2.76$ TeV and $\sqrt{s_{NN}} = 5.02$ TeV, respectively. Four intervals of transverse momentum are presented, each figure with a lower panel that shows the theory predictions normalized to the respective data from CMS. . . . .	98
Figure 7.4	Transverse momentum ratio of jets over photons in pp collisions (open circles) and p-Pb collisions (full circles) at $\sqrt{s} = 2.76$ TeV and $\sqrt{s_{NN}} = 5.02$ TeV, respectively. Four intervals of transverse momentum are given, each figure with a lower panel that shows the theory predictions normalized to the respective data from CMS. . . . .	99
Figure 7.5	The average jet-over-photon momentum ratio as a function of photon transverse momentum in pp collisions (open circles) and p-Pb collisions (full circles) at $\sqrt{s} = 2.76$ TeV and $\sqrt{s_{NN}} = 5.02$ TeV, respectively. The lower panel shows the ratio of theory over data. . . . .	100
Figure 7.6	Fraction of photons associated to a jet for the given kinematic cuts as a function of photon transverse momentum in pp collisions (open circles) and p-Pb collisions (full circles) at $\sqrt{s} = 2.76$ TeV and $\sqrt{s_{NN}} = 5.02$ TeV, respectively. The lower panel shows the ratio of theory over data. . . . .	101
Figure 7.7	Ratio of inclusive over decay photon production in pp collisions at $\sqrt{s} = 13$ TeV. LO predictions with PYTHIA 8 (green) are compared with those at NLO with JETPHOX (blue) and NLO+PS with POWHEG+PYTHIA 8 (red, full circles). The latter are also shown at $\sqrt{s} = 2.76$ TeV (red, open circles). . . . .	102
Figure 7.8	Measurement of the direct photon excess ratio in pp collisions at $\sqrt{s} = 2.76$ TeV and $\sqrt{s} = 8$ TeV with different theory descriptions at NLO [122]. . . . .	103
Figure 7.9	Transverse momentum spectrum for photon production in pp collisions at $\sqrt{s} = 7$ TeV for different values of the PS cutoff scale. . . . .	104
Figure 7.10	POWHEG+PYTHIA 8 prediction of observed parton momentum fraction $x_{pb}^{obs}$ reconstructed from photon-jet pairs with kinematic cuts for the central barrel detector system from ALICE. Two different collision systems are provided, $\sqrt{s} = 2.76$ TeV (pp), illustrating the scale uncertainty, and $\sqrt{s_{NN}} = 5.02$ TeV (p-Pb), showing nuclear PDF variations with nuclear PDF uncertainties. . . . .	106

Figure 7.11	POWHEG+PYTHIA 8 prediction of observed parton momentum fraction $x_{\text{pb}}^{\text{obs}}$ reconstructed from photon-jet pairs with kinematic cuts including forward-rapidity detectors from <a href="#">ATLAS</a> or <a href="#">CMS</a> . Two different collision systems are provided, $\sqrt{s} = 2.76$ TeV (pp), illustrating the scale uncertainty, and $\sqrt{s_{\text{NN}}} = 5.02$ TeV (p-Pb), showing nuclear PDF variations with nuclear PDF uncertainties. . . . .	107
Figure 7.12	POWHEG+PYTHIA 8 prediction of observed parton momentum fraction $x_{\text{pb}}^{\text{obs}}$ reconstructed from photon-jet pairs with kinematic cuts for mid-rapidity detectors from <a href="#">ATLAS</a> or <a href="#">CMS</a> . Two different collision systems are provided, $\sqrt{s} = 2.76$ TeV (pp), illustrating the scale uncertainty, and $\sqrt{s_{\text{NN}}} = 5.02$ TeV (p-Pb), showing nuclear PDF variations with nuclear PDF uncertainties. . . . .	108
Figure 7.13	POWHEG+PYTHIA 8 prediction of observed parton momentum fraction $x_{\text{pb}}^{\text{obs}}$ reconstructed from photon-jet pairs with kinematic cuts for the forward detector from <a href="#">LHCb</a> (Pb-going direction). Two different collision systems are provided, $\sqrt{s} = 2.76$ TeV (pp), illustrating the scale uncertainty, and $\sqrt{s_{\text{NN}}} = 5.02$ TeV (p-Pb), showing nuclear PDF variations with nuclear PDF uncertainties. . . . .	109
Figure 7.14	POWHEG+PYTHIA 8 prediction of observed parton momentum fraction $x_{\text{pb}}^{\text{obs}}$ reconstructed from photon-jet pairs with kinematic cuts for the forward detector from <a href="#">LHCb</a> (p-going direction). Two different collision systems are provided, $\sqrt{s} = 2.76$ TeV (pp), illustrating the scale uncertainty, and $\sqrt{s_{\text{NN}}} = 5.02$ TeV (p-Pb), showing nuclear PDF variations with nuclear PDF uncertainties. . . . .	110
Figure B.1	Left panel: comparison of the nuclear modification fit with (nCTEQ15) and without the inclusion of pion data (nCTEQ15_np) for $Q = 10$ GeV. Right panel: the actual nPDF for $Q = 10$ GeV [ <a href="#">129</a> ].	124
Figure B.2	Calculated nuclear modification $R_{\text{dAu}}$ on the basis of pion data and two different fragmentation functions BKK (blue) and KKP (violet) [ <a href="#">129</a> ]. . . . .	124

## LIST OF TABLES

---

Table 2.1	Examples for rapidity and pseudorapidity. . . . .	11
Table 5.1	Comparison of <a href="#">LHC</a> running conditions for selected periods and the design goals for proton-proton collisions. Note that the integrated luminosity is given per nucleon-nucleon collision [ <a href="#">92</a> ] [ <a href="#">93</a> ]. . . . .	52



## ACRONYMS

---

ACORDE	ALICE Cosmic Ray Detector
ALICE	A Large Ion Collider Experiment
ATLAS	A Toroidal LHC Apparatus
BFKL	Balitsky-Fadin-Kuraev-Lipatov
CBM	Compressed Baryonic Matter Experiment
CCMF	Conv-Calo Mass Fit
CCRF	Conv-Calo Ratio Fit
CERN	European Organization for Nuclear Research
CGC	Color Glass Condensate
cm	center-of-mass
CMF	Calo Mass Fit
CMS	Compact Muon Solenoid experiment
CP	Charge Parity
CRF	Calo Ratio Fit
DESY	Deutsche Elektronen-Synchrotron
DGLAP	Dokshitzer-Gribov-Lipatov-Altarelli-Parisi
DIS	Deep Inelastic Scattering
ECAL	Electromagnetic Calorimeter
EMCal	Electromagnetic Calorimeter
FAIR	Facility for Antiproton and Ion Research
FO	Fixed-Order
FMD	Forward Multiplicity Detector
FSR	Final-State Radiation
HCAL	Hadronic Calorimeter
HERA	Hadron-Electron-Ring-Anlage
HEP	High-Energy Physics
HF	Heavy Flavor

HMPID	High Momentum Particle Identification Detector
HLT	High Level Trigger
IR	Infrared
ISR	Initial-State Radiation
ITS	Inner Tracking System
KLN	Kinoshita-Lee-Nauenberg
LEP	Large Electron-Positron Collider
LHC	Large Hadron Collider
LHCb	LHC beauty experiment
LO	Leading Order
LQCD	Lattice QCD
MB	Minimum Bias
ME	Matrix Element
MC	Monte Carlo
MCH	Muon Tracking System
mEMC	merged EMCal method
MIP	Minimum Ionizing Particle
MPI	Multiparton Interaction
MTR	Muon Trigger System
MWPC	Multi-Wire Proportional Chamber
NLO	Next-to-Leading Order
NNLO	Next-to-Next-to Leading Order
nPDF	nuclear Parton Density Function
pp	proton-proton collisions
p-Pb	proton-lead collisions
Pb-Pb	lead-lead collisions
PCM	Photon Conversion Method
PCM-EMCal	PCM-EMCal Method
PDF	Parton Distribution Function
PHOS	Photon Spectrometer



PID	particle identification
PMD	Photon Multiplicity Detector
PS	Parton Shower
pQCD	perturbative QCD
QA	quality assurance
QCD	Quantum Chromodynamics
QED	Quantum Electrodynamics
QFT	Quantum Field Theory
QGP	Quark-Gluon Plasma
RCT	Run Condition Table
RHIC	Relativistic Heavy Ion Collider
SDD	Silicon Drift Detector
SM	Standard Model
SPD	Silicon Pixel Detector
SPS	Super Proton Synchrotron
SSD	Silicon Strip Detector
T0	Timing and Trigger detector at ALICE
TCM	Two-Component Model
TOF	Time-Of-Flight detector
TOTEM	TOTEM
TPC	Time Projection Chamber
TRD	Transition Radiation Detector
TRU	Trigger Region Unit
UV	Ultraviolet
vdM	van der Meer
V0	V0 detector
ZDC	Zero Degree Calorimeter



## BIBLIOGRAPHY

---

- [1] Murray Gell-Mann. "A Schematic Model of Baryons and Mesons." In: *Phys. Lett.* 8 (1964), pp. 214–215. DOI: [10.1016/S0031-9163\(64\)92001-3](https://doi.org/10.1016/S0031-9163(64)92001-3).
- [2] G. Zweig. "An SU(3) model for strong interaction symmetry and its breaking. Version 2." In: *Developments in the Quark Theory of Hadrons. VOL. 1. 1964 - 1978*. Ed. by D.B. Lichtenberg and Simon Peter Rosen. 1964, pp. 22–101.
- [3] Bogdan Povh, Klaus Rith, Christoph Scholz, and Frank Zetsche. *Teilchen und Kerne. Eine Einfuehrung in die physikalischen Konzepte: Bogdan Povh, Klaus Rith, Christoph Scholz, Frank Zetsche*. Sixth. Springer-Verlag GmbH, 2004.
- [4] Donald Hill Perkins. *Introduction to high energy physics; 4th ed.* Cambridge: Cambridge Univ. Press, 2000. URL: <https://cds.cern.ch/record/396126>.
- [5] H. David Politzer. "Reliable Perturbative Results for Strong Interactions?" In: *Phys. Rev. Lett.* 30 (1973). [274(1973)], pp. 1346–1349. DOI: [10.1103/PhysRevLett.30.1346](https://doi.org/10.1103/PhysRevLett.30.1346).
- [6] David J. Gross and Frank Wilczek. "Ultraviolet Behavior of Nonabelian Gauge Theories." In: *Phys. Rev. Lett.* 30 (1973). [271(1973)], pp. 1343–1346. DOI: [10.1103/PhysRevLett.30.1343](https://doi.org/10.1103/PhysRevLett.30.1343).
- [7] J. I. Friedman and H. W. Kendall. "Deep Inelastic Electron Scattering." In: *Annual Review of Nuclear Science* 22.1 (1972), pp. 203–254. DOI: [10.1146/annurev.ns.22.120172.001223](https://doi.org/10.1146/annurev.ns.22.120172.001223).
- [8] A. Pickering. *Constructing Quark. A Sociological History of Particle Physics*. 1984. ISBN: 9780852244586.
- [9] D. P. Barber et al. "Discovery of Three Jet Events and a Test of Quantum Chromodynamics at PETRA Energies." In: *Phys. Rev. Lett.* 43 (1979), p. 830. DOI: [10.1103/PhysRevLett.43.830](https://doi.org/10.1103/PhysRevLett.43.830).
- [10] C. Patrignani et al. "Review of particle physics." English (US). In: *Chinese Physics C* 40.10 (Oct. 2016). ISSN: 1674-1137. DOI: [10.1088/1674-1137/40/10/100001](https://doi.org/10.1088/1674-1137/40/10/100001).
- [11] K. Hikasa et al. "Review of particle properties. Particle Data Group." In: *Phys. Rev.* D45 (1992). [Erratum: *Phys. Rev.*D46,5210(1992)], S1. DOI: [10.1103/PhysRevD.46.5210](https://doi.org/10.1103/PhysRevD.46.5210), [10.1103/PhysRevD.45.S1](https://doi.org/10.1103/PhysRevD.45.S1).
- [12] Ramona Vogt. *Ultrarelativistic heavy-ion collisions*. Elsevier, 2007.
- [13] D. J. Bird et Al. "Detection of a Cosmic Ray with Measured Energy Well Beyond the Expected Spectral Cutoff due to Cosmic Microwave Radiation." In: (Oct. 1994). DOI: [10.1086/175344](https://doi.org/10.1086/175344). arXiv: [9410067](https://arxiv.org/abs/9410067) [astro-ph]. URL: <http://arxiv.org/abs/astro-ph/9410067><http://dx.doi.org/10.1086/175344>.
- [14] Richard D. Ball et al. "Parton distributions from high-precision collider data." In: *Eur. Phys. J.* C77.10 (2017), p. 663. DOI: [10.1140/epjc/s10052-017-5199-5](https://doi.org/10.1140/epjc/s10052-017-5199-5). arXiv: [1706.00428](https://arxiv.org/abs/1706.00428) [hep-ph].
- [15] Frank Hinterberger. *Physik der Teilchenbeschleuniger und Ionenoptik*. 2nd ed. Berlin Heidelberg: Springer-Verlag, 2008. ISBN: 3-540-75281-3.

- [16] K. Yagi, T. Hatsuda, and Y. Miake. “Quark-gluon plasma: From big bang to little bang.” In: *Camb. Monogr. Part. Phys. Nucl. Phys. Cosmol.* 23 (2005), pp. 1–446.
- [17] Rolf Hagedorn. “Statistical thermodynamics of strong interactions at high energies.” In: *Nuovo Cimento, Suppl.* 3.CERN-TH-520 (1965), pp. 147–186. URL: <http://cds.cern.ch/record/346206>.
- [18] A. Bazavov et al. “Chiral crossover in QCD at zero and non-zero chemical potentials.” In: (2018). arXiv: [1812.08235 \[hep-lat\]](https://arxiv.org/abs/1812.08235).
- [19] C. Klein-Boesing. *Study of the Quark-Gluon Plasma with Hard and Electromagnetic Probes*. <http://qgp.uni-muenster.de/thesisdb/habil-klei-13.pdf>. 2013.
- [20] A. Chodos, R. L. Jaffe, K. Johnson, Charles B. Thorn, and V. F. Weisskopf. “A New Extended Model of Hadrons.” In: *Phys. Rev. D* 9 (1974), pp. 3471–3495. DOI: [10.1103/PhysRevD.9.3471](https://doi.org/10.1103/PhysRevD.9.3471).
- [21] Thomas A. DeGrand, R. L. Jaffe, K. Johnson, and J. E. Kiskis. “Masses and Other Parameters of the Light Hadrons.” In: *Phys. Rev. D* 12 (1975), p. 2060. DOI: [10.1103/PhysRevD.12.2060](https://doi.org/10.1103/PhysRevD.12.2060).
- [22] Y. Aoki, G. Endrodi, Z. Fodor, S. D. Katz, and K. K. Szabo. “The Order of the quantum chromodynamics transition predicted by the standard model of particle physics.” In: *Nature* 443 (2006), pp. 675–678. DOI: [10.1038/nature05120](https://doi.org/10.1038/nature05120). arXiv: [hep-lat/0611014 \[hep-lat\]](https://arxiv.org/abs/hep-lat/0611014).
- [23] Frithjof Karsch. “Lattice QCD at high temperature and the QGP.” In: *AIP Conf. Proc.* 842.1 (2006), pp. 20–28. DOI: [10.1063/1.2220177](https://doi.org/10.1063/1.2220177). arXiv: [hep-lat/0601013 \[hep-lat\]](https://arxiv.org/abs/hep-lat/0601013).
- [24] Kazuyuki Kanaya. “Lattice results on the phase structure and equation of state in QCD at finite temperature.” In: *AIP Conf. Proc.* 1343 (2011), pp. 57–62. DOI: [10.1063/1.3574942](https://doi.org/10.1063/1.3574942). arXiv: [1012.4235 \[hep-ph\]](https://arxiv.org/abs/1012.4235).
- [25] T. Ablyazimov et al. “Challenges in QCD matter physics –The scientific programme of the Compressed Baryonic Matter experiment at FAIR.” In: *Eur. Phys. J. A* 53.3 (2017), p. 60. DOI: [10.1140/epja/i2017-12248-y](https://doi.org/10.1140/epja/i2017-12248-y). arXiv: [1607.01487 \[nucl-ex\]](https://arxiv.org/abs/1607.01487).
- [26] F. Weber, R. Negreiros, P. Rosenfield, and M. Stejner. “Pulsars as Astrophysical Laboratories for Nuclear and Particle Physics.” In: (Dec. 2006). DOI: [10.1016/j.pnnp.2006.12.008](https://doi.org/10.1016/j.pnnp.2006.12.008). arXiv: [0612054 \[astro-ph\]](https://arxiv.org/abs/0612054). URL: <http://arxiv.org/abs/astro-ph/0612054><http://dx.doi.org/10.1016/j.pnnp.2006.12.008>.
- [27] Krishna Rajagopal and Frank Wilczek. “The Condensed Matter Physics of QCD.” In: (2000). ISSN: 978-981-02-4445-3. DOI: [10.1142/9789812810458\\_0043](https://doi.org/10.1142/9789812810458_0043). arXiv: [0011333 \[hep-ph\]](https://arxiv.org/abs/0011333). URL: <http://arxiv.org/abs/hep-ph/0011333>[http://dx.doi.org/10.1142/9789812810458{\\\_}0043](http://dx.doi.org/10.1142/9789812810458_{\_}0043).
- [28] J Adam et al. “Enhanced production of multi-strange hadrons in high-multiplicity proton–proton collisions.” In: *Nature Physics* (Apr. 2017). DOI: [10.1038/nphys4111](https://doi.org/10.1038/nphys4111).
- [29] K. Aamodt et al. “Two-pion Bose-Einstein correlations in central Pb-Pb collisions at  $\sqrt{s_{NN}} = 2.76$  TeV.” In: *Phys. Lett. B* 696 (2011), pp. 328–337. DOI: [10.1016/j.physletb.2010.12.053](https://doi.org/10.1016/j.physletb.2010.12.053). arXiv: [1012.4035 \[nucl-ex\]](https://arxiv.org/abs/1012.4035).

- [30] K Aamodt et al. “Elliptic flow of charged particles in Pb-Pb collisions at 2.76 TeV.” In: *Phys. Rev. Lett.* 105 (2010), p. 252302. DOI: [10.1103/PhysRevLett.105.252302](https://doi.org/10.1103/PhysRevLett.105.252302). arXiv: [1011.3914](https://arxiv.org/abs/1011.3914) [nucl-ex].
- [31] Chun Shen, Ulrich Heinz, Pasi Huovinen, and Huichao Song. “Radial and elliptic flow in Pb+Pb collisions at the Large Hadron Collider from viscous hydrodynamic.” In: *Phys. Rev.* C84 (2011), p. 044903. DOI: [10.1103/PhysRevC.84.044903](https://doi.org/10.1103/PhysRevC.84.044903). arXiv: [1105.3226](https://arxiv.org/abs/1105.3226) [nucl-th].
- [32] Anton Andronic. “Experimental results and phenomenology of quarkonium production in relativistic nuclear collisions.” In: *Nucl. Phys.* A931 (2014), pp. 135–144. DOI: [10.1016/j.nuclphysa.2014.10.009](https://doi.org/10.1016/j.nuclphysa.2014.10.009). arXiv: [1409.5778](https://arxiv.org/abs/1409.5778) [nucl-ex].
- [33] T. Ferbel and W. R. Molzon. “Direct-photon production in high-energy collisions.” In: *Rev. Mod. Phys.* 56 (2 Apr. 1984), pp. 181–221. DOI: [10.1103/RevModPhys.56.181](https://doi.org/10.1103/RevModPhys.56.181).
- [34] L. Bourhis, M. Fontannaz, and J. P. Guillet. “Quarks and gluon fragmentation functions into photons.” In: *Eur. Phys. J.* C2 (1998), pp. 529–537. DOI: [10.1007/s100520050158](https://doi.org/10.1007/s100520050158). arXiv: [hep-ph/9704447](https://arxiv.org/abs/hep-ph/9704447) [hep-ph].
- [35] Damir Buskulic et al. “First measurement of the quark-to-photon fragmentation function.” In: *Z. Phys. C* 69.CERN-PPE-95-89. FSU-SCRI-96-14 (June 1995), 365–377. 29 p. URL: <http://cds.cern.ch/record/285017>.
- [36] Michael Klasen and F. König. “New information on photon fragmentation functions.” In: *Eur. Phys. J.* C74.8 (2014), p. 3009. DOI: [10.1140/epjc/s10052-014-3009-x](https://doi.org/10.1140/epjc/s10052-014-3009-x). arXiv: [1403.2290](https://arxiv.org/abs/1403.2290) [hep-ph].
- [37] *Measurement of charged particle spectra in pp collisions and nuclear modification factor  $R_{pPb}$  at  $\sqrt{s_{NN}} = 5.02$  TeV with the ATLAS detector at the LHC.* Tech. rep. ATLAS-CONF-2016-108. Geneva: CERN, Sept. 2016. URL: <https://cds.cern.ch/record/2220376>.
- [38] Morad Aaboud et al. “Measurement of the nuclear modification factor for inclusive jets in Pb+Pb collisions at  $\sqrt{s_{NN}} = 5.02$  TeV with the ATLAS detector.” In: *Phys. Lett.* B790 (2019), pp. 108–128. DOI: [10.1016/j.physletb.2018.10.076](https://doi.org/10.1016/j.physletb.2018.10.076). arXiv: [1805.05635](https://arxiv.org/abs/1805.05635) [nucl-ex].
- [39] Hrayr H. Matevosyan, Anthony W. Thomas, and Wolfgang Bentz. “Monte Carlo Simulations of Hadronic Fragmentation Functions using NJL-Jet Model.” In: *Phys. Rev.* D83 (2011). [Erratum: *Phys. Rev.* D86,059904(2012)], p. 114010. DOI: [10.1103/PhysRevD.83.114010](https://doi.org/10.1103/PhysRevD.83.114010), [10.1103/PhysRevD.86.059904](https://doi.org/10.1103/PhysRevD.86.059904). arXiv: [1103.3085](https://arxiv.org/abs/1103.3085) [hep-ph].
- [40] Serguei Chatrchyan et al. “Study of the Production of Charged Pions, Kaons, and Protons in pPb Collisions at  $\sqrt{s_{NN}} = 5.02$  TeV.” In: *Eur. Phys. J.* C74.6 (2014), p. 2847. DOI: [10.1140/epjc/s10052-014-2847-x](https://doi.org/10.1140/epjc/s10052-014-2847-x). arXiv: [1307.3442](https://arxiv.org/abs/1307.3442) [hep-ex].
- [41] Betty Bezverkhny Abelev et al. “Production of charged pions, kaons and protons at large transverse momenta in pp and Pb–Pb collisions at  $\sqrt{s_{NN}} = 2.76$  TeV.” In: *Phys. Lett.* B736 (2014), pp. 196–207. DOI: [10.1016/j.physletb.2014.07.011](https://doi.org/10.1016/j.physletb.2014.07.011). arXiv: [1401.1250](https://arxiv.org/abs/1401.1250) [nucl-ex].

- [42] Shreyasi Acharya et al. “ $\pi^0$  and  $\eta$  meson production in proton-proton collisions at  $\sqrt{s} = 8$  TeV.” In: *Eur. Phys. J. C* 78.3 (2018), p. 263. DOI: [10.1140/epjc/s10052-018-5612-8](https://doi.org/10.1140/epjc/s10052-018-5612-8). arXiv: [1708.08745](https://arxiv.org/abs/1708.08745) [hep-ex].
- [43] Shreyasi Acharya et al. “Production of  $\pi^0$  and  $\eta$  mesons up to high transverse momentum in pp collisions at 2.76 TeV.” In: *Eur. Phys. J. C* 77.5 (2017). [*Eur. Phys. J. C* 77, no. 9, 586 (2017)], p. 339. DOI: [10.1140/epjc/s10052-017-5144-7](https://doi.org/10.1140/epjc/s10052-017-5144-7), [10.1140/epjc/s10052-017-4890-x](https://doi.org/10.1140/epjc/s10052-017-4890-x). arXiv: [1702.00917](https://arxiv.org/abs/1702.00917) [hep-ex].
- [44] Sourav Sarkar, Helmut Satz, and Bikash Sinha. “The physics of the quark-gluon plasma.” In: *Lect. Notes Phys.* 785 (2010), pp. 1–369. DOI: [10.1007/978-3-642-02286-9](https://doi.org/10.1007/978-3-642-02286-9).
- [45] Shreyasi Acharya et al. “Neutral pion and  $\eta$  meson production at mid-rapidity in Pb-Pb collisions at  $\sqrt{s_{NN}} = 2.76$  TeV.” In: *Phys. Rev. C* 98.4 (2018), p. 044901. DOI: [10.1103/PhysRevC.98.044901](https://doi.org/10.1103/PhysRevC.98.044901). arXiv: [1803.05490](https://arxiv.org/abs/1803.05490) [nucl-ex].
- [46] K. Adcox et al. “Formation of dense partonic matter in relativistic nucleus-nucleus collisions at RHIC: Experimental evaluation by the PHENIX collaboration.” In: *Nucl. Phys. A* 757 (2005), pp. 184–283. DOI: [10.1016/j.nuclphysa.2005.03.086](https://doi.org/10.1016/j.nuclphysa.2005.03.086). arXiv: [nucl-ex/0410003](https://arxiv.org/abs/nucl-ex/0410003) [nucl-ex].
- [47] Shreyasi Acharya et al. “Neutral pion and  $\eta$  meson production in p-Pb collisions at  $\sqrt{s_{NN}} = 5.02$  TeV.” In: *Eur. Phys. J. C* 78.8 (2018), p. 624. DOI: [10.1140/epjc/s10052-018-6013-8](https://doi.org/10.1140/epjc/s10052-018-6013-8). arXiv: [1801.07051](https://arxiv.org/abs/1801.07051) [nucl-ex].
- [48] Serguei Chatrchyan et al. “Measurement of isolated photon production in pp and PbPb collisions at  $\sqrt{s_{NN}} = 2.76$  TeV.” In: *Phys. Lett. B* 710 (2012), pp. 256–277. DOI: [10.1016/j.physletb.2012.02.077](https://doi.org/10.1016/j.physletb.2012.02.077). arXiv: [1201.3093](https://arxiv.org/abs/1201.3093) [nucl-ex].
- [49] T. Peitzmann. “Direct photon production in high-energy nuclear collisions.” In: *AIP Conf. Proc.* 1701 (2016), p. 060016. DOI: [10.1063/1.4938679](https://doi.org/10.1063/1.4938679).
- [50] Ivan Vitev and Ben-Wei Zhang. “A Systematic study of direct photon production in heavy ion collisions.” In: *Phys. Lett. B* 669 (2008), pp. 337–344. DOI: [10.1016/j.physletb.2008.10.019](https://doi.org/10.1016/j.physletb.2008.10.019). arXiv: [0804.3805](https://arxiv.org/abs/0804.3805) [hep-ph].
- [51] Jaroslav Adam et al. “Direct photon production in Pb-Pb collisions at  $\sqrt{s_{NN}} = 2.76$  TeV.” In: *Phys. Lett. B* 754 (2016), pp. 235–248. DOI: [10.1016/j.physletb.2016.01.020](https://doi.org/10.1016/j.physletb.2016.01.020). arXiv: [1509.07324](https://arxiv.org/abs/1509.07324) [nucl-ex].
- [52] M. Klasen, C. Klein-Bösing, F. König, and J. P. Wessels. “How robust is a thermal photon interpretation of the ALICE low- $p_T$  data?” In: *JHEP* 10 (2013), p. 119. DOI: [10.1007/JHEP10\(2013\)119](https://doi.org/10.1007/JHEP10(2013)119). arXiv: [1307.7034](https://arxiv.org/abs/1307.7034) [hep-ph].
- [53] Ahmed Ali, Jens Sören Lange, and Sheldon Stone. “Exotics: Heavy Pentaquarks and Tetraquarks.” In: *Prog. Part. Nucl. Phys.* 97 (2017), pp. 123–198. DOI: [10.1016/j.pnpnp.2017.08.003](https://doi.org/10.1016/j.pnpnp.2017.08.003). arXiv: [1706.00610](https://arxiv.org/abs/1706.00610) [hep-ph].
- [54] R. Keith Ellis, W. James Stirling, and B. R. Webber. “QCD and collider physics.” In: *Camb. Monogr. Part. Phys. Nucl. Phys. Cosmol.* 8 (1996), pp. 1–435.
- [55] M. Diehl. “Generalized parton distributions.” In: *Phys. Rept.* 388 (2003), pp. 41–277. DOI: [10.1016/j.physrep.2003.08.002](https://doi.org/10.1016/j.physrep.2003.08.002), [10.3204/DESY-THESIS-2003-018](https://doi.org/10.3204/DESY-THESIS-2003-018). arXiv: [hep-ph/0307382](https://arxiv.org/abs/hep-ph/0307382) [hep-ph].

- [56] Michael L. Miller, Klaus Reygiers, Stephen J. Sanders, and Peter Steinberg. “Glauber modeling in high energy nuclear collisions.” In: *Ann. Rev. Nucl. Part. Sci.* 57 (2007), pp. 205–243. DOI: [10.1146/annurev.nucl.57.090506.123020](https://doi.org/10.1146/annurev.nucl.57.090506.123020). arXiv: [nucl-ex/0701025](https://arxiv.org/abs/nucl-ex/0701025) [nucl-ex].
- [57] Charles Gale. “Direct photon production in relativistic heavy-ion collisions - a theory update.” In: *12th International Workshop on High-pT Physics in the RHIC/LHC Era (HPT 2017) Bergen, Norway, October 2-5, 2017*. 2018. arXiv: [1802.00128](https://arxiv.org/abs/1802.00128) [hep-ph].
- [58] Andy Buckley et al. “General-purpose event generators for LHC physics.” In: *Phys. Rept.* 504 (2011), pp. 145–233. DOI: [10.1016/j.physrep.2011.03.005](https://doi.org/10.1016/j.physrep.2011.03.005). arXiv: [1101.2599](https://arxiv.org/abs/1101.2599) [hep-ph].
- [59] Peter Skands. “Introduction to QCD.” In: *Proceedings, 2nd Asia-Europe-Pacific School of High-Energy Physics (AEPSHEP 2014): Puri, India, November 04–17, 2014*. [63(2017)]. 2013, pp. 341–420. DOI: [10.1142/9789814525220\\_0008](https://doi.org/10.1142/9789814525220_0008), [10.23730/CYRSP-2017-002.63](https://doi.org/10.23730/CYRSP-2017-002.63). arXiv: [1207.2389](https://arxiv.org/abs/1207.2389) [hep-ph].
- [60] John C. Collins, Davison E. Soper, and George F. Sterman. “Factorization of Hard Processes in QCD.” In: *Adv. Ser. Direct. High Energy Phys.* 5 (1989), pp. 1–91. DOI: [10.1142/9789814503266\\_0001](https://doi.org/10.1142/9789814503266_0001). arXiv: [hep-ph/0409313](https://arxiv.org/abs/hep-ph/0409313) [hep-ph].
- [61] Torbjorn Sjostrand. “Monte Carlo Generators.” In: *High-energy physics. Proceedings, European School, Aronsborg, Sweden, June 18-July 1, 2006*. 2006, pp. 51–74. arXiv: [hep-ph/0611247](https://arxiv.org/abs/hep-ph/0611247) [hep-ph]. URL: <http://weplib.cern.ch/abstract?CERN-LCGAPP-2006-06>.
- [62] F. D. Aaron et al. “A Precision Measurement of the Inclusive ep Scattering Cross Section at HERA.” In: *Eur. Phys. J. C* 64 (2009), pp. 561–587. DOI: [10.1140/epjc/s10052-009-1169-x](https://doi.org/10.1140/epjc/s10052-009-1169-x). arXiv: [0904.3513](https://arxiv.org/abs/0904.3513) [hep-ex].
- [63] Francois Gelis, Edmond Iancu, Jamal Jalilian-Marian, and Raju Venugopalan. “The Color Glass Condensate.” In: *Ann. Rev. Nucl. Part. Sci.* 60 (2010), pp. 463–489. DOI: [10.1146/annurev.nucl.010909.083629](https://doi.org/10.1146/annurev.nucl.010909.083629). arXiv: [1002.0333](https://arxiv.org/abs/1002.0333) [hep-ph].
- [64] Nestor Armesto. “Nuclear shadowing.” In: *J. Phys.* G32 (2006), R367–R394. DOI: [10.1088/0954-3899/32/11/R01](https://doi.org/10.1088/0954-3899/32/11/R01). arXiv: [hep-ph/0604108](https://arxiv.org/abs/hep-ph/0604108) [hep-ph].
- [65] J. J. Aubert et al. “The ratio of the nucleon structure functions  $F_{2n}$  for iron and deuterium.” In: *Phys. Lett.* 123B (1983), pp. 275–278. DOI: [10.1016/0370-2693\(83\)90437-9](https://doi.org/10.1016/0370-2693(83)90437-9).
- [66] Kari J. Eskola, Petja Paakkinen, Hannu Paukkunen, and Carlos A. Salgado. “EPPS16: Nuclear parton distributions with LHC data.” In: *Eur. Phys. J. C* 77.3 (2017), p. 163. DOI: [10.1140/epjc/s10052-017-4725-9](https://doi.org/10.1140/epjc/s10052-017-4725-9). arXiv: [1612.05741](https://arxiv.org/abs/1612.05741) [hep-ph].
- [67] Rikkert Frederix, Stefano Frixione, Fabio Maltoni, and Tim Stelzer. “Automation of next-to-leading order computations in QCD: The FKS subtraction.” In: *JHEP* 10 (2009), p. 003. DOI: [10.1088/1126-6708/2009/10/003](https://doi.org/10.1088/1126-6708/2009/10/003). arXiv: [0908.4272](https://arxiv.org/abs/0908.4272) [hep-ph].
- [68] F. Krauss. “Matrix elements and parton showers in hadronic interactions.” In: *JHEP* 08 (2002), p. 015. DOI: [10.1088/1126-6708/2002/08/015](https://doi.org/10.1088/1126-6708/2002/08/015). arXiv: [hep-ph/0205283](https://arxiv.org/abs/hep-ph/0205283) [hep-ph].

- [69] T. Sjöstrand. “The Lund String — a string that works.” New ideas in hadronization: Intersections between QCD, AdS/CFT and the QGP. 2009.
- [70] G. Antchev et al. “First measurement of elastic, inelastic and total cross-section at  $\sqrt{s} = 13$  TeV by TOTEM and overview of cross-section data at LHC energies.” In: *Eur. Phys. J. C* 79.2 (2019), p. 103. DOI: [10.1140/epjc/s10052-019-6567-0](https://doi.org/10.1140/epjc/s10052-019-6567-0). arXiv: [1712.06153](https://arxiv.org/abs/1712.06153) [hep-ex].
- [71] Gavin P. Salam. “Towards Jetography.” In: *Eur. Phys. J. C* 67 (2010), pp. 637–686. DOI: [10.1140/epjc/s10052-010-1314-6](https://doi.org/10.1140/epjc/s10052-010-1314-6). arXiv: [0906.1833](https://arxiv.org/abs/0906.1833) [hep-ph].
- [72] Ahmed Ali and Gustav Kramer. “Jets and QCD: A Historical Review of the Discovery of the Quark and Gluon Jets and its Impact on QCD.” In: *Eur. Phys. J. H* 36 (2011), pp. 245–326. DOI: [10.1140/epjh/e2011-10047-1](https://doi.org/10.1140/epjh/e2011-10047-1). arXiv: [1012.2288](https://arxiv.org/abs/1012.2288) [hep-ph].
- [73] Matteo Cacciari, Gavin P. Salam, and Gregory Soyez. “The anti- $k_t$  jet clustering algorithm.” In: *JHEP* 04 (2008), p. 063. DOI: [10.1088/1126-6708/2008/04/063](https://doi.org/10.1088/1126-6708/2008/04/063). arXiv: [0802.1189](https://arxiv.org/abs/0802.1189) [hep-ph].
- [74] J. R. Forshaw and D. A. Ross. *Quantum Chromodynamics and the Pomeron*. Cambridge Lecture Notes in Physics. Cambridge University Press, 1997. DOI: [10.1017/CB09780511524387](https://doi.org/10.1017/CB09780511524387).
- [75] Torbjörn Sjöstrand, Stefan Ask, Jesper R. Christiansen, Richard Corke, Nishita Desai, Philip Ilten, Stephen Mrenna, Stefan Prestel, Christine O. Rasmussen, and Peter Z. Skands. “An Introduction to PYTHIA 8.2.” In: *Comput. Phys. Commun.* 191 (2015), pp. 159–177. DOI: [10.1016/j.cpc.2015.01.024](https://doi.org/10.1016/j.cpc.2015.01.024). arXiv: [1410.3012](https://arxiv.org/abs/1410.3012) [hep-ph].
- [76] Peter Skands, Stefano Carrazza, and Juan Rojo. “Tuning PYTHIA 8.1: the Monash 2013 Tune.” In: *Eur. Phys. J. C* 74.8 (2014), p. 3024. DOI: [10.1140/epjc/s10052-014-3024-y](https://doi.org/10.1140/epjc/s10052-014-3024-y). arXiv: [1404.5630](https://arxiv.org/abs/1404.5630) [hep-ph].
- [77] Stefano Frixione and Bryan R. Webber. “Matching NLO QCD computations and parton shower simulations.” In: *JHEP* 06 (2002), p. 029. DOI: [10.1088/1126-6708/2002/06/029](https://doi.org/10.1088/1126-6708/2002/06/029). arXiv: [hep-ph/0204244](https://arxiv.org/abs/hep-ph/0204244) [hep-ph].
- [78] Paolo Nason. “A New method for combining NLO QCD with shower Monte Carlo algorithms.” In: *JHEP* 11 (2004), p. 040. DOI: [10.1088/1126-6708/2004/11/040](https://doi.org/10.1088/1126-6708/2004/11/040). arXiv: [hep-ph/0409146](https://arxiv.org/abs/hep-ph/0409146) [hep-ph].
- [79] Stefano Frixione, Paolo Nason, and Carlo Oleari. “Matching NLO QCD computations with Parton Shower simulations: the POWHEG method.” In: *JHEP* 11 (2007), p. 070. DOI: [10.1088/1126-6708/2007/11/070](https://doi.org/10.1088/1126-6708/2007/11/070). arXiv: [0709.2092](https://arxiv.org/abs/0709.2092) [hep-ph].
- [80] Simone Alioli, Paolo Nason, Carlo Oleari, and Emanuele Re. “A general framework for implementing NLO calculations in shower Monte Carlo programs: the POWHEG BOX.” In: *JHEP* 06 (2010), p. 043. DOI: [10.1007/JHEP06\(2010\)043](https://doi.org/10.1007/JHEP06(2010)043). arXiv: [1002.2581](https://arxiv.org/abs/1002.2581) [hep-ph].
- [81] *Homepage of the POWHEG BOX*. <http://powhegbox.mib.infn.it/>. Accessed: 2019-04-20.
- [82] Tomas Jezo, Michael Klasen, and Florian König. “Prompt photon production and photon-hadron jet correlations with POWHEG.” In: *JHEP* 11 (2016), p. 033. DOI: [10.1007/JHEP11\(2016\)033](https://doi.org/10.1007/JHEP11(2016)033). arXiv: [1610.02275](https://arxiv.org/abs/1610.02275) [hep-ph].



- [83] Patrick Aurenche, Michel Fontannaz, Jean-Philippe Guillet, Eric Pilon, and Monique Werlen. “A New critical study of photon production in hadronic collisions.” In: *Phys. Rev. D* 73 (2006), p. 094007. DOI: [10.1103/PhysRevD.73.094007](https://doi.org/10.1103/PhysRevD.73.094007). arXiv: [hep-ph/0602133](https://arxiv.org/abs/hep-ph/0602133) [hep-ph].
- [84] S. Catani, M. Fontannaz, J. P. Guillet, and E. Pilon. “Cross-section of isolated prompt photons in hadron hadron collisions.” In: *JHEP* 05 (2002), p. 028. DOI: [10.1088/1126-6708/2002/05/028](https://doi.org/10.1088/1126-6708/2002/05/028). arXiv: [hep-ph/0204023](https://arxiv.org/abs/hep-ph/0204023) [hep-ph].
- [85] Morad Aaboud et al. “Measurement of the cross section for inclusive isolated-photon production in  $pp$  collisions at  $\sqrt{s} = 13$  TeV using the ATLAS detector.” In: *Phys. Lett. B* 770 (2017), pp. 473–493. DOI: [10.1016/j.physletb.2017.04.072](https://doi.org/10.1016/j.physletb.2017.04.072). arXiv: [1701.06882](https://arxiv.org/abs/1701.06882) [hep-ex].
- [86] “LHC Guide.” Mar. 2017. URL: <https://cds.cern.ch/record/2255762>.
- [87] Hendrik Poppenborg. “Charged Jet Properties Measured with the ALICE Experiment.” MA thesis. Germany: Westfälische Wilhelms-Universität Münster, 2015.
- [88] The ATLAS Collaboration et al. “The ATLAS Experiment at the CERN Large Hadron Collider.” In: *J. Instrum.* 3.08 (Aug. 2008), So8003–So8003. ISSN: 1748-0221. DOI: [10.1088/1748-0221/3/08/S08003](https://doi.org/10.1088/1748-0221/3/08/S08003).
- [89] S. Chatrchyan et al. “The CMS experiment at the CERN LHC.” In: *J. Instrum.* 3.8 (2008). ISSN: 17480221. DOI: [10.1088/1748-0221/3/08/S08004](https://doi.org/10.1088/1748-0221/3/08/S08004).
- [90] Betty Bezverkhny Abelev et al. “Performance of the ALICE Experiment at the CERN LHC.” In: *Int. J. Mod. Phys. A* 29 (2014), p. 1430044. DOI: [10.1142/S0217751X14300440](https://doi.org/10.1142/S0217751X14300440). arXiv: [1402.4476](https://arxiv.org/abs/1402.4476) [nucl-ex].
- [91] The LHCb Collaboration et al. “The LHCb Detector at the LHC.” In: *J. Instrum.* 3.08 (Aug. 2008), So8005–So8005. ISSN: 1748-0221. DOI: [10.1088/1748-0221/3/08/S08005](https://doi.org/10.1088/1748-0221/3/08/S08005). URL: <http://stacks.iop.org/1748-0221/3/i=08/a=S08005?key=crossref.358ac80e1a6b6ba36f68c89dc0c4bed4>.
- [92] Pascal Dominik Hermes, Johannes Peter Wessels, Roderik Bruce, Johannes Peter Wessels, and Roderik Bruce. “Heavy-Ion Collimation at the Large Hadron Collider: Simulations and Measurements.” Presented 19 Dec 2016. Sept. 2016. URL: <https://cds.cern.ch/record/2241364>.
- [93] Mirko Pojer et al. “LHC Operational Experience of the 6.5 TeV Proton Run with ATS Optics.” In: *Proceedings, 9th International Particle Accelerator Conference (IPAC 2018): Vancouver, BC Canada, April 29-May 4, 2018*. 2018, MOPMF050. DOI: [10.18429/JACoW-IPAC2018-MOPMF050](https://doi.org/10.18429/JACoW-IPAC2018-MOPMF050).
- [94] Albert M Sirunyan et al. “Study of jet quenching with isolated-photon+jet correlations in PbPb and  $pp$  collisions at  $\sqrt{s_{NN}} = 5.02$  TeV.” In: *Phys. Lett. B* 785 (2018), pp. 14–39. DOI: [10.1016/j.physletb.2018.07.061](https://doi.org/10.1016/j.physletb.2018.07.061). arXiv: [1711.09738](https://arxiv.org/abs/1711.09738) [nucl-ex].
- [95] A. M. Sirunyan et al. “Particle-flow reconstruction and global event description with the CMS detector.” In: *JINST* 12.10 (2017), P10003. DOI: [10.1088/1748-0221/12/10/P10003](https://doi.org/10.1088/1748-0221/12/10/P10003). arXiv: [1706.04965](https://arxiv.org/abs/1706.04965) [physics.ins-det].
- [96] Roel Aaij et al. “Measurement of forward  $W$  and  $Z$  boson production in association with jets in proton-proton collisions at  $\sqrt{s} = 8$  TeV.” In: *JHEP* 05 (2016), p. 131. DOI: [10.1007/JHEP05\(2016\)131](https://doi.org/10.1007/JHEP05(2016)131). arXiv: [1605.00951](https://arxiv.org/abs/1605.00951) [hep-ex].

- [97] Thomas Boettcher. “Direct photon production at LHCb.” In: *Nucl. Phys.* A982 (2019), pp. 251–254. DOI: [10.1016/j.nuclphysa.2018.10.046](https://doi.org/10.1016/j.nuclphysa.2018.10.046).
- [98] K Aamodt et al. “Alignment of the ALICE Inner Tracking System with cosmic-ray tracks.” In: *JINST* 5 (2010), P03003. DOI: [10.1088/1748-0221/5/03/P03003](https://doi.org/10.1088/1748-0221/5/03/P03003). arXiv: [1001.0502](https://arxiv.org/abs/1001.0502) [[physics.ins-det](#)].
- [99] J. Alme et al. “The ALICE TPC, a large 3-dimensional tracking device with fast readout for ultra-high multiplicity events.” In: *Nuclear Instruments and Methods in Physics Research A* 622 (Oct. 2010), pp. 316–367. DOI: [10.1016/j.nima.2010.04.042](https://doi.org/10.1016/j.nima.2010.04.042). arXiv: [1001.1950](https://arxiv.org/abs/1001.1950) [[physics.ins-det](#)].
- [100] U. Abeysekara et al. “ALICE EMCal Physics Performance Report.” In: (2010). arXiv: [1008.0413](https://arxiv.org/abs/1008.0413) [[physics.ins-det](#)].
- [101] C. W. Fabjan and F. Gianotti. “Calorimetry for particle physics.” In: *Rev. Mod. Phys.* 75 (2003), pp. 1243–1286. DOI: [10.1103/RevModPhys.75.1243](https://doi.org/10.1103/RevModPhys.75.1243).
- [102] U. Abeysekara et al. “ALICE EMCal Physics Performance Report.” In: (2010). arXiv: [1008.0413](https://arxiv.org/abs/1008.0413) [[physics.ins-det](#)].
- [103] A. Akindinov et al. “Performance of the ALICE Time-Of-Flight detector at the LHC.” In: *Eur. Phys. J. Plus* 128 (2013), p. 44. DOI: [10.1140/epjp/i2013-13044-x](https://doi.org/10.1140/epjp/i2013-13044-x).
- [104] Betty Abelev et al. “Centrality determination of Pb-Pb collisions at  $\sqrt{s_{NN}} = 2.76$  TeV with ALICE.” In: *Phys. Rev.* C88.4 (2013), p. 044909. DOI: [10.1103/PhysRevC.88.044909](https://doi.org/10.1103/PhysRevC.88.044909). arXiv: [1301.4361](https://arxiv.org/abs/1301.4361) [[nucl-ex](#)].
- [105] Arturo Fernandez Tellez. “ACORDE, The ALICE Cosmic Ray Detector.” In: *Proceedings, 30th International Cosmic Ray Conference (ICRC 2007): Merida, Yucatan, Mexico, July 3-11, 2007*. Vol. 5. 2007, pp. 1201–1204.
- [106] S. van der Meer. *Calibration of the effective beam height in the ISR*. Tech. rep. CERN-ISR-PO-68-31. ISR-PO-68-31. Geneva: CERN, 1968. URL: <http://cds.cern.ch/record/296752>.
- [107] “ALICE luminosity determination for pp collisions at  $\sqrt{s} = 8$  TeV.” In: (2017). URL: <https://cds.cern.ch/record/2255216>.
- [108] Rene Brun and Fons Rademakers. “ROOT — An object oriented data analysis framework.” In: *Nucl. Instruments Methods Phys. Res. Sect. A Accel. Spectrometers, Detect. Assoc. Equip.* 389.1-2 (Apr. 1997), pp. 81–86. ISSN: 01689002. DOI: [10.1016/S0168-9002\(97\)00048-X](https://doi.org/10.1016/S0168-9002(97)00048-X). URL: <http://linkinghub.elsevier.com/retrieve/pii/S016890029700048X>.
- [109] S. Agostinelli et al. “GEANT4: A Simulation toolkit.” In: *Nucl. Instrum. Meth.* A506 (2003), pp. 250–303. DOI: [10.1016/S0168-9002\(03\)01368-8](https://doi.org/10.1016/S0168-9002(03)01368-8).
- [110] Fritz W. Bopp, R. Engel, and J. Ranft. “Rapidity gaps and the PHOJET Monte Carlo.” In: *High energy physics. Proceedings, LAFEX International School, Session C, Workshop on Diffractive Physics, LISHEP'98, Rio de Janeiro, Brazil, February 16-20, 1998*. 1998, pp. 729–741. arXiv: [hep-ph/9803437](https://arxiv.org/abs/hep-ph/9803437) [[hep-ph](#)].
- [111] G. Antchev et al. “Luminosity-Independent Measurement of the Proton-Proton Total Cross Section at  $\sqrt{s} = 8$  TeV.” In: *Phys. Rev. Lett.* 111.1 (2013), p. 012001.

- [112] Simone Alioli, Paolo Nason, Carlo Oleari, and Emanuele Re. “NLO vector-boson production matched with shower in POWHEG.” In: *JHEP* 07 (2008), p. 060. DOI: [10.1088/1126-6708/2008/07/060](https://doi.org/10.1088/1126-6708/2008/07/060). arXiv: [0805.4802](https://arxiv.org/abs/0805.4802) [hep-ph].
- [113] Louis Lyons, Duncan Gibaut, and Peter Clifford. “How to Combine Correlated Estimates of a Single Physical Quantity.” In: *Nucl. Instrum. Meth.* A270 (1988), p. 110. DOI: [10.1016/0168-9002\(88\)90018-6](https://doi.org/10.1016/0168-9002(88)90018-6).
- [114] A. A. Bylinkin and A. A. Rostovtsev. “Parametrization of the shape of hadron-production spectra in high-energy particle interactions.” In: *Phys. Atom. Nucl.* 75 (2012). [*Yad. Fiz.*75,1060(2012)], pp. 999–1005.
- [115] Michael Klasen, Christian Klein-Bösing, and H. Poppenborg. “Prompt photon production and photon-jet correlations at the LHC.” In: *JHEP* 03 (2018), p. 081. DOI: [10.1007/JHEP03\(2018\)081](https://doi.org/10.1007/JHEP03(2018)081). arXiv: [1709.04154](https://arxiv.org/abs/1709.04154) [hep-ph].
- [116] Richard D. Ball, Valerio Bertone, Stefano Carrazza, Luigi Del Debbio, Stefano Forte, Alberto Guffanti, Nathan P. Hartland, and Juan Rojo. “Parton distributions with QED corrections.” In: *Nucl. Phys.* B877 (2013), pp. 290–320. DOI: [10.1016/j.nuclphysb.2013.10.010](https://doi.org/10.1016/j.nuclphysb.2013.10.010). arXiv: [1308.0598](https://arxiv.org/abs/1308.0598) [hep-ph].
- [117] L. Bourhis, M. Fontannaz, and J. P. Guillet. “Quarks and gluon fragmentation functions into photons.” In: *Eur. Phys. J.* C2 (1998), pp. 529–537. DOI: [10.1007/s100520050158](https://doi.org/10.1007/s100520050158). arXiv: [hep-ph/9704447](https://arxiv.org/abs/hep-ph/9704447) [hep-ph].
- [118] John M. Campbell, R. Keith Ellis, and Ciaran Williams. “Direct Photon Production at Next-to-Next-to-Leading Order.” In: *Phys. Rev. Lett.* 118.22 (2017), p. 222001. DOI: [10.1103/PhysRevLett.118.222001](https://doi.org/10.1103/PhysRevLett.118.222001). arXiv: [1612.04333](https://arxiv.org/abs/1612.04333) [hep-ph].
- [119] *Study of Isolated photon jet correlation in PbPb and pp collisions at 2.76TeV and pPb collisions at 5.02TeV*. Tech. rep. CMS-PAS-HIN-13-006. Geneva: CERN, 2013. URL: <http://cds.cern.ch/record/1631991>.
- [120] S. Acharya et al. “Transverse momentum spectra and nuclear modification factors of charged particles in pp, p-Pb and Pb-Pb collisions at the LHC.” In: *JHEP* 11 (2018), p. 013. DOI: [10.1007/JHEP11\(2018\)013](https://doi.org/10.1007/JHEP11(2018)013). arXiv: [1802.09145](https://arxiv.org/abs/1802.09145) [nucl-ex].
- [121] Pingal Dasgupta, Somnath De, Rupa Chatterjee, and Dinesh K. Srivastava. “Photon production from Pb+Pb collisions at  $\sqrt{s_{NN}} = 5.02$  TeV at LHC and at  $\sqrt{s_{NN}} = 39$  TeV at FCC.” In: *Phys. Rev.* C98.2 (2018), p. 024911. DOI: [10.1103/PhysRevC.98.024911](https://doi.org/10.1103/PhysRevC.98.024911). arXiv: [1804.02828](https://arxiv.org/abs/1804.02828) [nucl-th].
- [122] Shreyasi Acharya et al. “Direct photon production at low transverse momentum in proton-proton collisions at  $\sqrt{s} = 2.76$  and 8 TeV.” In: *Phys. Rev.* C99.2 (2019), p. 024912. DOI: [10.1103/PhysRevC.99.024912](https://doi.org/10.1103/PhysRevC.99.024912). arXiv: [1803.09857](https://arxiv.org/abs/1803.09857) [nucl-ex].
- [123] Michael Klasen. “Theory of hard photoproduction.” In: *Rev. Mod. Phys.* 74 (2002), pp. 1221–1282. DOI: [10.1103/RevModPhys.74.1221](https://doi.org/10.1103/RevModPhys.74.1221). arXiv: [hep-ph/0206169](https://arxiv.org/abs/hep-ph/0206169) [hep-ph].
- [124] Muhammad Goharipour and Hossein Mehraban. “Study of isolated prompt photon production in p-Pb collisions for the ALICE kinematics.” In: *Phys. Rev.* D95.5 (2017), p. 054002. DOI: [10.1103/PhysRevD.95.054002](https://doi.org/10.1103/PhysRevD.95.054002). arXiv: [1702.05738](https://arxiv.org/abs/1702.05738) [hep-ph].

- [125] Jaroslav Adam et al. "Measurement of charged jet production cross sections and nuclear modification in p-Pb collisions at  $\sqrt{s_{NN}} = 5.02$  TeV." In: *Phys. Lett. B* 749 (2015), pp. 68–81. DOI: [10.1016/j.physletb.2015.07.054](https://doi.org/10.1016/j.physletb.2015.07.054). arXiv: [1503.00681](https://arxiv.org/abs/1503.00681) [nucl-ex].
- [126] Thomas Peitzmann. "Measurement of forward direct photon production in p-A at the LHC with ALICE - A probe for nuclear PDFs and saturation." In: *PoS DIS2016* (2016), p. 273. DOI: [10.22323/1.265.0273](https://doi.org/10.22323/1.265.0273). arXiv: [1607.01673](https://arxiv.org/abs/1607.01673) [hep-ex].
- [127] *Production of pairs of isolated photons in association with jets in pp collisions at  $\sqrt{s} = 7$  TeV.* Tech. rep. CMS-PAS-SMP-14-021. Geneva: CERN, 2015. URL: <http://cds.cern.ch/record/2035758>.
- [128] Roel Aaij et al. "First experimental study of photon polarization in radiative  $B_s^0$  decays." In: *Phys. Rev. Lett.* 118.2 (2017), p. 021801. DOI: [10.1103/PhysRevLett.118.021801](https://doi.org/10.1103/PhysRevLett.118.021801), [10.1103/PhysRevLett.118.109901](https://doi.org/10.1103/PhysRevLett.118.109901). arXiv: [1609.02032](https://arxiv.org/abs/1609.02032) [hep-ex].
- [129] K. Kovarik et al. "nCTEQ15 - Global analysis of nuclear parton distributions with uncertainties in the CTEQ framework." In: *Phys. Rev. D* 93.8 (2016), p. 085037. DOI: [10.1103/PhysRevD.93.085037](https://doi.org/10.1103/PhysRevD.93.085037). arXiv: [1509.00792](https://arxiv.org/abs/1509.00792) [hep-ph].
- [130] D. Bourilkov, R. C. Group, and M. R. Whalley. "LHAPDF: PDF use from the Tevatron to the LHC." In: *TeV4LHC Workshop - 4th meeting Batavia, Illinois, October 20-22, 2005*. 2006. arXiv: [hep-ph/0605240](https://arxiv.org/abs/hep-ph/0605240) [hep-ph].





## LEBENS LAUF

---

Name: Hendrik Poppenborg  
Geburtsdatum: 17.11.1987  
Staatsangehörigkeit: Deutsch  
Eltern: Michael Poppenborg und Doris Poppenborg (geb. Brünemann)

### **Schulbildung**

08/1994 – 07/1997 Kardinal-von-Galen Grundschule, Sendenhorst  
08/1997 – 06/2006 St. Michael Gymnasium, Ahlen  
06/2006 Allgemeine Hochschulreife

### **Wehrdienst**

10/2006 – 06/2007 Pflichtwehrdienst in Bückeberg und Münster-Handorf

### **Studium**

Seit 10/2007 Studium der Physik an der WWU Münster  
09/2011 Bachelor of Science  
09/2015 Master of Science  
Seit 10/2015 Promotionsstudium an der WWU Münster





## DANKSAGUNG

---

Zum Ende möchte ich mich bei allen bedanken, die zum Gelingen dieser Arbeit beigetragen haben.

Zuerst möchte ich mich bei den Verantwortlichen des Graduiertenkollegs und der DFG bedanken, die nicht nur diese Arbeit ermöglicht haben, sondern auch die vielen Reisen und Weiterbildungen, und nicht zuletzt den interessanten Austausch mit den theoretischen Physikern.

Bezüglich des theoretischen Projekts danke ich Florian König für seine Hilfe und dafür, dass ich weitere Früchte ernten konnte aufgrund seiner Doktorarbeit. I would like to thank Ilkka Helenius for his assistance in modifying Jetphox and Tomas Jezo for his assistance in publishing the direct photon code of POWHEG. Im Bezug auf die experimentelle Arbeit danke ich Daniel, Nico und Fredi für den Einstieg und die weitere Hilfe.

Ich möchte Christian und Michael danken für die Begutachtung dieser Arbeit, aber vor allem für die Betreuung und die gute Zusammenarbeit. Die viele Diskussionen über die Physik haben mir am meisten Spaß gemacht.

Christian danke ich vor allem, weil er der tägliche Ansprechpartner für wissenschaftliche und unwissenschaftliche Angelegenheiten war — Vielen Dank für deine gelassene und gleichzeitig gewissenhafte Art.

Ich möchte der Arbeitsgruppe danken, und vor allem jenen Leuten, die mich jetzt schon länger begleiten. Ich danke euch für die Hilfsbereitschaft im Alltag oder in speziellen Phasen, wie z.B. im Endspurt einer Doktorarbeit, aber vor allem für den ganzen Spaß und den ganzen Quatsch im Kaffeeraum und abseits der Waschbetonmauern unserer kleinen Welt.

Zuletzt und vor allem bedanke ich mich bei meinen wichtigsten Stützen: bei meiner Familie und meiner Sophia.